UNIVERSITY OF SOUTHAMPTON

FACULTY OF ENGINEERING AND THE ENVIRONMENT

Aerodynamics and Flight Mechanics

An investigation of the fluid dynamics and heat transfer of high pressure flows in integrated gas delivery systems

by

Vishagen Ramasamy

Thesis for the degree of Doctor in Engineering

May 08, 2018

ABSTRACT

Fast filling of high-pressure gas storage cylinders causes heating that can damage the cylinder. This thesis presents the development of computational models that predict the thermal response during the fast filling of high-pressure gas storage cylinders with hydrogen or natural gas. The new computational models are validated and then used to assess a range of approaches for achieving rapid filling, without overheating the cylinder. A two-dimensional axisymmetric computational fluid dynamic (CFD) simulation of the fast refuelling of a hydrogen cylinder was performed and successfully validated by comparing the mass-averaged gas temperature throughout the fill to the published experimental results. Heat transfer models for fast-filling of cylinders with a range of length-to-diameter ratios (L/D) were developed with the heat transfer coefficient models calibrated using the CFD simulation data. A single-zone model was implemented for cylinders having a L/D less than 3.3 and a two-zone model for cylinders with a higher L/D. Both models model have shown a reasonable accuracy and robustness in simulating the fast-filling of hydrogen cylinders having different material properties and also for different fill times, while significantly lowering the computational time. The single-zone model was included as part of a series of elements that were used to model a hydrogen/CNG fast-filling station. Two case studies were performed that involved the fast-filling of a hydrogen vehicle (Toyota Mirai) and a natural gas vehicle (Honda Civic GX). The simulations showed that the filling of the hydrogen vehicle can be performed within one minute over a range of ambient temperatures and the use of phase change materials as part of the structure of the cylinder reduces the pre-cooling requirement. A study of the effects of inlet pressure profiles showed that, in the case of the Honda Civic GX, a fill time of approximately 19 seconds can be achieved, while gaining an increase of approximately 6 % in the final mass of gas by applying a step pressure profile at the exit of the dispenser.

Contents

ABSTRACT ..... **iii**

List of Figures ..... **xi**

List of Tables ..... **xxvii**

Declaration of Authorship ..... **xxxi**

Publications ..... **xxxiii**

Acknowledgements ..... **xxxv**

Nomenclature ..... **xxxvii**

Latin Symbols xxxvii

Greek Symbols xl

Abbreviations xli

1 Introduction **1**

1.1 Gaseous fuels 1

1.2 Physics of cylinder filling 2

1.3 Thermodynamics of the filling process 3

1.4 Modelling of the filling process 6

1.5 Aims and Objectives 6

1.6 Structure of the report 7

2 Literature Review **9**

2.1 Introduction 9

2.2 Filling Process 9

2.3 CNG & H_2 10

2.3.1 Hydrogen Refuelling Protocol 11
2.3.2 Natural Gas Refuelling Protocol....13
2.4 Cylinder filling experiments....14
2.5 Multi-dimensional CFD modelling of cylinder filling....26
2.6 Low order modelling of cylinder filling/discharging....37
2.7 Compressible flows in pipes & pipe components....46
2.8 Discharge Coefficient 48
2.9 Heat Storage & Heat transfer enhancement....50
2.10 Modelling of filling stations....51
2.11 Summary 52
3 Formulation....55
3.1 Introduction....55
3.2 2D numerical model....55
3.2.1 Cylinder filling....55
3.2.2 Pipe flow (Modelling the discharge coefficient) 62
3.3 Isentropic pipe flow (Modelling the discharge coefficient)....62
3.3.1 Calculation of the isentropic mass flow rate....62
3.3.2 Equation of State 63
3.4 Modelling of the filling station 63
3.4.1 Energy equation for the filling of the cylinder 63
3.4.2 Computing the mass flow rate into the cylinder....64
3.4.3 Computing heat transfer to the structure of the cylinder 65

3.4.4 Modelling the emptying of the bank 68
3.4.5 Modelling the flow in the piping system....68
3.5 Modelling heat transfer with a PCM....71
3.5.1 PCM as part of the structure 72
3.6 CFD (FLUENT) v/s Low order model....74
3.7 Summary 75
4 CFD model for the filling of the cylinder 77
4.1 Introduction....77
4.2 2D axisymmetric model of the fast-fill 77
4.2.1 Computational grid....77
4.2.2 Initial and boundary conditions....78
4.2.3 Grid independence & calculation activities....78
4.2.4 Resolution of the boundary layer 82
4.2.5 Validation of the CFD model 83
4.3 Increasing the L/D of the cylinder 89
4.3.1 Results....90
4.3.2 Effect of inlet diameter 94
4.4 Different inlet configurations 98
4.5 Summary 102
5 Low order model for the filling of the cylinder 105
5.1 Introduction....105
5.2 Modelling the viscous discharge coefficient....105

5.2.1 Determination of the isentropic mass flow rate and Reynolds number…….....105

5.2.2 Determination of the actual mass flow rate 107

5.3 C_{d1} of methane v/s hydrogen 110

5.4 Real gas effects on the viscous discharge coefficient 111

5.5 Modelling the heat transfer coefficient 114

5.5.1 Cylinders geometries and computational grids 114

5.6 Implementing the single-zone model 122

5.7 Implementing the two-zone model 124

5.8 Inclusion of conjugate heat transfer 127

5.9 Effect of the viscous discharge coefficient (C_{d1}) 128

5.10 Validation of the model 130

5.11 Effect of Natural convection 132

5.12 Inclusion of a phase change material (PCM) 134

5.13 Summary 137

6 Modelling of the fast-filling station 139

6.1 Introduction 139

6.2 Hydrogen fast-filling station 139

6.2.1 Refuelling at a pressure ramp rate of 28.5 MPa/min 142

6.2.2 Increasing the pressure ramp rate 147

6.2.3 Type III v/s Type IV cylinder 153

6.2.4 Inclusion of the phase change material 155

6.2.5 Step pressure profile at exit of the dispenser 159

6.3 CNG fast-filling station 162
6.3.1 Refuelling at a pressure ramp rate of 7.7 MPa/min 164
6.3.2 Varying the volume of the banks 167
6.3.3 Type III v/s Type IV cylinder 171
6.3.4 Increasing the pressure ramp rate 172
6.3.5 Effect of the ambient temperature 175
6.3.6 Step pressure profile at exit of the dispenser 176
6.3.7 Bank Pressure requirement 178
6.3.8 Inclusion of the phase change material 180
6.4 Summary 181
7 Conclusions & Recommendations 185
7.1 Computational modelling of cylinder filling 185
7.2 Analysis of the fast filling process 186
7.2.1 Improved heat transfer in large aspect ratio cylinders 186
7.2.2 Heat absorption with phase change materials 186
7.3 Modelling of the CNG/H_2 filling station 187
7.4 Recommendations for future work 188
Bibliography 189
Appendix A1 - Thermal properties of hydrogen gas 199
Appendix A2 - Thermal properties of methane 205
Appendix A3 - Closure Strategies 207
A3.1 The Reynolds stress 207

A3.2 The turbulent kinetic energy.....207

A3.3 The Reynolds heat flux.....208

A3.4 The turbulent transport and molecular diffusion terms.....208

Appendix A4 - Tank Dimensions & Material Properties [7].....209

Appendix A5 - Inlet boundary conditions [7] 211

Appendix A6- Isentropic relations for pipe flow 213

Appendix A7 - Diameter & Isentropic Reynolds number values for different pressure ratios and Mach number (H_2).....215

Appendix A8 - Pipe length with the l/d of 28.6 (H_2).....219

Appendix A9 - Diameter & length of pipe for different pressure ratios and isentropic Reynolds number (CH_4) 221

Appendix A10 - Diameters, pipe lengths and isentropic Mach numbers using the real gas EOS 223

Appendix A11 - Tank Material Properties [28, 86].....225

Appendix A12 – Inlet Boundary Conditions [27, 28, 30].....227

Appendix A13 – Reynolds number & Pressure drop within the piping system 229

Appendix A14 - Pressure of bank and dispenser (step profile) for H_2 filling 231

Appendix A15 - Comparison of Mach numbers at the exit of dispenser 233

Appendix A16 - Reynolds number & heat transfer coefficient (methane) ..235

Appendix A17 - Reynolds number and Pressure drop in the piping system (methane) 237

List of Figures

Figure 1.1: Physics involved in filling of tank. 2

Figure 1.2: Schematic of the filling process from an infinite reservoir. 3

Figure 1.3: Gas Temperature v/s mass of gas in the cylinder during the fill. 5

Figure 1.4: Gas Temperature v/s Gas Pressure in the cylinder during the fill. 5

Figure 2.1: Approaches of gaseous filling stations [10]. 9

Figure 2.2: Worldwide production of NGVs [13]. 11

Figure 2.3: Hydrogen fuelling window [17]. 12

Figure 2.4: Hydrogen filling pressure & temperature development in vehicle [17]. 12

Figure 2.5: Hydrogen filling communication system [17] 13

Figure 2.6: Layout of Toyota Mirai [20]. 13

Figure 2.7: Components of the fuel system of the Honda Civic GX [25]. 14

Figure 2.8: Experimental set up for the fast-filling of hydrogen [6]. 15

Figure 2.9: Standard variation of temperature v/s normalised time [6]. 16

Figure 2.10: Average gas temperature variation with different initial cylinder pressure [6] 16

Figure 2.11: Type IV cylinder with thermocouple locations [27]. 17

Figure 2.12: Gas temperature history [27]. 18

Figure 2.13: Schematic diagram of filling station [28]. 18

Figure 2.14: Structure of cylinder and location of thermocouples [28]. 19

Figure 2.15: Pressure and temperature variation during the fill [28]. 19

Figure 2.16: Experimental set-up [29]. 20

Figure 2.17: Inlet temperature for the 5 minutes 35 MPa fill [29]. 20

Figure 2.18: Cylinder and thermocouples locations [29]. 21

Figure 2.19: Temperature measurement for the five minute fill [29]. 21

Figure 2.20: Structure of cylinder and thermocouples locations [30]. 22

Figure 2.21: Measured and computed wall temperatures [30]. 23

Figure 2.22: Experimental set-up by Kim et al. [5]. 23

Figure 2.23: Gas temperature results with different initial pressure conditions [5]. 24

Figure 2.24: Influence of inlet gas temperature & mass flow rate on SOC (Type III cylinder) [32]. 25

Figure 2.25: Influence of inlet gas temperature & mass flow rate on SOC (Type IV cylinder) [32]. 25

Figure 2.26: Mean gas temperature throughout the fill [7]. 27

Figure 2.27: Mean gas temperature using various turbulence models [33]. 27

Figure 2.28: Mean gas temperature for the 35 MPa fill using various equations of state [41]. 28

Figure 2.29: Mean gas temperature for the 70 MPa fill using various equations of state [27]. 29

Figure 2.30: Heat flux along the inner wall [7]. 29

Figure 2.31: Mean streamlines using the four turbulence models 30s into the fill [36].....30

Figure 2.32: Mid-plane velocity vectors five seconds into the fill [41]. 30

Figure 2.33: Mid-plane contours of temperature during the fill [41].....31

Figure 2.34: Streamlines mid-plane at 294 s into the fill from an initial pressure of 0 MPa [5]. 32

Figure 2.35: Contours of temperature at 294 s into the fill from an initial pressure of 0 MPa [5]. 32

Figure 2.36: Structure of cylinder along with the thermocouple locations [46]. 32

Figure 2.37: Predicted local temperature comparison with experiment for 245 s fill [52]. 33

Figure 2.38: Comparison of the temperature results of the 2D and 3D model [27]. 33

Figure 2.39: Comparison of the gas temperature results for the various 2D meshes [27]. 34

Figure 2.40: Comparison of the average gas temperature obtained from experimental data and simulation [27]. 34

Figure 2.41: Temperature distribution at the end of the fill [28].....35

Figure 2.42: Temperature distribution at the end of the fill of cylinder with L/D of 4.4 [28]. 35

Figure 2.43: Gas temperature predictions with different ambient temperatures [28]. 36

Figure 2.44: Comparison of estimated and measured gas temperature [55]. 38

Figure 2.45: Comparison of predicted and experimental temperatures during the filling of vessel A [29]. 39

Figure 2.46: Comparison of predicted and experimental temperatures during the filling of vessel B [29]. 39

Figure 2.47: Comparison of predicted and experimental temperatures during the filling of vessel C [29].....40

Figure 2.48: Comparison of predicted and experimental temperatures during the discharge of Bank 2 [29]. 40

Figure 2.49: Predicted gas temperatures: (a) rectangular coordinates, (b) cylindrical coordinates [29]. 41

Figure 2.50: Structure of cylinder and thermocouple locations [28]. 41

Figure 2.51: Comparison of the predicted and measured gas temperature during the fill [56]. 42

Figure 2.52: Comparison of the predicted and measured gas temperature during the discharge [56]. 42

Figure 2.53: Dimensions of cylinder in mm and thermocouple locations inside (TC) and outside (TS) [63]. 43

Figure 2.54: Comparison of the predicted (straight line) and measured (shaded region) gas temperature for different initial gas pressures in the cylinder [63]. 43

Figure 2.55: Comparison of the predicted (straight line) and measured (shaded region) gas temperature for different pressure ramp rates [63]. 44

Figure 2.56: Structure of the cylinder with the different control volumes [30]. 44

Figure 2.57: Comparison of the predicted and measured gas temperature during the fill [30]. 45

Figure 2.58: Temperature profile of the NGV cylinder and bank during the fill [66]. 45

Figure 2.59: Velocity profile at the entrance of a pipe [63]. 47

Figure 2.60: Mid-plane section of the cylinder with the delivery tube [5]. 49

Figure 2.61: Fill time versus thickness of PCM for filling at ambient temperatures of 284 K and 293 K [80]. 51

Figure 3.1*:* Flow through a pipe. 62

Figure 3.2: 1D unsteady heat transfer across the cylinder wall. 67

Figure 3.3: Enthalpy (h) as a function of temperature: (a) pure substance, (b) mixed substance [73] 72

Figure 3.4: 1d unsteady heat transfer across cylinder walls that include PCM 72

Figure 4.1: Inner length-to-diameter ratio (L/D) of a cylinder. 77

Figure 4.2: 2D axisymmetric domain of the Type III cylinder. 78

Figure 4.3: Locations of instantaneous velocity measurements. 79

Figure 4.4: Instantaneous velocity magnitude across plane A (t = 6s).....80

Figure 4.5: Instantaneous velocity magnitude across plane B (t = 6s).....80

Figure 4.6: Instantaneous velocity magnitude across plane A (t = 18s).....80

Figure 4.7: Instantaneous velocity magnitude across plane B (t = 18s).....81

Figure 4.8: Instantaneous velocity magnitude across plane for the two time steps. 81

Figure 4.9: Instantaneous velocity magnitude across plane for the two time steps. 82

Figure 4.10: Maximum y* value throughout the fill. 83

Figure 4.11: Comparison of the mass-average gas temperatures. 84

Figure 4.12: Contours of total temperature: (a) 1 s, (b) 5 s, (c) 15 s, (d) 35 s. 84

Figure 4.13: Mass flow rate throughout the fill. 85

Figure 4.14: Average heat flux from the gas to the inner wall throughout the fill. 85

Figure 4.15: Flow field of the gas in the cylinder: (a) 1s, (b) 5s, (c) 15s, (d) 35s. 86

Figure 4.16: Magnitude of the velocity at the inlet during the fill. 86

Figure 4.17: Heat flux across the inner wall at different times during the fill. 87

Figure 4.18: Locations of temperature measurement 88

Figure 4.19: Temperature of liner and laminate (t = 1s).....88

Figure 4.20: Temperature of liner and laminate (t = 15s).....88

Figure 4.21: Temperature of liner and laminate (t = 35s).....88

Figure 4.22: 2D axisymmetric domains of the cylinders with varying length-to-diameter ratio (L/D).....89

Figure 4.23: Comparison of the mass-averaged gas temperature in cylinders with different L/D. 90

Figure 4.24: Comparison of the local maximum gas temperatures in cylinders with different L/D. 91

Figure 4.25: Difference between the maximum gas temperature and the mass averaged gas temperature 30s into the fill for the different cylinders with varying L/D. 91

Figure 4.26: Comparison of the contours of gas temperature 30 s into the fill for the different cylinders with varying L/D. 92

Figure 4.27: Flow field within the cylinders with varying L/D at the fill time of 30 s. 93

Figure 4.28: Schematic of the 2 fluid regions within the cylinder with a L/D > 3 ..93

Figure 4.29: Heat flux at the inner wall of the cylinder with L/D of 8 at different times during the 37 s fill. 94

Figure 4.30: Comparison of the mass-averaged gas temperatures in the cylinder (L/D =8) with different inlet sizes during the fill. 95

Figure 4.31: Comparison of the maximum local gas temperatures in the cylinder (L/D =8) with different inlet sizes.....95

Figure 4.32: Comparison of the mass flow rate in the cylinder (L/D=8) with different inlet sizes.....96

Figure 4.33: Comparison of the momentum flow rate at the different inlets five seconds and beyond into the fill. 96

Figure 4.34: Flow field within the cylinders with an L/D of 8 at the fill time of 30 s having different inlet diameters: (a) 5mm, (b) 7.07 mm and (c) 20mm. 97

Figure 4.35: Axial velocity of the gas in the axial direction half way between the centreline and the diameter of the cylinder 30s into the fill. 97

Figure 4.36: Long dual injector. 98

Figure 4.37: Comparison of the mass-averaged gas temperatures in the cylinder (L/D =8) with different inlet configurations. 99

Figure 4.38: Comparison of the maximum local gas temperatures in the cylinder (L/D =8) with different inlet configurations. 99

Figure 4.39: Comparison of the contours of gas temperature 30 s into the fill in the cylinder (L/D =8) with the different inlet configurations. 100

Figure 4.40: Flow field within the cylinders (L/D=8) with the different inlet configurations at the fill time of 30 s. 100

Figure 4.41: Comparison of the area average heat flux in the cylinder (L/D =8) throughout the fill with different inlet configurations 101

Figure 4.42: Comparison of the maximum temperature of the structure of the cylinder (L/D =8) throughout the fill with the different inlet configurations 101

Figure 5.1: Flow through the delivery pipe. 105

Figure 5.2: 2D axisymmetric domain of pipe with the length-to-diameter ratio of 28.6.....108

Figure 5.3: $\mathrm{Cd1}$ in a pipe of l/d of 28.6 with respect to the isentropic exit Mach number and Reynolds number. 109

Figure 5.4: $Cd1$ v/s Isentropic Reynolds number. 110

Figure 5.5: Comparison of C_{d1} of hydrogen and methane.....111

Figure 5.6: Mass flow rates comparison for case 1 ($\mathrm{Rei} = 5 \times 107$ and pressure ratio of 0.527). 113

Figure 5.7: Mass flow rates comparison for case 1 ($\mathrm{Rei} = 3.57 \times 106$ and pressure ratio of 0.8). 113

Figure 5.8: 2D axisymmetric domains of the cylinders with varying length-to-diameter ratio (L/D).....114

Figure 5.9: 2D axisymmetric computational grid of the cylinder having a L/D of 2. 115

Figure 5.10: Comparison of the mass-averaged gas temperature in the cylinders with different L/D with isothermal inner wall conditions.....116

Figure 5.11: Contours of the gas temperature 5s into the fill with isothermal inner wall conditions. 116

Figure 5.12: Flow field within the cylinders with varying L/D at the fill time of 5 s with isothermal inner wall conditions.....117

Figure 5.13: Schematic of the 2 fluid regions within the cylinder with a L/D > 3. 118

Figure 5.14: Mass-averaged gas temperature in the cylinder with a L/D of 2 with isothermal wall conditions.....118

Figure 5.15: Mass-averaged gas temperature in the cylinder with a L/D of 5 with isothermal wall conditions.....118

Figure 5.16: Mass-averaged gas temperature in the cylinder with a L/D of 8 with isothermal wall conditions.....119

Figure 5.17: Nusselt number v/s Inlet Reynolds number for cylinders with L/D of 5 and 8 for a single-zone model. 120

Figure 5.18: Nusselt number v/s Inlet Reynolds number for cylinders with L/D of 5 and 8 in Zone 1.....120

Figure 5.19: Relationship between the Nusselt numbers in zone 1 and zone 2.121

Figure 5.20: Comparison of the mass-averaged gas temperatures obtained from the 2D CFD model during the fill of cylinders having a L/D = 1.5, 2 and 3 with isothermal inner wall conditions. 122

Figure 5.21: Comparison of the mass-averaged gas temperatures between the 2D CFD and the single-zone model for the cylinder with a L/D of 2 with isothermal inner wall conditions. 123

Figure 5.22: Comparison of the mass-averaged gas temperatures between the 2D CFD and the single-zone model for the cylinder with a L/D of 3 with isothermal inner wall conditions. 124

Figure 5.23: Comparison of the mass-averaged gas temperatures between the 2D CFD and the single-zone model for the different cylinders with a L/D = 2 having different inlet diameters with isothermal inner wall conditions. 124

Figure 5.24: Comparison of the mass-averaged gas temperatures between the 2D CFD and the two-zone model for the different cylinders with isothermal inner wall conditions. 125

Figure 5.25: Comparison of the mass-averaged gas temperatures between the 2D CFD and the two-zone model for the different cylinders with a L/D = 5 having different inlet diameters with isothermal inner wall conditions. 126

Figure 5.26: Comparison of the mass-averaged gas temperatures between the 2D CFD and the two-zone model for the different cylinders with a L/D = 8 having different inlet diameters with isothermal inner wall conditions. 126

Figure 5.27: Comparison of the mass-averaged gas temperature obtained throughout the fill from the single-zone model and the experiment [7] 127

Figure 5.28: Comparison of the mass-averaged gas temperatures between the 2D CFD and the two-zone model including conjugate heat transfer for cylinders with L/D =4 and 8. 128

Figure 5.29: Comparison of the gas temperature profiles for different values of $Cd1$. 129

Figure 5.30: Comparison of the mass flow rate profiles for different values of $Cd1$ 129

Figure 5.31: Comparison of the inlet pressure and gas pressures within the cylinder for different values of C_{d1} 130

Figure 5.32: Comparison of the mass-averaged gas temperatures between the single-zone model and the experiment of Johnson et al. [30]. 131

Figure 5.33: Comparison of the mass-averaged gas temperatures between the single-zone model and the experiment and 2D CFD model of Zheng et al. [28]. 132

Figure 5.34: Comparison of the mass-averaged gas temperatures between the single-zone model and the experiment and 2D CFD model of Baraldi et al. [27]. 132

Figure 5.35: Profiles of the heat coefficients during the fill.....133

Figure 5.36: Comparison of the mass-averaged gas temperatures with and without natural convection.....134

Figure 5.37: Comparison of the final gas temperature with PCM thickness for PCM-1 and PCM-2. 135

Figure 5.38: Comparison of the final mass of gas with PCM thickness for PCM-1 and PCM-2. 135

Figure 5.39: Ratio of the final mass of gas to the structural mass with PCM thickness for PCM-1 and PCM-2. 136

Figure 6.1: Schematic diagram of a hydrogen filling station. 140

Figure 6.2: Pressure profile at the dispenser (Ramp rate of 28.5 MPa/min). 143

Figure 6.3: Gas temperature profiles in the cylinders with a ramp rate of 28.5 MPa/min with pre-cooling and no pre-cooling (ambient temperature = 293 K). .143

Figure 6.4: Gas temperature at the exit of the dispenser with pre-cooling and no pre-cooling (ramp rate = 28.5 MPa/min & ambient temperature = 293 K). 144

Figure 6.5: Pressure drop across the dispenser and piping network with pre-cooling temperature of 233 K (ramp rate = 28.5 MPa/min & ambient temperature = 293 K). 145

Figure 6.6: Pressure drop due to the components in the piping system with pre-cooling temperature of 233 K (ramp rate = 28.5 MPa/min & ambient temperature = 293 K). 146

Figure 6.7: Bank Pressures and dispenser pressure during the fill with pre-cooling temperature of 233 K (ramp rate = 28.5 MPa/min & ambient temperature = 293 K). 147

Figure 6.8: Bank temperatures during the fill with the pre-cooling temperature of 233 K (ramp rate = 28.5 MPa/min & ambient temperature = 293 K). 147

Figure 6.9: Gas temperature profiles in the 60 L cylinder at different ramp rates with pre-cooling temperature of 233 K (ambient temperature = 293 K).....149

Figure 6.10: Gas temperature profiles in the 60 L cylinder at different ramp rates with pre-cooling temperature of 243 K (ambient temperature = 293 K). 149

Figure 6.11: Gas temperature profiles in the 60 L cylinder at different ramp rates with pre-cooling temperature of 253 K (ambient temperature = 293 K). 149

Figure 6.12: Pressure drop across the piping system for pressure ramp rates of 28.5 MPa/min & 85.5 MPa/min (pre-cooling temperature = 233 K, ambient temperature = 293 K).....150

Figure 6.13: Pressure profiles of the banks and at the entrance and exit of dispenser for pressure ramp rate of 85.5 MPa/min (pre-cooling temperature = 233 K, ambient temperature = 293 K).....151

Figure 6.14: Amount of pre-cooling required to achieve a safe fill for the different ambient temperatures. 151

Figure 6.15: Gas temperature profiles in the 60 L cylinder at different ramp rates with maximum pre-cooling temperature (ambient temperature = 293 K). 152

Figure 6.16: Gas temperature profiles in the 60 L Type III cylinder at different ramp rates at an ambient temperature = 293 K (pre-cooling temperatures in parentheses). 153

Figure 6.17: Comparison of the maximum pre-cooling temperatures for the Type III and IV cylinders at an ambient temperature of 293 K for the different fill times. 154

Figure 6.18: Gas temperature profiles v/s mass of gas in Types III & IV 60 L cylinder as well as the adiabatic case (pre-cooling temperature = 258 K, ramp rate = 85 MPa/min & ambient temperature = 293 K). 154

Figure 6.19: Gas temperature profiles v/s mass of gas in Types III & IV 60 L cylinder with and without PCM-2 (pre-cooling temperature = 258 K, ramp rate = 85.50 MPa/min & ambient temperature = 293 K). 156

Figure 6.20: Structural temperature in the Type IV cylinder with PCM-2 at different times during the fill (pre-cooling temperature = 258 K, ramp rate = 85 MPa/min & ambient temperature = 293 K). 156

Figure 6.21: Structural temperature in the Type III cylinder with PCM-2 at different times during the fill (pre-cooling temperature = 258 K, ramp rate = 85 MPa/min & ambient temperature = 293 K). 157

Figure 6.22: Measure of the amount of pre-cooling required at the different ambient temperatures for a complete safe fill of the original Type IV cylinders and the newly designed Type III cylinders with PCM-2.....158

Figure 6.23: Comparison of the specific exergy for pre-cooling at the different ambient temperatures for a complete safe fill of the original Type IV cylinders and the newly designed Type III cylinders with PCM-2. 158

Figure 6.24: Step pressure profile of 88 MPa prescribed at the exit of the dispenser 159

Figure 6.25: Pressure profiles at the exit of the dispenser for the filling of the of the newly designed cylinders (step profile, ambient temp = 313 K, pre-cooling temp = 233 K) 160

Figure 6.26: Gas temperature profiles in both the 60 L and 62.4 L of the newly designed cylinders (step profile, ambient temp = 313 K, pre-cooling temp = 233 K) 160

Figure 6.27: Gas temperature profiles in both the 60 L and 62.4 L of the newly designed cylinders (step profile, ambient temp = 313 K, pre-cooling temp = 203 K) 161

Figure 6.28: Schematic diagram of a CNG filling station during the filling of 2015 Honda Civic GX. 163

Figure 6.29: Pressure at the exit of the dispenser (initial ramp rate = 7.7 MPa/min). 164

Figure 6.30: Comparison of the gas temperatures in the Type II cylinder for the first 15 seconds of the fill for methane and natural gas. 165

Figure 6.31: Gas temperature during the fill of the 100 L cylinder (ramp rate = 7.7 MPa/min & ambient temperature = 293 K). 166

Figure 6.32: Pressure profiles of the banks and at the entrance and exit of dispenser for a pressure ramp rate of 7.7 MPa/min (ambient temperature = 293 K). 167

Figure 6.33: Gas temperature at the exit of the dispenser (ramp rate = 7.7 MPa/min & ambient temperature = 293 K). 167

Figure 6.34: Pressure profiles of the banks with volumes of 400 L and 1200 L (ramp rate 7.7 MPa/min & ambient temperature = 293 K). 168

Figure 6.35: Pressure profiles of the banks with volumes of 200 L (ramp rate 7.7 MPa/min & ambient temperature = 293 K). 168

Figure 6.36: Comparison of the gas temperature at the exit of the dispenser with bank volumes of 400 L & 1200 L (ramp rate = 7.7 MPa/min & ambient temperature = 293 K). 169

Figure 6.37: Comparison of the gas temperatures in the banks with volumes of 400 L & 1200 L (ramp rate = 7.7 MPa/min & ambient temperature = 293 K). 170

Figure 6.38: Pressure drop across the dispenser with banks volumes of 400 L and 1200 (ramp rate = 7.7 MPa/min & ambient temperature = 293 K). 171

Figure 6.39: Comparison of the gas temperatures for the Type III and IV cylinders as well as for adiabatic conditions (ramp rate = 7.7 MPa/min & ambient temperature = 293 K).....171

Figure 6.40: Comparison of the gas temperature Comparison for the Type III 100 L cylinder at different ramp rates (ambient temperature = 293 K).....173

Figure 6.41: Heat flux for the different pressure ramp rates (ambient temperature = 293 K).....173

Figure 6.42: Pressure profiles of the banks and at the entrance and exit of dispenser for a pressure ramp rate of 22.8 MPa/min (ambient temperature = 293 K).....174

Figure 6.43: Comparison of the gas temperature profiles at the different ambient temperatures (ramp rate = 22.8 MPa/min).....175

Figure 6.44: Step pressure profile of 25 MPa prescribed at the exit of the dispenser 176

Figure 6.45: Comparison of the pressure profiles in the cylinder at different ambient temperatures with a step pressure profile at the exit of the dispenser.....177

Figure 6.46: Comparison of the gas temperature profiles in the cylinder at the different ambient temperatures with a ramp pressure profile of 22.8 MPa/min v/s a step pressure profile at the exit of the dispenser. 177

Figure 6.47: Comparison of the final mass of gas in the cylinder at the different ambient temperatures with a ramp pressure profile of 22.8 MPa/min v/s a step pressure profile at the exit of the dispenser. 178

Figure 6.48: Pressure profile at the entrance and exit of the dispenser as well as the bank pressure for the step pressure profile of 25 MPa at ambient temperatures of 273 K, 293 K and 313 K.....178

Figure 6.49: Comparison of the mass flow rate with a step pressure profile of 25 MPa being applied at the exit of the dispenser (ambient temperature = 273 K, 293 K, 313 K).....179

Figure 6.50: Comparison of the gas temperature profiles in the cylinder at the different ambient temperatures with a step pressure profile at the exit of the dispenser for the cylinder with and with PCM. 180

Figure A1.1: Specific enthalpy of hydrogen at different temperatures and pressures. 199

Figure A1.2: Specific entropy of hydrogen at different temperatures and pressures. 200

Figure A1.3: Joule-Thomson coefficient of hydrogen at different temperatures and pressures.....201

Figure A1.4: Specific internal energy of hydrogen at different pressures and temperatures. 202

Figure A1.5: Compressibility factor of hydrogen at different pressures and temperatures. 203

Figure A2.1: Specific enthalpy of methane at different temperatures and pressures. 205

Figure A2.2: Specific entropy of methane at different temperatures and pressures. 206

Figure A2.3: Joule-Thomson coefficient of methane at different temperatures and pressures.....207

Figure A2.4: Specific internal energy of methane at different pressures and temperatures. 208

Figure A2.5: Compressibility factor of methane at different pressures and temperatures. 209

Figure A5.1: Inlet boundary conditions [7]. 211

Figure A12.1: (a) Inlet pressure [27], (b) Inlet temperature [27]…….....227

Figure A12.2: (c) Inlet pressure [28], (d) Inlet temperature [28]. 227

Figure A12.3: (e) Inlet pressure [30], (f) Inlet temperature [30]. 227

Figure A13.1: Comparison of the Reynolds number in piping system (ramp of 85.5 MPa/min v/s step profile)…….....229

Figure A13.2: Comparison of the pressure drop in piping system (ramp of 85.5 MPa/min v/s step profile) 229

Figure A14.1: Pressure profile at the entrance and exit of the dispenser as well as the bank…….....231

Figure A15.1: Comparison of Mach numbers at the exit of the dispenser at the ambient temperature of 313 K (Step profile v/s ramp rate = 85.5 MPa/min)…..233

Figure A16.1: Comparison of the Reynolds number at the exit of the dispenser for the different pressure ramp rates……235

Figure A16.2: Comparison of the heat transfer coefficient in the cylinder for the different pressure ramp rates.....235

Figure A17.1: Comparison of the Reynolds number in the piping system with the pressure at the exit of the dispenser having step profile of 25 MPa and ramp rate of 7.7 MPa/min for the different ambient temperatures……..237

Figure A17.2: Comparison of the pressure drop in the piping system with the pressure at the exit of the dispenser having step profile of 25 MPa and ramp rate of 7.7 MPa/min for the different ambient temperatures.....237

List of Tables

Table 1.1: Types of pressure cylinders [5] 2

Table 2.1: Fuel tank capacity [25]. 14

Table 2.2: Computational time using the various turbulence models [33]. 27

Table 2.3: Loss coefficients of some pipe components [68]. 48

Table 3.1*:* Resistance coefficients of angle and ball valve [68]. 70

Table 3.2: Resistance coefficients of 45^0 and 90^0 smooth bend. 70

Table 4.1: Convergence criteria [81]. 79

Table 4.2: Inner surface areas and the ratio Dcyl/Dinlet of the cylinders having different L/D. 89

Table 4.3: Comparison of the ratio of the inner diameter of the cylinder having a L/D of 8 to the diameter of the inlet for the different inlet sizes. 94

Table 4.4: Comparison of the final mass-averaged gas temperatures and final mass of gas in the cylinder (L/D = 8) using the different inlet configurations. 98

Table 4.5: Comparison of the final mass-averaged gas temperatures and final mass of gas in the cylinder (L/D = 8) using the different inlet configurations. ..100

Table 5.1: Determination of the isentropic Mach numbers.....106

Table 5.2: Pressure ratios for methane for the different isentropic Mach numbers. 111

Table 5.3*:* Upstream conditions of pressure and temperature. 112

Table 5.4: Comparison of the computational times (Two-zone model v/s 2D CFD). 127

Table 5.5: Comparison of the final gas temperature and final mass of gas for different values of C_{d1} 129

Table 5.6: Material properties of PCM-1 and PCM-2 [76, 77]. 134

Table 5.7: Drop in gas temperature with increase in PCM-2 thickness.....136

Table 6.1: Product info of the 2016 Toyota Mirai [20]. 139

Table 6.2: Fill times and the final state of the gas at the end of the fill for the four different cases (ramp rate = 28.5 MPa/min & ambient temperature = 293 K). ...144

Table 6.3: Pressure ramp rate and expected fill times. 148

Table 6.4: Final pressure in bank 3 for pressure ramp rates of 28.5 MPa/min and 85.5 MPa/min. 150

Table 6.5: Maximum pre-cooling temperature to achieve a full and safe fill for the different delivery pressure ramp rates (Ambient temperature = 293 K). 152

Table 6.6: Comparison of the requirements and fill times for a ramp pressure profile of 85.5 MPa/min and a step profile for the newly designed cylinders 161

Table 6.7: Product info of the 2015 Honda Civic GX [25] 162

Table 6.8: Comparison of the computational time using methane and natural gas. 165

Table 6.9: Fill time and the final state of the gas at the end of the fill (ambient temperature = 293 K).....166

Table 6.10: Fill time and the final state of the gas at the end of the fill for the different bank volumes (ramp rate = 7.7 MPa/min & ambient temperature = 293 K).....169

Table 6.11: Pressure ramp rate and expected fill times.....172

Table 6.12: Fill times and the final state of the gas at the end of the fill for the different ramp rates (ambient temperature = 293 K).....174

Table 6.13: Fill times and the final state of the gas at the end of the fill for the ambient temperatures (ramp rate = 22.8 MPa/min).....176

Table 6.14: Comparison of the final mass of gas at the different ambient temperatures with a step pressure profile at the exit of the dispenser in the cylinder with and without PCM. 180

Table A4.1: Tank dimensions [7]…….209

Table A4.2: Tank material properties [7].....209

Table A7.1: Diameter & isentropic Reynolds number values for pressure ratio of 0.9 (Mach number = 0.120)…….....215

Table A7.2: Diameter & isentropic Reynolds number values for pressure ratio of 0.9 (Mach number = 0.390). 215

Table A7.3: Diameter & isentropic Reynolds number values for pressure ratio of 0.8 (Mach number = 0.573). 216

Table A7.4: Diameter & isentropic Reynolds number values for pressure ratio of 0.7 (Mach number = 0.731). 216

Table A7.5: Diameter & isentropic Reynolds number values for pressure ratio of 0.6 (Mach number = 0.885). 217

Table A7.6: Diameter & isentropic Reynolds number values for pressure ratio of 0.5274 (Mach number = 1). 217

Table A8.1: Length of pipe for the different isentropic Reynolds number with Mach number of 0.120…….219

Table A8.2: Length of pipe for the different isentropic Reynolds number with Mach number of 0.390. 219

Table A8.3: Length of pipe for the different isentropic Reynolds number with Mach number of 0.573. 219

Table A8.4: Length of pipe for the different isentropic Reynolds number with Mach number of 0.731. 220

Table A8.5: Length of pipe for the different isentropic Reynolds number with Mach number of 0.885. 220

Table A8.6: Length of pipe for the different isentropic Reynolds number with Mach number of 1 220

Table A9.1: Diameter of pipe for different pressure ratios when $\mathrm{Re}_{isen} = 10^4$…221

Table A9.2: Diameter of pipe for different pressure ratios when $\mathrm{Re}_{isen} = 2.23 \times 10^5$ 221

Table A9.3: Diameter of pipe for different pressure ratios when $\mathrm{Re}_{isen} = 1.78 \times 10^6$ 221

Table A9.4: Diameter of pipe for different pressure ratios when $\mathrm{Re}_{isen} = 1 \times 10^7$ 222

Table A10.1: lengths and pipe diameters for $\mathrm{Re}_{isen} = 5 \times 10^7$ and pressure ratio of 0.527 using real gas EOS…….....223

Table A10.2: lengths and pipe diameters for $\mathrm{Re}_{isen} = 3.57 \times 10^6$ and pressure ratio of 0.8 using real gas EOS.....223

Table A11.1: Material properties of liner and laminate of Type III cylinder [28]..225

Table A11.2: Material properties of liner and laminate of Type IV cylinder [86]. 225

Declaration of Authorship

I, Vishagen Ramasamy, declare that the thesis entitled: *An investigation of the fluid dynamics and heat transfer of high pressure flows in integrated gas delivery systems* and the work presented in the thesis are both my own, and have been generated by me as the result of my own original research. I confirm that:

- this work was done wholly or mainly in candidature for a research degree at the University of Southampton;
- where I have consulted the published work of others, this is always clearly attributed;
- where I have quoted from the work of others, the source is always given. With the exceptions of such quotations, this thesis is entirely my own work.
- I have acknowledged all main sources of help.

Signed:……..

Date:……May 08, 2018…….

Publications

Ramasamy, V., Richardson, E., Reed P., Hepples, W., Wheeler, A. (2017). EXPLOITATION OF PHASE CHANGE MATERIALS FOR TEMPERATURE CONTROL DURING THE FAST-FILLING OF HYDROGEN CYLINDERS., International Conference of Heat and Mass Transfer, Napoli, Italy.

Ramasamy, V., Richardson, E., Reed P., Hepples, W., Wheeler, A. (2018). INVESTIGATING THE USE OF PHASE CHANGE MATERIALS FOR TEMPERATURE CONTROL DURING THE FAST-FILLING OF HYDROGEN CYLINDERS, Journal of Computational Thermal Sciences.

Ramasamy, V., Richardson, E., Reed P., Hepples, W., Wheeler, A. A CFD STUDY OF FAST-FILLING STRATEGIES FOR HYDROGEN CYLINDERS, International Journal of Hydrogen Energy. (To be submitted – Waiting for approval from Luxfer Gas Cylinders)

Ramasamy, V., Richardson, E., Reed P., Hepples, W., Wheeler, A. THE IMPLEMENTATION OF A ZERO DIMENSIONAL FOR THE FAST-FILLING OF HYDROGEN CYLINDERS, International Journal of Hydrogen Energy. (To be submitted – Includes Chapter 5 of this thesis)

Acknowledgements

I would like to thank my four supervisors: Dr Andrew Wheeler, Dr Edward Richardson, Prof Philippa Reed and Dr Warren Hepples who each provided unique perspectives and advice throughout this research. I would also like to acknowledge the sponsors of this project: EPSRC and Luxfer Gas Cylinders. Finally, I would like to express my gratitude to my family: Vassen, Assodah, Hansen and Trickshi who have constantly supported me throughout this long academic journey.

Nomenclature

Latin Symbols

A – Inner surface area of cylinder [m^2]

A_{exit} – Area at the exit of nozzle [m^2]

a – Speed of sound [m/s]

$C_{1\varepsilon}$, $C_{2\varepsilon}$, $C_{3\varepsilon}$ – Constants in *k-ε* model

c_{cas} – Specific heat capacity of the casing of the encapsulated PCM [J/kg-K]

C_{d1}- Viscous discharge coefficient

$C_{laminate}$ – Specific heat capacity of the laminate [J/kg]

C_{liner} - Specific heat capacity of the liner [J/kg]

C_{PCM} - Specific heat capacity of the PCM [J/kg]

C_{μ} – Constant in turbulence model

c – Specific heat capacity [J/kg-K]

c_{sol} – Specific heat of solid [J/kg-K]

c_{liq} - Specific heat of liquid [J/kg-K]

D_{cyl} – Inner diameter of cylinder [m]

D_{inlet} – Inlet diameter [m]

d – Diameter of pipe [m]

d_{exit} – Diameter at the exit of nozzle [m]

E – Total energy per unit mass [J/kg]

f – Friction factor

G_b – Rate of generation of k due to buoyancy [m^2/s^3]

G_k – Rate of production of turbulent kinetic energy [m^2/

g – Acceleration due to gravity [m/s^2]

H – Favre average total enthalpy per unit mass [J/kg]

$h_{0_{bank}}$ - Specific stagnation enthalpy of the gas in the bank [J/kg]

$h_{0_{in}}$– Specific stagnation enthalpy of the gas at the inlet [J/kg]

H_l - Specific enthalpy of the liquid [J/kg]

H_{mix} – Specific enthalpy of solid and liquid mixture [J/kg]

H_{solid} – Specific enthalpy of the solid [J/kg]

h_{coef} – Heat transfer coefficient [W/m^2-K]

h_f – Heat transfer coefficient due to forced convection [W/m^2-K]

h_n – Heat transfer coefficient due to natural convection [W/m2-K]

h_{static} – Specific static enthalpy [J/kg]

j – Index for spatial nodes

K_L – Resistance coefficient

k – Turbulent kinetic energy per unit mass [m^2/s^2]

k_{exp} – Thermal expansion of gas [K^{-1}]

k_{gas} - Thermal conductivity of gas [W/m-K]

$k_{laminate}$ – Thermal conductivity of laminate [W/m-K]

k_{liner} – Thermal conductivity of liner [W/m-K]

k_{PCM} – Thermal conductivity of phase change material [W/m-K]

k_s – Thermal conductivity of solid material [W/m-K]

L – Specific latent heat of fusion [J/kg]

M – Mach number

m – Index for time step

m_{bank}- Mass of gas in the storage bank [kg]

m_{cas}- Mass of the casing of the encapsulated phase change material [kg]

m_{gas} – Mass of gas in the cylinder [kg]

m_{PCM} – Mass of Phase change material [kg]

$\dot{m}$ – Mass flow rate [kg/s]

$\dot{m}_{actual}$ – Actual mass flow rate [kg/s]

$\dot{m}_{isen}$ – Isentropic mass flow rate [kg/s]

m_{PCM} – Mass of phase change material

Nu_f – Nusselt number due to forced convection

Nu_n - Nusselt number due to natural convection

$\bar{P}$ – Mean pressure [Pa]

P_{loss} – Pressure loss in the pipe [Pa]

P_0 – Upstream stagnation pressure [Pa]

p – Downstream static pressure [Pa]

$\dot{Q}$ - Heat transfer rate at the wall of the bank [W]

$\dot{Q}_{wall}$ – Heat transfer rate at the inner wall of the cylinder [W]

$\dot{Q}_{PCM}$ – Heat transfer rate from the gas to the encapsulated PCM [W]

$\dot{q}$ – Heat flux [W/m^2]

R – Gas constant [J/kg-K]

Ra – Rayleigh number

Re_{isen} – Isentropic Reynolds number

Re_d – Reynolds number with respect to the diameter of the pipe

s – stability parameter in discretised heat equation

T_{gas} – Gas temperature [K]

T_{liq} – Temperature of phase change material in liquid state [K]

T_{mix} – Temperature of solid and liquid mixture [K]

T_{outer} – Temperature of outer surface of cylinder [K]

T_{PCM} – Temperature of phase change material [K]

T_S – Temperature of solid material [K]

T_{sol} – Temperature of phase change material in solid state [K]

T_{wall} – Inner wall temperature of cylinder [K]

t – Time [s]

U^* - Non-dimensional velocity

u_{bank}- Specific internal energy of gas in the bank [J/kg]

u_{gas} – Specific internal energy of gas in the cylinder [J/kg]

$\tilde{u}_i$ – Favre-averaged velocity [m/s]

V_{exit} – Velocity of gas at exit of the nozzle [m/s]

v – Average velocity of the gas [m/s]

ν_T – Eddy viscosity [Pa-s]

y* - Non-dimensional wall distance

Greek Symbols

α_s– Thermal diffusivity of solid material [m^2/s]

β – Coefficient of thermal expansion [K^{-1}]

ϵ – Roughness of pipe [m]

ε – Turbulent rate of dissipation [m^2/s^3]

δ_{ij} – Kronecker delta tensor

γ – Ratio of specific heats

μ – Dynamic viscosity [Pa-s]

ρ – Density [kg/m^3]

$\bar{\rho}$ - Mean density [kg/m^3]

ρ_s – Density of solid material [kg/m^3]

$\rho_{laminate}$ – Density of solid material [kg/m^3]

ρ_{liner} – Density of solid material [kg/m^3]

ρ_{PCM} – Density of solid material [kg/m^3]

τ_w – Wall shear stress [Pa]

Abbreviations

CNG – Compressed Natural gas

CFD – Computational Fluid Dynamics

DNS – Direct Numerical Simulation

NGV – Natural Gas Vehicle

NIST - National Institute of Standards and Technology

PCM – Phase Change Material

1 Introduction

1.1 Gaseous fuels

The growth in the use of energy in the past century has led to dwindling supplies of fossil fuels, rising levels of pollution and a lasting change in the global climate. Both compressed natural gas (CNG) and hydrogen have long been touted as an adequate substitute to petroleum fuels as a primary source of energy for vehicles. One major advantage of the use of such alternative fuels is the lower carbon dioxide emissions when combusted as opposed to conventional petroleum products.

Most transportation applications use liquids such as petrol and diesel as fuel due to their high energy storage. Natural gas and hydrogen are gases at ambient temperatures and exist as a liquid state only at cryogenic conditions. Liquid natural gas is normally stored in cryogenic tanks at -162 °C [1], while liquid hydrogen is kept at -253 °C [2]. Thus, for practical reasons, in order to increase the energy density of either natural gas or hydrogen, these gases are typically stored at high pressures in cylinders on board of alternative fuel vehicles. The development of the hydrogen economy as well as the full implementation of CNG have been hindered by the technological challenges associated with transport and delivery of high pressure gas, which is vital for the development of alternative fuel vehicles. The combination of fast-filling in the range of 3 to 5 minutes and high pressure storage (typically 35-70 MPa for H_2 & 24.8 MPa for CNG) are requirements that would meet the standards set by conventional vehicles in terms of refuelling time and driving range [17, 21]. The downside of a short filling time is an increase in temperature within the pressure vessel that can lead to its structural failure. As such, the maximum allowed temperature inside the vessel is set at 358 K by various international standards and regulations, while the maximum allowable pressure is 1.25 times the cylinder's design pressure [3, 4].

The development of valves and pressure vessels capable of meeting those requirements are key for the growth of alternative fuel vehicles. Solving these technological problems requires an understanding of the flow through the complex geometries within the valves and inside the pressure vessel. Conjugate heat transfer which is due to the interaction between the solid and compressed gases

within the vessel needs to be addressed so as to determine the appropriate material of the inner lining, which should be able to sustain high temperatures. In addition, with the gases being subjected to high pressures during the filling, significant deviation is expected from ideal gas behaviour and the compressibility factor of the gases in question needs consideration.

Gas cylinders are used for the storage of CNG and H_2 in vehicles and are classified from Type I to Type IV as shown in Table 1.1 [5].

Type I	All metal cylinder
Type II	Metal liner with hoop wrapping
Type III	Metal liner with full wrapping
Type IV	Plastic liner with full wrapping

Table 1.1: Types of pressure cylinders [5]

The Types III and IV cylinders are currently used as on-board storage for both CNG and hydrogen powered cars. The main function of the liner is leak-tightness, while the outer laminate, which is made of a carbon fibre reinforced polymer (CFRP), provides the structural strength.

1.2 Physics of cylinder filling

The physics associated with the flow and the thermal aspect of gas refuelling is shown in figure 1.1.

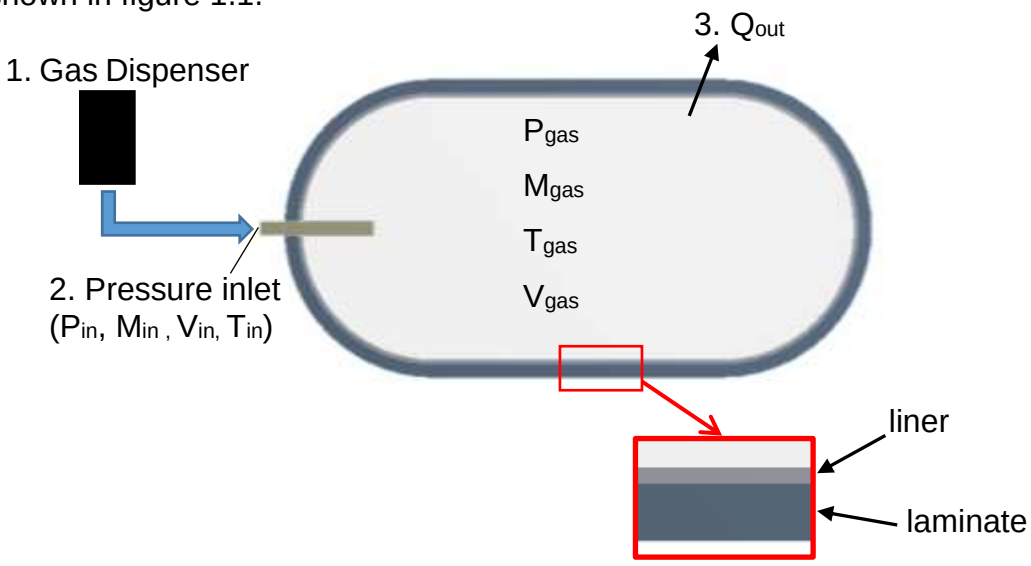

Figure 1.1: Physics involved in filling of tank.

At the filling station, the gas is stored in high pressure storage tanks and passes through a dispenser to the inlet and finally into the tank [6, 7]. The increase in gas temperature within the tank can be attributed for the following reasons:

1. The filling process consists of an inlet but no outlet, thus the PV work at the inlet is converted into the internal energy of the gas in the cylinder.
2. The gas already present in the vessel is compressed by the incoming high pressure gas at the inlet.

In the case of hydrogen filling, its negative Joule-Thompson coefficient at typical filling pressures and temperatures [6-8] and leads to a further increase in the gas temperature within the tank as the gas flows from a higher pressure into the cylinder.

1.3 Thermodynamics of the filling process

Figure 1.2 shows the schematic diagram of the filling process of a hydrogen cylinder that has a volume of 74 L from an infinite reservoir of hydrogen gas.

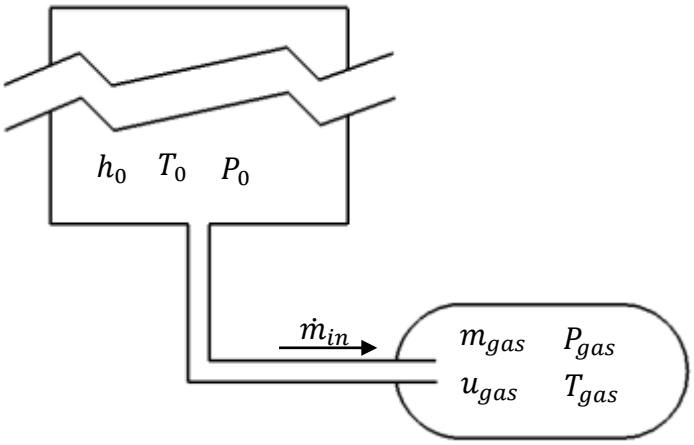

Figure 1.2: Schematic of the filling process from an infinite reservoir.

The pressure difference between the infinite reservoir and cylinder results in the gas being dispensed into the cylinder. Once the pressure equilibrium is achieved between the reservoir and the cylinder, mass transfer no longer occurs and the value of the mass flow rate $(\dot{m}_{in})$ is zero.

In this current thermodynamic model, the pressure (P_0) and temperature (T_0) of the gas in the infinite reservoir are set to 100 MPa and 293 K respectively. The initial pressure (P_0) and initial temperature in the cylinder are set to 2 MPa and 293

K respectively. Thus, assuming ideal gas conditions, the initial mass of hydrogen gas in the cylinder is 0.12 kg.

The energy equation for the filling of the cylinder without heat transfer is as follows:

$$\frac{d(m_{gas}u_{gas})}{dt} = h_0\dot{m}_{in} \tag{1.1}$$

where m_{gas} is the mass of gas in the tank, u_{gas} is the specific internal energy of the gas in the cylinder. h_0 is the stagnation enthalpy of the gas in the infinite reservoir. Equation 1.1 can also be written as:

$$\frac{d(U_{gas})}{dt} = h_0\dot{m}_{in} \tag{1.2}$$

where U_{gas} is the internal energy of the gas in the cylinder. Integrating Equation 1.2 on both sides with respect to time results in the following:

$$dU_{gas} = h_0\int_0^{\infty}\dot{m_{in}}\,dt \tag{1.3}$$

Equation 1.3 can also be written as follows:

$$\Delta U = h_0\Delta m_{gas} \tag{1.4}$$

Ideal gas conditions are assumed during the filling process. The stagnation enthalpy (h_0) for the gas in the infinite reservoir is constant during the filling the filling process and is only a function of the temperature obtained as follows:

$$h_0 = C_pT_0 \tag{1.5}$$

where C_p is the specific heat of hydrogen at constant pressure. Since hydrogen is a diatomic molecule, $C_p = \frac{7}{2}R_{spec}$ [94] and has a value of 14.5 KJ/(kg-K). R_{spec} is the specific gas constant of hydrogen and has a value of 4.124 KJ/(kg-K) [95].

The gas temperature in the cylinder during the fill is obtained as follows:

$$T_{gas} = \left(\frac{U_{gas}}{m_{gas}}\right)/C_v \tag{1.6}$$

where C_v is the specific heat of hydrogen at constant volume. Since hydrogen is a diatomic molecule, $C_v = \frac{5}{2}R_{spec}$ [94] and has a value of 10.4 KJ/(kg-K).

The gas pressure in the cylinder is obtained using the ideal gas equation of state:

$$P_{gas} = \frac{m_{gas} R_{spec} T_{gas}}{V} \tag{1.7}$$

where V is the volume of the cylinder and has a constant value of 0.074 m^3.

Figures 1.3 show that mass flow into the cylinder results in an increase in the gas temperature. Subsequently, this results in a rise in the gas pressure (Figure 1.4). Once the pressure in the cylinder reaches 100 MPa, pressure equilibrium is achieved between the cylinder and the infinite reservoir. At that point, no mass transfer occurs.

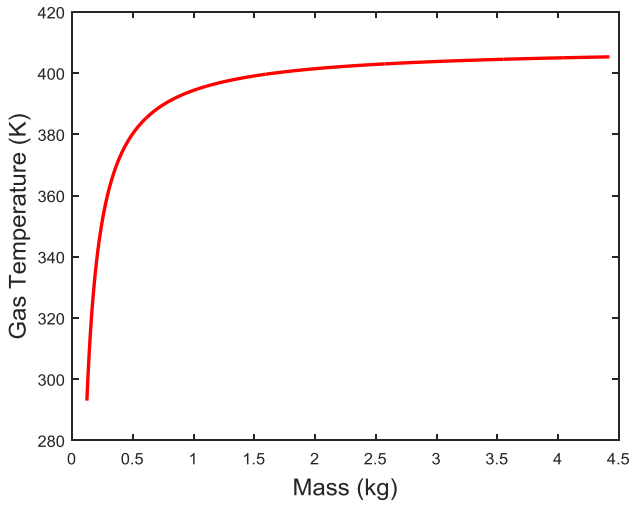

Figure 1.3: Gas Temperature v/s mass of gas in the cylinder during the fill.

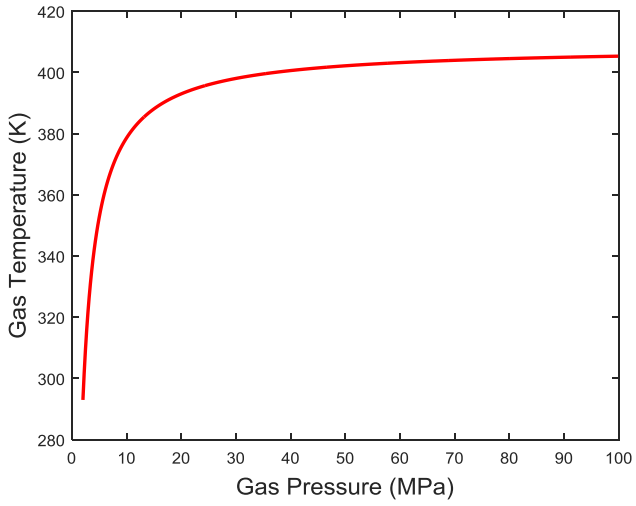

Figure 1.4: Gas Temperature v/s Gas Pressure in the cylinder during the fill.

1.4 Modelling of the filling process

The tank filling process is a transient problem which consists of an inlet but no outlet. For the correct simulations of tank filling, the inlet boundary conditions must accordingly vary with time similar to the real conditions. Tank filling is characterised by the high level of turbulence that exists within the tank and is due to the creation of fluctuating velocity fields by the high pressure of the incoming gas [7, 8]. Throughout the years, a large number of turbulence models have been developed which vary in complexity, from the one equation model to the more complicated ones such as the seven equation Reynolds Stress Model [9]. Each turbulence model has its own pros and cons and no model can accurately simulate every fluid flow without deviations from experimental results. Thus, the identification of the most appropriate turbulence model for a particular engineering flow is vital in CFD analysis.

The CFD simulation of a cylinder filling process is computationally very expensive, mainly due to its unsteadiness. While such computational resources may be readily available in research institutions, only a handful of industrial companies can afford to possess a supercomputer. In addition, CFD models require grid generation of the domain, which can be very time consuming. Thus, the development of a universal low order model that requires negligible computational time and is capable of predicting the heat transfer, temperature, pressure and mass of gas throughout the fill will be a useful tool for industry. Following its validation, the low order model can potentially also be used as a tool to optimize the fill and improve the design and materials used in cylinders.

1.5 Aims and Objectives

The study has been carried out with the aim to:

I. *Determine a turbulence model that capable of modelling the fast-filling of cylinders, while computing the conjugate heat transfer.*
II. *Produce a robust and a highly accurate low order model that simulates the filling of cylinders.*
III. *Develop network model that simulates the functioning of a CNG/H_2 filling station.*

IV. Develop new strategies that will lower the fill time of hydrogen/CNG vehicles while keeping the gas temperature below the required limit of 358 K.

To achieve the stated aim, the objectives of the study are:

- The CFD modelling and the subsequent validation of the filling of cylinders based on the literature review.
- The modelling of the Nusselt number that will be obtained from the CFD model and will be implemented in the low order model.
- The validation of the model with actual data of the fast-filling of vehicles.

1.6 Structure of the report

This report is divided into 7 chapters:

- Following this initial chapter, coverage of the literature related to previous research based on the filling of cylinder for vehicles that run on either CNG or hydrogen is discussed and analysed. The accuracy and reliability of the current numerical models that simulate the fast-filling of the cylinders is examined. The network of one-dimensional elements, such as compressible pipe flows and the emptying of the storage banks that is required to model the whole filling station is investigated. Finally, the use of phase change materials to enhance heat transfer during the fast-fill is explored.
- Chapter 3 describes the formulas that were used in the different models. Initially, the equations that are required for a two-dimensional axisymmetric CFD model of a fast-fill are described: the Navier-Stokes equations, the real gas equation of state, equations of the turbulence model and the transient heat equation. The numerical techniques and equations involved in the modelling of a fast-fill station are described and simulate the following:
    - Emptying of the high pressure banks.
    - The flow of the gas in a series of interconnecting pipes and valves from the banks to the dispenser.
    - The fast-filling of the cylinder.
    - The heat transfer through a phase change material that is either part of the structure of the cylinder or completely separate.
- Chapter 4 shows the validation of the 2D model for the fast refuelling of the cylinder. The effect of the length-to-diameter ratio (L/D) of the cylinder on the flow field and gas temperature during the fill is examined. Different filling

strategies are examined for cylinders with relatively large L/D using the CFD model.

- Chapter 5 includes the methodologies used in the modelling of the Nusselt number for cylinders with different L/D during the fast-fill. In addition, modelling of the discharge coefficient and its effect on the final gas temperature and mass of gas are also explained. In addition, the pros and cons of using phase change materials both as part of the structure of the cylinder for the fast-filling of hydrogen is discussed and analysed.
- Chapter 6 consists of case studies for both the hydrogen and the CNG filling station. The feasibility of a faster fill as opposed to the conventional 3 to 5 minutes is addressed along with pre-cooling strategies, higher delivery rates and the use of a phase change material as part of the structure of the cylinder. The thermal properties of hydrogen and methane at the relevant pressures and temperatures are shown in Appendix A1 and Appendix A2 respectively.
- Chapter 7 consists of the general conclusions that can be reached by this current work and recommendations for future work.

2 Literature Review

2.1 Introduction

This chapter will provide a review of the literature concerning the filling process of cylinders in vehicles that use gaseous fuels (compressed natural gas (CNG) and hydrogen), including experimental and computational studies. The previous modelling attempts for the filling of cylinders involves both multi-dimensional (2D and 3D) and low order models are discussed. The low order models that have been published are examined and the need for improvement of those models is highlighted. Examples of enhanced heat transfer and heat absorption involving the use of phase change materials as part of the structure of cylinder is examined. Finally, current models of entire filling stations are explored, which includes the modelling of different components of the filling station such as the piping network and valves.

2.2 Filling Process

There are currently two types of infrastructure that are used for the filling of CNG or hydrogen vehicles (Figure 2.1): time-fill and fast-fill [10].

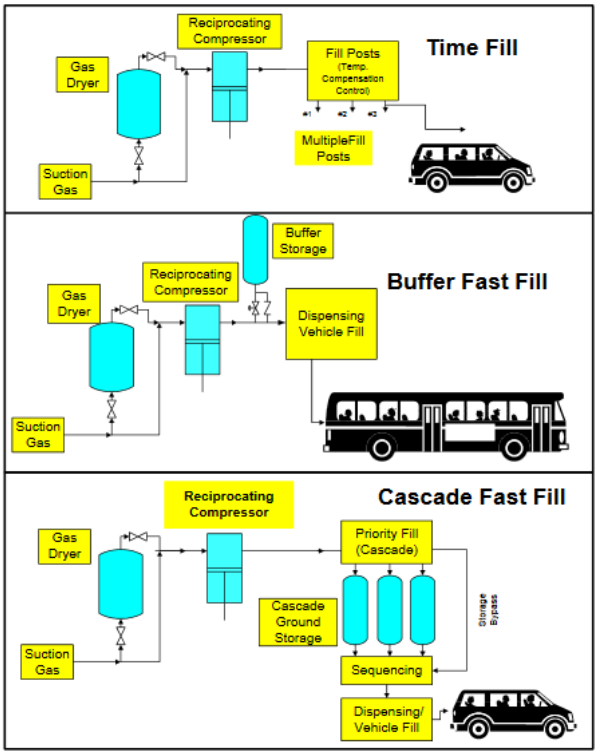

Figure 2.1: Approaches of gaseous filling stations [10].

Fleets such as buses with large cylinders, typically use the time-fill stations in which compressors are used directly for overnight filling. Fast-fill implies that the cylinders in the vehicles are filled within three to five minutes [10]. Fast-fill stations can be further broken down into the buffer fill and the cascade fill stations. In the buffer fill stations, compressors are used to fill a single bank, which is in turn used for the fast-filling of vehicles. The cascade fill involves the use of three or more storage banks that operate at different minimum pressure levels. The sizing of a fast-filling station, including the size of the compressors and the storage capacity is dependent upon the frequencies and quantities with which vehicles need refuelling during satisfy peak periods.

2.3 CNG & H_2

There are several factors that needs to be satisfied to convince consumers to switch from conventional gasoline powered cars to CNG/H_2 vehicles. Some of those factors are [11]:

1. The reliability of the vehicle.
2. The cost of the gaseous fuel.
3. The driving range of the vehicle.
4. The development of a network of CNG/H_2 filling stations
5. The filling time at station – drivers expect to spend a few minutes (less than 3 minutes) to refill the tanks.
6. Cost of the vehicle.

The development of hydrogen vehicles is still in its infancy as opposed to natural gas vehicles and according to a study by the China North Vehicle Research Institute [11], by 1995, more that 1.5 million vehicles were using natural gas as fuel. Natural gas has become one the most important sources of energy and currently accounts for 23% of the worldwide consumption [12]. In the meantime, over the past decade, the production of Natural Gas Vehicles (NGVs) has experienced an annual growth of 24% (Figure 2.2) and a similar trend is expected over the next couple of decades [13].

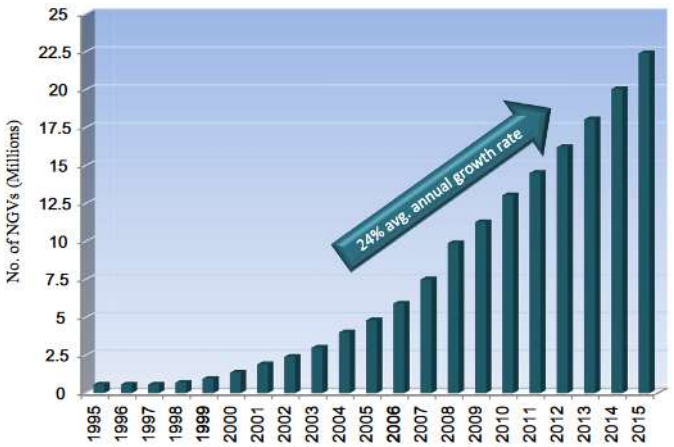

Figure 2.2: Worldwide production of NGVs [13].

As opposed to hydrogen, whose fuel measuring unit is in kilogram (kg), CNG is sold at the filling station in terms of gasoline gallon equivalent (GGE) [14]. One GGE represents the energy equivalent of a US gallon of gasoline (petrol). In terms of mass, one gasoline gallon equivalent of CNG is equal to 2.567 Kg [15].

The fuel mileage of a conventional by powered subcompact petrol vehicle (city car) is on average 27 MPG [16]. For example the 2015 Audi Quattro has a fuel mileage of 27 MPG with a tank size of 14.5 US gallons and a range 391.5 miles. To achieve similar range with acceptable tank sizes, the cylinders within the CNG and hydrogen vehicles must be filled to very high pressures.

2.3.1 Hydrogen Refuelling Protocol

The refuelling of light duty hydrogen vehicles is governed by the SAE TIR J2601 specification [17], which describes the safety limits and performance requirements for gaseous hydrogen fuel dispensers. SAE TIR J2601 includes protocols for two pressure classes; namely 35 MPa and 70 MPa and three fuel delivery temperatures (233 K, 243 K and 253 K). The rapid compression of the gas coupled with the negative Joule-Thompson coefficent of hydrogen at the filling pressure and temperature leads to an increase in the gas temperature and reduces the density of the gas. The State of Charge (SOC) is defined as the ratio (in percentage) between the density of the gas at the end of the fill and the density at 70 MPa and 283 K or at 87.5 MPa and 358 K, which correponds to 40.2 kg/m^3. In the case of a 70 MPa rated cylinder, the SOC indicates the level of the fill and is related to the pressure and temperature of the gas (Figure 2.3). While it is desirable to achieve

a SOC close to 100%, which will result into a larger driving range, the SOC must however not exceed the 100% as described in the SAE TIR J2601 [17].

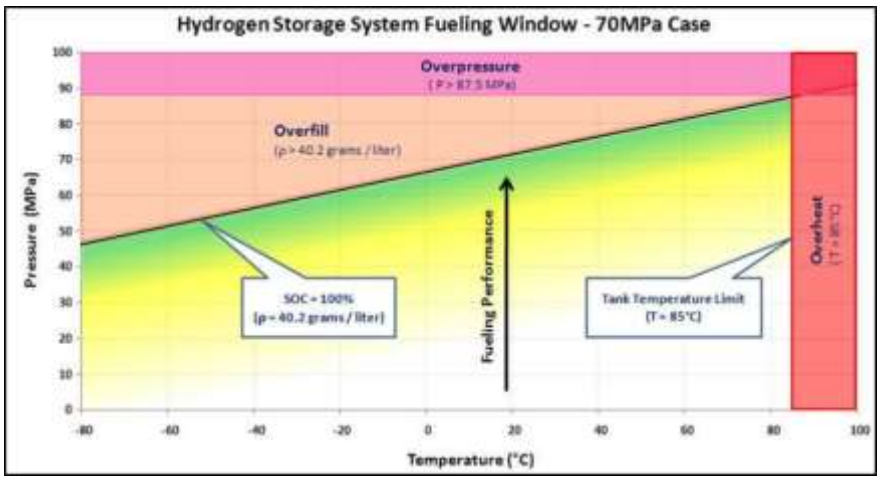

Figure 2.3: Hydrogen fuelling window [17].

The dispenser in hydrogen filling stations consists of an adjustable pressure control valve that is used to set a pressure ramp rate of the gas entering the cylinders in the vehicles (Figure 2.4). The dispenser is also capable of communicating with the vehicle being fuelled through an infrared transmitter that reports the gas temperature and pressure within the cylinder (Figure 2.5) and the total amount of gas dispensed to the vehicle is adjusted accordingly.

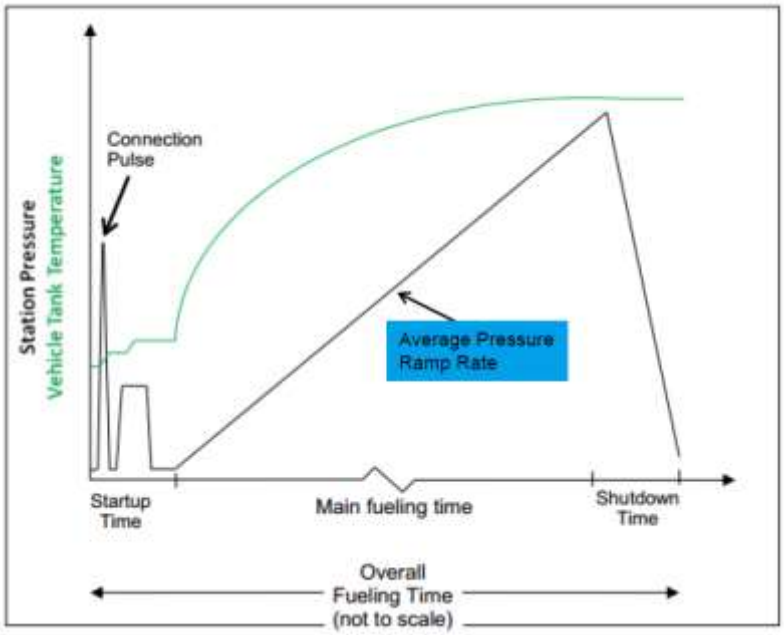

Figure 2.4: Hydrogen filling pressure & temperature development in vehicle [17].

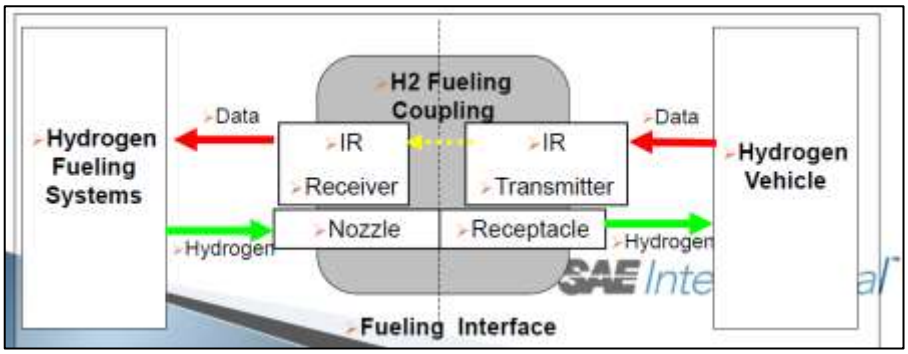

Figure 2.5: Hydrogen filling communication system [17].

Unlike conventional vehicles which are mechanically driven from the combustion of fossil fuels, hydrogen vehicles may make use of a fuel cell to generate electricity from the electrochemical reaction of hydrogen and oxygen, which can be stored temporarily in an on-board battery [18]. There are currently three hydrogen fuel cell powered vehicles available in the UK market – the Toyota Mirai, the Hyundai ix35 and the Honda Clarity [19]. The layout of the Toyota Mirai is shown in Figure 2.6.

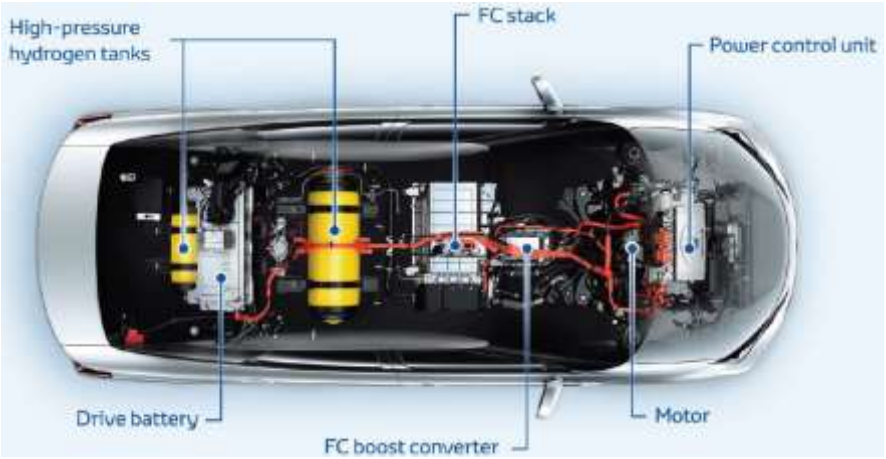

Figure 2.6: Layout of Toyota Mirai [20].

2.3.2 Natural Gas Refuelling Protocol

Recommended practice for the fast-filling of Natural Gas Vehicles (NGVs) is specified in SAE J1616 [21]. Natural gas is typically stored between 20.69 MPa and 24.8 MPa in NGVs to reduce the on-board storage volume [21]. The CNG filling protocol SAE TIR J1616 [21], makes no mention of pre-cooling of the natural gas, which suggests that the filling of NGVs occurs at ambient temperatures.

As opposed to public transport vehicles such as CNG powered buses that typically use private time-fill stations for refuelling, CNG powered cars are basically non-

existent in the UK due to the lack of a public fast-filling infrastructure [22]. The Honda Civic GX (Figure 2.7), which was available only to US consumers was the only car that ran exclusively on natural gas until, production was stopped in 2016 [23]. Currently, as of 2016, only Bi-Fuel cars that use either CNG or petrol are under production and are available only in the USA [24].

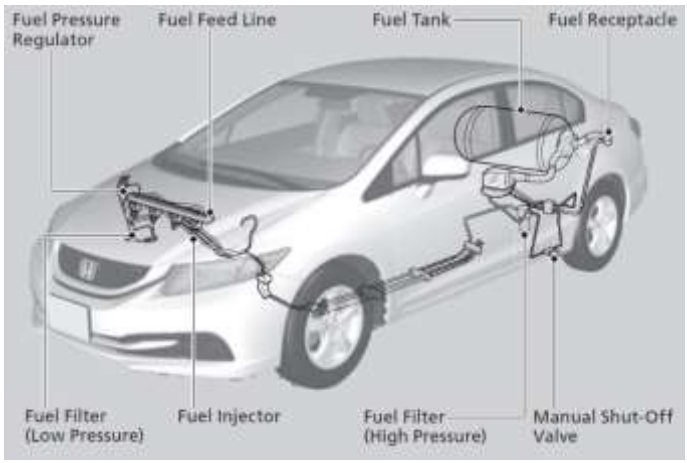

Figure 2.7: Components of the fuel system of the Honda Civic GX [25].

According to its manual, the CNG tank within the Honda Civic GX is of Type III and has a volume of 100 L [25]. The fuel tank capacity for both the time-filling and fast-filling is shown in Table 2.1.

Fill Type	**Final Pressure**	**GGE**
Time	20.7 MPa	6.96
Time	24.8 MPa	7.77
Fast	20.7 MPa	5.84
Fast	24.8 MPa	6.51

Table 2.1: Fuel tank capacity [25].

As expected, a larger mass of gas is obtained for the time-fill as the gas is compressed over a longer period, during which heat losses lead to a negligible rise in gas temperature.

2.4 Cylinder filling experiments

Dicken and Merida [6], performed experiments on the fast-filling of hydrogen in a 74 L Type III cylinder with different fill times of 40 s, 190 s and 370 s. The fills were

performed at initial cylinder pressures of 5 MPa, 7.5 MPa, 10 MPa, 15 MPa and 20 MPa. Four high pressure storage banks each at 48.3 MPa were used for the filling and were connected in parallel to the dispenser (Figure 2.8) and the gas was fed into the cylinder without being pre-cooled. A pressure ramp rate was applied by the dispensing valve until the final pressure in the cylinder was 35 MPa. Sixty-three thermocouples were placed at various locations inside the tank to record the gas temperature.

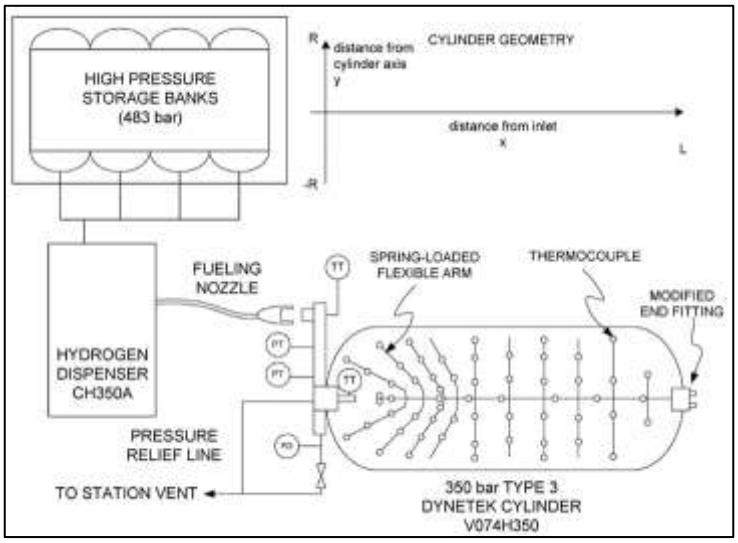

Figure 2.8: Experimental set up for the fast-filling of hydrogen [6].

Results from those experiments showed that the temperature rise within the tank is the largest for the short filling time (40 s) and smallest for the longest filling time (370 s). The lower temperature rise for the longer fill time is due to the larger amount of time available for heat to transfer from the gas to the cylinder walls. In all three cases, the largest increase in gas temperature occurred at the start of fill and gradually diminished as the filling proceeded. The temperature variation within the tank was also found to decrease with the shorter fill time as shown in Figure 2.9, which depicts the instantaneous standard deviation (σ_T) of the 63 temperature readings with normalised time. An increase in the variation of the gas temperature was observed for the longer fill times. This is likely because buoyancy forces play a larger role for slower filling rates and leads to large differences in the local gas temperatures within the cylinder [6].

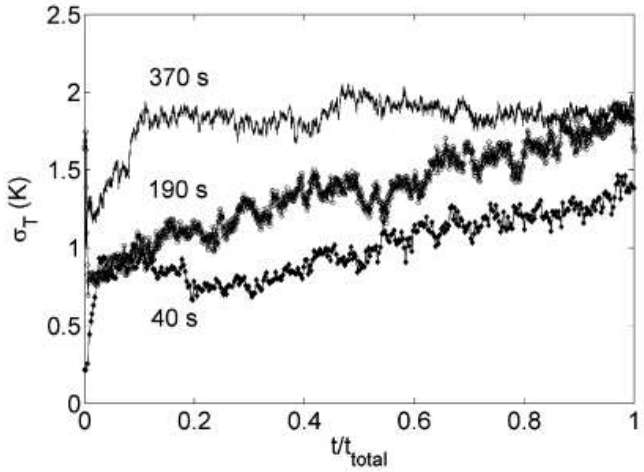

Figure 2.9: Standard variation of temperature v/s normalised time [6].

The experiments [6] also showed that the initial pressure in the cylinder significantly affects the minimum safe fill time and temperature. A lower initial cylinder pressure leads to a longer fill time and also increases the average gas temperature (Figure 2.10).

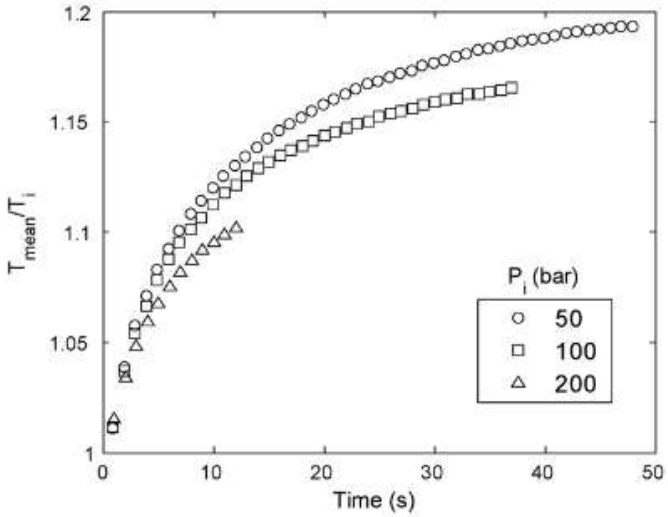

Figure 2.10: Average gas temperature variation with different initial cylinder pressure [6].

The research conducted by Dicken and Merida [6, 7] focussed mainly on the gas temperature within the tank and did not report the heat being dissipated through the cylinder walls. An understanding of the heat transfer phenomena is vital in determining the most appropriate wall material, which can potentially lead to higher heat losses and will lower the gas temperature within the tank. The importance of the liner material was further displayed in the experiments conducted by Hirotani et al. [26] whereby the rate of temperature rise in a Type IV cylinder was found to be higher than that of a Type III cylinder. The difference in the rate of temperature

rise was due to the different thermal properties of aluminium and polyethylene, which are used as liners in Type III and Type IV cylinders respectively. Aluminium has a higher thermal conductivity and diffusivity than polyethylene, which explained the higher temperature rise in the Type IV cylinder. However, in their experiments, Hirotani et al. [26], used different volumes for the Types III and IV cylinders (64 L for the Type III and 74 L for the Type IV). A more representative comparison of the effect of the lining material would have been to use the cylinders of the same volume and thereby to match all of the relevant non dimensional numbers. Another approach in lowering the gas temperature within the tank involves decreasing the temperature of the incoming high pressure gas at the inlet. Baraldi et al. [27] experimentally assessed the pre-cooling method on a 28.9 L Type IV tank. The temperature of the gas was lowered prior to entering the tank using heat exchangers. Six thermocouples were placed at various locations inside the tank for the measurement of the gas temperature during the filling (Figure 2.11). The initial pressure in the cylinder was 2.2 MPa and the cylinder was filled until the final pressure was 77.5 MPa.

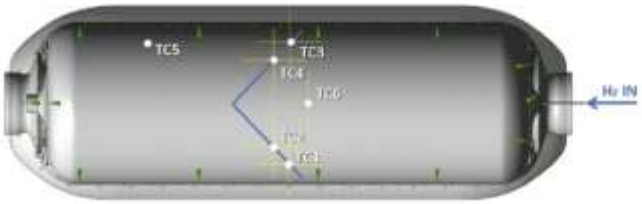

Figure 2.11: Type IV cylinder with thermocouple locations [27].

The highest temperature of the gas occurred at the end of the fill (Figure 2.12), having a value of approximately 331 K, which is much lower than the 358 K limit that is imposed by the International Standard Organisation [3,4]. The pre-cooling technique of Baraldi et al. [27] for the fast-filling of hydrogen is similar to the filling protocol set by SAE TIR J2601 [17]. The experiments of Baraldi et al. [27] were conducted at an ambient temperature of 289 K and did not address the effect of initial ambient temperatures on the pre-cooling requirements.

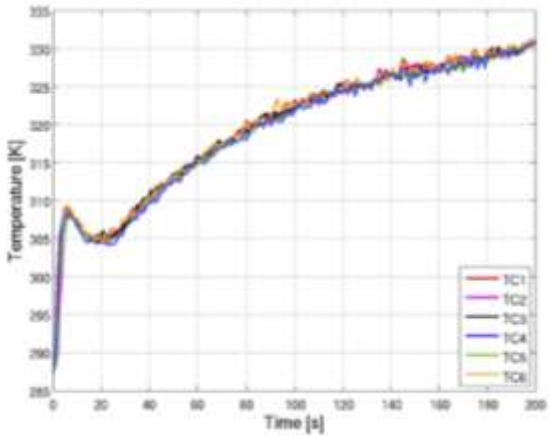

Figure 2.12: Gas temperature history [27].

The experiments conducted by Baraldi et al. [27] and Dicken and Merida [6] both show that for the filling of cylinder, a rather uniform temperature is reached in tank. However, thermal homogeneity of the gas was not observed in the hydrogen filling experiments conducted by Zheng at al. [28] and Woodfield et al. [29]. Hydrogen filling experiments performed by Zheng et al. [28] on a 74 L Type III, 70 MPa cylinder showed that discrepancy existed between the gas temperatures in various regions of the cylinder. The filling of the cylinder that was performed by Zheng et al. [28], involved a cascade process along with the pre-cooling of the gas (Figure 2.13).

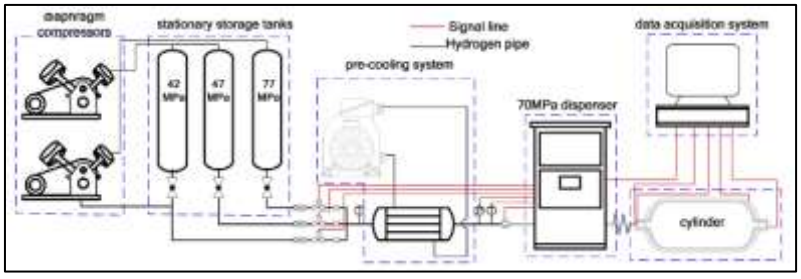

Figure 2.13: Schematic diagram of filling station [28].

Various thermocouples were placed on the inside as well as on the outside of the 74 L cylinder (Figure 2.14). The fill was broken down into two stages: stage 1 in which the cylinder is filled from the stationary storage tanks and stage 2 whereby the fill is completed by the compressor. In stage 1, the rise in gas temperature is due to the Joule-Thompson effect and gas compression being greater than the heat dissipation, which subsequently leads to a rise in gas temperature and in stage 2, a drop in gas temperature is observed since the heat transfer to the wall of the cylinder is greater than the energy input (Figure 2.15).The fill time of 900

seconds that was performed by Zheng et al. [28] is not really considered as a fast-fill which typically varies between 180 and 300 seconds. Thus, buoyancy most probably plays a role in the variation of the local gas temperatures (Figure 2.15).

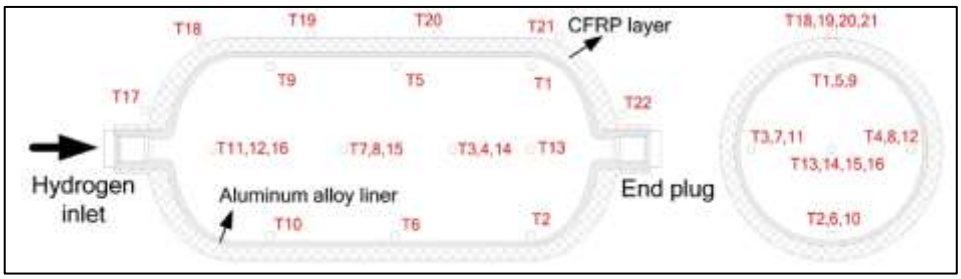

Figure 2.14: Structure of cylinder and location of thermocouples [28].

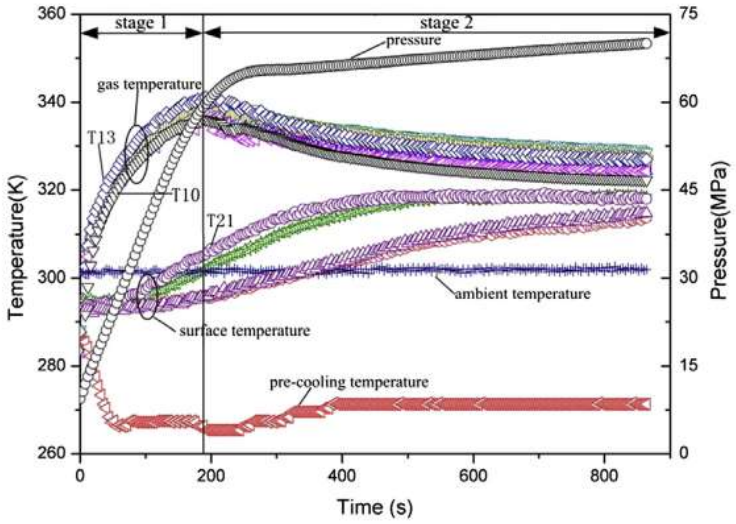

Figure 2.15: Pressure and temperature variation during the fill [28].

Hydrogen filling experiments were conducted by Woodfield et al. [29] for Type III test vessels with volumes of 39 L, 130 L and 205 L. Fills of 35 MPa and 70 MPa were both conducted. The fill times ranged from five minutes for 35 MPa fill to twenty minutes for the 70 MPa fill. The experimental set-up consisted of three banks that were used in the cascade fill and no heat-exchanger was used to pre-cool the gas (Figure 2.16).

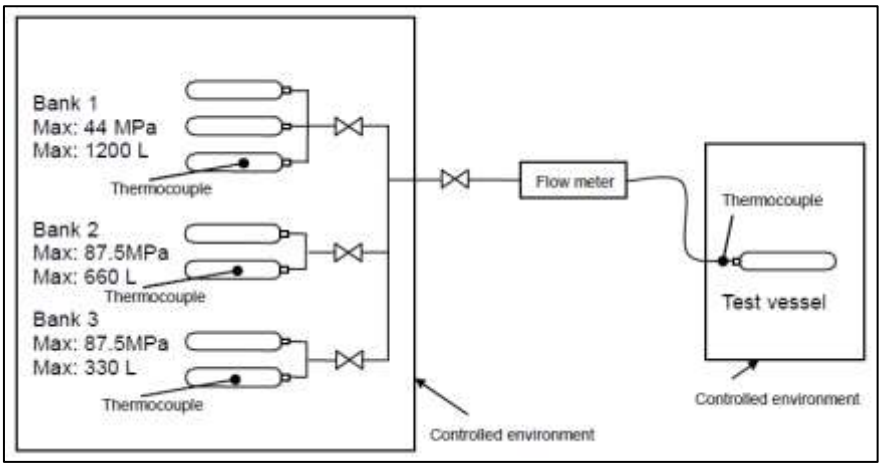

Figure 2.16: Experimental set-up [29].

Figure 2.17 shows the inlet temperature profile of the 205 L cylinder that was filled to 35 MPa. An initial temperature rise at inlet at the beginning of the fill is noted as the gas is being dispensed from a high pressure bank (Bank 1) to the test vessel which is at a lower pressure. At the particular filling pressures and temperatures, the Joule-Thompson of hydrogen lies outside of the region of the inversion curve [29]. A drop in the inlet temperature is noted afterwards since the gas temperature in the bank also decreases due to isentropic cooling. At some point during the fill, the isentropic cooling exceeds the Joule-Thompson heating leading to the inlet temperature being lower than the ambient temperature. When the fill switches to the higher pressure bank, another spike in the inlet temperature is observed, since the gas temperature in the higher pressure banks are at the ambient conditions.

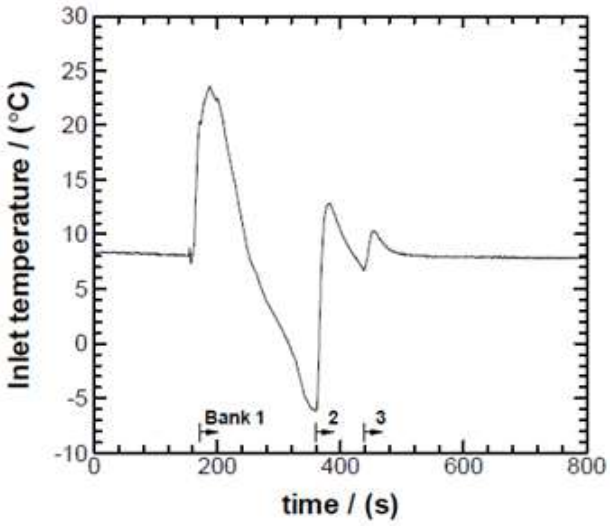

Figure 2.17: Inlet temperature for the 5 minutes 35 MPa fill [29].

In their experiments, Woodfield et al. [29] placed thermocouples on the inner and the outer parts of the cylinder (Figure 2.18) for temperature measurement. The results of the near-wall temperature measurements all showed that the local gas temperature is larger at the dome region opposite to the inlet (TB) and decreases towards the inlet (Figure 2.19). It should be noted that the measurements have a similar trend to those of Zheng et al. [28].

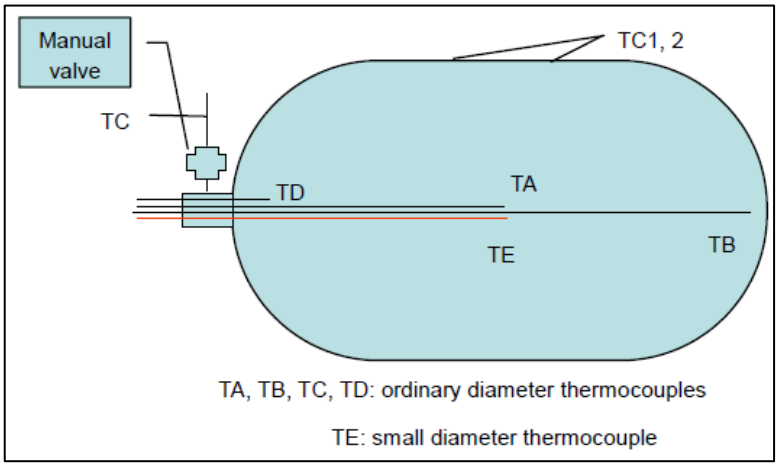

Figure 2.18: Cylinder and thermocouples locations [29].

The experiments that were conducted by Woodfield et al. [29] are however not representative of the filling of high pressure vessels in filling station that typically includes a dispenser that feeds the gas into the cylinder at a prescribe pressure profile.

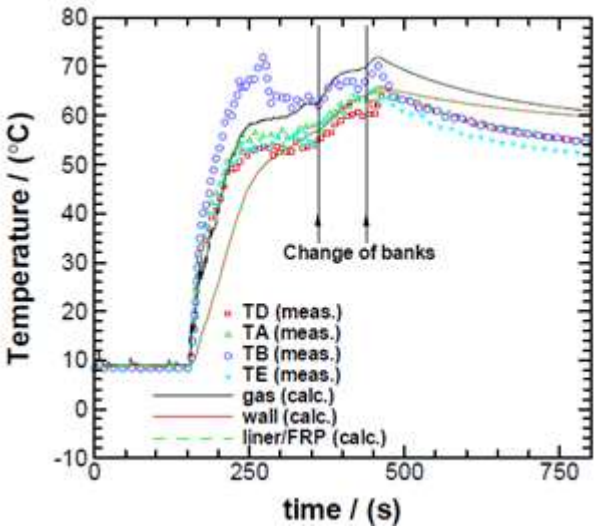

Figure 2.19: Temperature measurement for the five minute fill [29].

The hydrogen filling experiments that performed by Johnson et al. [30] were on a 36.9 L Type IV cylinder. Five thermocouples (1-5) were placed along the axis of the cylinder for the gas temperature measurement during the fill (Figure 2.20).

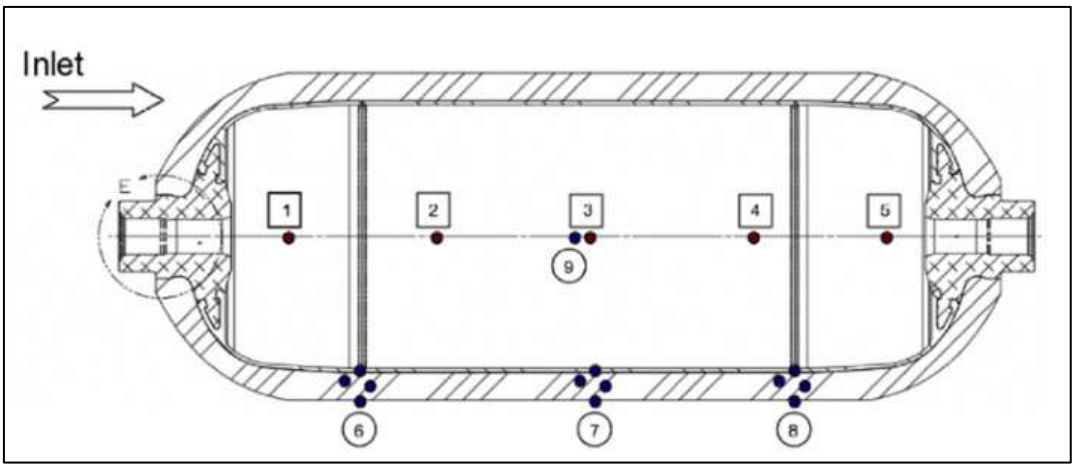

Figure 2.20: Structure of cylinder and thermocouples locations [30].

Locations (6-9) each contained four thermocouples that were placed at the inner liner surface, at the interface between the liner and laminate, in the middle of the laminate and on the outer surface of the cylinder. The cylinder was mounted in such a way that it could be rotated and experiments could thus be repeated with the thermocouples (6-9) being positioned at different angular locations with respect to the incoming flow. Johnson et al. [30] did not mention the size of the banks or whether a cascade process for the fill was involved. Ramp inlet-pressure profiles were applied at the inlet for forty-five and ninety seconds until the final gas pressure was 13.79 MPa, which is a really low final pressure, since according to the hydrogen filling protocol SAE TIR J2601 [17], hydrogen fills of 35 MPa and 70 MPa are required for an adequate driving range of a hydrogen vehicle. Experiments for the ninety second fill showed that the inner wall temperature in the upper portion of the cylinder is fifteen degrees higher at the end of the fill when compared to inner wall in the bottom portion of the cylinder (Figure 2.21). This suggests that the heat transfer rate from the gas to the structure is non-uniform within the cylinder.

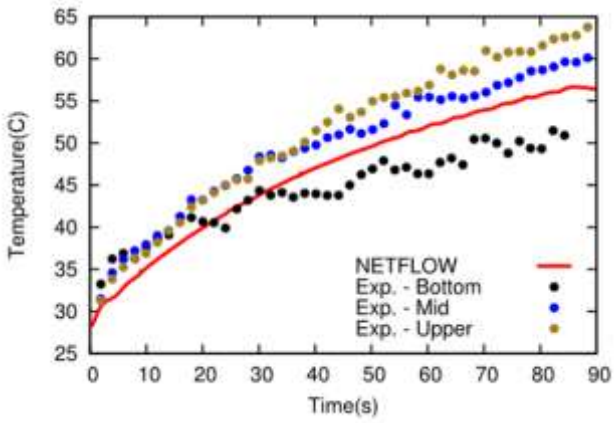

Figure 2.21: Measured and computed wall temperatures [30].

Hydrogen filling experiments conducted for the filling of a 72 L Type IV cylinder by Kim et al. [5], showed that the initial pressure of the gas in the cylinder affects the final gas temperature. The fast-filling was conducted with initial gauge pressures of 0 MPa, 10 MPa and 20 MPa, with the final pressure set to 35 MPa in all three cases. The experimental set-up did not include pre-cooling of the gas and six thermocouples were used to measure the gas temperature within the cylinder during the fill (Figure 2.22).

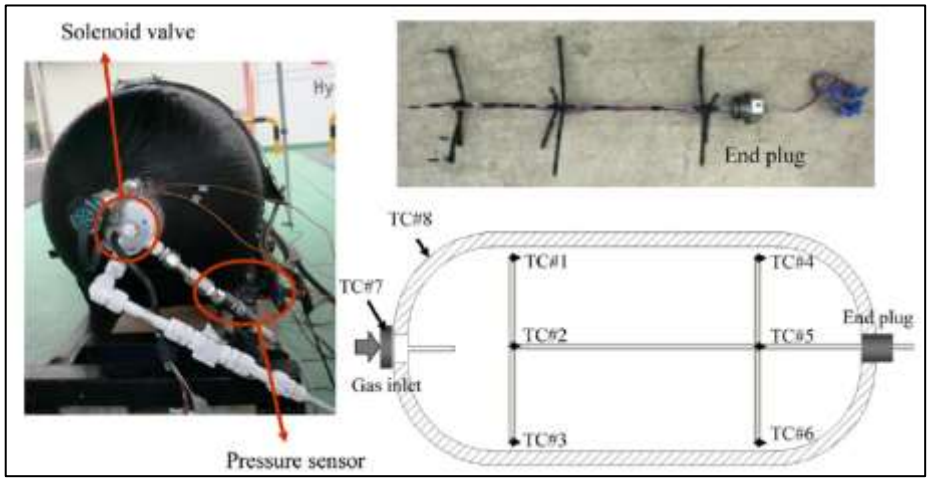

Figure 2.22: Experimental set-up by Kim et al. [5].

The experiments were conducted at the same ambient temperature of 20° C in all three cases and it was determined that a lower initial pressure leads to a higher final gas temperature (Figure 2.23).

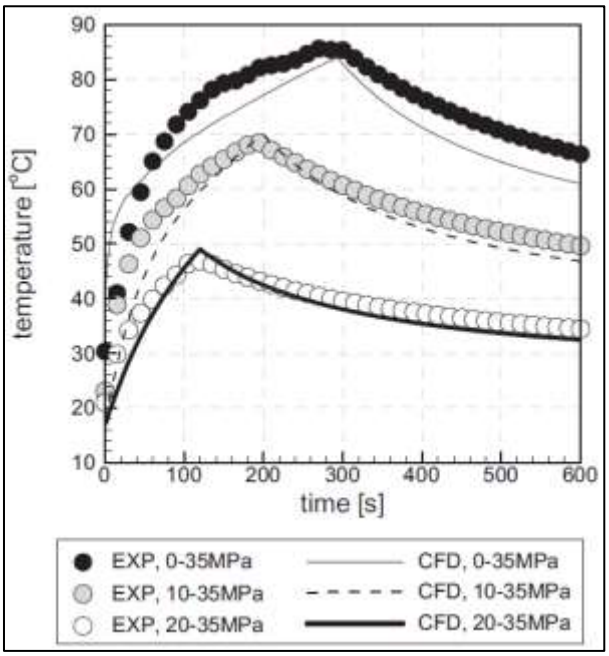

Figure 2.23: Gas temperature results with different initial pressure conditions [5].

The maximum gas temperature was found to exceed the maximum allowable temperature of 85° C for the case whereby the initial gauge pressure was 0 MPa. In addition, the experiment was conducted at an ambient temperature of 20° C, which is not the worst case scenario, since higher ambient temperatures are expected during the summer time in some regions of the world [31]. Thus pre-cooling is essential as described in the SAE TIR J2601 protocol even for 35 MPa fills to prevent the gas temperature from exceeding the 85° C limit.

Cebolla et al. [32] investigated experimentally the effect of the pre-cooling of the gas and mass flow rate on the filling of a hydrogen cylinder. In their experiments, both Types III and IV cylinders were filled at different inlet temperatures until a final pressure of 77-78 MPa was reached. The average value of the mass flow rate was determined by dividing the mass of gas delivered to the cylinder by the fill time. The experiments showed that the higher inlet gas temperatures lead to a lower State of Charge (SOC) in the filling of both the Type III and IV cylinders (Figures 2.24 & 2.25). In addition, the mass flow rate was shown to highly influence the final SOC at higher inlet temperatures: the larger the mass flow rate, the lower the SOC.

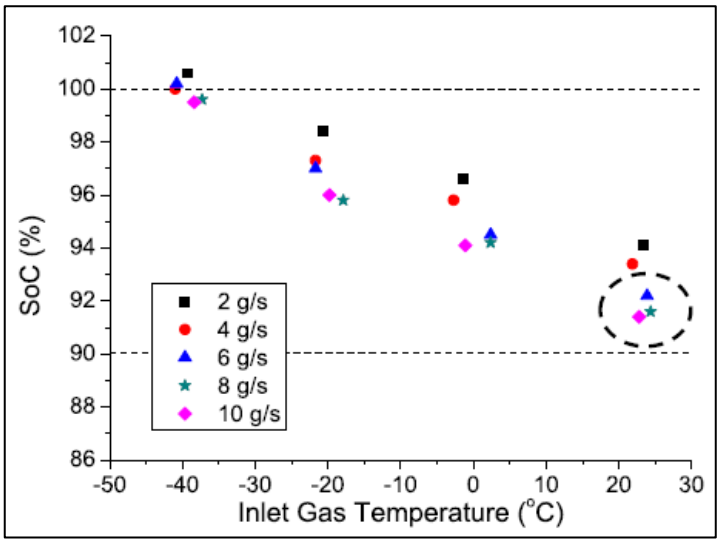

Figure 2.24: Influence of inlet gas temperature & mass flow rate on SOC (Type III cylinder) [32].

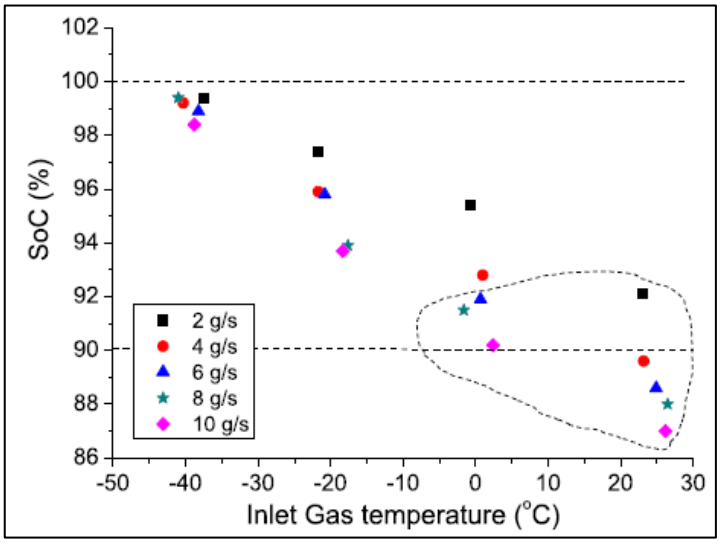

Figure 2.25: Influence of inlet gas temperature & mass flow rate on SOC (Type IV cylinder) [32].

The 'circular' dotted lines on Figures 2.24 and 2.25 indicate the filling cases in which the temperature of the gas in the cylinder exceeded the limit of 85° C. The number of filling cases in which the gas temperatures was higher than 85° C was larger when the Type IV cylinder was used as the test vessel. This is likely due to the higher conductivity and specific capacity of the Type III aluminium liner that is capable of transferring and storing a larger amount of heat from the gas than the plastic liner of the Type IV cylinder. However, aside from having different material properties, the volumes of the Type III and IV vessels used in the experiments were also different. The volume of the Type III cylinder was 40 L and the Type IV cylinder was 29 L. Thus a direct comparison on the effect of the SOC for the cylinders with different material properties from this particular sets of experiments is not realistic.

2.5 Multi-dimensional CFD modelling of cylinder filling

The Reynolds numbers in the flows simulated by Dicken and Merida [7], were 8.2 x 10^5 and 7.2 x 10^5 at the beginning and the end of the fill respectively. Direct Numerical Simulation (DNS), which resolves all turbulent length scales is not feasible at these Reynolds numbers because the wide range of scales would require too many grid points for current supercomputers to be able to compute. Thus, researchers still prefer using the Reynolds-Averaged Navier Stokes (RANS) equations combined with various turbulence models to predict the fluid behaviour of the gas and its thermal history during the filling process.

Due to the high pressures during filling, it is necessary to employ a real gas equation of state [5, 7, 8, 27-30, 33, 41, 46-48]. Dicken and Merida [7] and Kim et al. [33], both used the Redlich-Kwong real gas equation of state [34] in their respective simulations. The behaviour of real gases deviates to various degrees from the ideal gas equation and the deviations increase at high pressures and low temperatures [36]. The following assumptions are made for an ideal gas [35, 36]:

1. The molecules of the gas are point particles occupying a negligible volume of the gas.
2. No intermolecular forces exist in between the gas molecules.

A two-dimensional axisymmetric CFD model of hydrogen refuelling of a type III cylinder was performed by Dicken and Merida [7], in which the standard k-ε turbulence model [37] was used. The gas temperature prediction obtained from the numerical model was found to slightly overestimate the average gas temperature readings that were acquired from the thermocouples (Figure 2.26).

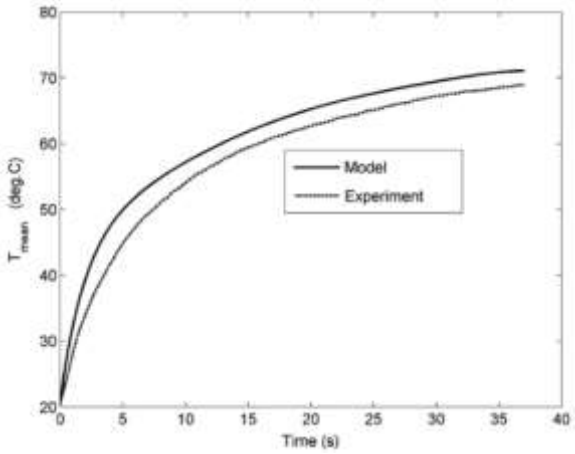

Figure 2.26: Mean gas temperature throughout the fill [7].

Two-dimensional axisymmetric simulations of the cylinder filling based on the experiments of Dicken and Merida [7] were also performed by Kim et al. [33] for four different turbulence models namely the Realizable k-ε model [38], the Re-Normalization Group (RNG) k-ε model [39], the shear stress transport (SST) k-ω model [40] and the Reynolds stress model (RSM) [37]. All four turbulence models showed almost identical variation of gas temperature with time, and slightly overestimated the temperatures in the experiments (Figure 2.27). The study by Kim et al. [33] also showed that the Realizable k-ε model [38] is computationally more efficient than the other turbulence models in their implementation (Table 2.2).

	Realizable k-ε	**RNG k-ε**	**SST k-ω**	**RSM**
CPU time	1	1.14	1.7	3.10

Table 2.2: Computational time using the various turbulence models [33].

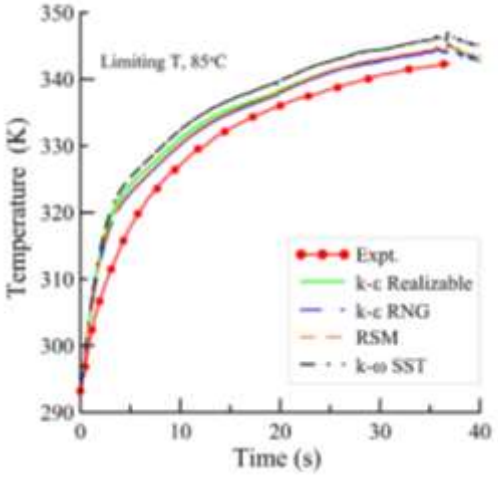

Figure 2.27: Mean gas temperature using various turbulence models [33].

Kim et al. [41] performed several three-dimensional simulations of the tank filling using data from Dicken and Merida [7] using the SST k-ω model [37] along with four real gas equations of state to account for the deviations from the ideal gas equation. The equations used were: the Redlich-Kwong equation (RKEoS) [34], the Soave's modified Redlich-Kwong equation (SRKEoS) [42], the Aungier's modified Redlich-Kwong equation (ARKEoS) [43] and the Peng-Robinson equation (PREoS) [44]. The mass-averaged gas temperature during the fill as determined by the simulations (Figure 2.28) showed that all four real gas equations basically produced similar gas temperature profiles during the fill. The real gas equations were much more accurate in predicting the gas temperature in the final stages of the fill as opposed to the ideal gas equation (IGEoS), which underestimated the final gas temperature.

The two-dimensional simulations performed for the hydrogen filling of a 38.9 L Type IV by Baraldi et al. [27] further showed significant deviations in the gas temperature when the ideal gas equation was used as opposed to real gas equations (Figure Figure 2.29). The real gas equations used in the simulations were the Redlich-Kwong equation (STdRK) [34], Soave's modified Redlich-Kwong equation (SoaveRK) [42], Aungier's modified Redlich-Kwong equation (AunRK) [43] and the Peng-Robinson equation (PenRob) [44]. A comparison of Figure 2.28 and Figure 2.29 shows a larger deviation in gas temperature between the real gas equations and ideal gas equation. This is mainly due to the fact that real gas effects are less at lower pressures. The simulations of Baraldi et al. [27] were conducted with the final gas pressure being 70 MPa as opposed to Kim et al. [41] in which the final gas pressure was 35 MPa.

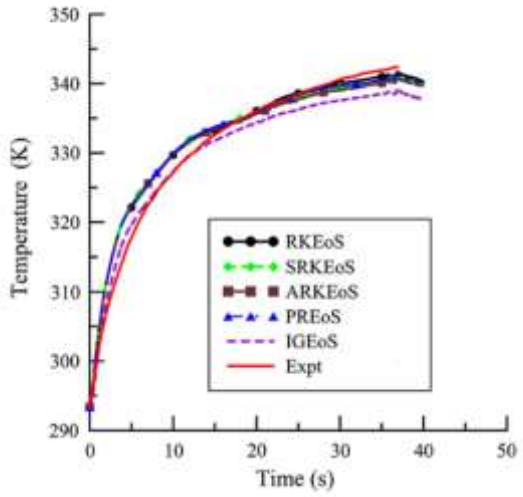

Figure 2.28: Mean gas temperature for the 35 MPa fill using various equations of state [41].

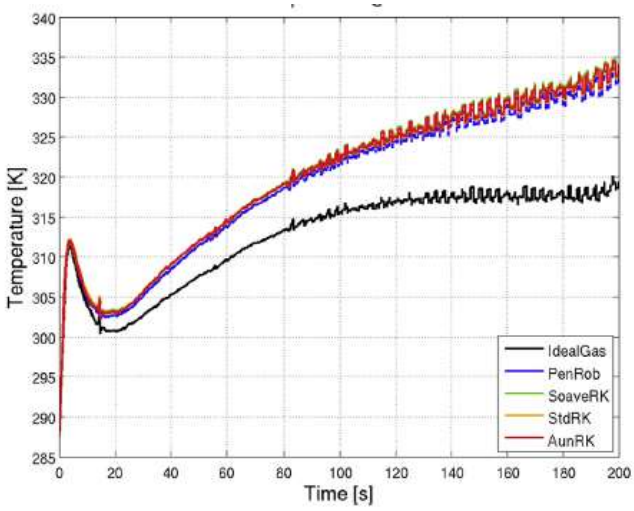

Figure 2.29: Mean gas temperature for the 70 MPa fill using various equations of state [27].

In their two-dimensional simulation, Dicken and Merida [7], showed that the heat transfer between the gas and the lining material is non-uniform during the fill, but is somewhat related to the mass flow rate, i.e. the heat transfer rate is highest when the mass flow rate is at its maximum [7]. There are three modes of heat transfer: conduction, convection and radiation [45] and heat transfer in the fast-filling of cylinders is predominantly due to convection at the near the inner walls of the cylinders. The heat flux is also locally different within the cylinder (Figure 2.30) and is at a maximum at dome opposite to the inlet in the case reported in Ref [7].

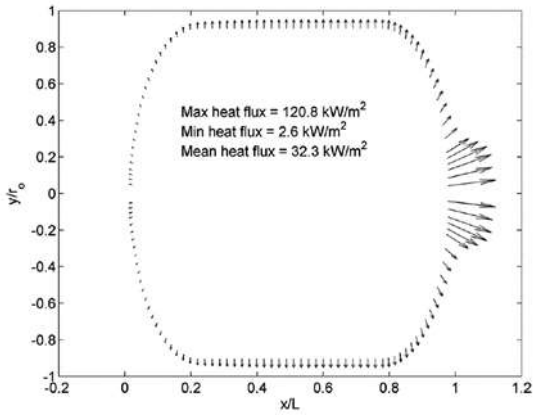

Figure 2.30: Heat flux along the inner wall [7].

The convective heat transfer during the filling of the cylinder is dependent upon the flow field [7] and in their two-dimensional simulations, Kim et al. [33] showed that the incoming jet of gas impinges on the dome opposite to the inlet and recirculates within the cylinder. The simulations of Kim et al. [33] were performed using four different turbulence models and while the choice of turbulence model did not

significantly affect the average gas temperature during the fill (Figure 2.27), the models predicted slightly different flow patterns (Figure 2.31). The RSM and SST k-ω models showed a similar location for the recirculating zone centre as opposed to the Realizable k-ε and RNG k-ε models

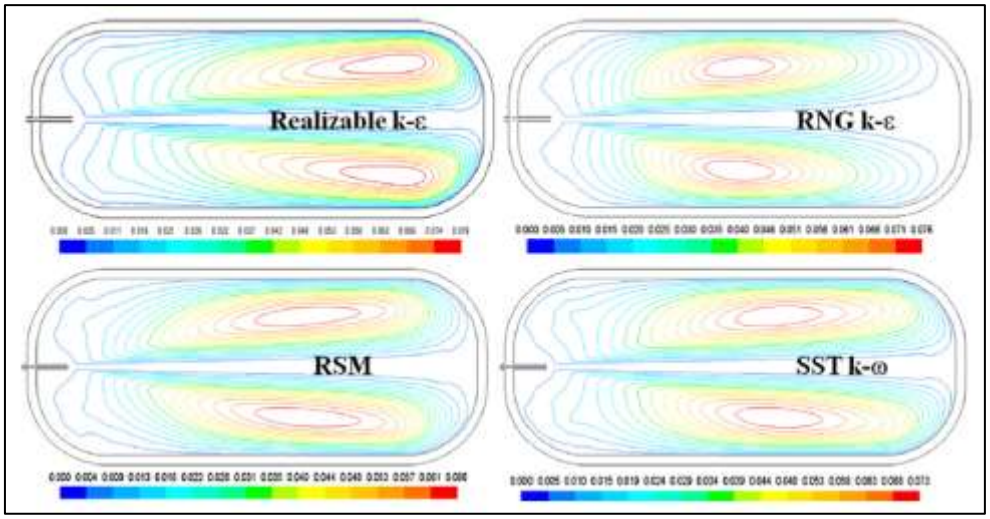

Figure 2.31: Mean streamlines using the four turbulence models 30s into the fill [36].

Kim et al. [41] further performed a three-dimensional simulation using the same parameters as in their two-dimensional model [33] and a similar flow field was obtained at the mid-plane (Figure 2.32). In addition, the mid-plane contour plots of the temperature showed that the gas temperature is mostly uniform during the fill (Figure 2.34).

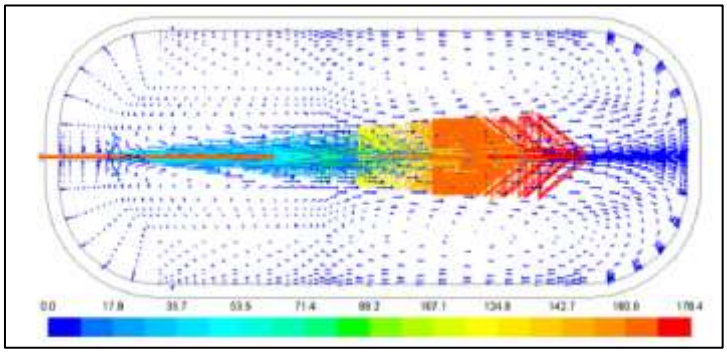

Figure 2.32: Mid-plane velocity vectors five seconds into the fill [41].

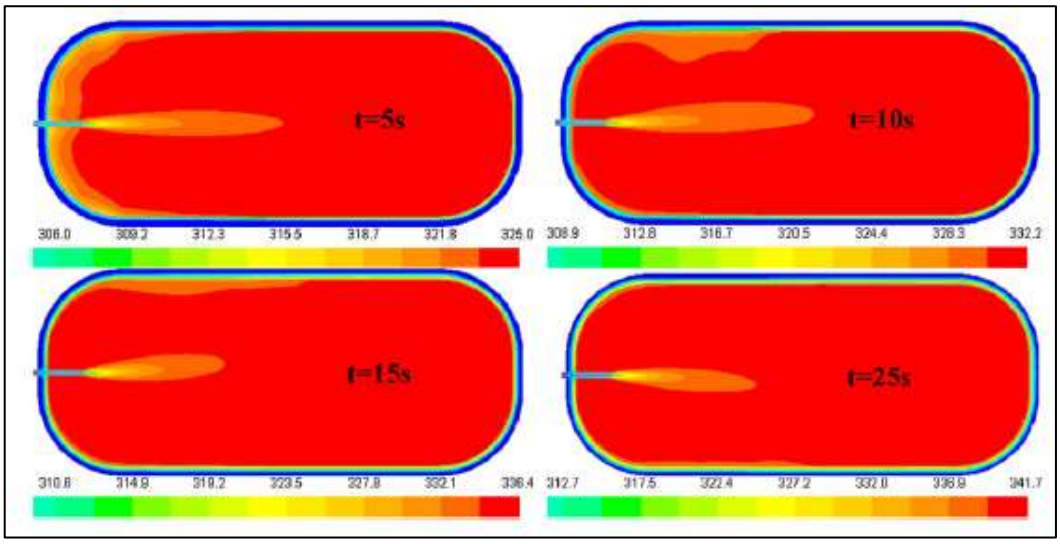

Figure 2.33: Mid-plane contours of temperature during the fill [41].

Kim et al. [5], also carried out a three-dimensional simulation of the filling of a 72 L Type IV cylinder in which the final pressure was 35 MPa. The k-ε turbulence model [37] and the Redlich-Kwong equation of state [34] were respectively chosen to model the Reynolds stress term and to consider the effect of compressibility due the high gas pressure being involved during the fill. Three cases were considered in which the initial gauge pressure of the gas in the tank was at 0 MPa, 10 MPa and 20 MPa. The average gas temperatures that were obtained from the CFD simulations during those three fills were found to be similar to the experiments (Figure 2.23). In contrast to the simulations of Kim et al. [41], in which the flow field showed that the circulation region is axisymmetric in nature (Figure 2.32), Kim at al. [5] showed the jet entering the cylinder flows downwards due to the effect of gravity and leads to multiple recirculating regions (Figure 2.34), with a larger recirculating region being formed at the dome opposite to the inlet. The gas temperature in the cylinder was found to be non-uniform (Figure 2.35), with the gas temperature in upper portion of the cylinder being 10° C hotter than in the lower part. This sharply contrasts the findings of Kim et al. [41], in which the gas temperature was mostly the same throughout the cylinder (Figure 2.33).

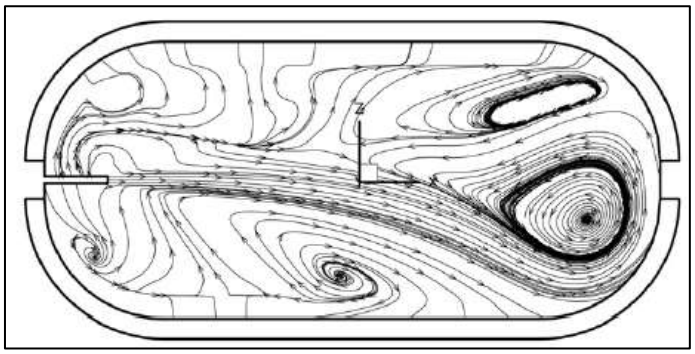

Figure 2.34: Streamlines mid-plane at 294 s into the fill from an initial pressure of 0 MPa [5].

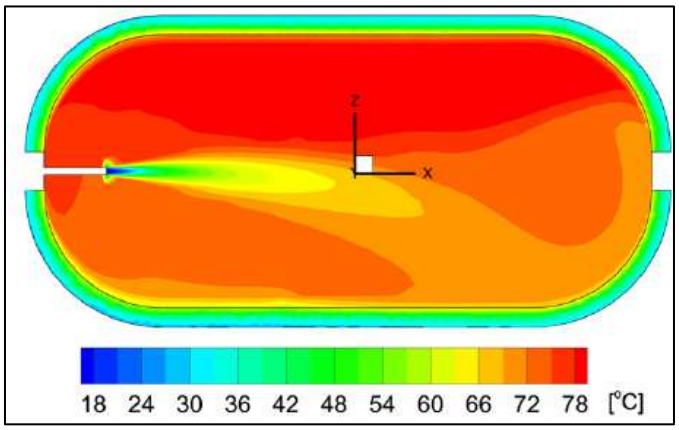

Figure 2.35: Contours of temperature at 294 s into the fill from an initial pressure of 0 MPa [5].

The three-dimensional simulations of Galassi et al. [46], used the k-ε turbulence model to compare the local gas temperatures at 5 different positions in the cylinder with their experiments. In their publication, Galassi et al. [46], did not mention the size of the cylinder that was being filled. Two sets of experiments were carried out with fill times of 330 s and 245 s, until a pressure of 70 MPa was reached in both cases. The locations of some of the inner thermocouples were different in both cases (Figure 2.36): the blue thermocouples for the 330 s fill, the red thermocouples for the 245 s fill, while an inner white thermocouple was fixed along with the external black thermocouples.

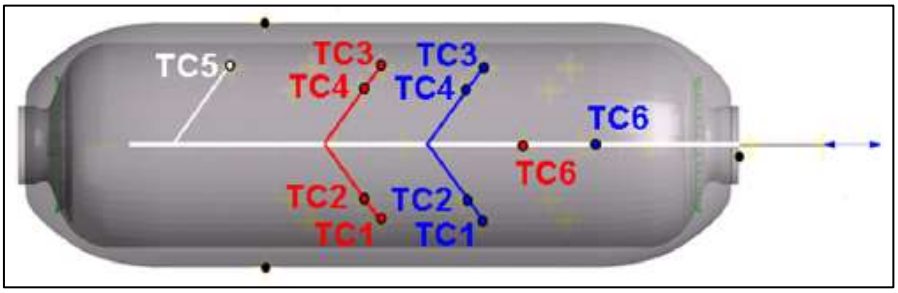

Figure 2.36: Structure of cylinder along with the thermocouple locations [46].

The local gas temperatures that was obtained for the 245 s fill from the CFD simulation was found to be similar to those obtained from the experiment (< 4% discrepancy). In addition, the local temperatures that were obtained from both the simulation and experiment were all nearly similar (Figure 2.37), which suggests that the gas temperature is mostly uniform throughout the cylinder during the fill.

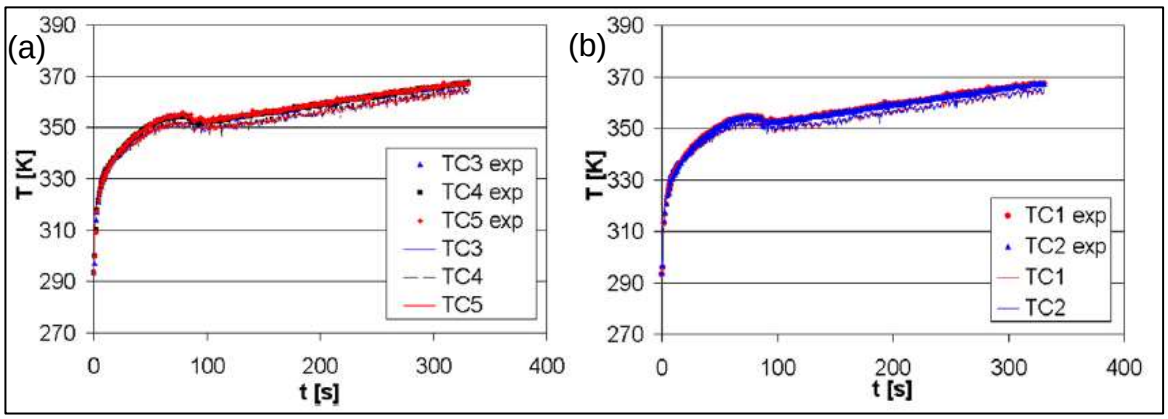

Figure 2.37: Predicted local temperature comparison with experiment for 245 s fill [52].

The experiment of Baraldi et al. [27] that was conducted for a 77.5 MPa fill on a 28.9 L cylinder also showed no difference in local temperatures (Figure 2.12) and the fill was also numerically simulated in both two and three dimensions. The CFD simulations of Baraldi et al. [27] showed that the average gas temperature from the three-dimensional model was mostly similar to that of the two-dimensional axisymmetric model (Figure 2.38).

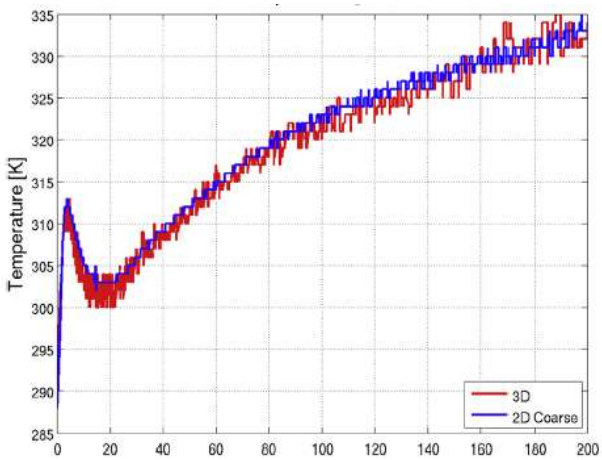

Figure 2.38: Comparison of the temperature results of the 2D and 3D model [27].

The three-dimensional domain consisted of 290,382 nodes, while the two-dimensional model had 23,668 nodes. The three-dimensional model, according to Baraldi et al. [27], required several weeks for a complete run. Since the three-

dimensional domain had around twelve times the number of nodes than the axisymmetric two-dimensional domain, the computational time will also approximately be twelve times faster for the two-dimensional model. The axisymmetric two-dimensional domain was further modified in which a thin mesh was included in the boundary layer in between the fluid and the liner, which raised the number of nodes to 27,548. In addition, a third domain in which a fine mesh with the number of nodes rising to 94,436 was also tested. The results of the average gas temperature from the simulations of the different two-dimensional meshes showed negligible differences (Figure 2.40).

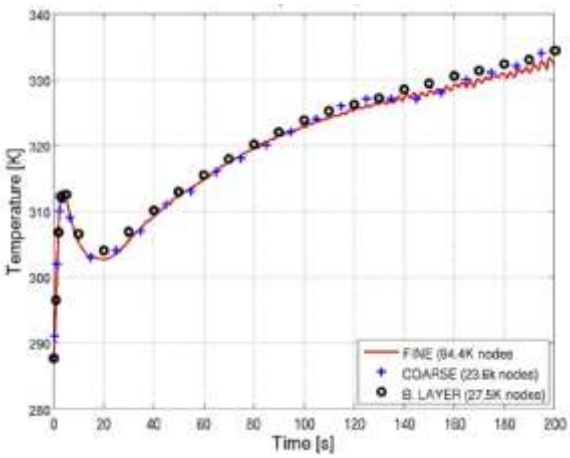

Figure 2.39: Comparison of the gas temperature results for the various 2D meshes [27].

In their publication, Baraldi et al. [27], did not mention the wall resolution or if wall function was employed for any of the three cases with the different meshes. However, a good agreement between the gas temperature results of the coarse mesh and experiment was obtained (Figure 2.40).

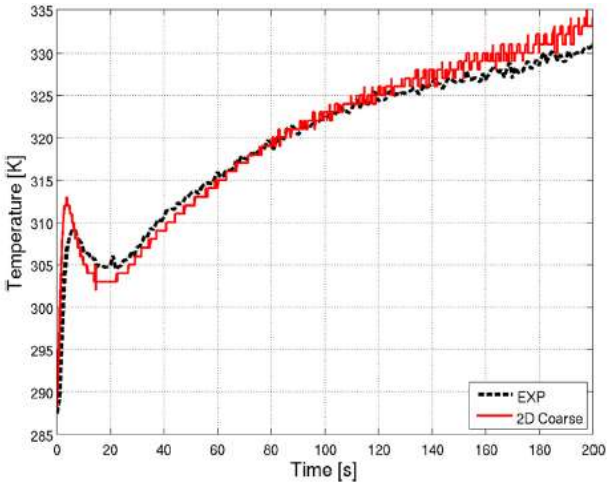

Figure 2.40: Comparison of the average gas temperature obtained from experimental data and simulation [27].

The review of the literature has so far shown that uniformity in gas temperature has been obtained in all the simulation cases with cylinders ranging from 28.9 L to 74 L with the exception of the CFD filling case of Kim et al. [5] that involved the filling of a 72 L cylinder (Figure 2.35). The uniformity of the gas temperature during the fill was also demonstrated by the two-dimensional simulations of Zheng et al. [28], which was based on their experiment and consisted the filling of a 74 L cylinder, with a final pressure of 70 MPa (Figure 2.41). The findings of Zheng et al. [28] was further confirmed by the two-dimensional axisymmetric simulations of Wang et al. [47] using similar data.

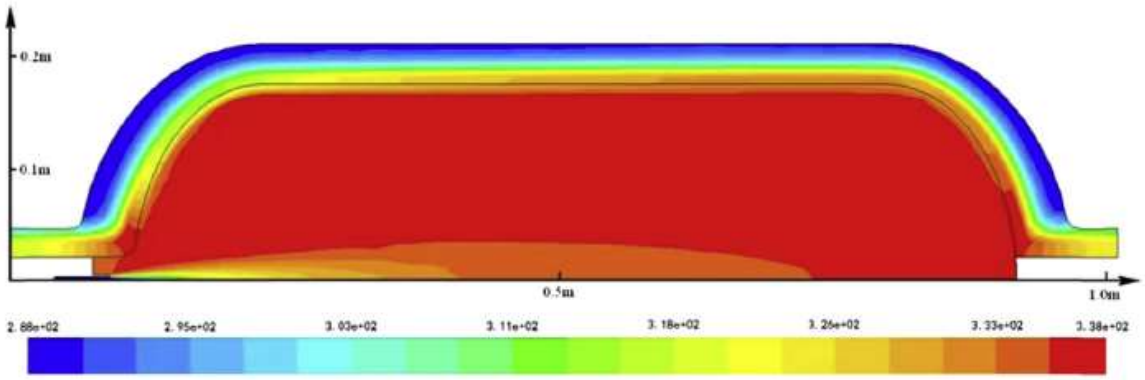

Figure 2.41: Temperature distribution at the end of the fill [28].

The geometry of the cylinders that have been used in the either the experiments or the simulations that have been discussed all have an inner length to inner diameter ratio ranging from two to three [5-8, 26-30, 32, 33, 41, 46-48]. Zheng et al. [28], also numerically investigated the effect of increasing the length-to-diameter ratio to 4.4 and found that the homogeneity of the gas temperature disappears as it increases axially (Figure 2.42). However, the volume of the cylinder was also changed from 74 L to 150 L and thus a definite conclusion regarding the effect of length-to-diameter ratio cannot be properly established.

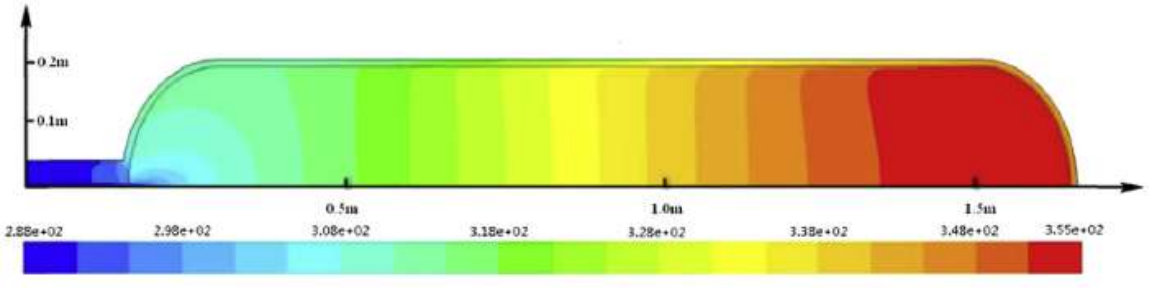

Figure 2.42: Temperature distribution at the end of the fill of cylinder with L/D of 4.4 [28].

Zheng et al. [28] made no mention of the flow field in the cylinders during the fill, which according to the simulations of Kim et al. [33, 41] play an important role in the uniformity in the gas temperature.

Zheng et al. [28], also carried out simulations by varying the ambient temperature for the hydrogen filling. The inlet temperature was kept at a constant and the results of those simulations showed that the average gas temperature increases accordingly (Figure 2.43).

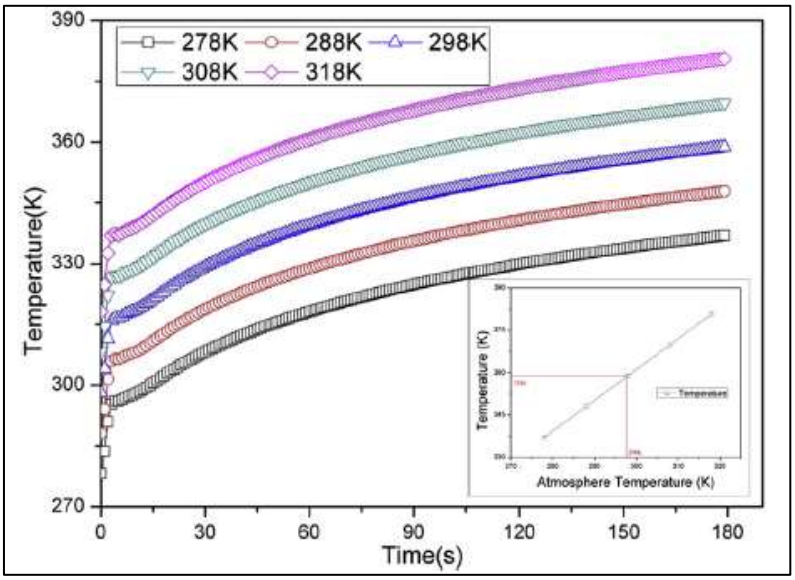

Figure 2.43: Gas temperature predictions with different ambient temperatures [28].

With the inlet temperature being kept constant during the fill, Zheng et al. [28], assumed that the reservoir of gas that is supplying the gas to the cylinder is infinite, which is certainly not the case in filling stations. In addition, in a filling gas station, an adjustable pressure control valve is used to lower the gas pressure from the banks and is dispensed accordingly [17]. Thus the resulting drop in pressure at the dispenser will alter the gas temperature due to the Joule-Thompson effect. Similarly, Melideo and Baraldi [48], numerically investigated several cylinder filling cases: (1) the inlet temperature was changed while keeping a similar inlet ramp pressure profile, (2) the inlet pressure profile was changed from the conventional ramp while keeping the same inlet temperature. However, in both cases the inlet temperature profile were kept at a constant throughout the fill.

2.6 Low order modelling of cylinder filling/discharging

A single-zone conjugate heat transfer model for the CNG fast-filling of cylinders was proposed by Kountz [49] in which the mass flow through the orifice was considered as isenthalpic. The model proposed assumed that the upstream conditions, i.e. the stagnation pressure and stagnation temperature were constant throughout the fill. However, the infinite reservoir of gas which was assumed in the model does not mirror the actual filling scenarios in fuel stations. In addition, only natural convection was assumed throughout the fill and the heat transfer coefficient was set at a constant value. Archimedes Number which is the ratio of the Grashof Number to the square of the Reynolds Number parameterizes the relative strength of natural and forced convection [50]. The Grashof represents a ratio of the buoyancy forces to viscous forces [50]. When the value of Archimedes is less than unity, forced convection dominates. Thus, the assumption of accounting for heat transfer due only to natural convection set in Kountz [49] is inaccurate, since it is mostly likely that forced convection is the principle mode of heat transfer due to the high inlet Reynolds number [7] involved in the fast-filling of cylinders. Farzaneh-Gord [51] also used a thermodynamic model for the filling of CNG cylinders. Isentropic expansion through an orifice was considered. The model, however, assumed that the filling is adiabatic, which is not the case in real situations. In their models, Kountz [49] and Farzaneh-Gord [51] both used ideal gas assumptions in the computation of the mass flow rate, which likely leads to inaccuracies, since significant deviation of the gas from the ideal behaviour is expected at the high gas pressures involved in fast-filling.

Since forced convection is the principal mode of heat transfer in the fast-filling of cylinders, the calculation of the heat transfer coefficient is vital for the creation of a low order model. The heat transfer coefficient can be determined by the modelling of the Nusselt number, which is a non-dimensional representation of the heat transfer coefficient [52]. Means [53], proposed the modelling of the Nusselt number that is calculated based on the diameter of inlet, the Reynolds number at the inlet, the Prandtl number of the gas and the diameter of the cylinder. However, Means's correlation [53], is only valid for choked conditions and ideal gas. Choking occurs at the exit of the delivery pipe and is dependent upon the pressure ratio of the gas being delivered and the gas within the vessel. The CFD simulation of Galassi et al.

[46] for the fast-filling of a 70 MPa cylinder showed that the flow was only choked for only the first four seconds of the two hundred and forty seconds fill, which only represents 1.7% of the total fill time. Clark [54], used a modified version of Means's correlation [53] to successfully predict the heat transfer coefficient, but however, the model didn't account for the modelling of the pressure control valve at the dispenser. In addition, Clark [54], only calculated the filling of a cylinder with helium in which the gauge initial and final pressures were only 0 MPa and 2 MPa respectively.

Monde et al. [55], assumed that the heat transfer coefficient is fixed throughout the filling of 1.38 L cylinder with a final pressure of 35 MPa. In their experiment, Monde et al. [55], measured the gas temperature at different locations within the cylinder. A single-zone conjugate heat transfer model of the filling that included the heat transfer coefficient set at fixed values of 250 W/m^2-K and 500 W/m^2-K was used to compute the gas temperature during the fill (Figure 2.44).

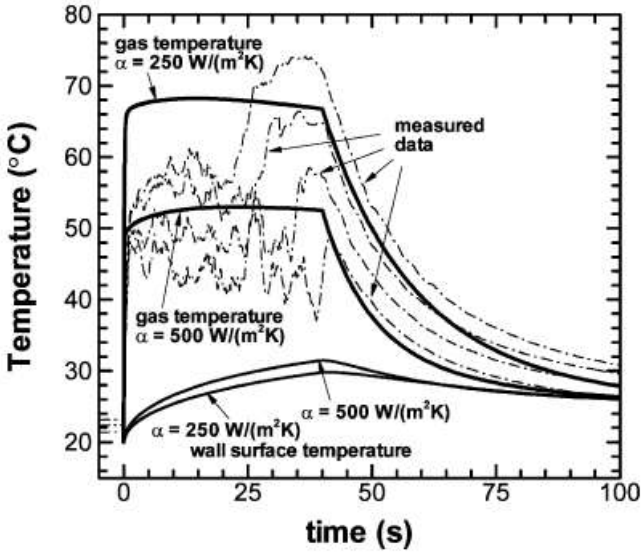

Figure 2.44: Comparison of estimated and measured gas temperature [55].

According to Figure 2.44, the gas temperature that is predicted with the heat transfer coefficient of 500 W/m^2-K is almost equal to the average of gas temperature that were measured. Conversely, with the heat transfer coefficient set to 250 W/m^2-K, the single-zone model overestimates the gas temperature.

Woodfield et al. [29] also used the fixed transfer coefficient of 500 W/m^2-K in their single-zone model to predict the gas temperature during the filling of three test vessels of volumes 205 L (vessel A), 39 L (vessel B) and 130 L (vessel C). A

comparison of the gas temperature obtained by the single-zone conjugate heat transfer model to the experimental values showed promising results for the filling of vessel A, while large over predictions of the gas temperature was obtained for vessels B and C (Figures 2.45 - 2.47).

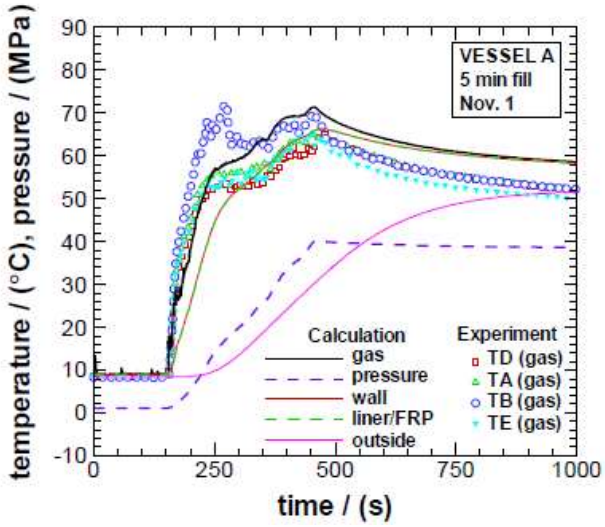

Figure 2.45: Comparison of predicted and experimental temperatures during the filling of vessel A [29].

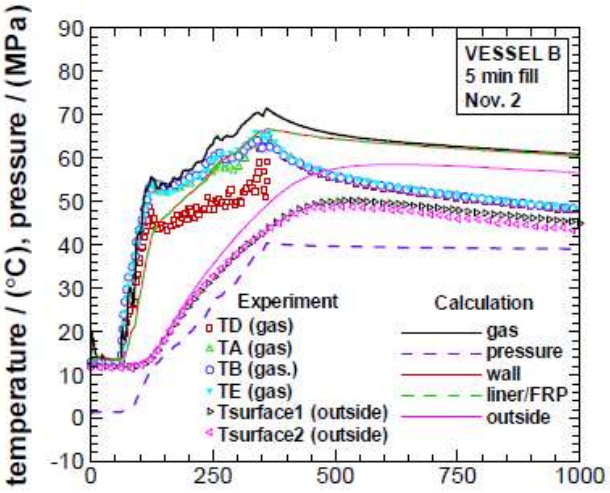

Figure 2.46: Comparison of predicted and experimental temperatures during the filling of vessel B [29].

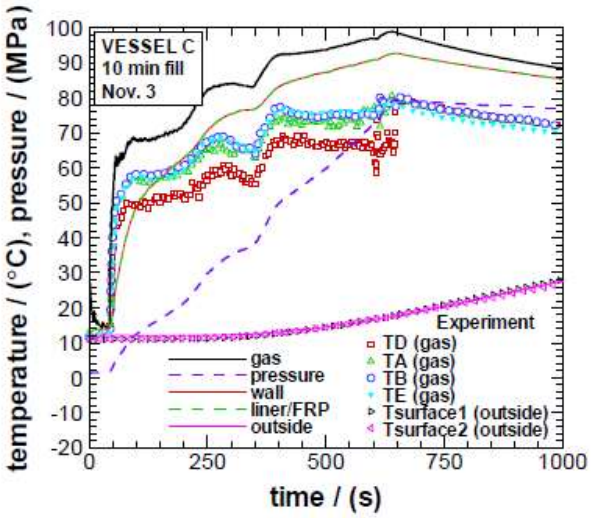

Figure 2.47: Comparison of predicted and experimental temperatures during the filling of vessel C [29].

The experimental set-up of Woodfield et al. [29] also consisted of high pressure banks (Figure 2.16), and a fixed heat transfer coefficient of 250 W/m^2-K was used to predict the gas temperature in the banks during the discharge of the gas. The model successfully estimated the gas temperature during the discharge of the gas in all three banks. Figure 2.48 shows the comparison of the computed and experimental gas temperature during the discharge of Bank 2.

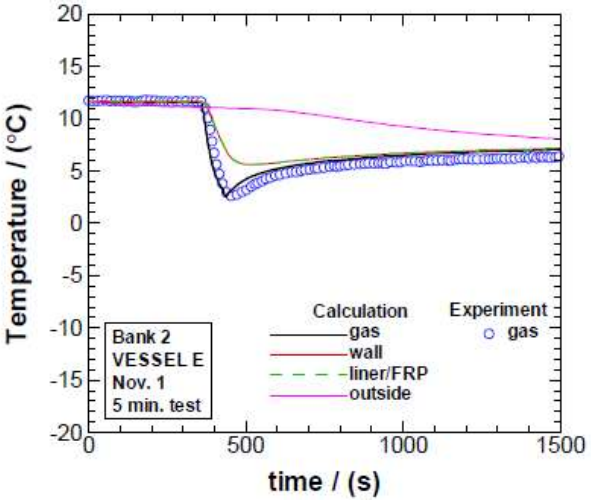

Figure 2.48: Comparison of predicted and experimental temperatures during the discharge of Bank 2 [29].

The comparison of the effect of wall curvature in the one dimensional model was also investigated by Woodfield et al. [29]. Rectangular coordinates which were used to compute the heat conduction across the wall of the cylinder were replaced by cylindrical coordinates. Switching the coordinate system showed little to no difference in the prediction of the gas temperature by the single-zone model (Figure 2.49).

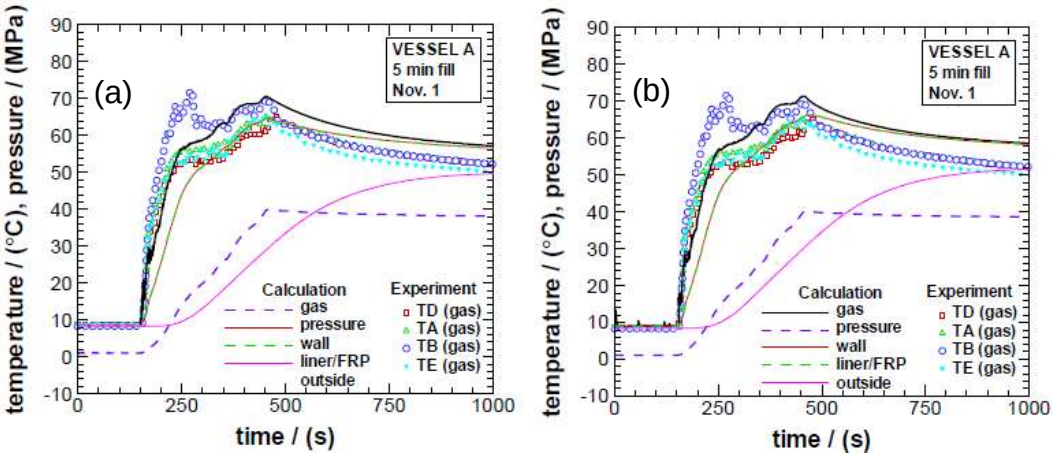

Figure 2.49: Predicted gas temperatures: (a) rectangular coordinates, (b) cylindrical coordinates [29].

The models of Woodfield et al. [29] and Monde el al. [61] both require the following for the computation of the cylinder filling: (1) the mass flow rate to compute the density, (2) the pressure of the gas in the cylinder – a linear increase is assumed, (3) the heat transfer coefficient to compute the heat transfer from the gas to the walls of the cylinder.

Zheng et al. [56] also proposed a single-zone conjugate heat transfer model for the fast-filling and discharging of cylinders used in vehicles. For the filling case, a similar approach to Woodfield et al. [29] and Monde el al. [55] was used whereby the heat transfer coefficient was kept at a constant 500 W/m^2-K. As for the discharging process, the Nusselt number was modelled as a function of the Rayleigh number [60]. The model was compared to experiments of Zheng et al. [28] that were performed on a 74 L Type III hydrogen pressure vessel was found to accurately predict the average gas temperatures during both the filling and the discharging. The thermocouple locations in the cylinder, the average gas temperature during the filling and gas temperature during the discharging process are respectively shown in Figures 2.50 to 2.52.

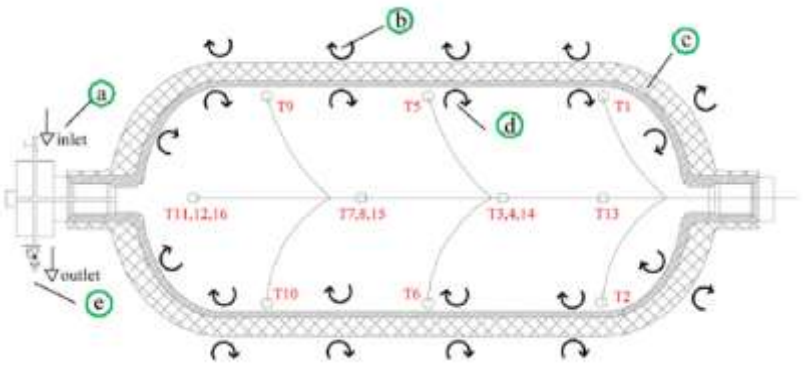

Figure 2.50: Structure of cylinder and thermocouple locations [28].

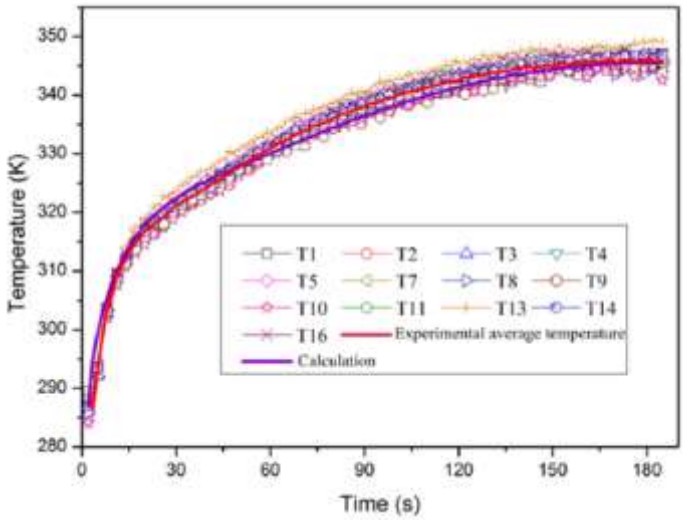

Figure 2.51: Comparison of the predicted and measured gas temperature during the fill [56].

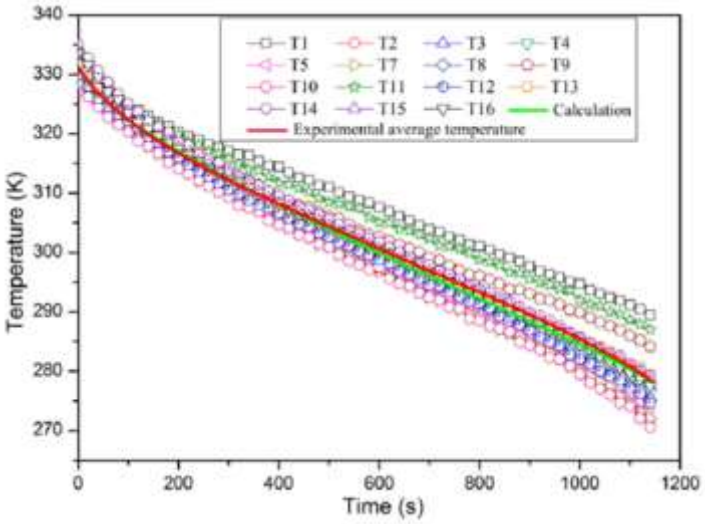

Figure 2.52: Comparison of the predicted and measured gas temperature during the discharge [56].

Striednig et al. [57] also modelled the filling of hydrogen in a 23.5 L, Type IV cylinder based on their experiments. Thermocouples were placed axially along the cylinder for temperature measurement during the filling as shown in Figure 2.53. Experiments were carried out in which a single bank with an initial pressure of 35 MPa was used for the filling of the test cylinder, which had initial gauge pressures ranging from 0.5 MPa to 20 MPa. In addition, the effect of pressure ramp rate on fill time and gas temperature was also investigated. In their single-zone conjugate heat transfer model, Striednig et al. [57] made use of the mass flow rate that was obtained from the experiments for the computation of the density of the gas in the cylinder. In addition, the model assumed that during the fill, the gas pressure inside the cylinder was equal to the gas pressure being supplied by the dispenser. Striednig et al. [57], assumed that the flow in the cylinder is similar to the flow in a

pipe and computed the Nusselt number for the heat transfer in the inner section of the cylinder based on the empirical relations of Petukhov [58]. On the outer surface of the cylinder, a constant heat transfer coefficient of 10 W/m^2-K was applied. The model was found to be successful in predicting the gas temperature during the fill with two different scenarios: (1) the filling of the cylinder with different ramp pressure rates being applied by the dispenser (Figure 2.54), (2) the filling of the cylinder having different initial gauge pressures (Figure 2.55).

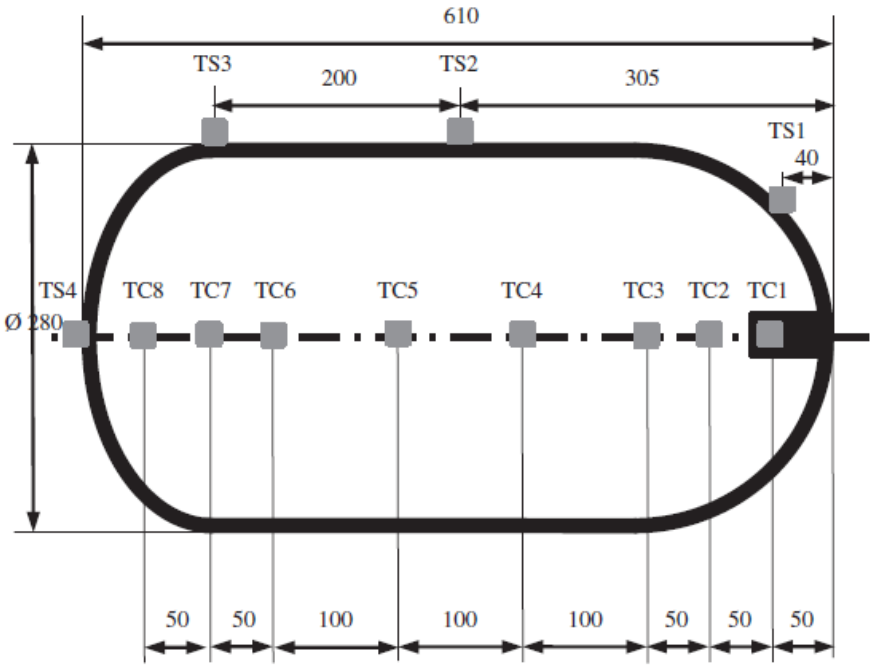

Figure 2.53: Dimensions of cylinder in mm and thermocouple locations inside (TC) and outside (TS) [63].

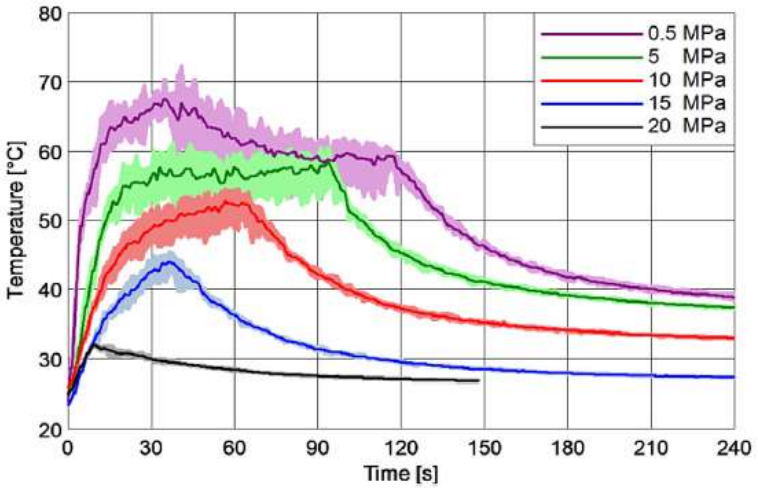

Figure 2.54: Comparison of the predicted (straight line) and measured (shaded region) gas temperature for different initial gas pressures in the cylinder [63].

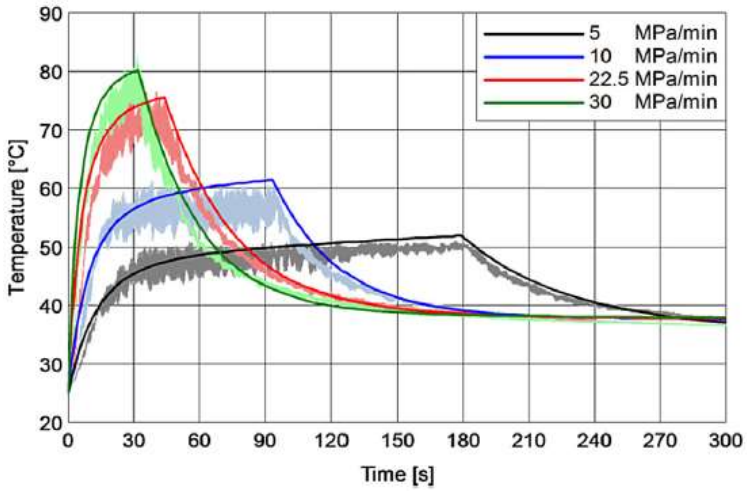

Figure 2.55: Comparison of the predicted (straight line) and measured (shaded region) gas temperature for different pressure ramp rates [63].

Johnson et al. [30] proposed a multi-zone conjugate heat transfer model for the fast-filling of a hydrogen pressure vessel, in which both the forced and natural heat transfer coefficients were modelled using the approach of Means [59] and Clark [60]. The cylinder was modelled as a connected series of three control volumes (Figure 2.56), whereby at each time step, the mass that initially enters Volume 1 is transferred to Volume 2 and finally ends up in Volume 3.

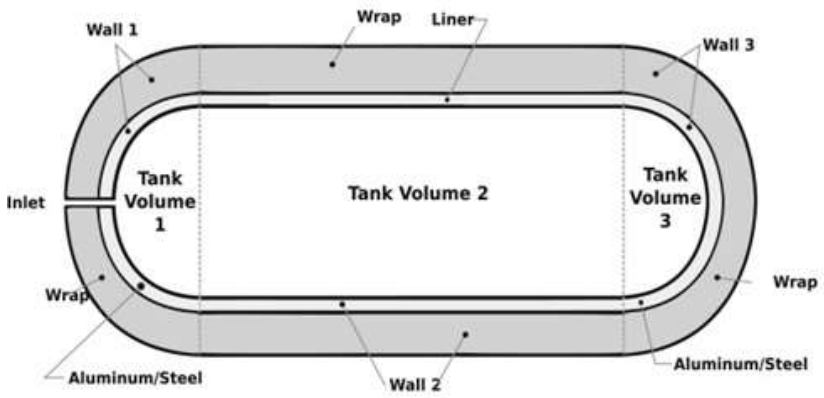

Figure 2.56: Structure of the cylinder with the different control volumes [30].

Similar to the previous single-zone models [29, 55 - 57], the mass flow rate and the pressure rise in the cylinder, which was assumed in being similar to the pressure applied by the dispenser were used along with the modelled heat transfer coefficient for the computation of the gas temperature. In their model, Johnson et al. [30], combined the forced and natural heat transfer coefficients using the approach of Ranong et al. [59]. The model was developed using a network flow analysis code NETFLOW and was successful in predicting the gas temperature

during the fill (Figure 2.57). However, the model assumes that the gas is perfect as it assumes that the specific heats are constant, which are used to determine the specific enthalpy and internal energy.

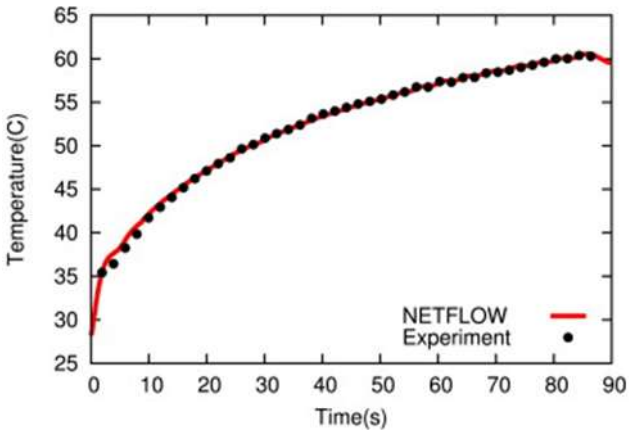

Figure 2.57: Comparison of the predicted and measured gas temperature during the fill [30].

A thermodynamic model for the fast-filling of a NGV was put forward by Deymi-Dashtebayaz et al. [60] that did not include the heat transfer in either in the cylinder or the banks. Filling simulations were performed ambient temperatures varying between 270 K and 340 K, with the bank pressure initially at 20.8 MPa and the test cylinder at 0.1 MPa. The main conclusion that was obtained from the model was that the ambient temperature has big effects on the filling process; at higher temperatures, the mass of gas that is delivered to the vehicles decreases, thereby lowering its driving range. The model also showed that at the start of the fill, the gas temperature in the cylinder initially decreases before rising to a final value (Figure 2.58).

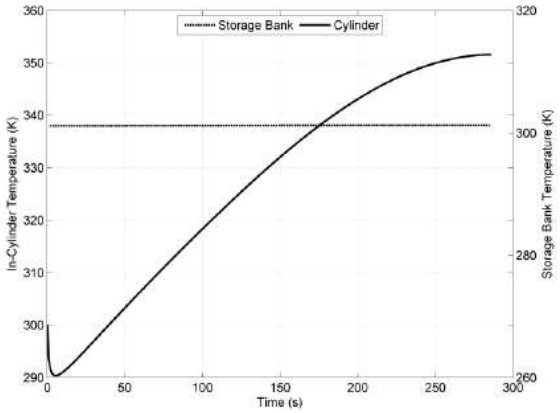

Figure 2.58: Temperature profile of the NGV cylinder and bank during the fill [66].

The initial dip in the gas temperature is due to the Joule-Thomson effect, as the gas undergoes an isenthalpic expansion from a high pressure to a low pressure region [60]. However, as the filling proceeds, the compression of the gas overcomes the Joule-Thomson effect and a rise in the gas temperature is observed. As shown in Figure 2.58, the gas temperature in the storage bank is constant during the filling process, which suggests that in their model, Dashtebayaz et al. [60] assumed that the bank is an infinite reservoir.

2.7 Compressible flows in pipes & pipe components

According to the filling protocols [17, 21], the components present in CNG and hydrogen fast-fill stations are similar with the exception of the presence of a heat exchanger for the filling of hydrogen vehicles. Both fill stations consist of a network of interconnecting pipes that transport the gas from the high pressure banks to the dispenser during the refuelling of the vehicles [61].

Fluid flow in a pipe is laminar when the Reynolds number is less than 2300, turbulent when the Reynolds number is greater than 4000 and transitional in between those values [62, 63]. Turbulence is characterised by the rapid fluctuations of the fluid since the inertial forces are relatively large with respect to the viscous forces. At low Reynolds number, the viscous forces are able to suppress the inertial forces and leads to an ‘orderly’ motion of the fluid. When a fluid enters a pipe, the fluid particles that are in contact with the inner surface of the pipe come to a stop and leads to the formation of a boundary layer whose thickness layer increases until it reaches the center of the pipe [68, 69]. The region of the pipe from the inlet until the boundary layer fills the entire pipe is known as the entrance region, beyond which the flow is fully developed (Figure 2.59). The velocity profile for a fully developed flow is parabolic for the laminar flow and is flatter for the turbulent flow [62, 63].

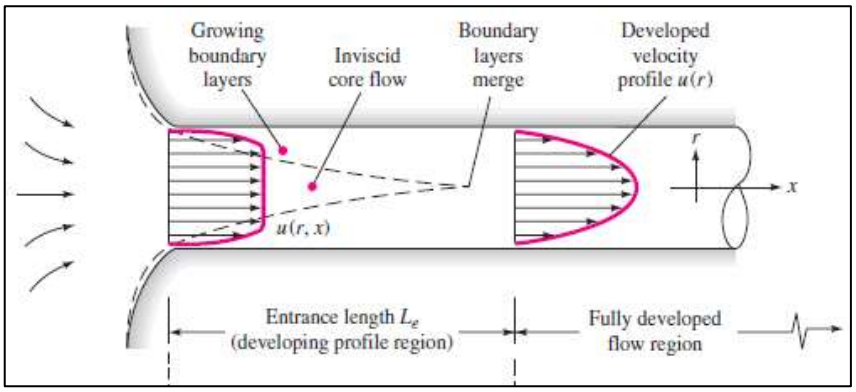

Figure 2.59: Velocity profile at the entrance of a pipe [63].

Fluid flow in pipes/ducts experience a pressure drop due to the friction that occurs between the fluid and the inside wall [62, 63]. Pressure drops larger than 40% are often encountered between the entrance and the exit of long pipe lines of tens of miles [64]. Thus, for the distribution of natural gas cross hundreds of miles, compressor stations are usually placed between 50 and 100 miles apart along the major pipelines to further boost the gas pressure [65]. The pressure drop for a given flow rate in long pipelines that typically cover ten of miles can be determined using either the Weymouth [66] or the Panhandle [67] formulas, while for relatively short pipes of a few hundred meters, Darcy's formula can be applied [64]. The Darcy formula contains the following terms: the Darcy friction factor, the length of the pipe, the diameter of the pipe, the average velocity of the fluid and the gravitational constant [62]. For a given mass flow rate/Reynolds number and pipe roughness, the Darcy friction factor can be determined from the Moody chart [68]. In the analysis of piping systems, pressure losses are often defined in terms of the head loss 'h_L', which is defined as the ratio of the pressure drop and the product of the density and gravitational constant [62].

In a hydrogen/CNG filling station, the gas that travels in the piping system that connects the banks and the dispenser, passes through various fittings such as valves, bends, elbows, tees, enlargements and contractions in addition to the pipe [61]. The presence of these components leads to additional losses in pressure as they induce flow separation. Those losses are expressed in terms of the loss coefficient 'K_L' and are experimentally determined for each component [62, 63]. Table 2.3 displays the known K_L value of some components [62].

Component	Loss coefficient (K_L)
Globe valve – fully open	10
Tee - Flanged	1.0
90° smooth bend - Threaded	0.9
Pipe exit	2 (laminar flow) & 1.05 (turbulent flow)

Table 2.3: Loss coefficients of some pipe components [68].

Once the K_L value of a component is known, the equivalent length L_{equi} can be determined as the ratio of the product of the pipe diameter and loss coefficient K_L to the Darcy friction factor [68]. Thus the contribution of a particular component to the head loss of an overall piping system can be accounted by adding the equivalent length to the total pipe length.

2.8 Discharge Coefficient

A review of the recent literature on the low order models of the fast-filling of cylinders [29, 30, 55-57] have shown that most models share one main commonality: the mass flow rates that have been determined from experiments are being used to determine the mass of gas that is being supplied in the cylinders. On the other hand, in their single-zone model, Kountz [55] and Dashtebayaz et al. [66] used the mass flow rate equation across an orifice to determine the mass of gas being dispensed into the cylinder. However, the mass flow rate equation [55], assumes ideal gas behaviour and is not suitable for the simulation of the filling of cylinders. According to the experiments and the CFD simulations that have been performed on the filling of cylinders [5-8, 26-30, 32, 41, 46-48], the mass flow rate is not constant throughout the fill. Thus, without experimentally carrying out the fill to determine the mass flow rate, the low order models that have been proposed [29, 30, 55-57] cannot be used and would require an additional model for the mass flow rate. The filling protocols [17, 21] and hydrogen filling experiments [5, 6, 26–30, 32, 57] explicitly mention that a ramp pressure profile is applied by the pressure control valve at the dispenser. When filling occurs, the exit of the dispensing unit delivers the gas throughout a tube that protrudes into the cylinder (Figure 2.60).

Figure 2.60: Mid-plane section of the cylinder with the delivery tube [5].

The gas transfer from the dispensing unit to the cylinder occurs due to the higher pressure of the gas being delivered than the gas pressure in the cylinder. Assuming that the mass flow through the delivery tube is isentropic, the mass flow rate can be determined using the following gas properties: the upstream delivery pressure, the upstream total temperature or enthalpy of the gas being delivered and the gas pressure in the cylinder [69]. However, the isentropic assumption is not valid in the boundary layer adjacent to the inner wall of the delivery tube as friction occurs in between the fluid and the inside wall, leading to a pressure drop [62, 63]. Since the actual mass flow rate is unknown, the pressure drop along the pipe cannot be determined from the Moody chart. Thus in order to correctly determine the actual mass flow rate, the isentropic mass flow rate must be multiplied by a discharge coefficient to account for the pressure drop along the delivery tube [70, 71].

A review of the literature has shown that while the discharge coefficients for the flow through nozzles [70, 71] and across an orifice/constriction in a pipe [72] have been well established, there is no mention of a discharge coefficient for the flow in a pipe without any constrictions. The discharge coefficient for the flow in a nozzle can be broken down as follows [70, 71]:

1. The viscous discharge coefficient $C_{d,1}$ - accounts for the boundary layer development along the nozzle. The viscosity of the fluid retard the fluid motion in the boundary layer that is close to the inside wall of the nozzle. This leads to a reduction in fluid velocity in the boundary layer region leading to a decrease in mass flow.
2. The inviscid discharge coefficient $C_{d,2}$ - accounts for the inviscid core at the center beyond the boundary layer. The flow beyond the boundary layer is multidimensional with a parabolic profile.

3. The virial discharge coefficient $C_{d,3}$ – accounts for the real gas effects that alter the speed of sound and density. This results in changes in the heat capacity of the gas which is constant for a perfect gas.

According to Johnson and Wright [70], the total discharge coefficient can be obtained by multiplying the individual discharge coefficients together. The discharge coefficients that are applied to the flow in a nozzle [70, 71] can in theory also be applied to pipe flows. In addition, for turbulent pipe flows, which are expected in the fast-filling of cylinders [7], $C_{d,2}$ can be ignored since the velocity profile is 'flat' for turbulent flow in a pipe [62, 63].

2.9 Heat Storage & Heat transfer enhancement

The experiments and simulations that have been performed on the filling of cylinders [5-8, 26-30, 32, 36, 52-54] have all shown in an increase in the gas temperature during the fill. As described in the SAE TIR J2601 [17], for hydrogen filling, pre-cooling of the gas, which requires additional energy is needed to lower the gas temperature in the cylinder below the limit of 85°. Thus, the development of methodologies that are capable of enhancing the heat transfer from the gas to the environment or to a heat sink during the fill, may lessen the need for pre-cooling.

The most common method for the storage of thermal energy is as sensible heat, in which heat is transferred to the storage medium, leading to an increase in temperature of the latter [73]. For example, hot water storages in the form of boilers are used for domestic heating during cold winters. The storage of heat as latent heat, requires a phase change material (PCM) that will undergo a phase change by melting and for pure substances, the phase change occurs without a change in the temperature [73]. For the solid to liquid phase change, the energy stored is referred as the latent heat of fusion or the solid-liquid phase change enthalpy [73].

In 2014, Air Liquide patented the inclusion of phase change material (PCM) that is included within the structure of the cylinder [74]. According to the patent [74], simulations on the hydrogen filling at a final pressure of 87.5 MPa of a 100 L, Type IV cylinder in which a layer of PCM was added to the inner surface of the liner showed a decrease in fill time by more than 70 %. Figure 2.61 shows the change in the fill time (y-axis) with respect to the thickness (x-axis) of the PCM for fillings with ambient temperatures of 293 K and 284 K.

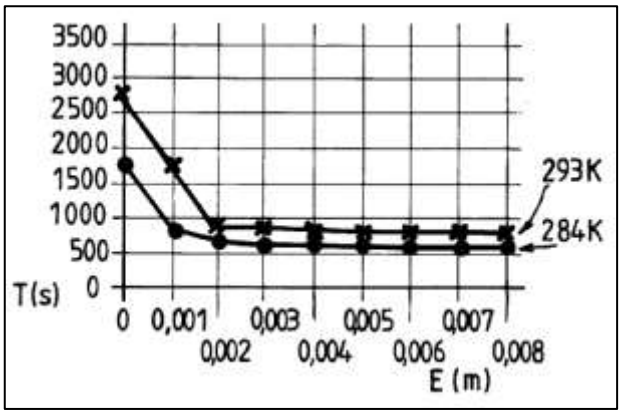

Figure 2.61: Fill time versus thickness of PCM for filling at ambient temperatures of 284 K and 293 K [80].

The patent did not mention what type of PCM was used in the simulation, but it can be assumed that a solid-solid phase change material was used since the PCM was located on the inside surface of the liner. However, solid-solid PCMs have to lower phase change enthalpy than solid-liquid PCMs and the transition temperature of solid-solid PCMs are often above the 85° C limit [73, 75]. Many non-metallic PCMs such as salt hydrates and paraffin undergo a solid-liquid phase change at temperatures ranging from 30° C to 60° C, but have a very low thermal conductivity, which acts as a barrier for rapid heat transfer. For example, the Suntech P116 paraffin wax [76] has a thermal conductivity of 0.24 W/m-K, while the thermal conductivity of the aluminium alloy that was used as the liner in the Type III cylinder in the filling experiment of Dicken and Merida [7] is 167 W/m-K. However, the enhancement of the thermal conductivity of non-metallic PCMs can be achieved by adding metallic pieces or graphite particles to the PCM [77, 78]. One major disadvantage of solid-liquid PCMs is the requirement for encapsulation to prevent leakages and stress caused by the thermal expansion during phase change.

2.10 Modelling of filling stations

The modelling of a whole filling station have been developed by Rothuizen et al. [79] and Omdahl [80]. The model of Rothuizen et al. [79] showed the efficiency of the cascade filling during the fast-fill of the hydrogen station. However, the model assumed that the heat transfer coefficient during the filling of the cylinder has the constant value of 500 W/m^2-K throughout the fill similar to model that was put forward by Monde et al. [55]. In addition, the model was not been validated using experimental results to determine its accuracy in predicting the gas temperature in the cylinder. The model proposed by Omdahl [80] consisted of all components of

a hydrogen filling station including an electrolyser for the production of hydrogen. However, the model assumed that that the filling process in the cylinder is adiabatic and pressure loses in the piping system in the filling station are negligible.

2.11 Summary

The review of the literature has shown that there are two types of fill stations that can be used by CNG/H_2 vehicles: the fast-fill station and the time-fill station. According to the filling protocols, the filling procedures for both types of vehicles is similar with the exception of pre-cooling of the gas for hydrogen filling. The literature involving experiments and CFD simulations of the filling of cylinders only focuses on hydrogen filling, leaving a gap on the filling of natural gas vehicles. The experiments on the fast-filling of hydrogen pressure vessels have shown an increase in temperature due to the Joule-Thomson effect, the conversion of the PV work into the internal energy of the gas and the compression of the gas.

Both two and three-dimensional simulations of hydrogen filling have shown that the k-ε turbulence model is capable of accurately predicting the gas temperature in the cylinder during the fill and have also demonstrated that the mass flow rate is not constant during the fill. In addition, the need for a real gas equation of state is vital for the CFD modelling of the fill. The development of a low order model that simulates the filling of cylinder whilst determining the mass flow rate using ideal gas assumption is therefore incorrect. With the mass flow rate varying during the fill, most researchers have used the mass flow rate that has been obtained from experiments in their low order model to simulate the fast-fill. The inability of the low order models to predict the mass flow rate coupled with their reliance on experimental values limit their capability to be used as tool to simulate the filling of cylinders. Thus there is a need to develop a model that is capable of determining the mass flow rate without assuming ideal gas behaviour. In addition, the determination of a discharge coefficient through the delivery pipe using the pressure ratio across the pipe is key in determining the mass flow rate since the flow through the pipe is not isentropic.

A fast-fill station consists of a series of interconnecting pipes over tens of meters along with valves and bends. For such ‘short’ pipe lengths and configurations, the Moody chart can be used in the development of the low order model of the filling

station to predict the pressure losses the piping system as the gas flows from the banks to the dispenser.

The experiments and simulations of the fast-filling of hydrogen, have not addressed the effect of the initial ambient temperature on the final state of the gas following refuelling and thus needs to be investigated. In addition, there is a lack in the literature regarding the effect of the length-to-diameter ratio of a cylinder on the flow field and the resulting gas temperature. The use of phase of change materials in cylinders has been suggested in being able to lower the fill time of hydrogen pressure vessels. Solid-liquid PCMs are preferable than solid-solid PCMs due to their higher phase change enthalpy. However, the feasibility of adding a PCM to the structure of a cylinder must be addressed along with the type of PCM that is required to enhance the heat transfer.

3 Formulation

3.1 Introduction

This chapter describes the formulas and their usage in this work. Initially, the equations that were used in the two-dimensional axisymmetric CFD modelling of the fast-filling of a Type III hydrogen vessel are given. The modelling of the viscous discharge coefficient that involves equations from both the two-dimensional axisymmetric CFD modelling and the isentropic modelling of the pipe flow are described. The methodologies used in the low order model for computing heat conduction across the structure of the cylinder as well as heat transfer through a phase change material (PCM) that is part of the structure of the cylinder are explained. In addition, the equations involved for the filling of the cylinder are given. Finally, the modelling of the filling station is illustrated, which in addition to the filling of the cylinder also includes equations for the flow in the piping network and the emptying of the high pressure banks.

3.2 2D numerical model

The two-dimensional simulations for the filling of the hydrogen vessel and the pipe flow to model the viscous discharge coefficient were both performed using the FLUENT software. FLUENT was chosen because of its capability to use real gas models to accurately solve for the fluid flow and heat transfer problems despite the working fluid behaviour deviating from the ideal gas assumption [81].

3.2.1 Cylinder filling

The filling of the hydrogen pressure vessels involves unsteady compressible flow. Thus along with pressure and velocity fluctuations, density and temperature fluctuations must also be accounted for. The governing equations used in the current study are the unsteady Favre-averaged continuity, momentum and energy equations [9]. A compressible flow is one in which significant density changes occur, even with small pressure changes. This includes low-speed flows with large heat transfer rates [9]. Thus, the fast-filling process is considered compressible due to the significant heat transfer that occurs from the gas to the structure of the cylinder. Following the review of the literature, the standard k-ε turbulence model was chosen for the two-dimensional simulation of the fast-fill.

3.2.1.1 Favre-averaged v/s Reynolds-averaged Equations

The instantaneous equations of mass, momentum and energy are as follows [9]:

$$\frac{\partial \rho}{\partial t} + \frac{\partial}{\partial x_i}(\rho u_i) = 0 \tag{3.1}$$

$$\frac{\partial}{\partial t}(\rho u_i) + \frac{\partial}{\partial x_j}(\rho u_j u_i) = -\frac{\partial p}{\partial x_i} + \frac{\partial}{\partial x_j}(t_{ji}) \tag{3.2}$$

$$\frac{\partial}{\partial t}\left[\rho\left(e + \frac{1}{2}u_i u_i\right)\right] + \frac{\partial}{\partial x_j}\left[\rho u_j\left(h + \frac{1}{2}u_i u_i\right)\right] = \frac{\partial}{\partial x_j}(u_i t_{ji}) - \frac{\partial q_j}{\partial x_j} \tag{3.3}$$

where the vectors u_i and x_i are velocity and position, p is pressure, ρ is density, e is the specific internal energy, $h = e + {}^{p}/_{\rho}$ is the specific enthalpy, q_j is the heat flux vector and t is time.

The term t_{ji} is the viscous stress tensor and is defined as follows:

$$t_{ij} = 2\mu S_{ij} + \lambda \frac{\partial u_k}{\partial x_k}\delta_{ij} \tag{3.4}$$

where μ is the dynamic viscosity, S_{ij} is the strain-rate tensor, λ is the second viscosity and δ_{ij} is Kronecker delta. The second term on the right hand-side of Equation 3.4 is zero for incompressible flows (since $\frac{\partial u_i}{\partial x_i} = 0$ for incompressible flows). The strain-rate tensor is expressed as follows:

$$S_{ij} = \frac{1}{2}\left(\frac{\partial u_i}{\partial x_j} + \frac{\partial u_j}{\partial x_i}\right) \tag{3.5}$$

The second viscosity λ is related to the dynamic viscosity μ as follows:

$$\lambda = -\frac{2}{3}\mu \tag{3.6}$$

For incompressible flows, Reynolds-averaging is typically performed. Since the density is constant for incompressible flows, Equations 3.1 and 3.2 can be simplified resulting to:

$$\frac{\partial u_i}{\partial x_i} = 0 \tag{3.7}$$

$$\rho\frac{\partial u_i}{\partial t} + \rho u_j\frac{\partial u_i}{\partial x_j} = -\frac{\partial p}{\partial x_i} + \frac{\partial}{\partial x_j}(2\mu S_{ij}) \tag{3.8}$$

It can be observed from Equations 3.7 and 3.8 that only two flow properties need to be decomposed for Reynolds-averaging: the velocity and pressure:

$$u_i = U_i + u'$$
$$p = P + p' \tag{3.9}$$

where u_i and p are respectively the instantaneous velocity and pressure and represented and the sum their respective mean values (U_i and P) and fluctuating parts (u' and p').

Reynolds-averaging involves either an integral (time average and spatial average) or a summation (ensemble average) [9]. Time-averaging is typically used for stationary turbulence whereby the turbulent flow does not vary with time. Spatial-averaging is normally used for homogeneous turbulence whereby the turbulent flow on average is uniform in all directions. Ensemble-averaging is the most general type of Reynolds-averaging and is suitable for flows that decay with time.

Using the instantaneous velocity as an example, the time-averaged velocity can be expressed as follows:

$$\bar{u}_i = \lim_{T\to\infty} \frac{1}{T}\int_t^{t+T} u_i \, dt = \lim_{T\to\infty} \frac{1}{T}\int_t^{t+T} U_i \, dt + \lim_{T\to\infty} \frac{1}{T}\int_t^{t+T} u' \, dt \tag{3.10}$$

The time-averaged of the mean value is the same as the mean while the time average of the fluctuating part is zero. Thus time-averaged of the instantaneous velocity is equal to the mean:

$$\bar{u}_i = U_i \tag{3.11}$$

Time-averaging of Equations 3.7 and 3.8 results in the Reynolds-averaged Equations:

$$\frac{\partial U_i}{\partial x_i} = 0 \tag{3.12}$$

$$\rho \frac{\partial U_i}{\partial t} + \rho U_j \frac{\partial U_i}{\partial x_j} = -\frac{\partial P}{\partial x_i} + \frac{\partial}{\partial x_j}\left(2\mu S_{ij} - \rho\overline{u_j' u_i'}\right) \tag{3.13}$$

Aside from the replacement of the instantaneous variables by the mean values, one major difference between the instantaneous equations (Equations 3.7 and 3.8) and the Reynolds-averaged equations (Equations 3.12 and 3.13) is the

appearance of the term $-\rho\overline{u_j'u_i'}$ in the Reynolds–averaged momentum equation. The correlation $\overline{u_j'u_i'}$ represents the time-averaged rate of momentum transfer due to turbulence [9]. The quantity $-\rho\overline{u_j'u_i'}$ is known as the Reynolds-stress tensor, which can be denoted as $-\rho\tau_{ij}$, whereby τ_{ij} is the specific Reynolds-stress tensor and is given by:

$$\tau_{ij} = \overline{u_j'u_i'} \tag{3.14}$$

It can be observed from Equation 3.14 that $\tau_{ij} = \tau_{ij}$ and thus the specific Reynolds-stress tensor is symmetric in nature and six independent components. Thus Reynolds-averaging of the instantaneous equations (Equations 3.7 and 3.8) has produced six unknown quantities ($\overline{u_1'u_1'}$, $\overline{u_2'u_2'}$, $\overline{u_3'u_3'}$, $\overline{u_1'u_2'}$, $\overline{u_1'u_3'}$, $\overline{u_2'u_3'}$) in addition to the pressure (P) and the three velocity components (U_1, U_2, U_3). Thus, there are ten unknowns and four equations leading to an unclosed system. The closure strategy for incompressible flows only involves modelling the specific Reynolds stresses.

Since the fast-filling process involves compressible flows, density and temperature fluctuations must be accounted in addition to velocity and pressure fluctuations. If the standard Reynolds-averaging procedure is performed, this leads to additional terms in the mean conservation equations. To further illustrate this point, the Reynolds-averaging of the conservation of mass equation (Equation 3.1) is considered.

The instantaneous density ρ is decomposed as the sum of the mean density $\bar{\rho}$ and its fluctuating component ρ':

$$\rho = \bar{\rho} + \rho' \tag{3.15}$$

The instantaneous velocity is decomposed in a similar fashion (Equation 3.9) and substituting into Equation 3.1 yields

$$\frac{\partial}{\partial t}(\bar{\rho} + \rho') + \frac{\partial}{\partial x_i}(\bar{\rho}U_i + \rho'U_i + \bar{\rho}u_i' + \rho'u_i') = 0 \tag{3.16}$$

Time-averaging of Equation 3.16 results in the Reynolds-averaged continuity equation for compressible flow:

$$\frac{\partial\bar{\rho}}{\partial t} + \frac{\partial}{\partial x_i}(\bar{\rho}U_i + \overline{\rho'u_i'}) = 0 \tag{3.17}$$

Aside from the replacement of the instantaneous variables by the mean values, one major difference between the instantaneous continuity equation (Equation 3.1) and the Reynolds-averaged continuity equation for compressible flow (Equation 3.17) is the appearance of the term $\overline{\rho' u_i'}$. Thus, in order to achieve closure of the continuity equation for compressible flow, a correlation between ρ' and u_i' is required. Reynolds-averaging of the momentum equation (Equation 3.2) leads to more complex additional terms whereby the Reynolds stress tensor will originate by the time-averaging of the product $\rho u_j u_i$. Hence, a triple correlation between ρ, u_i and u_j is required to establish closure.

The complexity of establishing time-averaged equations for compressible flow can be simplified by using a density-weighted averaging procedure that is suggested by Favre [93].

Favre-averaging involves decomposing the following flow properties into a mass-averaged and a fluctuating part:

- The instantaneous velocity - $u_i = \tilde{u}_i + u''$
- The instantaneous specific internal energy - $e = \tilde{e}_i + e''$
- The instantaneous specific enthalpy - $h = \tilde{h}_i + h''$

The pressure and density are conventionally decomposed as sum of their respective mean values and their fluctuating components:

$$\begin{aligned} \rho &= \bar{\rho} + \rho' \\ p &= P + p' \end{aligned} \tag{3.18}$$

The heat flux vector q_j is decomposed as the sum of the laminar flux vector q_{L_j} and its fluctuating component q_j':

$$q_j = q_{L_j} + q_j' \tag{3.19}$$

Using the instantaneous velocity as an example, its mass-averaged part is defined as follows:

$$\tilde{u}_i = \frac{1}{\bar{\rho}} \lim_{T \to \infty} \frac{1}{T} \int_t^{t+T} \rho u_i \, dt \tag{3.20}$$

Multiplying Equation 3.19 by $\bar{\rho}$ on both sides results into the following:

$$\bar{\rho}\tilde{u}_i = \lim_{T\to\infty}\frac{1}{T}\int_t^{t+T}\rho u_i\,dt = \overline{\rho u_\iota} \tag{3.21}$$

The value of this type of averaging is referred as Favre-averaging.

Expansion of the term on the right hand side of Equation 3.20 and performing the indicated Reynolds-averaging process results in the following:

$$\begin{aligned}\overline{\rho u_\iota} &= \overline{(\bar{\rho}+\rho')(U_\iota + u')}\\ &= \overline{\bar{\rho}U_\iota + \bar{\rho}u' + \rho' U_\iota + \rho' u'}\\ &= \bar{\rho}U_i + \overline{\rho' u'}\end{aligned} \tag{3.22}$$

From Equations 3.21 and 3.22, it is obvious that:

$$\bar{\rho}\tilde{u}_i = \overline{\rho u_\iota} = \bar{\rho}U_i + \overline{\rho' u'} \tag{3.23}$$

An inspection of Equation 3.17 shows that the continuity equation for compressible flows can be expressed as:

$$\frac{\partial\bar{\rho}}{\partial t} + \frac{\partial}{\partial x_i}(\bar{\rho}\tilde{u}_i) = 0 \tag{3.24}$$

A comparison of Equations 3.17 and 3.24, show that Favre-averaging eliminates the density fluctuations from the averaged equations. Thus, Favre-averaging is a mathematical simplification and does not explain the physics of the flow [9].

The decomposition of the flow properties followed by the respective substitutions in Equations 1-3 and performing the mass-averaging operations results in the Favre-averaged equations [9]:

$$\frac{\partial\bar{\rho}}{\partial t} + \frac{\partial}{\partial x_i}(\bar{\rho}\tilde{u}_i) = 0 \tag{3.25}$$

$$\frac{\partial}{\partial t}(\bar{\rho}\tilde{u}_i) + \frac{\partial}{\partial x_j}\left(\bar{\rho}\tilde{u}_j\tilde{u}_i\right) = -\frac{\partial P}{\partial x_i} + \frac{\partial}{\partial x_j}\left(\bar{t}_{ji} - \overline{\rho u_j'' u_\iota''}\right) \tag{3.26}$$

$$\begin{aligned}&\frac{\partial}{\partial t}\left[\bar{\rho}\left(\tilde{e}+\frac{\tilde{u}_i\tilde{u}_i}{2}\right) + \frac{\overline{\rho u_\iota'' u_\iota''}}{2}\right] + \frac{\partial}{\partial x_j}\left[\bar{\rho}\tilde{u}_j\left(\tilde{h}+\frac{\tilde{u}_i\tilde{u}_i}{2}\right) + \tilde{u}_j\frac{\overline{\rho u_\iota'' u_\iota''}}{2}\right]\\ &\quad= \frac{\partial}{\partial x_j}\left(\tilde{u}_i\left(\tilde{t}_{ji} - \overline{\rho u_j'' u_\iota''}\right)\right)\\ &\quad+ \frac{\partial}{\partial x_j}\left(-q_{L_J} - \overline{\rho u_j'' h''} - \overline{\rho u_j''\frac{1}{2}u_\iota'' u_\iota''} + \overline{t_{j\iota}u_\iota''}\right)\end{aligned} \tag{3.27}$$

In Equation 3.26, the Favre-averaged Reynolds stresses $(\overline{u_j'' u_i''})$ is multiplied by mean density ($\bar{\rho}$) and results into the term $\overline{\rho u_j'' u_i''}$. In the incompressible case, the density is not decomposed since it is a constant and thus the multiplication of the Reynolds stresses ($\overline{u_j' u_i'}$) by the density (ρ) results into $\rho\overline{u_j' u_i'}$.

The Favre-averaging of the 3 equations, results in several unclosed terms due to the presence of the fluctuating terms and are listed as follows:

1. The Reynolds stress $\overline{\rho u_j'' u_i''}$
2. The Reynolds heat flux $\overline{\rho u_j'' h''}$
3. The kinetic energy of the turbulent fluctuations $\frac{\overline{\rho u_i'' u_i''}}{2}$
4. The turbulent transport of the turbulent kinetic energy $\overline{\rho u_j'' \frac{1}{2}\ u_i'' u_i''}$
5. The molecular diffusion of turbulent kinetic energy of $\overline{t_{ji} u_i''}$

The closure strategies of the standard k-ε model is further discussed in Appendix A3.

The transient heat equation for the walls is shown in Equation 3.28.

$$\frac{\partial T_s}{\partial t} = \frac{\partial}{\partial x_i}\left(\alpha_s \frac{\partial T_s}{\partial x_i}\right) \tag{3.28}$$

where α_s is the thermal diffusivity of the solid material.

The thermal conductivities of both the liner and laminate were kept constant during the fill for simplicity. Coupling of energy equations of the gas and that of the liner wall enables the computation of heat transfer to the walls.

3.2.1.2 Equation of State

The equation of state chosen for the filling simulation is the 33 term modified Webb-Rubin equation of state [88] and is obtained from the NIST database: REFPROP 9.0. The modified Webb-Rubin Equation of state [88] was chosen as opposed to the cubic equations of states [34, 42-44]. The advantages of the modified Webb-Rubin equation of state are as follows [82]:

1. It is versatile and is appropriate for use with multiproperty fitting techniques.

2. It is an accurate model over a wide range of temperature and pressure.

3.2.2 Pipe flow (Modelling the discharge coefficient)

The pipe flow is modelled as a steady compressible flow. Equations 3.1, 3.2 and 3.4 were used in the 2D CFD simulations with the exception of the unsteady terms, which are not required. Similar to the fast-filling of the cylinder, the standard k-ε turbulence model was also chosen to model the pipe flow. Both the ideal gas equation of state (Equation 3.9) and the modified Webb-Rubin equation of state [88] were to determine real gas effects on the viscous discharge coefficient. The viscous discharge coefficient is the ratio of the actual mass flow rate, which is determined by the 2D CFD model and the isentropic mass flow rate. (Equation 3.10).

$$P = \rho RT \tag{3.29}$$

$$C_{d1} = \frac{\dot{m}_{actual}}{\dot{m}_{isen}} \tag{3.30}$$

where $\dot{m}_{actual}$ is the actual mass flow rate that is determined from the 2D CFD simulations in FLUENT. $\dot{m}_{isen}$ represents the isentropic mass flow rate in which the gas is assumed to be inviscid and is determined from Equation 3.32.

3.3 Isentropic pipe flow (Modelling the discharge coefficient)

3.3.1 Calculation of the isentropic mass flow rate

The modelling for the isentropic pipe flow were carried out in Matlab. Figure 3.1 shows the two-dimensional drawing of a flow through a pipe in which the following properties are known: the upstream stagnation pressure (P_0), the stagnation temperature(T_0), the static back pressure(p).

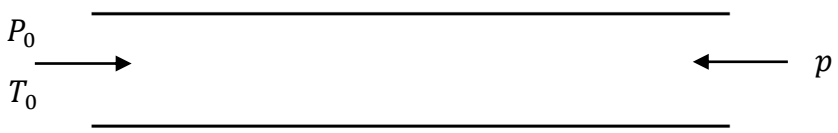

Figure 3.1: Flow through a pipe.

If the viscosity of the fluid is neglected, the following isentropic relationship applies for an ideal gas [83]:

$$\frac{P_0}{p} = \left(1 + \frac{\gamma - 1}{2} M^2\right)^{\frac{\gamma}{\gamma-1}} \tag{3.31}$$

γ is the ratio of the specific heats and M is the Mach number at the exit. The Mach number cannot be greater than unity, which is the condition whereby choking occurs at the exit. Once the Mach number is known, the isentropic mass flow rate for an ideal gas can be obtained using Equation 3.32 [83]:

$$\dot{m}_{isen} = \sqrt{\frac{\gamma}{R}} \frac{P_0}{\sqrt{T_0}} A.M \left(\frac{1}{1 + \frac{\gamma - 1}{2} M^2}\right)^{\frac{\gamma+1}{2(\gamma-1)}} \tag{3.32}$$

The terms R and A respectively represent the gas constant and the cross-sectional area of the pipe.

3.3.2 Equation of State

For real gas cases, the mass flow rate is calculated by determining the thermodynamic properties of the gas from modified Webb-Rubin equation of state from the NIST database: REFPROP 9.0. The procedure in determining the isentropic mass flow rate for a real gas is further explained in section 3.4.2 of this chapter.

3.4 Modelling of the filling station

The code for the modelling of the filling station is written in Matlab. The model of the filling station consists of a network of elements: the emptying of the banks, the flow in piping system that connects the banks to the dispenser and the filling of the cylinder.

3.4.1 Energy equation for the filling of the cylinder

The energy equation for the filling of the cylinder is as follows:

$$\frac{d(m_{gas} u_{gas})}{dt} = h_{0_{in}} \dot{m}_{in} + \dot{Q}_{wall} \tag{3.33}$$

where m_{gas} is the mass of gas in the tank, u_{gas} is the specific internal energy of the gas in the tank, $\dot{m}_{in}$ is the mass flow rate at the inlet, $h_{0_{in}}$ is the specific stagnation enthalpy of the gas at the inlet and $\dot{Q}_{wall}$ is the heat transfer rate.

3.4.2 Computing the mass flow rate into the cylinder

Initially, the flow of the gas through the small delivery tube and into the cylinder is considered isentropic. At the inlet, the stagnation pressure is known along with either the stagnation temperature of the stagnation enthalpy. To account for the real gas effects, the thermodynamic properties of the gas were calculated by the NIST database: REFPROP 9.0. The specific stagnation entropy is obtained from the aforementioned stagnation values.

The specific entropy of the gas is similar at both the static and the stagnation conditions. At the first time step in the model, the static pressure at the exit of the valve is set to the gas pressure in the tank. The specific enthalpy and speed of sound at static conditions is determined by REFPROP 9.0 from the static pressure and specific entropy values. The velocity of the gas at the exit of the nozzle and into the cylinder is determined from Equation 3.34.

$$V_{exit} = \sqrt{2\left(h_{0_{in}} - h_{static}\right)} \tag{3.34}$$

where h_{static} is the specific static enthalpy

The Mach number at the exit of the valve is given in Equation 3.35.

$$M = \frac{V_{exit}}{a} \tag{3.35}$$

If the Mach number is greater than one, this implies that the static pressure is greater than the gas pressure, which represents the case of an underexpanded nozzle. An iteration procedure is thus used in which the static pressure is incrementally increased and is used along with the constant specific entropy to determine new values of static specific enthalpy and speed of sound, until the Mach number calculated is equal to one. A similar procedure is used for all of the other time steps.

The static density of the gas at any other time step is thus determined by any two of these static properties that have already been computed: the specific enthalpy, the static pressure and the specific entropy.

The isentropic mass flow rate of the gas at the inlet is determined from Equation 3.36.

$$\dot{m}_{isen} = \rho_{static} V_{exit} A_{exit} \tag{3.36}$$

The actual mass flow rate is obtained from the Equation 3.10 in which the viscous discharge coefficient C_{d1} is multiplied by the isentropic mass flow rate (Equation 3.37).

$$\dot{m}_{actual} = \dot{m}_{isen} \times C_{d1} \tag{3.37}$$

3.4.3 Computing heat transfer to the structure of the cylinder

The heat transfer rate ($\dot{Q}_{wall}$) can be expressed as shown in Equation 3.38

$$\dot{Q}_{wall} = -A h_{coef} \left(T_{gas} - T_{wall}\right) \tag{3.38}$$

where A is the inner surface area of the liner inside of the cylinder, h_{coef} is the heat transfer coefficient, T_{gas} is the gas temperature and T_{wall} is the temperature at the inner surface of the wall.

The heat flux at the inner wall is expressed in Equation 3.39.

$$\dot{q} = \frac{\dot{Q}_{wall}}{A} \tag{3.39}$$

The Nusselt number due to the forced convection can also be expressed as follows:

$$Nu_f = \frac{h_f L}{k_{gas}} \tag{3.40}$$

where, h_f is the forced heat transfer coefficient, L is the length scale, which is the inner diameter of the cylinder and k_{gas} is the thermal conductivity of the gas. Thus, for the 2D axisymmetric CFD simulation of the hydrogen fill based on the experiment of Dicken and Merida [7], the total heat transfer coefficient h_{coef} is equal to the heat transfer coefficient h_f that is only due to the forced convection. This is due to the fact that buoyancy cannot be applied to axisymmetric CFD cases.

In the filling station, slightly longer fill times are considered; i.e. fill times up to 5 minutes. Thus, heat transfer due to natural convection may also be considered. The Nusselt number for the natural convection is dependent whether the flow is laminar or turbulent. The flow is laminar at low Rayleigh number and the transition to turbulent flow is around $Ra = 10^8$. The correlation is the same for each regime and is a function of the Rayleigh number [54]:

$$Nu_n = CRa^n \tag{3.41}$$

The values of 'C ' and 'n ' that were determined by Means [53] are $C = 0.53$, $n = 0.25$ for the laminar case and $C = 0.12$, $n = 0.333$ for the turbulent case. However, the values obtained by Means were in the vertical position only and the Deaver and Eckert [84] obtained a separate correlation for horizontal vessels in which $C = 1.181, n = 0.214$ for the laminar case and $C = 0.14, n = 0.333$ for the turbulent regime.

The Rayleigh number Ra is determined using Equation 3.42.

$$Ra = \left|\frac{g\beta\left(T_{wall} - T_{gas}\right)D^3}{v\alpha}\right| \tag{4.42}$$

where g is the acceleration due to gravity, β is the coefficient of thermal expansion of the fluid, D is the inner cylinder diameter, v is the kinematic viscosity and α is the thermal diffusivity of the fluid.

The Nusselt number due to the natural convection can also be expressed as follows:

$$Nu_n = \frac{h_n L}{k_{gas}} \tag{3.43}$$

where, h_n is the natural heat transfer coefficient.

The total heat transfer coefficient h_{coef} that is due to both the forced convection and the natural convection is determined using the method of Ranong et al. [65] as shown in Equation 3.44.

$$h_{coef} = \left(h_n^4 + h_f^4\right)^{1/4} \tag{3.44}$$

Heat transfer across the wall of the cylinder is treated as an unsteady heat transfer conduction in accordance with Equation 3.45.

$$\frac{\partial T_s}{\partial t} = \alpha_s \frac{\partial^2 T_s}{\partial x^2} \tag{3.45}$$

where T_s is the temperature of the solid material, and x is the distance from the inner surface of the cylinder. The term α_s is the thermal diffusivity and is obtained by Equation 3.46.

$$\alpha_s = \frac{k_s}{\rho_s c} \tag{3.46}$$

where k_s is the thermal conductivity of the solid, ρ_s is the density and c is the specific heat capacity.

A schematic diagram of the 1D heat transfer through the walls of the cylinder is shown in Figure 3.2.

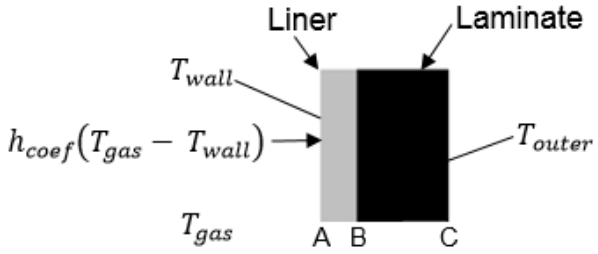

Figure 3.2: 1D unsteady heat transfer across the cylinder wall.

The explicit scheme which is forward in time and centered in space was used to solve the heat Equation and is discretised as given in Equation 3.47.

$$T_j^{m+1} = T_j^m + S\left[T_{j+1}^m - 2T_j^m + T_{j-1}^m\right] \tag{3.47}$$

where m and j are the indices for the time step and the spatial nodes respectively. The term s must less than 0.5 to ensure the stability of the explicit method is given by Equation 3.48.

$$s = \frac{\alpha_s \Delta t}{\Delta x^2} \tag{3.48}$$

The discretised heat equation at the inner wall boundary 'A' is given in Equation 3.49.

$$T_A^{m+1} = T_A^m + 2S\left[T_{A+1}^m - T_A^m + \Delta x h_{coef}\left(T_{gas}^m - T_A^m\right)/k_{liner}\right] \tag{3.49}$$

The discretised heat equation at the interface ‘B’ is given in Equation 3.50.

$$T_B^{m+1} = T_B^m + \frac{\Delta t}{\Delta x^2}\left[\frac{\left(k_{laminate}(T_{B+1}^m - T_B^m) - k_{liner}(T_B^m - T_{B-1}^m)\right)}{0.5(C_{liner}\rho_{liner} + C_{laminate}\rho_{laminate})}\right] \quad (3.50)$$

At the outer wall ‘C’, two different types of boundary conditions can be applied:

1. The Dirichlet boundary condition, in which a temperature is applied.
2. The Neumann boundary condition whereby the heat flux is applied. Thus for adiabatic wall conditions at the outer wall, the heat flux is set to zero (Equation 3.51).

$$\frac{\partial T_c}{\partial x} = 0 \quad (3.51)$$

3.4.4 Modelling the emptying of the bank

The energy equation for the emptying of the bank is as follows:

$$\frac{d(m_{bank}u_{bank})}{dt} = -\dot{m}h_{0_{bank}} + \dot{Q}_{wall} \quad (3.52)$$

Where $\dot{m}$ is the mass flow rate out of the bank and is equal to the mass flow rate at the inlet of the cylinder, $h_{0_{bank}}$ is the specific total enthalpy of the gas in the bank, m_{bank} is the mass of gas in the bank, u_{bank} is the specific internal energy of the gas in the bank.

According to Clark [60], heat transfer during the emptying of a vessel is mainly due to natural convection. Thus Equations 3.41 – 3.43 are used to compute the natural heat transfer coefficient. Similar to the filling of the cylinder, Equations 3.45 – 3.51 are used for the computation of the heat transfer across the walls of the banks.

3.4.5 Modelling the flow in the piping system

The flow of gas from the banks to the cylinders passes through a piping system that consists of interconnecting pipes, valves and bends. The determination of the pressure drop upstream of the dispenser within the piping system can be broken down as follows:

1. Losses due to friction in the pipes
2. Loses due to the presence of valves in the system.

3. Loses due to the presence of bends and branches in the piping system.
4. Losses due to the change in the cross-sectional area of the pipes within the system.

Losses in the pipes

In the current model, the interior surface of the pipe is considered as smooth. With the mass flow rate having already been determined (Equation 3.37), the Reynolds number of the flow in the pipe can be determined using Equation 3.53.

$$Re_d = \frac{4\dot{m}_{atual}}{\pi d \mu} \tag{3.53}$$

where d is the pipe diameter and μ is the dynamic viscosity.

The friction factor f can be determined using the Colebrook equation (Equation 3.54) [90] which is the accepted formula for the determination of the friction factor in pipe flows.

$$\frac{1}{f^{1/2}} = -2.0 \log\left(\frac{\epsilon/d}{3.7} + \frac{2.51}{Re_d f^{1/2}}\right) \tag{3.55}$$

The main disadvantage of the Colebrook equation is that it is implicit in f and therefore the determination of the friction factor requires an iteration procedure, which increases the computational time. In the current model, the friction factor is determined explicitly by the Haaland equation (Equation 3.55) [89], in which the determined values of the friction factor vary within 2% of the Colebrook formula [90].

$$\frac{1}{f^{1/2}} = -1.8 \log\left(\frac{6.9}{Re_d} + \left(\frac{\epsilon/d}{3.7}\right)^{1.11}\right) \tag{3.56}$$

The term ϵ/d is the relative roughness and since only a pipe with a smooth interior, this particular term is set to zero in the model. The pressure loss due to friction is determined using Equation 3.56.

$$P_{loss} = f \frac{L}{d} \frac{\rho v^2}{2} \tag{3.57}$$

where L is the length of the pipe, ρ is the density of the gas, d is the diameter of the pipe, v is the average velocity of the gas and f is the friction factor that is determined from Equation 3.55.

Losses due to the valves

The losses due to the presence of the valves are determined by using the resistance coefficient (K_L). Two types of valves were chosen in the model: the angle valve, which typical of the type of valve that is used for the filling and empty of cylinder and the ball valve, which was selected due to its low resistance coefficient. Each valve has a specific resistance coefficient as shown in Table 3.1 [68].

Angle valve	Fully open	$K_L = 5$
Ball valve	Fully open	$K_L = 0.05$

Table 3.1: Resistance coefficients of angle and ball valve [68].

Loses in valves are expressed in terms of the length equivalent as shown in Equation 3.57.

$$L_{equi} = \frac{D}{f} K_L \tag{3.58}$$

where D is the diameter of the pipe that contains the valve and f is the friction factor. Once the value of L_{equi} is known, the pressure loss due to the valves is determined from Equation 3.56.

Losses in the bends and connector

Similar to valves, bends and branches have a resistance coefficient. The model includes 45^0 and 90^0 smooth bends. Each component has a specific resistance coefficient as shown in Table 3.2 [68].

45^0 smooth bend	$K_L = 0.4$
90^0 smooth bend	$K_L = 0.3$

Table 3.2: Resistance coefficients of 45^0 and 90^0 smooth bend.

The length equivalent for every bend within the piping network is determined using Equation 3.57 and the respective pressure losses are calculated using Equation 3.56.

Losses due to change in pipe size

The K_L value due to the sudden expansion of the pipe is given as follows [68]:

$$K_L = \alpha\left(1 - \frac{d_{small}^2}{d_{large}^2}\right)^2 \tag{3.59}$$

where α is the kinetic energy correction factor and has a value of 2 for a fully developed laminar flow and 1.05 for a turbulent flow [68]. Once the K_L value that due to the change in the size of the pipe is determined from Equation 3.38, the length equivalent is determined using Equation 3.57 and the pressure losses are calculated using Equation 3.56.

3.5 Modelling heat transfer with a PCM

As opposed to pure crystalline substances in which the phase change occurs at a discrete temperature, the phase change for a mixed substance such paraffin wax occurs over a temperature range. The phase change of a material involves a moving boundary at the solid-liquid interface and can tedious to simulate. The enthalpy method was thus chosen to solve the phase change associated with the PCM in part due to its simplicity as it does not involve tracking the moving boundary [85]. The enthalpy-temperature relationships for both a pure and a mixed substance are respectively shown in Figures 3.3(a) and 3.2(b) [68]. The terms shown in Figure 3.3 are as follows: T_{liq} is the liquid temperature, T_{sol} is the solid temperature, c_{liq} is the specific heat of the liquid, c_{sol} is the specific heat of the liquid, $\Delta_{pc}h$ is the phase change enthalpy which is also the latent heat of fusion, T_0 is the initial temperature of the solid and h is the specific enthalpy.

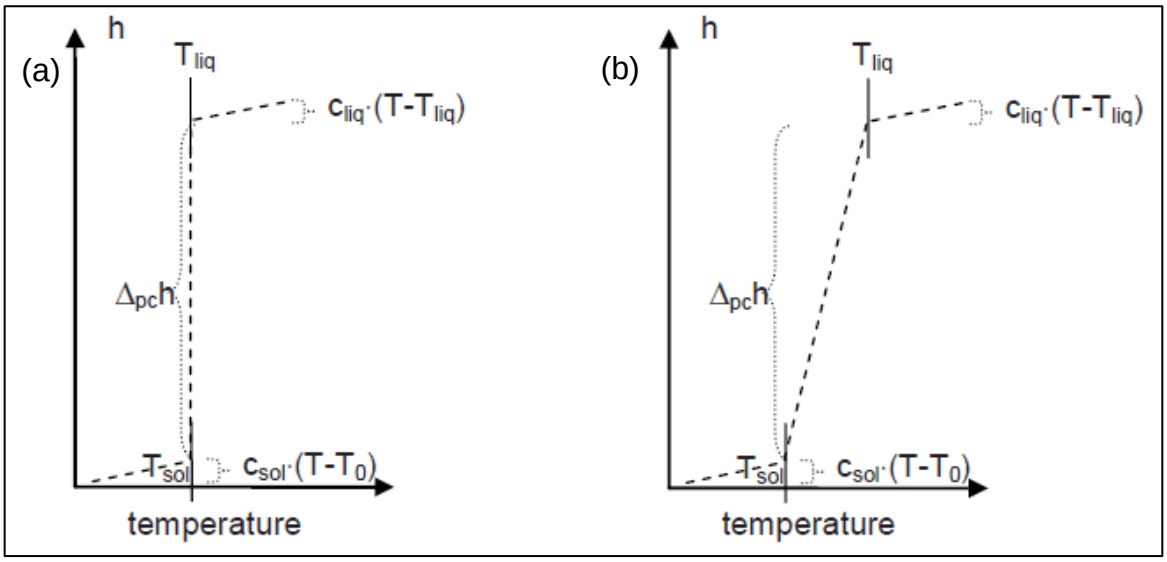

Figure 3.3: Enthalpy (h) as a function of temperature: (a) pure substance, (b) mixed substance [73]

3.5.1 PCM as part of the structure

Figure 3.4 shows a schematic diagram of the 1D heat transfer through the walls of the cylinder that includes the presence of a solid-liquid PCM in between the liner and laminate. It should be noted that this particular configuration is based upon the patent application of Air Liquide [74].

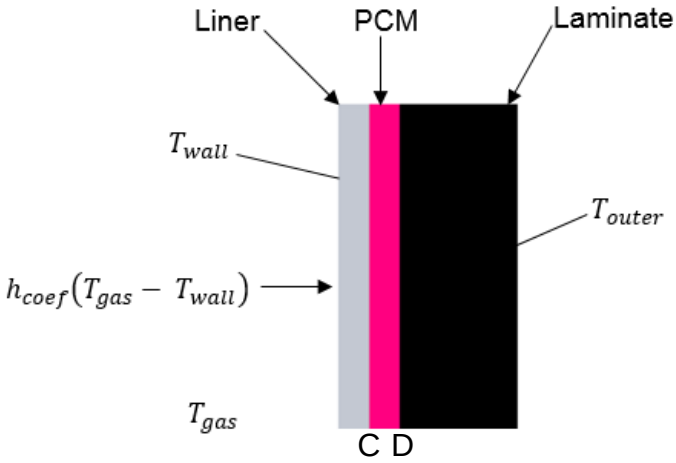

Figure 3.4: 1d unsteady heat transfer across cylinder walls that include PCM

The enthalpy form of the heat conduction (Equation 3.59) can be expressed as follows:

$$\rho \frac{\partial H}{\partial t} = k \frac{\partial^2 T}{\partial x^2} \tag{3.510}$$

The latent heat of fusion is equal to the phase change enthalpy and is given by Equation 3.60.

$$L = \Delta_{pc} h \tag{3.60}$$

In numerical simulations, typically a reference temperature is used to determine the enthalpy changes. However, the choice of the reference temperature has no influence in the final results of the temperature of the PCM [68]. The reference temperature chosen in the model is zero. The specific enthalpy for the solid state at temperature T is obtained from Equation 3.61.

$$H_{solid} = c_{sol}\, T \tag{3.61}$$

The specific enthalpy at any point in the mushy region that contains a mixture of solid and liquid is in between temperatures T_{sol} and T_{liq} is determined using interpolation. The enthalpy rise is assumed to be linear with temperature (Figure 3.3) [73]. The enthalpy of the mixture at a temperature T_{mix} is obtained from Equation 3.42.

$$H_{mix} = c_{sol} T_{sol} + \frac{L(T_{mix} - T_{sol})}{T_{liq} - T_{sol}} \tag{3.62}$$

The specific enthalpy for the liquid state at temperature T, which is above T_{liq} is given by Equation 3.63.

$$H_l = c_{sol} T_{sol} + L + c_{liq}\left(T - T_{liq}\right) \tag{3.63}$$

The explicit method is used to discretize the conduction equation (Equation 3.39) and is utilized to determine the enthalpy of the PCM during the filling of the gas as shown in Equation 3.64.

$$H_j^{m+1} = H_j^m + \frac{k\Delta t}{\rho \Delta x^2}\left(T_{j-1}^m - 2T_j^m + T_{j+1}^m\right) \tag{3.64}$$

From the Von Neumann stability analysis, the parameter $\frac{k\Delta t}{\rho \Delta x^2}$ must be less than 0.5 to ensure the stability of the explicit scheme.

If the specific enthalpy is less than $c_{sol} T_{sol}$, the temperature of the solid phase of the material is obtained from Equation 3.65.

$$T_j^{m+1} = \frac{H_j^{m+1}}{c_{sol}} \tag{3.65}$$

If the specific enthalpy calculated falls in between $c_{sol}T_{sol}$ and $c_{liq}T_{liq}$, the temperature for the mushy state is determined from Equation 3.66.

$$T_j^{m+1} = T_{sol} + \frac{\left(H_j^{m+1} - c_{sol}T_{sol}\right)\left(T_{liq} - T_{sol}\right)}{L} \tag{3.66}$$

If the specific enthalpy is larger than $c_{liq}T_{liq}$, the temperature of the liquid is obtained from Equation 3.67.

$$T_j^{m+1} = T_{liq} + \frac{(H_l - c_{sol}T_{sol} - L\ )}{c_{liq}} \tag{3.67}$$

The discretised heat equation at the interface between the liner and the PCM (denoted by 'C' in Figure 3.4) is given by Equation 3.48.

$$T_C^{m+1} = T_C^m + \frac{\Delta t}{\Delta x^2}\left[\frac{\left(k_{PCM}(T_{C+1}^m - T_C^m) - k_{liner}(T_C^m - T_{C-1}^m)\right)}{0.5(C_{liner}\rho_{liner} + C_{PCM}\rho_{PCM})}\right] \tag{3.48}$$

The discretised heat equation at the interface between the laminate and the PCM (denoted by 'D' in Figure 3.4) is given by Equation 3.69.

$$T_D^{m+1} = T_D^m + \frac{\Delta t}{\Delta x^2}\left[\frac{\left(k_{laminate}(T_{C+1}^m - T_C^m) - k_{PCM}(T_C^m - T_{C-1}^m)\right)}{0.5(C_{laminate}\rho_{liner} + C_{laminate}\rho_{PCM})}\right] \tag{3.69}$$

3.6 CFD (FLUENT) v/s Low order model

In the CFD model, heat transfer from the gas to the inner wall of the cylinder is computed using Fourier's law:

$$\dot{q} = k_f\left(\frac{\partial T}{\partial n}\right)_{wall} \tag{3.70}$$

where $\dot{q}$ is the heat flux, k_f is the thermal conductivity of the fluid, T is the temperature and n is the local coordinate normal to the wall. The heat flux is computed by determining the difference between the gas temperature in the first cell off the wall and the wall temperature. In the CFD model the fluid domain is discretised and the flow field is computed throughout the domain. In addition, a finer mesh is required at the interface between the fluid and the wall in order to accurately compute the velocity field in the boundary layer and the temperature field within the thermal

boundary layer. The fast-filling process is transient in nature and the discretisation of the flow field and the computation of the flow properties using Equations 3.1, 3.2 and 3.3 along with the relevant turbulence model is computationally expensive.

As opposed to the CFD model, the low-order model does not compute the flow field and will require negligible computational time. The heat flux is computed using:

$$\dot{q} = -h_{coef}(T_{gas} - T_{wall}) \tag{11}$$

T_{gas} is the gas temperature and T_{wall} is the temperature at the inner surface of the wall. h_{coef} is the heat transfer coefficient and is modelled (*please refer to chapter 5)*.

3.7 Summary

Initially, the two-dimensional simulation of the fast-filling of a hydrogen cylinder will be performed in FLUENT and validated based on the experiments of Dicken and Merida [7]. Further CFD simulations will performed for cylinders having the same volume but different length-to-diameter ratios (L/D). Conjugate heat transfer models for the fast-filling of the cylinders with varying L/D will be implemented with the heat transfer coefficient based on the data from the CFD simulations. The model of the fast-fill will also include the modelling of the viscous discharge coefficient that accounts for the pressure losses of the flow in delivery pipe that protrudes into the cylinder. Following the validation of the heat transfer models, the use of PCM in the enhancement of heat transfer and storage during the fast-fill will be investigated. Finally, the model for the filling process of the cylinder will be further expanded to include the emptying of storage banks and gas flow in the piping system of a fast-fill station.

4 CFD model for the filling of the cylinder

4.1 Introduction

Initially, an axisymmetric two-dimensional simulation of the refuelling of a hydrogen pressure vessel for 37 seconds was conducted on a Type III cylinder and was based on the data from the experiment of Dicken and Merida [7]. The tank dimensions and materials as well their respective thermal properties were obtained from Dicken and Merida [7] (*please refer to Appendix A4*). Isotropic material properties were assumed for both the liner and laminate, with both regions having a uniform thickness. The volume of the cylinder is 74 L, with an inner length-to-diameter ratio (L/D) of 2.4 (Figure 4.1). Following the validation of the 2D model, the L/D of the cylinder is increased incrementally while keeping the volume of 74 L constant to determine the resulting effect on the flow field and gas temperature during the fill.

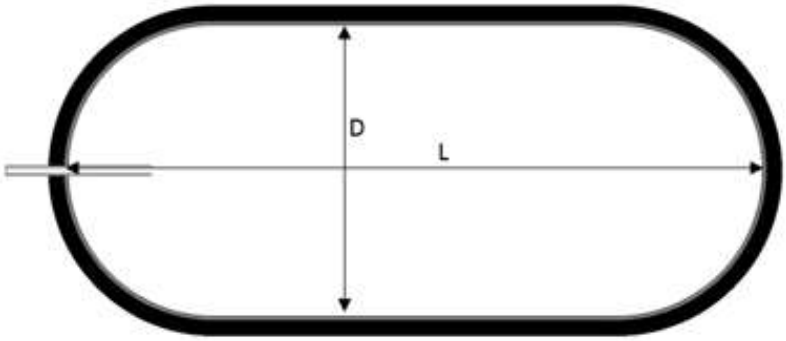

Figure 4.1: Inner length-to-diameter ratio (L/D) of a cylinder.

4.2 2D axisymmetric model of the fast-fill

4.2.1 Computational grid

The axisymmetric domain of the cylinder based on the geometry of Dicken and Merida [7] was split into fifty one blocks that were discretised using a structured mesh using the ICEM software (Figure 4.2). Finer grids were placed within the delivery pipe and at the exit into the cylinder so as to capture the high velocity incoming gas while the rest of the fluid region was discretised with a much coarser mesh. The liner and laminate regions were discretised with a structured mesh and in addition, a fine mesh was placed at the interface of the fluid-wall region in order to resolve the boundary layer.

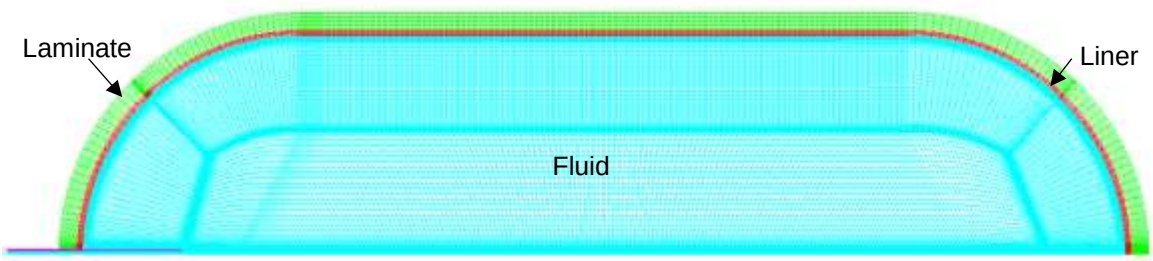

Figure 4.2: 2D axisymmetric domain of the Type III cylinder.

4.2.2 Initial and boundary conditions

The initial pressure and temperature of the hydrogen gas were assumed to be uniform throughout the tank and were set at 9.36 MPa and 293.4 K respectively. Initially, the liner and laminate were assumed to be in thermal equilibrium with the gas. At the inlet of the delivery pipe, a pressure boundary condition was used with the total pressure and total temperature varying with time similar to the experimental data from Dicken and Merida [7] (*please refer to Appendix A5*). At the outer wall of the laminate and the delivery pipe two different cases are considered:

1. Isothermal conditions are applied and are set similar to the initial temperature condition of 293.4 K.
2. Adiabatic conditions are applied.

These two outer wall boundary conditions were chosen since they represent the two extreme case scenarios whereby either maximum heat transfer occurs to the atmosphere (isothermal conditions) or no heat is transferred to the surroundings of the cylinder (adiabatic conditions).The no slip boundary condition (v = 0 m/s) was used at the inner wall of the liner and the walls of the delivery pipe that are adjacent to the fluid. To enable heat transfer, the energy equation of the fluid was coupled to that of the inner liner wall. Adiabatic wall conditions were applied to the walls of the pipe that are in direct contact to the fluid. Since the cylinder has an axisymmetric geometry, the axis boundary condition is used for its centreline.

4.2.3 Grid independence & calculation activities

Grid independence tests were performed for such that the cell count within the computational domain no longer affects the model solution. The criteria chosen for the mesh sensitivity analysis was the instantaneous velocity magnitude of the gas

at two different plane locations (A & B) within the tank (Figure 4.3), six seconds and eighteen seconds into the fill.

Figure 4.3: Locations of instantaneous velocity measurements.

As opposed to the pressure based solver, convergence of both the mass flow rate and that of the residual levels could not be reached using the density based solver. The pressure based solver with an implicit scheme was thus used for the simulations. The convergence of the mass flow rate at each time step up to four significant figures was obtained once the residual levels of the continuity equation reached 10^{-4} which is similar to the residual convergence criteria that is suggested by the FLUENT guideline [81]. Thus, the convergence criteria for the various equations at each time step from the FLUENT guideline was applied (Table 4.1).

Equations	**Convergence criteria**
Continuity	10^{-4}
x-velocity	10^{-4}
y-velocity	10^{-4}
Energy	10^{-7}
Turbulent kinetic energy (k)	10^{-4}
Dissipation rate per unit mass (ε)	10^{-4}

Table 4.1: Convergence criteria [81].

The grid independence tests were carried out in which the grid distances were proportionally changed within each of the fifty one blocks within the domain. The initial domain consisted of 32841 cells and tests were further carried out on four other domains with cell counts of 49851, 72389 and 94721. Following the mesh sensitivity analysis, 72389 cells were used for the discretization of the axisymmetric domain of the cylinder for further simulations since the velocity profiles across planes A and B remained mostly unchanged when the cell count was increased from 72389 to 94721 (Figures 4.4-4.7).

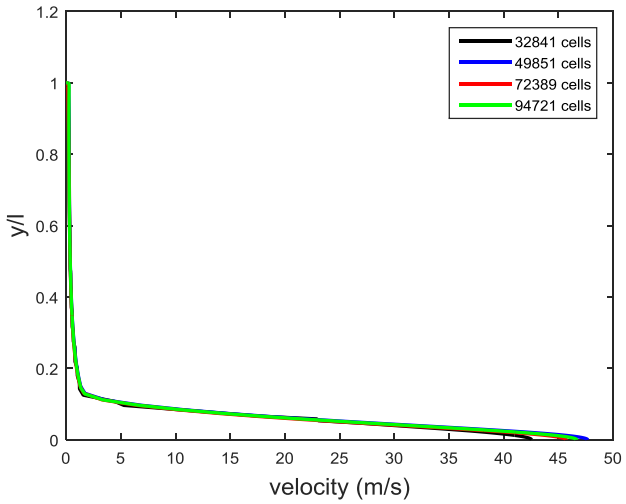

Figure 4.4: Instantaneous velocity magnitude across plane A (t = 6s).

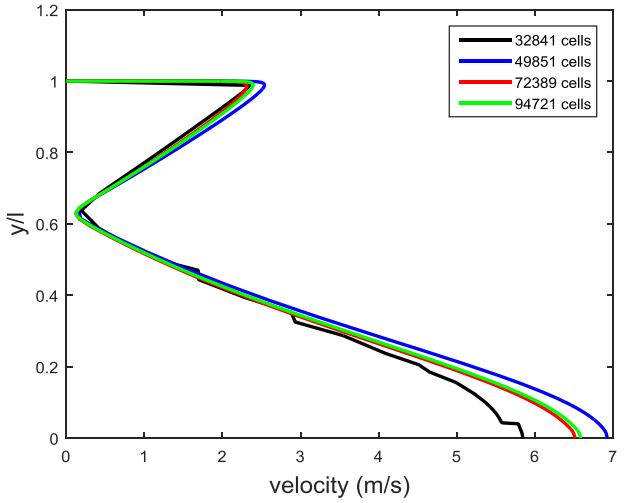

Figure 4.5: Instantaneous velocity magnitude across plane B (t = 6s).

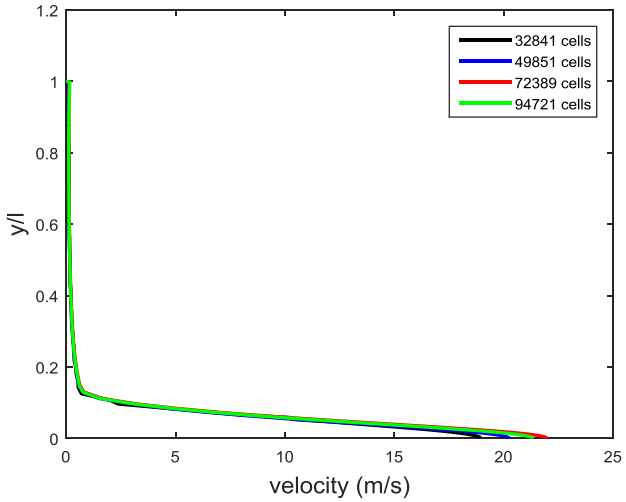

Figure 4.6: Instantaneous velocity magnitude across plane A (t = 18s).

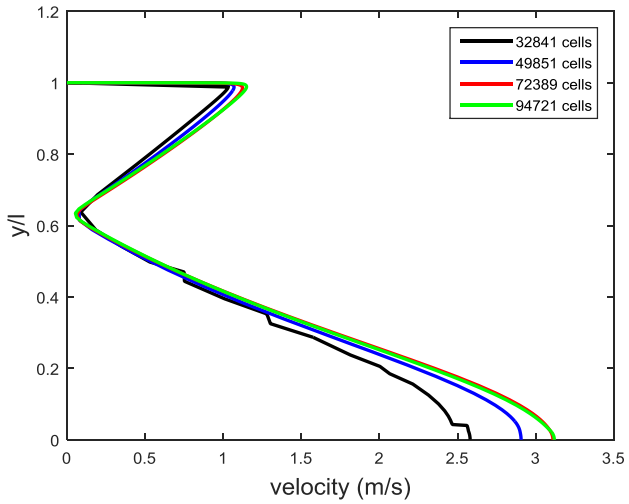

Figure 4.7: Instantaneous velocity magnitude across plane B (t = 18s).

A time step of 10^{-4} s was chosen for the simulation of the fast-fill since lower time steps of 10^{-2} s and 10^{-3} s led to the divergence of the residuals and the simulation is interrupted. Further reduction of the time step to 10^{-5} s led to the convergence of the residuals. As shown in Figures 4.8 and 4.9, the velocity profiles across planes A and B five seconds into the fill for time steps of 10^{-4} s and 10^{-5} s remained mostly unchanged. Thus a time step of 10^{-4} s was chosen for computational time savings without affecting the accuracy of the solution.

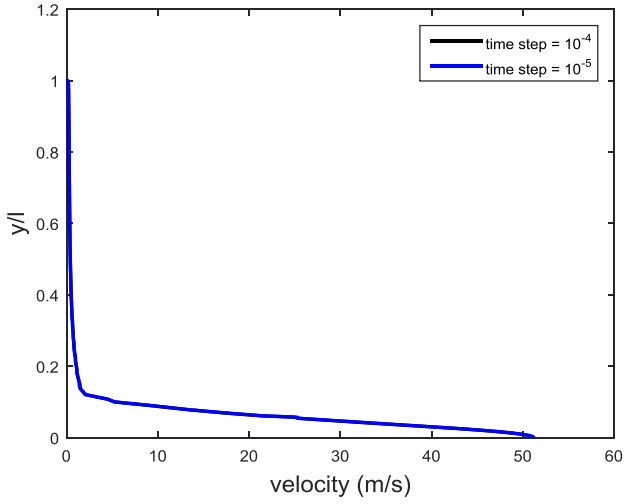

Figure 4.8: Instantaneous velocity magnitude across plane for the two time steps.

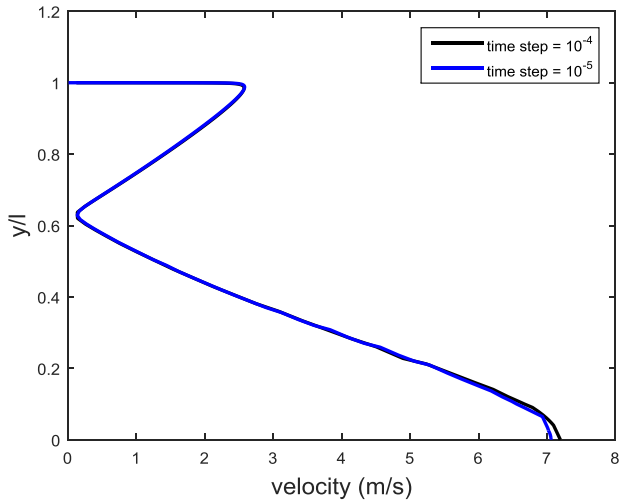

Figure 4.9: Instantaneous velocity magnitude across plane for the two time steps.

4.2.4 Resolution of the boundary layer

Standard wall functions [81] were used for the simulations and the resolution of the boundary layer that results when the fluid comes into contact with a solid wall. This was achieved by ensuring that the non-dimensional distance (y*) of first 8 to 10 grids points off the inner wall of the tank were less than 300.

The non-dimensional wall distance (y*) and the non-dimensional velocity U* are determined as follows [81]:

The log law of the wall for the mean velocity is given in Equation 4.1.

$$U^* = \frac{1}{\kappa}\ln(Ey^*) \tag{4.1}$$

where U^* is the non-dimensional velocity, E is an empirical constant (9.793), y^* is the non-dimensional distance from the wall and κ is the Von Karman constant.

The non-dimensional velocity is obtained from Equation 4.2.

$$U^* \equiv \frac{UC_\mu^{1/4}k^{1/2}}{\tau_w/\rho} \tag{4.2}$$

The non-dimensional wall distance is obtained from Equation 4.3.

$$y^* \equiv \frac{\rho C_\mu^{1/4}k^{1/2}y}{\mu} \tag{4.3}$$

where U is the mean velocity, $C_\mu^{1/4}$ is a constant of the turbulence model and has a value of 0.09, k is the turbulent kinetic energy, τ_w is the wall shear stress ,ρ is the density, y is the distance from the wall and μ is the dynamic viscosity.

In FLUENT, the log law (Equation 4.1) is used when 11.225 < y^* < 300. If y^* < 11.225, Equation 4.4 is used instead of the log law.

$$U^* = y^* \tag{4.4}$$

Twenty cells were placed in the fluid region right off the walls and a growth factor of 1.03 was used to ensure that at least eight cells were located within the boundary layer throughout the fill. The maximum y* value of the first grid point off the walls that are in contact with the fluid at each second throughout the fill is shown in Figure 4.10.

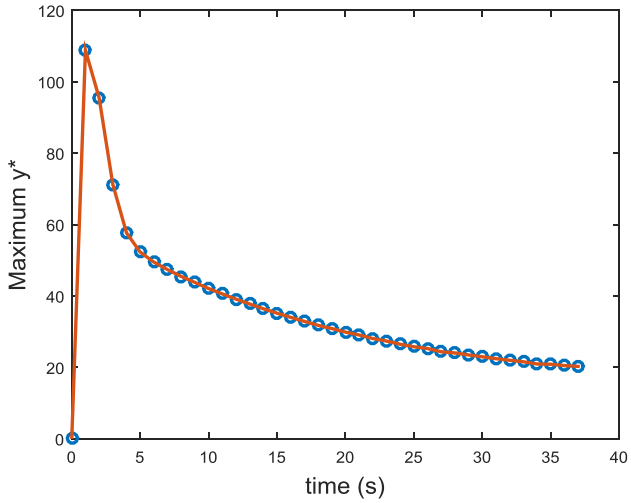

Figure 4.10: Maximum y* value throughout the fill.

4.2.5 Validation of the CFD model

Figure 4.11 shows that the boundary condition at the outer wall of the laminate does not play a role in the heat transfer from the gas to the structure of the cylinder. The mass-averaged gas temperature is similar for either outer wall boundary conditions and is mainly due to the low thermal conductivity of the laminate. The mass averaged gas temperature that is obtained by the CFD models for both outer wall boundary conditions accurately predicts the rise in gas temperature when compared to the experiment. The predicted final gas temperature is within 1 K of the experimental data. The largest discrepancy between the predicted temperature of the CFD model and the measured temperature from the experiment is 4 K and occurs 2.5 s into the fill. The 2D axisymmetric CFD simulations also shows that heat transfer to the structure of the cylinder occurs during the fast-fill, otherwise the gas temperature in the cylinder significantly exceeds the gas temperature that was

obtained from the experiment. In addition, without heat transfer, the gas temperature in the cylinder exceeds the maximum allowable limit of 358 K.

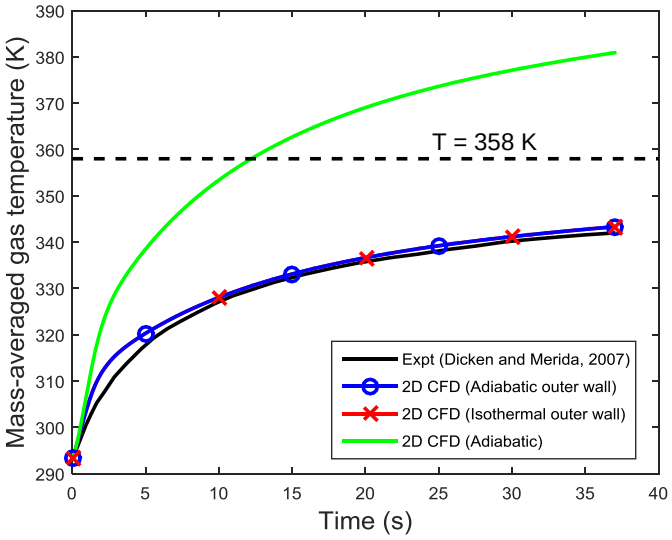

Figure 4.11: Comparison of the mass-average gas temperatures.

The contour plots of the temperature distribution at filling times of 1 s, 5 s, 15 s, 25s and 35 s (Figure 4.12) show the existence of a radial and axial temperature gradient that is significantly close to the inlet and diminishes with distance. An oval-shaped gas plume coming from the inlet is observed and has a different gas temperature than the surrounding gas within the tank. The temperature of the gas outside of the plume is homogeneous throughout the cylinder.

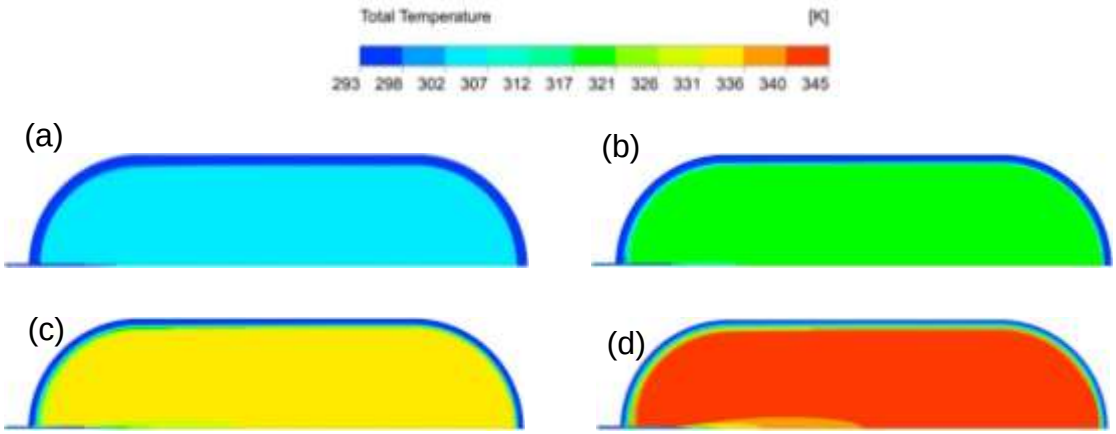

Figure 4.12: Contours of total temperature: (a) 1 s, (b) 5 s, (c) 15 s, (d) 35 s.

The computational model predicts a sharp rise in the mass flow rate during the first one and half seconds of the fill and reaches a maximum of 0.087 kg/s. A sharp drop in the mass flow rate over the next three and a half seconds is observed after

which the mass flow rate still decreases but a much slower rate until the filling is completed (Figure 4.13). A similar trend is observed for the wall average heat flux during the fill as heat transfer occurs from the gas the walls of the cylinder (Figure 4.14). This suggests that heat transfer from the gas to the inner wall of the cylinder is directly related to the mass flow rate.

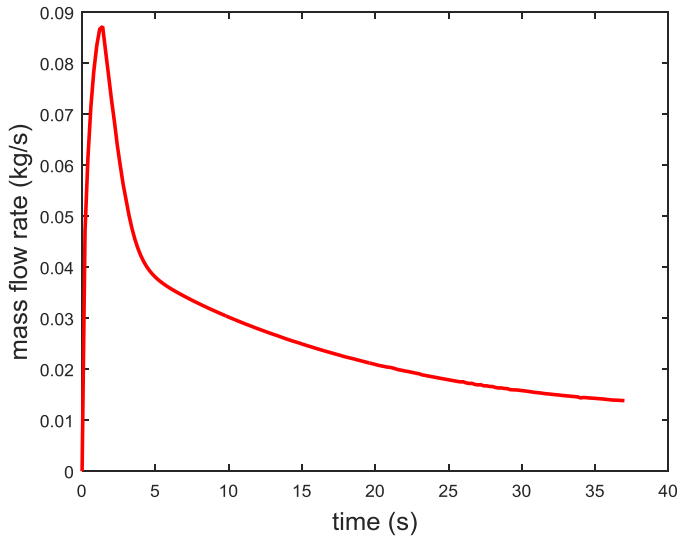

Figure 4.13: Mass flow rate throughout the fill.

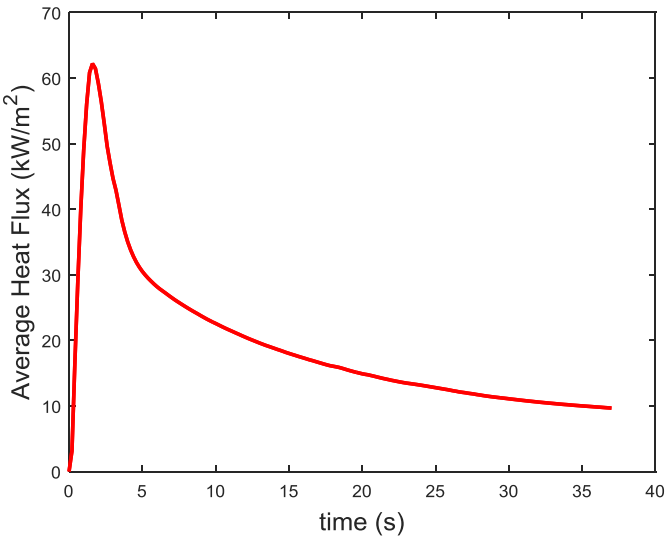

Figure 4.14: Average heat flux from the gas to the inner wall throughout the fill.

The flow field of the gas within the cylinder at fill times of 1s, 5s, 15s and 35s (Figure 4.15) shows that throughout the fill, the incoming gas from the inlet hits the opposite end of the cylinder and turns along the surface of the inner wall towards the inlet. This leads to the recirculation of the gas within the cylinder as the filling proceeds.

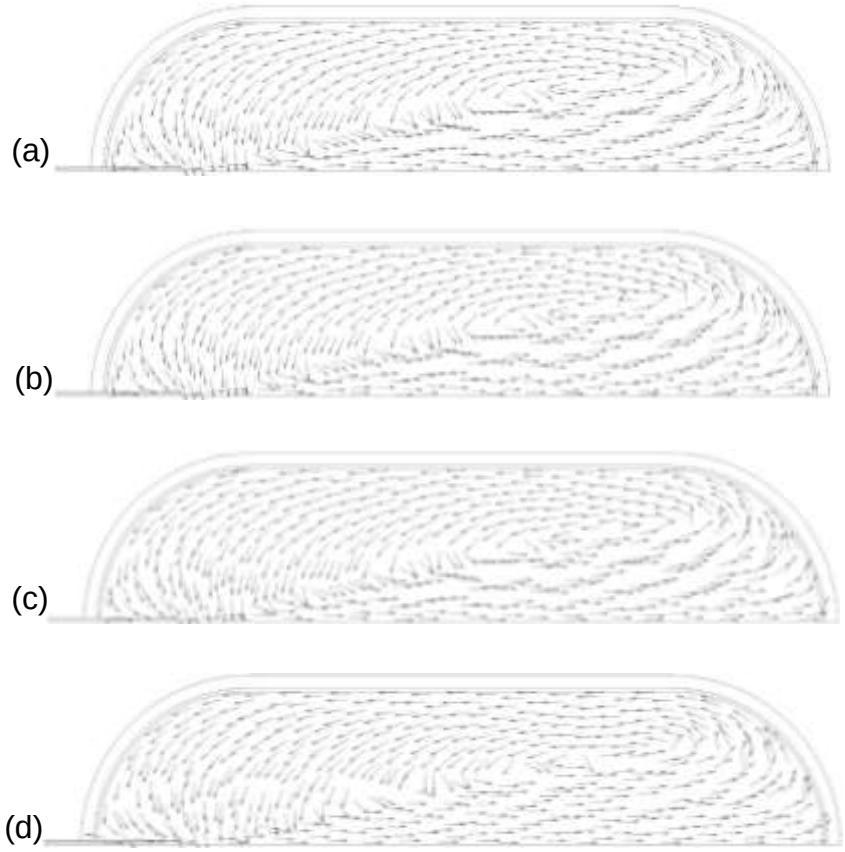

Figure 4.15: Flow field of the gas in the cylinder: (a) 1s, (b) 5s, (c) 15s, (d) 35s.

The profile of magnitude of the velocity of the gas at the inlet is reflection of that of the mass flow rate (Figure 4.16). A sharp rise in the magnitude of the velocity is observed during the first one and half seconds of the fill and is followed by a sharp drop until the filling is completed.

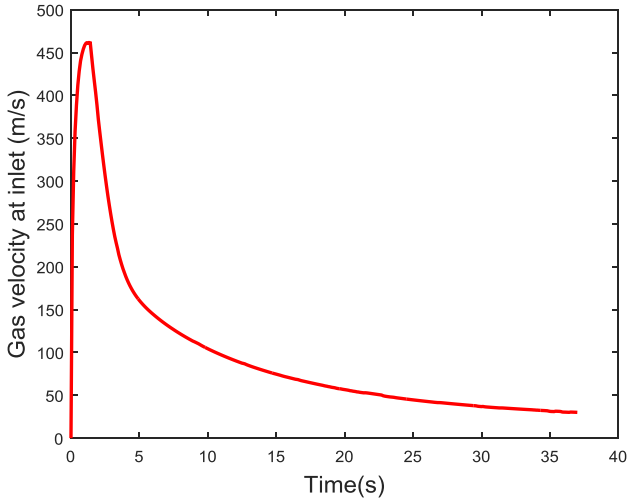

Figure 4.16: Magnitude of the velocity at the inlet during the fill.

Thus, the impingement of the gas onto the inner surface of the dome directly opposite to the inlet occurs at a much higher speed at the start of the fill and decreases as filling continues. This consequently leads to a much larger amount of heat being transferred due to forced convection to the walls in the far dome (caudal region of the cylinder) at the beginning of the fill but as the filling proceeds, the heat flux decreases and tends to be uniform across the entire inner wall of the cylinder (Figure 4.16).

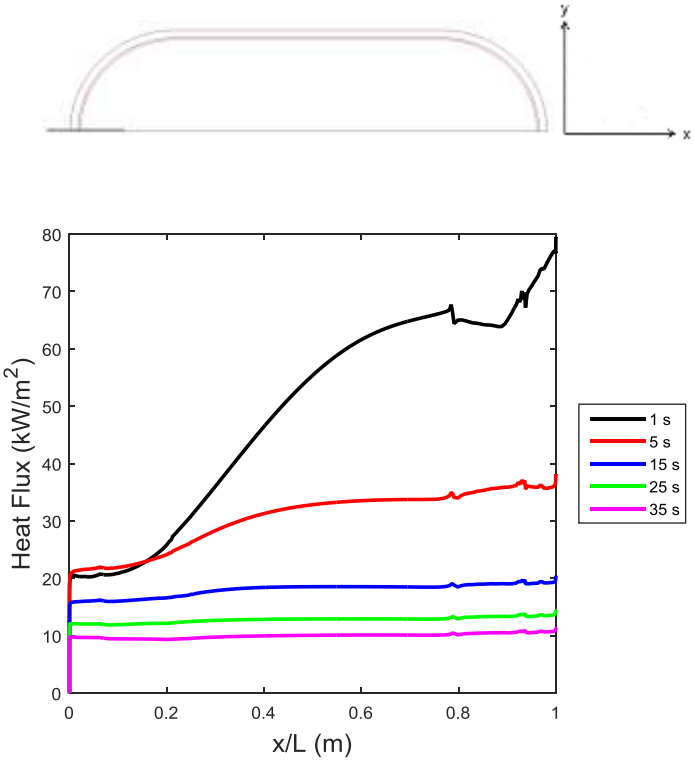

Figure 4.17: Heat flux across the inner wall at different times during the fill.

The temperature within the cylinder walls at various locations is plotted against the normalised wall thickness at filling times of 1s, 15s and 35s as shown in Figures 4.18 – 4.20. At the onset of the fill at time t = 1s, a temperature gradient exists within the liner. However, as the filling proceeds, the temperature in the liner is almost uniform due to its high thermal conductivity. In the case of the laminate, a high temperature gradient is observed throughout the fill owing to its low thermal conductivity. The largest temperature gradient within the laminate is observed at the beginning of the fill at t =1 s, which leads to the creation of the inflection points (Figure 4.18). In addition, it can be observed that the location of the highest wall temperature throughout the fill occurs at the opposite end of incoming impinging jet.

Figure 4.18: Locations of temperature measurement

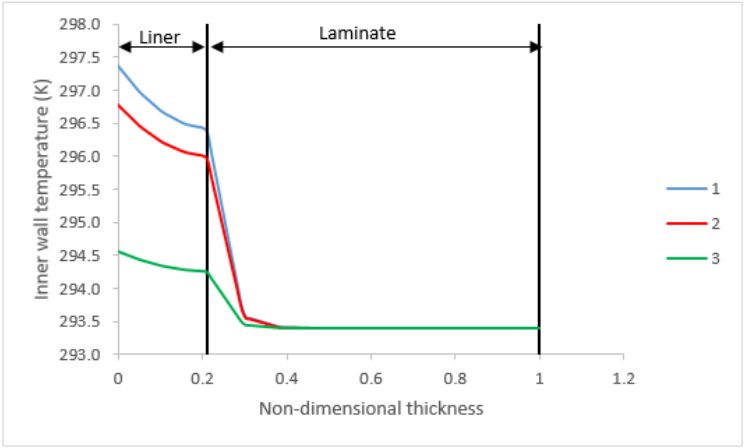

Figure 4.19: Temperature of liner and laminate (t = 1s).

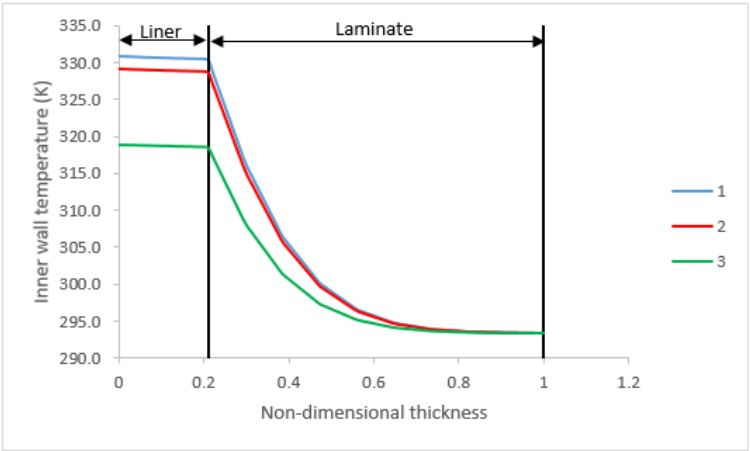

Figure 4.20: Temperature of liner and laminate (t = 15s).

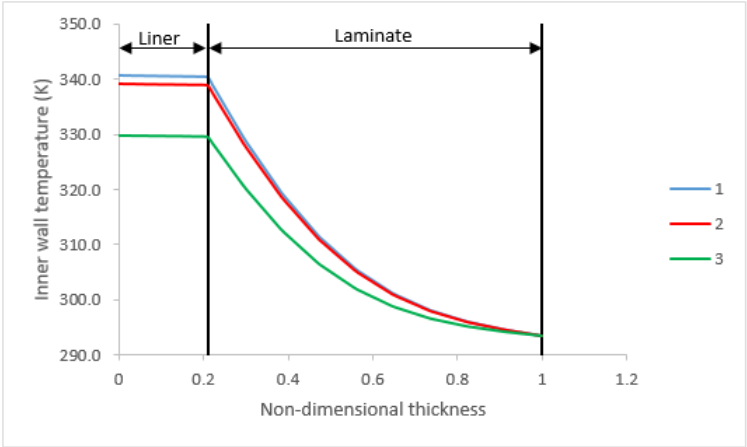

Figure 4.21: Temperature of liner and laminate (t = 35s).

4.3 Increasing the L/D of the cylinder

The length-to-diameter ratio (L/D) of the cylinder is changed such that its value ranges between 3 and 8, while keeping the volume constant (Figure 4.22). An increase in the L/D of the cylinder involves an increase in the length of the cylinder coupled with a decrease in its diameter. Since a mesh independence test was already carried out on the original cylinder with the L/D of 2.4, the discretisation of the axisymmetric domain of the cylinders with the L/D ranging from 3 to 8 was carried out by proportionally increasing the number of grids in the axial direction. In the lateral direction, the number of grids was unaltered for all cylinders. Similar to the material properties of the structure, the inlet diameter is also kept constant for all the cylinders. An increase in the L/D of the original cylinder also leads to an increase in the inner surface area of the cylinder and lowers the ratio (Dcyl/Dinlet) of the inner diameter of the cylinder to the diameter of the inlet (Table 4.2).

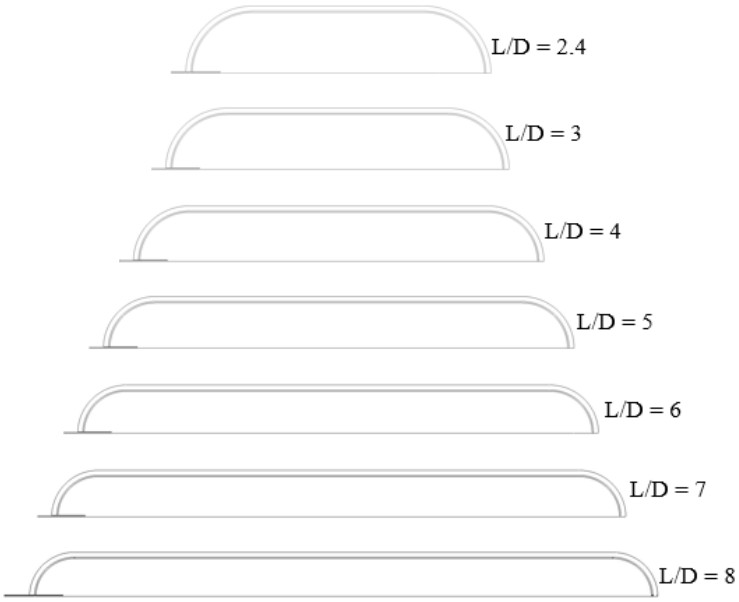

Figure 4.22: 2D axisymmetric domains of the cylinders with varying length-to-diameter ratio (L/D).

L/D	Surface area (m^2)	D_{cyl}/D_{inlet}
2.4	0.962	79.2
3	1.015	73.2
4	1.094	66.6
5	1.165	62.1
6	1.228	58.6
7	1.286	56.0
8	1.338	53.8

Table 4.2: Inner surface areas and the ratio Dcyl/Dinlet of the cylinders having different L/D.

4.3.1 Results

The mass-averaged gas temperature within the cylinder does not significantly change when the L/D of the cylinder is in between 2.4 and 5 (Figure 4.23) despite an increase in the inner surface area of the cylinder. A further increase in the L/D of the cylinder beyond a value of 5 shows that the mass-averaged gas temperature slightly increases. However, the rise in the mass-averaged gas temperature in the cylinder that has a L/D of 8 is lower than temperature rise that is observed in the cylinder that has a L/D of 7. This can be explained by the increase in the inner surface area of the cylinder as its L/D changes from 7 to 8. The increase in the L/D of the cylinder also leads to a rise in the local the maximum gas temperature (Figure 4.24). The maximum local gas temperature in cylinders that have a L/D larger than 5 is above than the maximum allowable limit of 358 K. At the start of the fill, maximum gas temperature within the cylinder occurs at the exit of the delivery pipe and is due to the Joule-Thompson effect. This explains the sharpe rise in the local value of the maximum gas temperature. As the filling proceeds, the occurance of the maximum gas temperature is only due to the compression of the gasin the caudal region of the cylinder, which explains the kink in the curves immediately after the start of the fill (Figure 4.24).

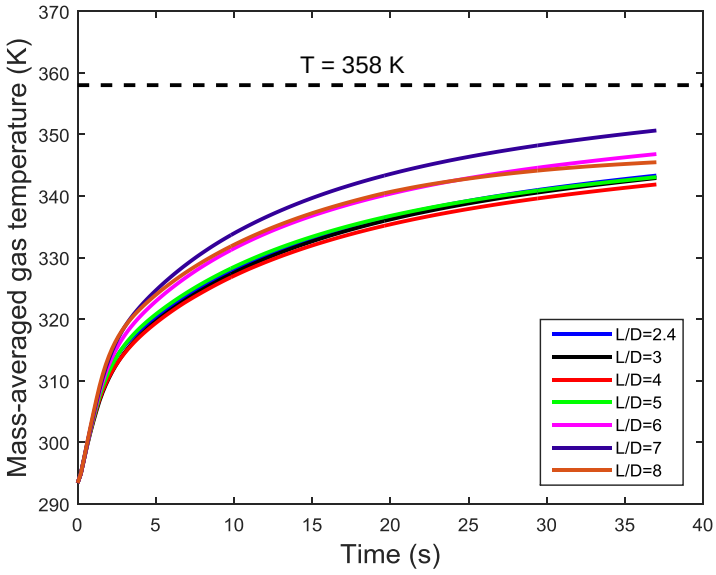

Figure 4.23: Comparison of the mass-averaged gas temperature in cylinders with different L/D.

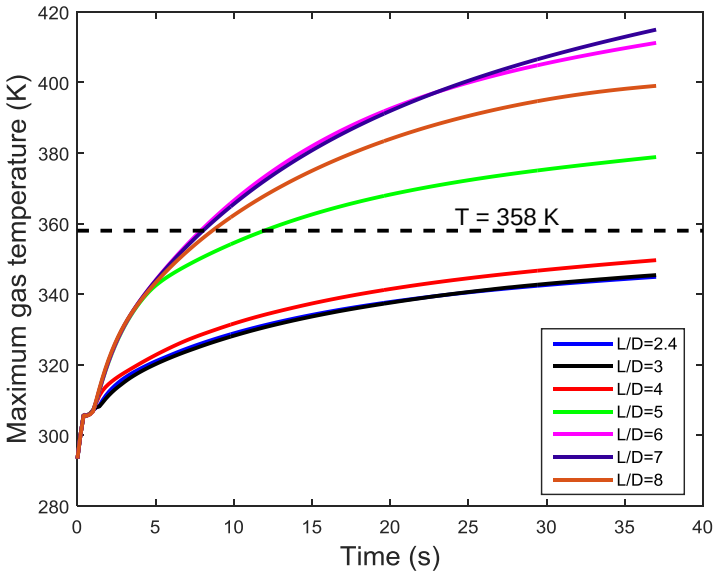

Figure 4.24: Comparison of the local maximum gas temperatures in cylinders with different L/D.

Figures 4.23 and 4.24 show that by increasing the L/D, the mass-averaged gas temperatures within the cylinders do not accurately represent the gas temperature. Figure 4.25 shows that the difference (δT) between the maximum gas temperature and the mass averaged gas temperature 30 s into the fill and the value of δT is significantly larger with the cylinders that have a higher L/D.

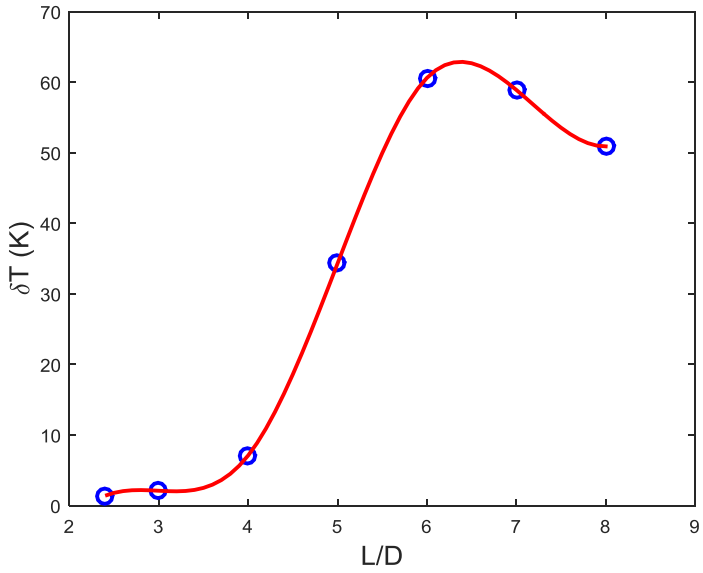

Figure 4.25: Difference between the maximum gas temperature and the mass averaged gas temperature 30s into the fill for the different cylinders with varying L/D.

Figure 4.26 shows the contours of gas temperature 30 s into the fill for the different cylinders. The temperature of the gas is homogeneous in the cylinders having a L/D of 2.4 and 3. Increasing the L/D to 4, leads to slight increase in the gas temperature in the caudal region of the cylinder. The contours of the gas temperature in cylinders with a L/D of 5 and greater show that the gas temperature within the cylinders are no longer homogeneous, with the gas temperature increasing axially and the maximum gas temperature is observed in the caudal region of the cylinder.

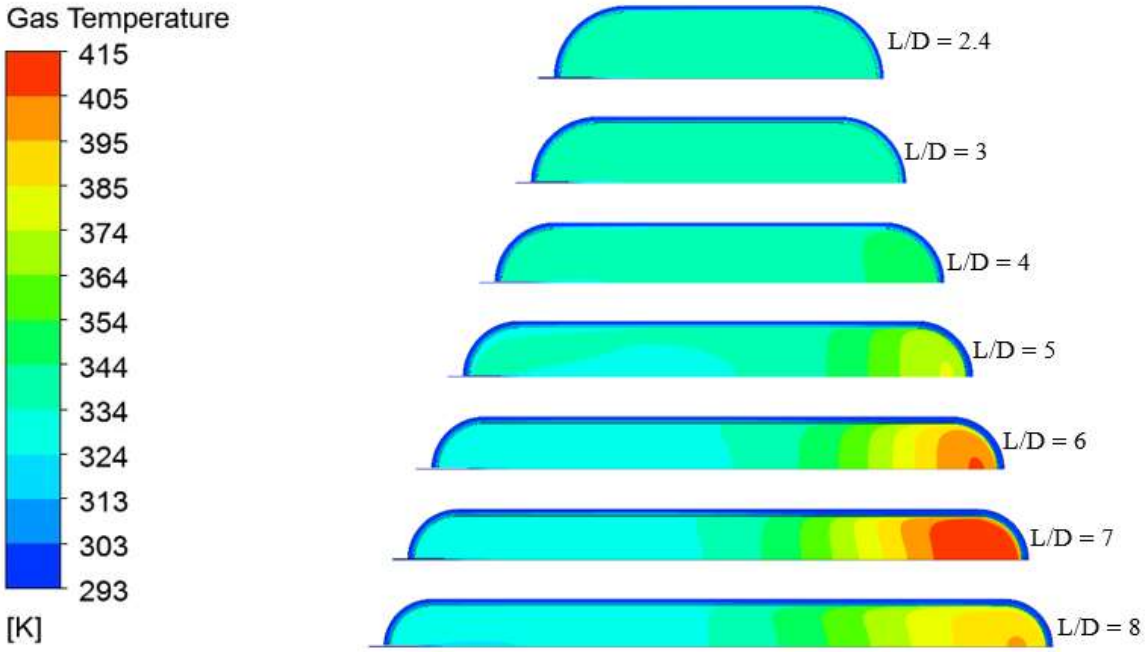

Figure 4.26: Comparison of the contours of gas temperature 30 s into the fill for the different cylinders with varying L/D.

Figure 4.27 shows the flow field within the cylinder at fill time of 30 s. The flow field in cylinders with a L/D of 2.4 and 3 consists of a circulating region with the gas exiting the delivery pipe impinging onto the opposite dome and recirculating within the cylinder. For cylinders having a L/D of 4 and greater, two distinct flow regions exist; a recirculating region close to the exit of the delivery pipe and a secondary region in which the gas moves axially toward the caudal region of the cylinders.

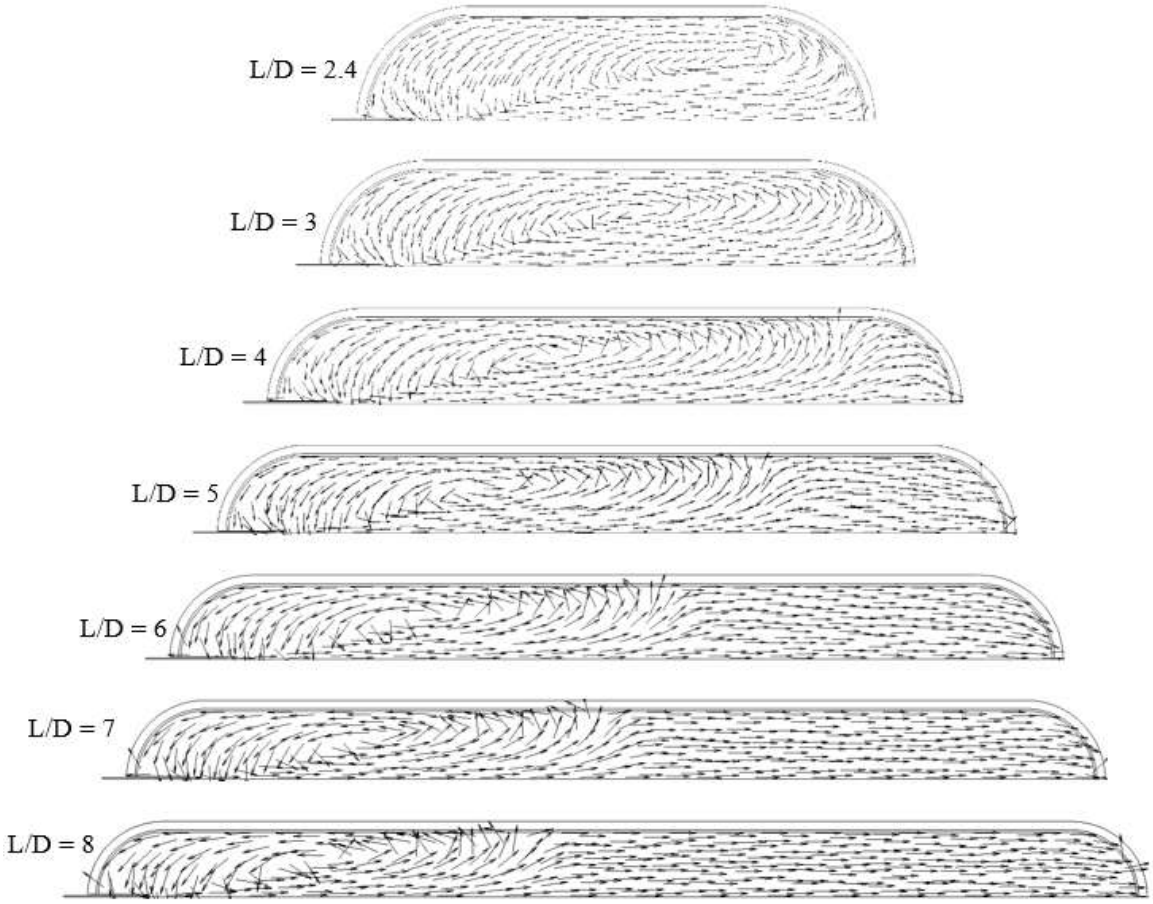

Figure 4.27: Flow field within the cylinders with varying L/D at the fill time of 30 s.

Based on the observations of Figures 4.26 and 4.27, the gas temperature is lower and homogeneous in the recirculating region and increases axially in the secondary region. The fluid domain for cylinders having a L/D between 4 and 8 can split into 2 parts as shown in Figure 4.28. Zone 1 is the recirculating region and in zone 2, the gas moves axially.

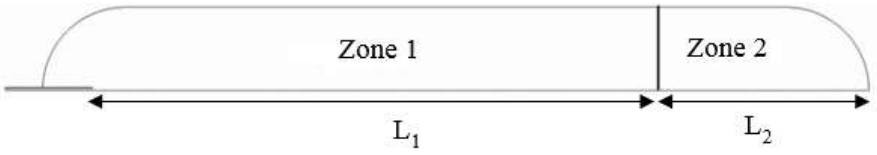

Figure 4.28: Schematic of the 2 fluid regions within the cylinder with a L/D > 3

Since the axial wall shear stress at the wall of the cylinder changes sign according to the direction of the flow within the cylinder, the distance L_1 and L_2 can be determined for the different cases. The simulations showed that for cylinders having a L/D between 4 and 8, the circulating regions extends three cylinder diameters from the exit of the delivery pipe; i.e. $L_1 = 3D_{cyl}$.

Figure 4.29 shows the heat flux at the inner wall of the cylinder at different times into the fill for the cylinder having a L/D of 8. The heat flux is significantly higher in zone 1 as opposed to zone 2 during the first 10 seconds of the fill. The recirculating of the gas close the exit of the delivery leads to a higher heat transfer coefficient, which increases the heat transfer from the gas to the structure of the cylinder and results in a lower gas temperature.

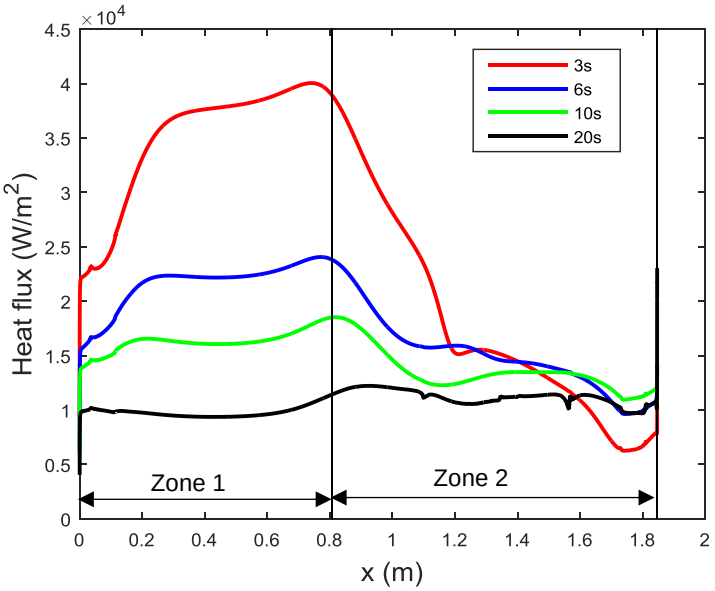

Figure 4.29: Heat flux at the inner wall of the cylinder with L/D of 8 at different times during the 37 s fill.

4.3.2 Effect of inlet diameter

Further simulations were performed for the fast-filling of the cylinder with the L/D of 8 whereby the inlet diameter is changed from 5 mm to 7.07 mm and 20 mm. An increase in the diameter of the inlet leads to a decrease in the ratio (Dcyl/Dinlet) of the inner diameter of the cylinder to the diameter of the inlet (Table 4.3). Figure 4.30 shows that the final mass-averaged gas temperature with the cylinder is mostly unaffected by the change in inlet diameter. However, increasing the inlet diameter leads to a decrease in the final maximum gas temperatures, which are still above the allowable limit of 358 K (Figure 4.31).

D_{inlet}	D_{cyl}/D_{inlet}
5 mm	53.8
7.07 mm	38.1
20 mm	13.5

Table 4.3: Comparison of the ratio of the inner diameter of the cylinder having a L/D of 8 to the diameter of the inlet for the different inlet sizes.

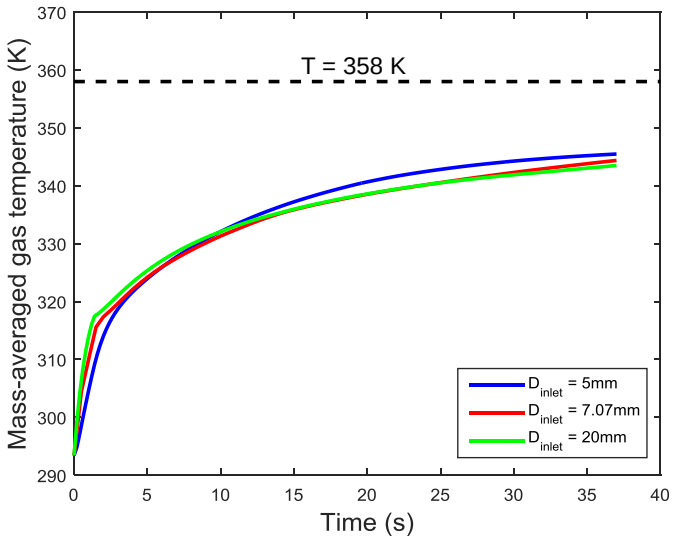

Figure 4.30: Comparison of the mass-averaged gas temperatures in the cylinder (L/D =8) with different inlet sizes during the fill.

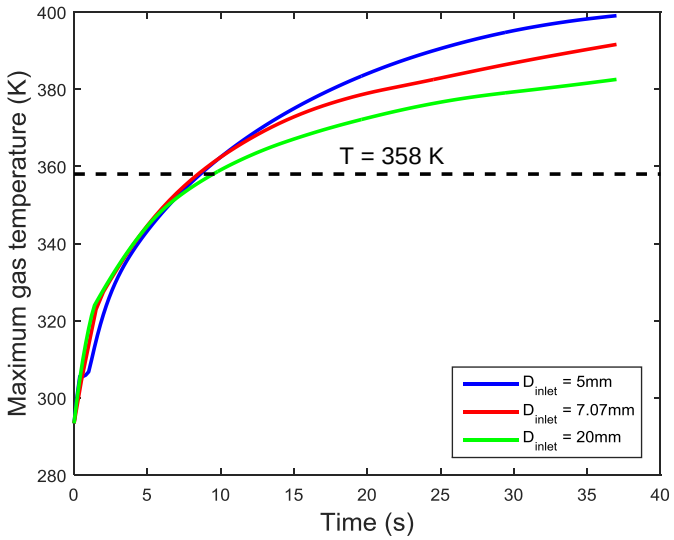

Figure 4.31: Comparison of the maximum local gas temperatures in the cylinder (L/D =8) with different inlet sizes.

Both Figures 4.30 and 4.31 show that increasing the inlet diameter leads to an increase in the gas temperature at the beginning of fill. This is due to a higher peak in the mass flow rate at the start of the fill with increasing inlet diameter (Figure 4.32), which results in the compression of a larger mass of gas in the cylinder. However, the larger initial peaks in the mass flow rate that is inherent for cases with bigger inlets lead to larger gas pressures within the cylinder. Accordingly, this leads to a sharp decrease in the mass flow rate, which is due to a smaller difference between the upstream inlet pressure and the gas pressure with the cylinder. The mass flow rate for all three cases are similar 5 seconds and beyond into the fill.

However, during the same filling period, the momentum flow rate at the inlet decreases with larger inlet diameters (Figure 4.33). The decrease in the maximum local gas temperature that occurs with increasing inlet diameter can be explained by the lower momentum flow rate from the inlet that decreases the extent upon which the gas is being compressed in the caudal region of the cylinders.

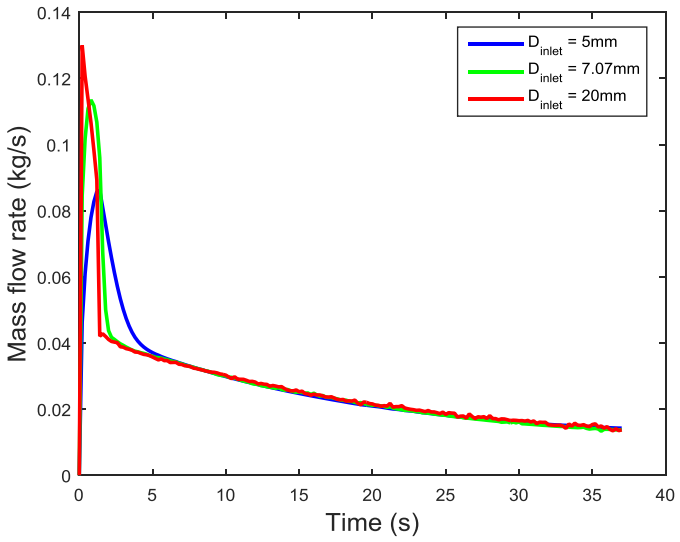

Figure 4.32: Comparison of the mass flow rate in the cylinder (L/D=8) with different inlet sizes.

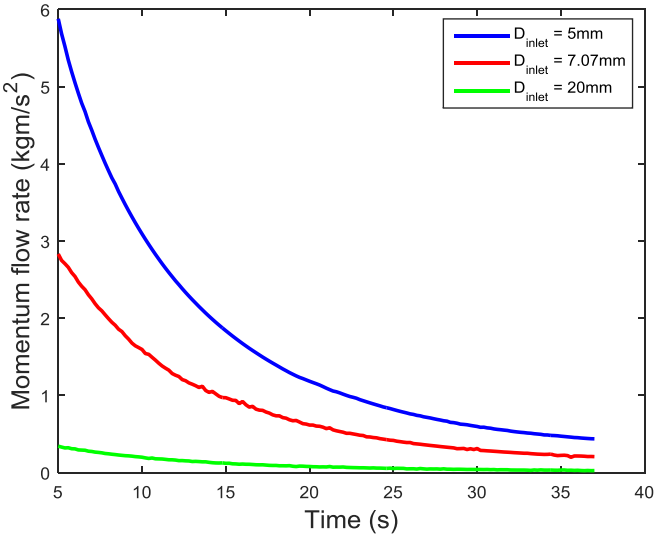

Figure 4.33: Comparison of the momentum flow rate at the different inlets five seconds and beyond into the fill.

Figure 4.34 shows the similarity in the flow field at the fill time of 30 s in the cylinder whose L/D is 8 with the different inlet diameters. The recirculating zone (zone 1) still extends three cylinder diameters from the exit of the delivery pipe for all three cases despite the change in the size of the diameter of the inlet.

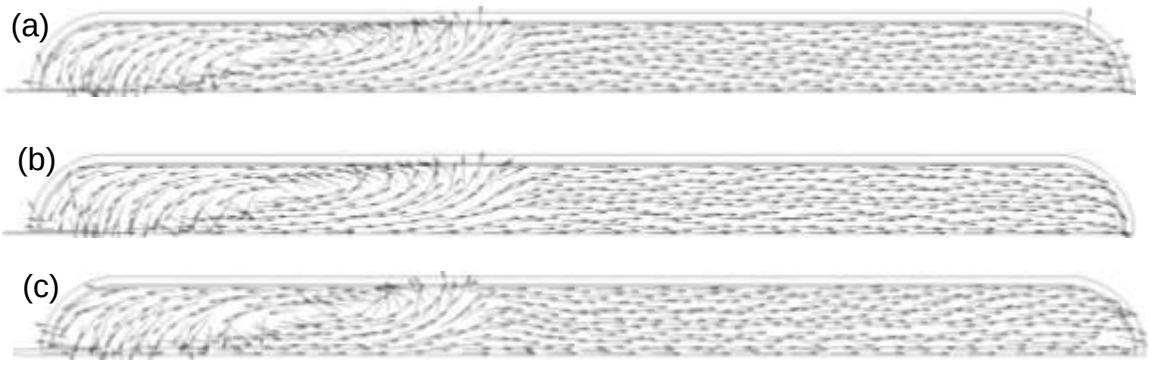

Figure 4.34: Flow field within the cylinders with an L/D of 8 at the fill time of 30 s having different inlet diameters: (a) 5mm, (b) 7.07 mm and (c) 20mm.

Figure 4.35 compares the axial velocity of the gas in the cylinder that has a L/D of 8 with varying inlet diameters 30 s into the fill in the axial direction at a distance half way between the centreline and the inner diameter of the cylinder. The location of the centre of the circulating region whereby the sign of the axial velocity changes from negative to positive along the axial direction remains unchanged for all three cases, which further confirms the self-similarity of the flow field with varying inlet diameters.

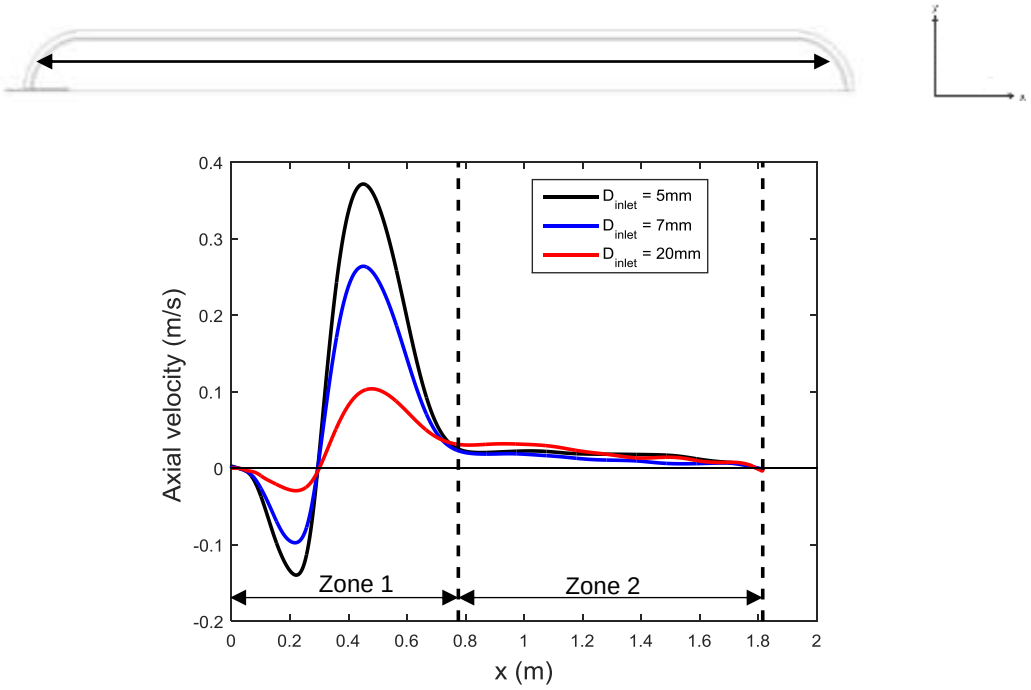

Figure 4.35: Axial velocity of the gas in the axial direction half way between the centreline and the diameter of the cylinder 30s into the fill.

4.4 Different inlet configurations

The simulations have shown that the recirculation of the gas within the cylinder is crucial in the heat transfer from the gas to the structure. In order to create the recirculation of the gas throughout the cylinders with a high aspect ratio (L/D > 4), the delivery method of the gas into the cylinders is altered as follows:

- The gas is delivered from both sides of the cylinder.
- A long dual injector is used to inject part of the fluid further downstream into the cylinder (Figure 4.36).

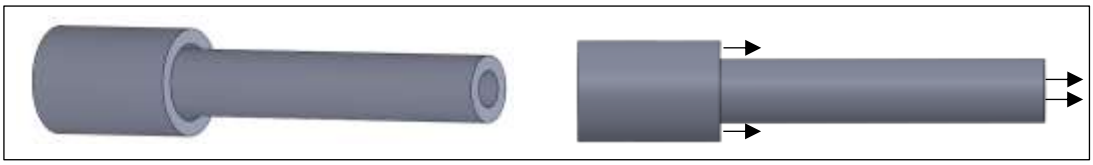

Figure 4.36: Long dual injector.

The fast-fill simulations were performed for the cylinder with a L/D of 8. Table 4.4 shows the different inlet configurations that are compared in this study.

	Number of inlets	Inlet(s) diameter	Inlet(s) total area	Note
Case 1	1	7.07 mm	19.6 mm^2	-
Case 2	2	5 mm	19.6 mm^2	Inlets on opposite sides of cylinder
Case 3-A	2	-	19.6 mm^2	Middle part of the injector extends at a distance of four times the cylinder diameter into the cylinder
Case 3-B	2	-	19.6 mm^2	Middle part of the injector extends at a distance of five times the cylinder diameter into the cylinder

Table 4.4: Comparison of the final mass-averaged gas temperatures and final mass of gas in the cylinder (L/D = 8) using the different inlet configurations.

A decrease in the mass-averaged and maximum gas temperatures throughout the fill is obtained with the inlet configurations of cases 2, 3-A and 3-B as opposed to the conventional filling procedure of case 1 (Figures 4.37 and 4.38). The maximum local gas temperature with a single inlet (case 1) occurs at the end of the fill and

has a value of 391 K, which is well above the 358 K threshold. The maximum gas temperatures of cases 2 and 3-A are below the 358 K limit throughout the fill. The simulation of case 3-B shows that the local gas temperature reaches a maximum of approximately 360 K during the fill.

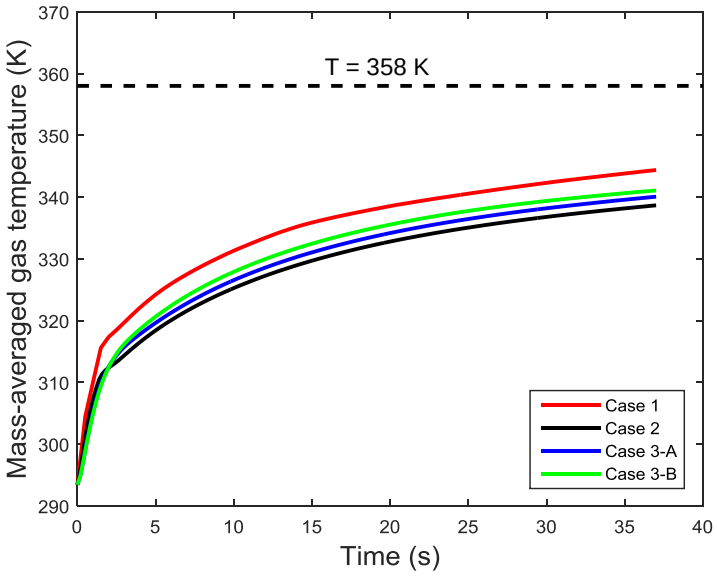

Figure 4.37: Comparison of the mass-averaged gas temperatures in the cylinder (L/D =8) with different inlet configurations.

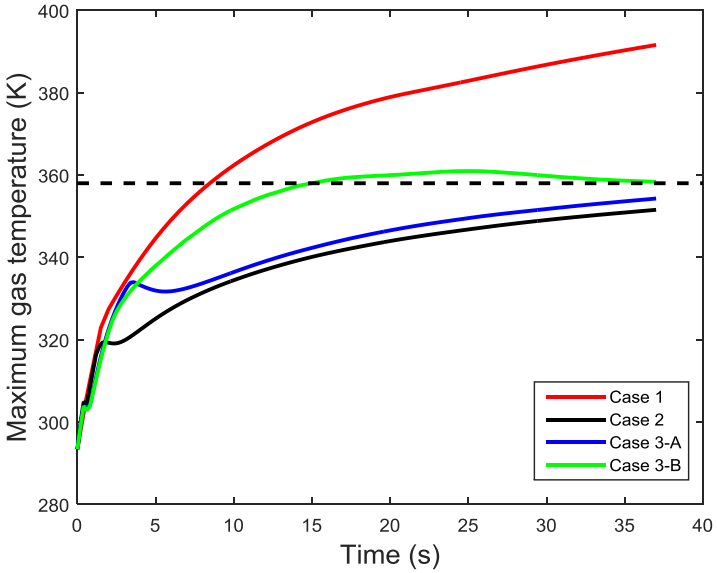

Figure 4.38: Comparison of the maximum local gas temperatures in the cylinder (L/D =8) with different inlet configurations.

The final mass-averaged gas temperatures for cases 2, 3-A and 3-B are slightly lower than in case 1 and subsequently this leads to a marginal increase in the final mass of gas in the cylinders (Table 4.5).

	Final average temperature	Final mass of gas	% increase in final mass of gas
Case 1	344.4 K	1.534 kg	-
Case 2	338.6 K	1.556 kg	1.4 %
Case 3-A	340.1 K	1.549 kg	1.0 %
Case 3-B	341.1 K	1.545 kg	0.7 %

Table 4.5: Comparison of the final mass-averaged gas temperatures and final mass of gas in the cylinder (L/D = 8) using the different inlet configurations.

Figure 4.39 shows the contours of gas temperature 30 s into the fill for the cylinders with the different inlet configurations. The local gas temperature is highest in the caudal region of the cylinder with inlet configuration of case 1. The recirculation of the gas throughout the cylinder for cases 2, 3-A and 3-B (Figure 4.40), leads to an increase in the heat transfer from the gas to the structure resulting in lower local gas temperatures.

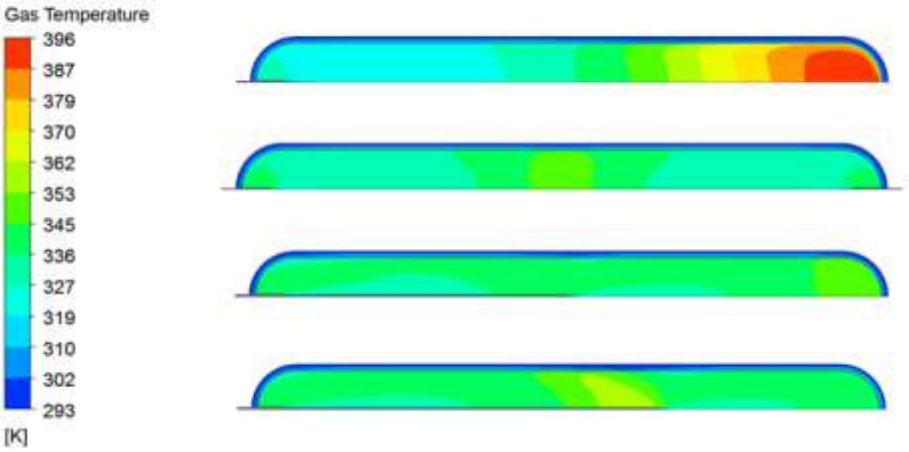

Figure 4.39: Comparison of the contours of gas temperature 30 s into the fill in the cylinder (L/D =8) with the different inlet configurations.

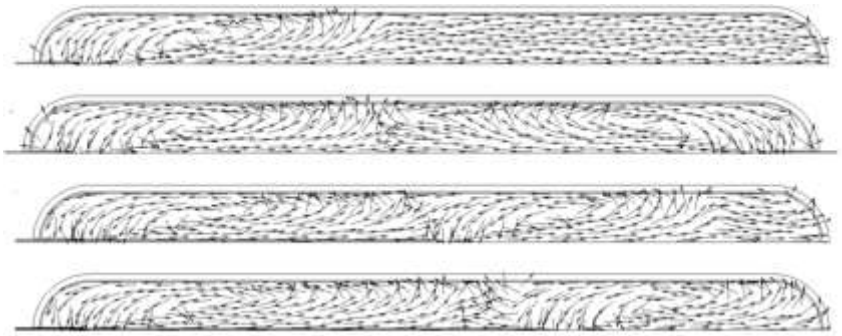

Figure 4.40: Flow field within the cylinders (L/D=8) with the different inlet configurations at the fill time of 30 s.

The purpose of having a 358 K temperature limit during the fast-filling of hydrogen cylinders is to prevent the thermal degradation of the structure. However, the increase in heat transfer from the gas to the structure in cases 2, 3-A and 3-B (Figure 4.41) results in an increase the maximum temperature of the structure (Figure 4.42). The significantly higher maximum gas temperature in the cylinder with one inlet (case 1) does not translate into a higher maximum temperature of the structure. The final maximum temperature of the structure is nearly similar for cases 2, 3-A and 3-B and approximately 7 degrees lower for case 1.

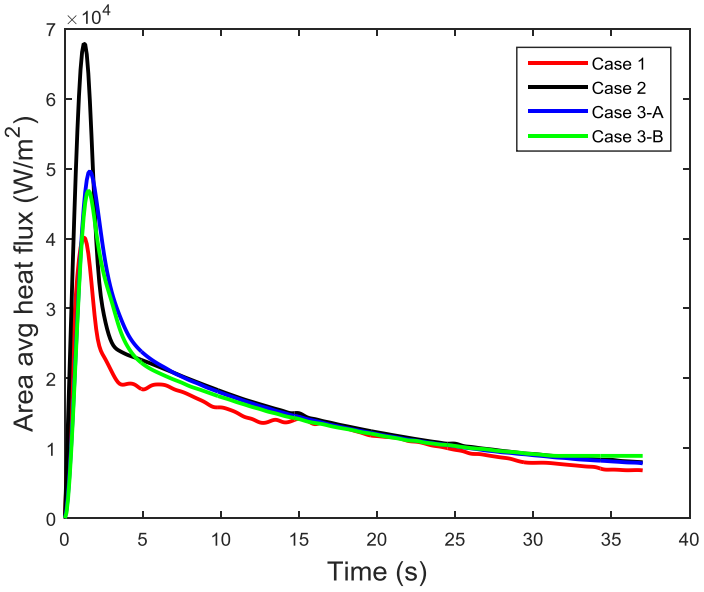

Figure 4.41: Comparison of the area average heat flux in the cylinder (L/D =8) throughout the fill with different inlet configurations

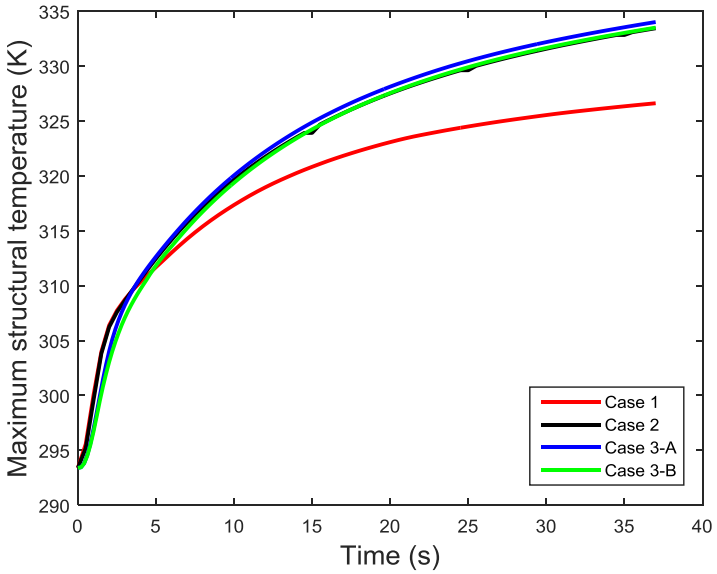

Figure 4.42: Comparison of the maximum temperature of the structure of the cylinder (L/D =8) throughout the fill with the different inlet configurations

4.5 Summary

The two-dimensional axisymmetric simulation of the fast-filling of a 74 L hydrogen cylinder has shown that the k-ε model along with the real gas equation of state is capable of accurately predicting the subsequent rise in gas temperature. According to the model, the outer wall boundary condition of the cylinder plays no significant role in heat transfer during the fill, which is due to the low thermal conductivity of the laminate. The following conclusions can be drawn from the simulations of the filling of the cylinder with a constant volume but with varying length-to-diameter ratios (L/D):

- A circulating flow field exists within the cylinder and extends three diameters from the exit of the delivery pipe.
- Two distinct flow regions are observed when the L/D of the cylinder is increased beyond a value of 3: a recirculating region close to exit of the delivery pipe that extends 3 cylinder diameters. Beyond the recirculating region, the gas moves axially into a rather stagnant region.
- The gas temperature is no longer homogeneous and increases axially during the fast-filling cylinders that have a L/D greater than 3.
- The recirculating region is crucial in heat transfer from the gas to the structure of the cylinder.
- The compression of the gas the caudal region of the cylinders that have a L/D greater than 3 results in high local gas temperatures.

The flow field during the fast-filling of the cylinder with a L/D of 8 is quasi-similar for different inlet diameters. The presence of the two distinct flow regions is unaffected and the location of the centre of the circulating region is similar despite the ratio of the diameter of the cylinder to the diameter of the inlet (Dcyl/Dinlet) varying between 13.5 and 53.8. An increase in the diameter of the inlet leads to a decrease in the maximum local temperature in the caudal region of the cylinder. This is due to a decrease in the momentum flow rate at the inlet that decreases the compression of the gas. However, the final maximum local temperatures are still above the 358 K threshold.

Several fast-filling simulations were performed by altering the delivery method of the gas to create a recirculating region throughout the cylinder that has a L/D of 8. The following conclusions were made from the different cases:

- The alteration of the flow field to create the recirculation of the gas throughout the whole cylinder increases heat transfer from the gas to the structure, which leads to a decrease in the final mass-averaged gas temperatures.
- A slight increase in the final mass of gas is obtained due to the lower final temperatures in the cylinder.
- The maximum local temperatures are significantly lowered throughout the fill.
- The maximum temperature of the structure increases due to the increase in heat transfer from the gas to the liner.

5 Low order model for the filling of the cylinder

5.1 Introduction

This chapter describes the procedures that were involved in the low order modelling for the filling of the cylinder. Initially, the viscous discharge coefficient of the flow through the delivery pipe is modelled. In addition, the heat transfer coefficient during the fast-filling of the cylinder is modelled for cylinders with varying length-to-diameter ratios (L/D). Once the low order model for the fast-filling is established and validated, the influence of using a solid-liquid PCM as part of the structure of the cylinder to enhance heat transfer is analysed.

5.2 Modelling the viscous discharge coefficient

For the test-cases considered, the delivery pipe that protrudes into the cylinder has the following dimensions [7]:

- Pipe length (l) = 0.143 m
- Inner diameter (d) = 0.005 m

The known values in the 2D CFD model of the fast-filling of the cylinders are: (1) the upstream stagnation pressure(P_0), (2) the stagnation temperature(T_0) . The static back pressure (p) is the gas pressure within the cylinder and varies throughout the fill. Figure 5.1 shows the two-dimensional drawing of the delivery pipe with known parameters.

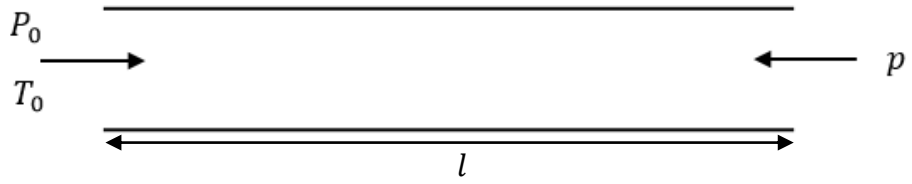

Figure 5.1: Flow through the delivery pipe.

5.2.1 Determination of the isentropic mass flow rate and Reynolds number

Initially, the isentropic Mach number was determined for hydrogen gas using ideal gas assumptions with the upstream pressure (P_0) and temperature (T_0) being kept at a constant of 1 MPa and 293 K respectively. The back pressure (p) was varied with of values of 0.527 MPa, 0.6 MPa, 0.7 MPa, 0.8 MPa, 0.9 MPa and 0.99 MPa.

The value of ratio of the specific heats (γ) for hydrogen assuming ideal gas behaviour is 1.41 [91] and from Equation 3.11, choked condition $(M = 1)$ is reached when the pressure ratio $\frac{p}{P_0}$ is 0.527. This explains the reasoning behind the minimum back pressure being set to 0.527 MPa. Since the upstream pressure was kept at a constant of 1 MPa, further lowering the back pressure from 0.527 MPa, will have no effect on the isentropic Mach number. The isentropic Mach numbers that are determined using Equation 3.11 for the corresponding upstream and downstream pressures are shown in Table 5.1.

P_0 (MPa)	p (MPa)	Isentropic Mach Number
1	0.527	1
1	0.6	0.885
1	0.7	0.731
1	0.8	0.573
1	0.9	0.390
1	0.99	0.120

Table 5.1: Determination of the isentropic Mach numbers.

The next step involved keeping the isentropic Reynolds number with respect to the diameter of the pipe at the exit constant over a range of values for the different Mach numbers. Eight different values were chosen for the isentropic Reynolds numbers that ranged from 1×10^4 to 5×10^7. This particular range was chosen since in their fast-filling model, Dicken and Merida [7], showed that the inlet Reynolds numbers at the start and end of fill were 8.2×10^5 and 7.23×10^5 respectively.

The calculations for the determination of the isentropic Reynolds number using hydrogen and assuming ideal gas conditions are as follows:

- The isentropic Mach numbers for the different pressure ratios were determined using Equation 3.11.
- The initial diameter of the pipe chosen was 0.005m.
- The isentropic mass flow rates $(\dot{m}_{isen})$ for the different Mach numbers from Table 5.1 were determined using Equation 3.12, with the value of the gas constant R for hydrogen being 4.124 KJ/kg-K [91].

- The corresponding isentropic Reynolds numbers were determined using the Equation 5.1.

$$Re_i = \frac{4\dot{m}_{isen}}{\pi\mu d} = \frac{\rho_{exit} v_{exit} d}{\mu} \tag{5.1}$$

- Since the flow is assumed to be isentropic, the dynamic viscosity (μ) at the exit is determined using REFPROP 9.0 as follows:

$$s = s(P_0, T_0) \tag{5.2}$$

$$\mu = \mu(s, p) \tag{5.3}$$

where s is the entropy and is a constant assuming isentropic flow.

- From Equation 5.1, it is clear that the isentropic Reynolds number at the exit can be modified to any value by simply changing the value of the diameter d of the pipe. The values of ρ_{exit}, v_{exit} and μ are unaffected by value of the diameter d (*please refer to Appendix A6*).
- The values of the eight isentropic Reynolds numbers chosen as well as the corresponding pipe diameters and Mach numbers for hydrogen gas are displayed in Appendix A7.

5.2.2 Determination of the actual mass flow rate

The length-to-diameter ratio $\left({}^{l}/_{d}\right)$ of the delivery pipe that protrudes into the cylinder is 28.6. The isentropic cases (*please refer to Appendix A7*) involve eight values for the Reynolds numbers ranging from 1×10^4 to 5×10^7 and six values for the Mach numbers that range from 0.12 to 1. This subsequently leads to 48 different values for the pipe diameter. With the length-to-diameter ratio kept at a constant of 28.6, forty-eight different values for the pipe length are obtained (*please refer to Appendix A8*). For each of these test cases, 2D axisymmetric CFD simulations were carried out using FLUENT with the standard k-ε turbulence model and the ideal gas equation of state to determine mass flow rate and thus discharge coefficient.

The axisymmetric domain consisted of a single block that was discretised using a structured mesh (Figure 5.2) using the ICEM software. A fine mesh was placed at the interface of the fluid-wall region in order to resolve the boundary layer.

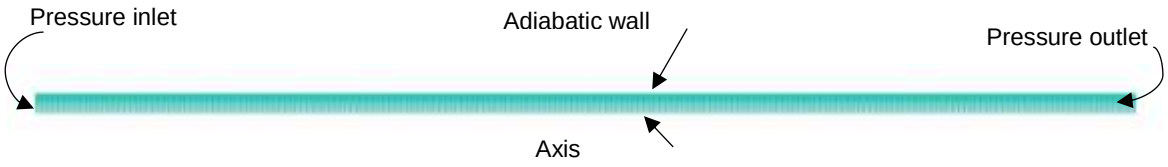

Figure 5.2: 2D axisymmetric domain of pipe with the length-to-diameter ratio of 28.6.

These simulations were performed with hydrogen gas as the fluid. At the inlet of the delivery pipe, a pressure boundary condition was used with the total pressure and total temperature being kept a constant of 1 MPa and 293 K respectively for all 48 simulations. At the upper wall of domain (Figure 5.2), adiabatic wall conditions and the no slip boundary condition (v = 0 m/s) were applied. Since the pipe has an axisymmetric geometry, the axis boundary condition is used for its centreline. At the outlet of the pipe, a pressure boundary condition was used, with the back pressure ranging from 0.527 MPa to 0.99 MPa, while the total temperature was set at a constant of 293 K.

Similar to the simulations of the fast-filling of the cylinder, standard wall functions were used and this was achieved by ensuring that the non-dimensional distance (y*) of first 8 to 10 grids points off the inner wall of the tank were less than 300.

The viscous discharge coefficient (C_{d1}) for each of the 48 cases was obtained by dividing the mass flow rate that was obtained from the CFD simulations to that of the isentropic mass flow rate. Figure 5.3 shows a plot of the viscous discharge coefficient for hydrogen gas in a pipe of a length-to-diameter ratio of 28.6 having different isentropic Mach numbers and isentropic Reynolds numbers ($\mathrm{Re_i}$) at the exit.

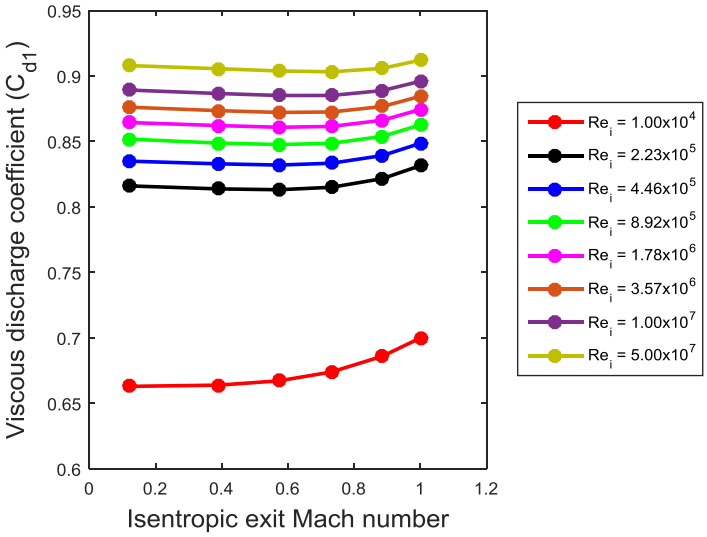

Figure 5.3: C_{d1} in a pipe of l/d of 28.6 with respect to the isentropic exit Mach number and Reynolds number.

As shown in Figure 4.24, C_{d1} increases with the isentropic Reynolds number. At the low Reynolds number of 1×10^4, the viscous discharge slightly increases as the exit Mach number increases. With the Reynolds number fixed at 1×10^4, C_{d1} has a value 0.663 when M_{exit} is equal to 0.120, while with M_{exit} equal to 1, the corresponding C_{d1} value is 0.7, which represents a change in $C_{d1}$of approximately 5%. However, as the Reynolds number is increased and is the order of 10^5 to 10^7, C_{d1} is mostly independent with respect to the exit Mach number and only a slight increase in its value (less than 3%) is observed when the Mach number is above 0.8. Since the Reynolds numbers involved in the fast-filling of cylinders are expected to be larger than 10^5 [7], relationships of C_{d1} with respect to the isentropic Reynolds number were determined for cases in which $Re_{isen} > 10^5$. The C_{d1} values for the unchoked cases are mostly similar at their respective Reynolds number and were thus averaged and curve fitted (Figure 5.4). For the choked case, a separate relationship was obtained as shown in Figure 5.4

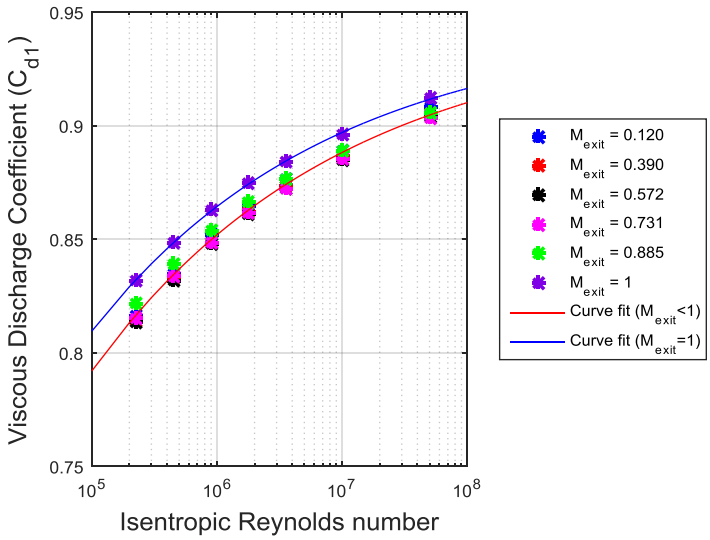

Figure 5.4: C_{d1} v/s Isentropic Reynolds number.

The form of the correlation of C_{d1} with respect to the isentropic Reynolds number is the same for both the choked and unchoked conditions (Equation 5.4).

$$C_{d1} = A + BRe_i^{\,n} \tag{5.4}$$

The values of A, B and n for the choked case and unchoked cases are as follows:

- $A = 0.938$, $B = -2.71$, $n = -0.25$ when $M_{exit} < 1$
- $A = 0.945$, $B = -1.82$, $n = -0.23$ when $M_{exit} = 1$

5.3 C_{d1} of methane v/s hydrogen

The next step of this study involves determining whether the correlation of C_{d1} with respect to the isentropic Reynolds number is also applicable for methane and thus for different gases. A similar procedure to the one previously used in the determination of C_{d1} for hydrogen was also performed for methane for which C_{d1} was determined for isentropic Reynolds numbers of 1×10^4, 2.2×10^5, 1.8×10^6 and 1×10^7 and at isentropic Mach numbers of 0.120, 0.390, 0.573, 0.731, 0.885 and 1. The value of ratio of the specific heats (γ) for methane is different to that of hydrogen assuming ideal gas behaviour and has a value of 1.30 as opposed to 1.41 [91]. Thus, to achieve the stated isentropic Mach numbers, different back pressures were determined (*please refer to Equation 3.11*), since the upstream stagnation pressure was kept at a constant of 1 MPa (Table 5.2).

Isentropic Mach Number	P_0 (MPa)	p (MPa)	p/P_0
0.12	1	0.991	0.991
0.39	1	0.906	0.906
0.573	1	0.810	0.810
0.731	1	0.713	0.713
0.885	1	0.614	0.614
1	1	0.542	0.542

Table 5.2: Pressure ratios for methane for the different isentropic Mach numbers.

The pipe length-to-diameter ratio was also kept at a constant of 28.6. The pipe diameters that were used in the determination of the isentropic mass flow rate and the corresponding lengths of pipe used in the CFD simulations are shown in Appendix A9. A comparison of the viscous discharge coefficient (C_{d1}) of both hydrogen and methane at the various isentropic exit Reynolds numbers and Mach numbers is shown in Figure 5.5. The viscous discharge coefficient of both hydrogen and methane are similar at various isentropic exit Reynolds numbers ($\mathrm{Re_i}$) and Mach numbers. This indicates that for perfect gases with ratios of specific heats in the range of 1.3-1.4, C_{d1} is relatively independent of the type of gas.

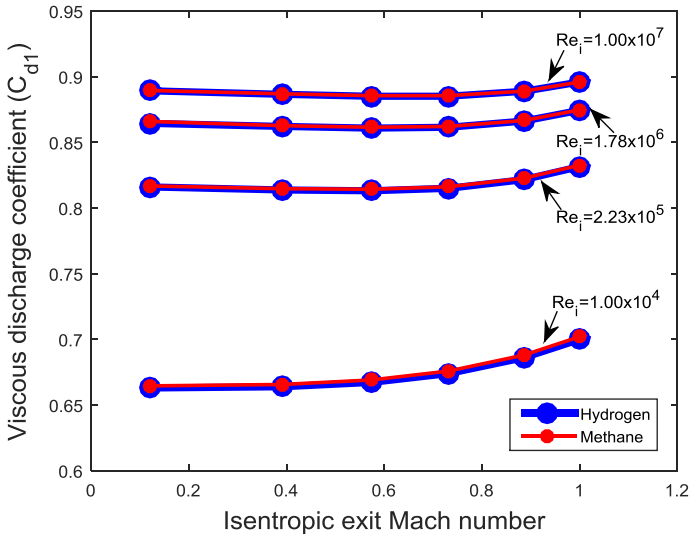

Figure 5.5: Comparison of C_{d1} of hydrogen and methane.

5.4 Real gas effects on the viscous discharge coefficient

The study on the viscous discharge coefficient has so far been based on ideal gas assumptions. However, the fast-filling of cylinders involves gases at high pressures

and a significant deviation from the ideal behaviour is expected. This section of this current chapter involves the investigation of real gas effects on the viscous discharge coefficient.

The isentropic mass flow rate for hydrogen was initially determined on MATLAB using the real gas equation of state from the NIST database in REFPROP 9.0 for two cases:

- Case 1: The isentropic Reynolds number for the real gas was kept at a constant of 5×10^7 with the pressure ratio $\left({}^{p}/_{P_0}\right)$ set to 0.572, which is the condition for which choking occurs under ideal gas behaviour.
- Case 2: The isentropic Reynolds number for the real gas was kept at a constant of 3.57×10^6 with the pressure ratio $\left({}^{p}/_{P_0}\right)$ set to 0.8, which is the condition for a Mach number of 0.573 under ideal gas behaviour.

In both cases, the upstream total temperature (T_0) was kept constant at 293 K, while the upstream total pressure (P_0) was incrementally increased (Table 5.3). The compressibility factor (Z) of the gas at upstream conditions is also displayed in Table 5.3.

$\boldsymbol{P_0\ (MPa)}$	$\boldsymbol{T_0\ (K)}$	$\boldsymbol{Z}$
30	293	1.191
40	293	1.258
50	293	1.325
60	293	1.392
70	293	1.459

Table 5.3: Upstream conditions of pressure and temperature.

Similar to the ideal gas cases, CFD simulations were carried out in FLUENT using the real gas equation of state from the NIST database to determine the actual mass flow rate. The pipe diameters that were used in the determination of the isentropic mass flow rate and the corresponding lengths of pipe used in the CFD simulations for the real gas cases are shown in Appendix A10.

The correlation of C_{d1} with respect to the isentropic Reynolds number (Equation 5.4) was determined using the ideal gas equation. To determine if real gas effects

influences the viscous discharge coefficient, the isentropic mass flow rates from the real gas cases are multiplied by the C_{d1} values that were obtained from the ideal gas equation and the results were compared to the mass flow rates that were obtained from FLUENT (Figures 5.6 & 5.7). The values of C_{d1} for cases 1 and 2 are obtained from the correlation of Equation 5.4 and have the following values:

- Case 1: $C_{d1} = 0.914$
- Case 2: $C_{d1} = 0.876$

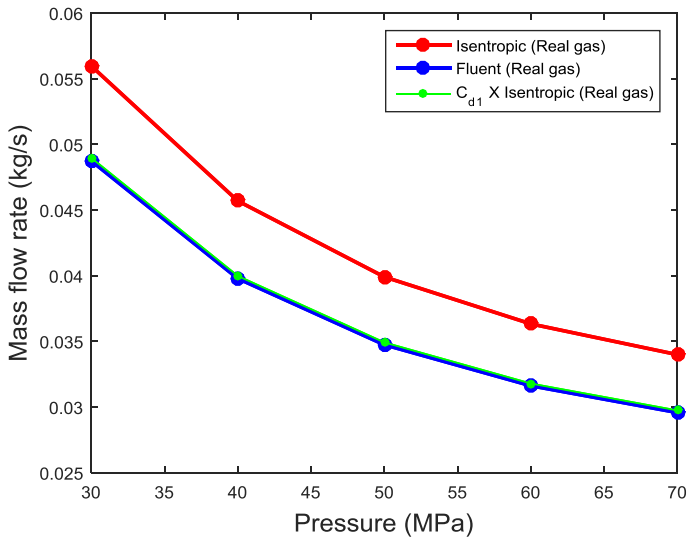

Figure 5.6: Mass flow rates comparison for case 1 ($\mathrm{Re_i} = 5 \times 10^7$ and pressure ratio of 0.527).

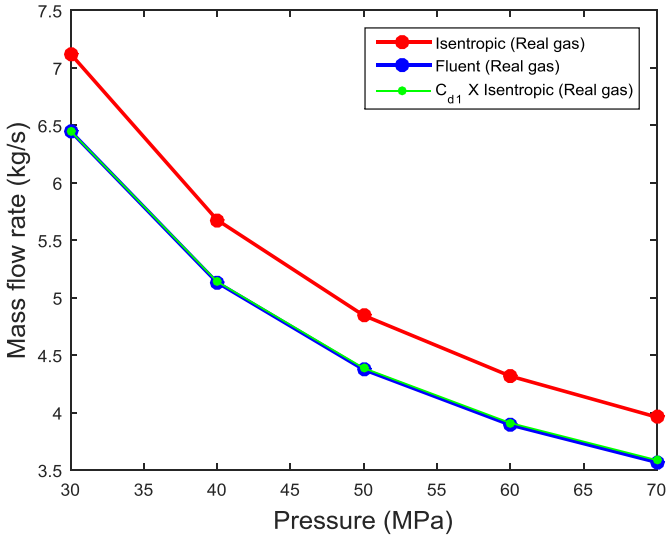

Figure 5.7: Mass flow rates comparison for case 1 ($\mathrm{Re_i} = 3.57 \times 10^6$ and pressure ratio of 0.8).

As shown in Figures 5.6 and 5.7, multiplying the isentropic mass flow rate at real gas conditions by the C_{d1} that is obtained from the ideal gas assumptions correctly predicts the actual mass flow rate at different isentropic Reynolds numbers and pressure ratios. Thus, it can be concluded that real gas effects do not influence the viscous discharge coefficient for the conditions tested here.

5.5 Modelling the heat transfer coefficient

The simulation of the fast-filling of the hydrogen cylinder with a length-to-diameter ratio (L/D) of 2.4 based on the experiments of Dicken and Merida [7] has been carried out and has been validated (*please refer to Figure 4.11*). The model also included heat conduction across the structure of the cylinder and heat transfer within the solid materials was found to be dependent upon the thermal conductivity of the materials (*please refer to Figures 4.19 – 4.21*). In order to eliminate the effect of the conjugate heat transfer on the aerodynamics of the flow within the cylinders, further axisymmetric CFD simulations of the fast-fill were performed in FLUENT whereby isothermal conditions were applied to inner walls of the cylinders to model the heat transfer due to the forced convection.

5.5.1 Cylinders geometries and computational grids

The volume of the cylinders were kept at a constant of 74 L, while varying the L/D from 2 to 8 in increments of one. The delivery pipe that feeds the gas into the cylinder protrudes 8.6 mm into all of the cylinders and has a diameter of 5 mm. Figure 5.8 shows the 2D axisymmetric geometry of the cylinders.

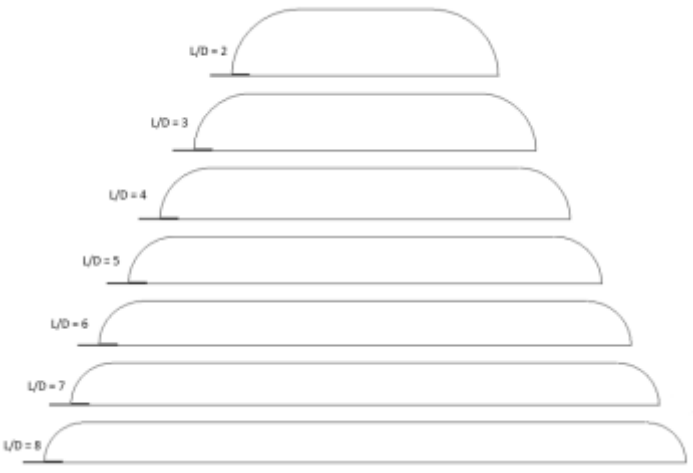

Figure 5.8: 2D axisymmetric domains of the cylinders with varying length-to-diameter ratio (L/D).

The axisymmetric domains that were used to model the fill did not include the liner and the laminate. It was mentioned in chapter 4 that mesh independence tests were carried out for the cylinder with a L/D of 2.4 that included the liner and laminate. Subsequently, for cylinders having a L/D of 3 and above, the number of grid points were proportionally increased in the axial direction of the cylinder with increasing L/D. In the lateral direction, the number of grid points was unaltered for all cylinders. Thus for the isothermal inner wall cases, the computational domains for cylinders having a L/D between 3 and 8 were obtained by simply removing the blocks that made up the liner and laminate. For the cylinder with the L/D of 2, the number of grid points was increased in the lateral direction and unaltered in the axial direction. Figure 5.9 shows the 2D axisymmetric computational grid of the cylinder having a L/D of 2.

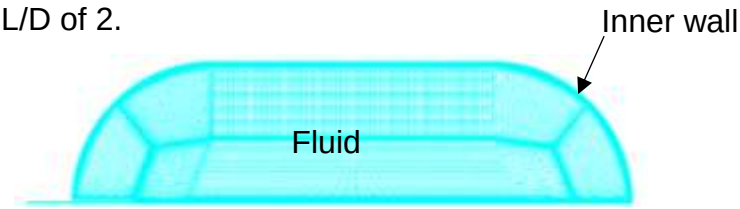

Figure 5.9: 2D axisymmetric computational grid of the cylinder having a L/D of 2.

The initial and boundary conditions were similar to the previous simulations of chapter 4, with only one exception: the inner wall of the cylinder was set a constant temperature of 293 K throughout the fill.

Initially, the inlet diameter was kept at a constant of 5 mm for all the cylinders with varying L/D. Further simulations were performed whereby the inlet diameter was changed to 10 mm and 20 mm for cylinders with the L/D of 2, 5 and 8 to determine its effect on the gas temperature.

Figure 5.10 shows the mass-averaged gas temperatures in the cylinders with varying L/D throughout the 37 s fill. The gas temperature within the cylinder is similar when the L/D of the cylinder is 2 and 3. An increase of L/D to 4 slightly lowers the gas temperature. However, further increasing the L/D of the cylinder from 5 to 8 leads to an increase in the gas temperature. The highest gas temperature is observed when the L/D of the cylinder is 8 even though the surface area of that particular cylinder is the largest.

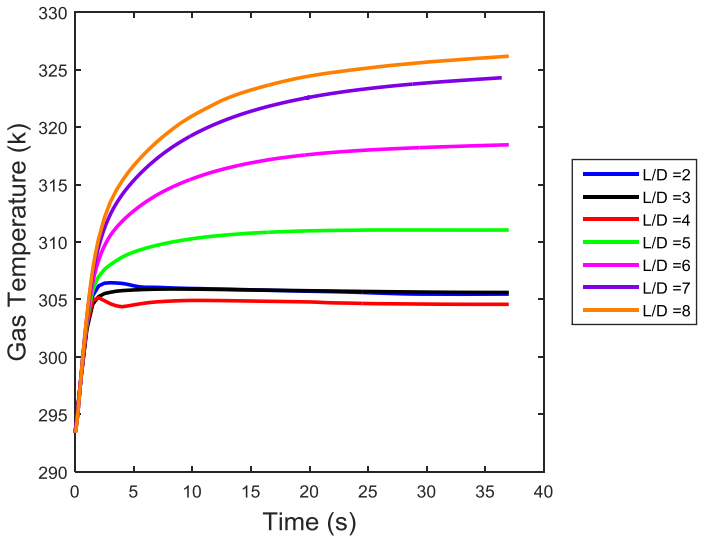

Figure 5.10: Comparison of the mass-averaged gas temperature in the cylinders with different L/D with isothermal inner wall conditions.

The flow pattern and gas temperature distribution in the cylinders with an isothermal inner wall is similar to the conjugate heat transfer cases of chapter 4. Figure 5.11 shows the contours of the gas temperature within the cylinders five seconds into the fill. The temperature of the gas is mostly homogeneous in the cylinders having a L/D of 2 and 3. Increasing the L/D to 4, leads to slight increase by 3 K in the gas temperature at the far end of the cylinder. The contours of the gas temperature in cylinders with a L/D of 5 and greater show that the gas temperature within the cylinders are no longer homogeneous.

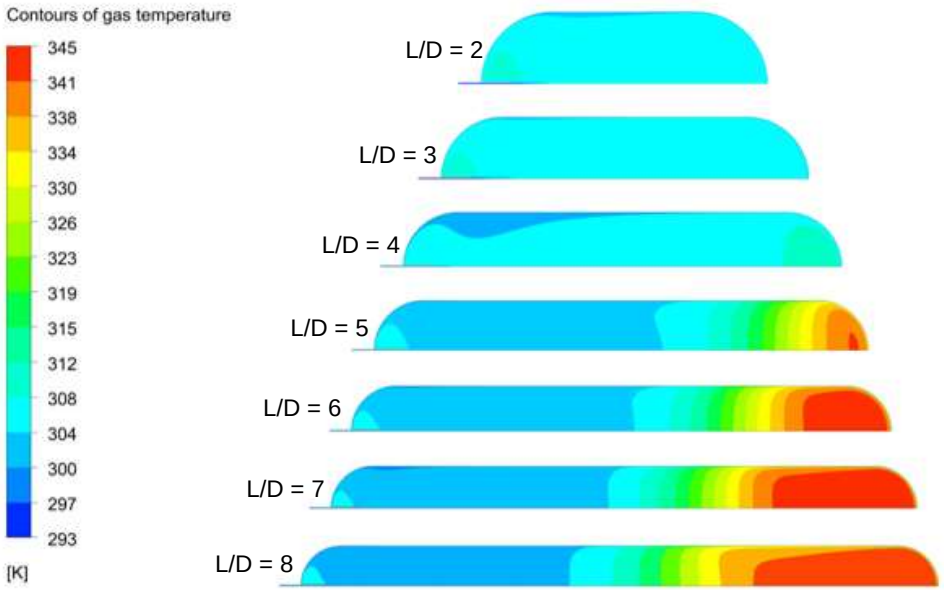

Figure 5.11: Contours of the gas temperature 5s into the fill with isothermal inner wall conditions.

Figure 5.12 shows the flow field within the cylinder at fill time of 5 s. The flow field in cylinders with a L/D of 2 and 3 consists of a circulating region with the gas that exits the delivery pipe impinging onto the opposite dome and recirculates within the cylinder. For cylinders having a L/D of 4 and greater, two distinct flow regions exist; a recirculating region close to the exit of the delivery pipe and a secondary region in which the gas moves axially toward the caudal region of the cylinders.

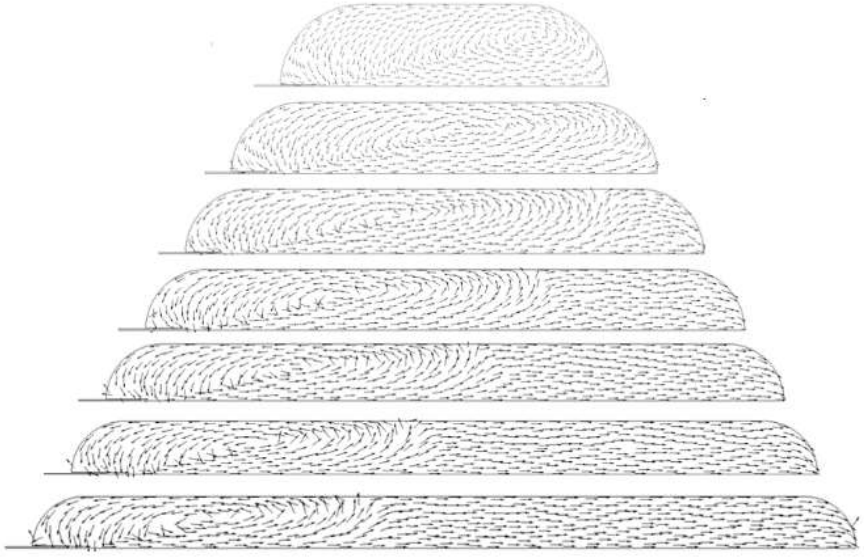

Figure 5.12: Flow field within the cylinders with varying L/D at the fill time of 5 s with isothermal inner wall conditions.

Similar to the conjugate heat transfer cases, the following observations can be made:

1. The gas temperature is approximately homogeneous in cylinders having a L/D less than 4.
2. For cylinder with a L/D of 4 and above, the gas temperature is lowest in the recirculating region and increases axially in the secondary region.
3. The fluid domain for cylinders having a L/D between 4 and 8 can split into 2 parts as shown in Figure 5.13. Zone 1 is the recirculating region and in zone 2, the gas moves axially.
4. The recirculating region extends to a distance of 3 diameters from the exit of the delivery pipe, i.e. $\mathrm{L_1 = 3D_{cyl}}$.

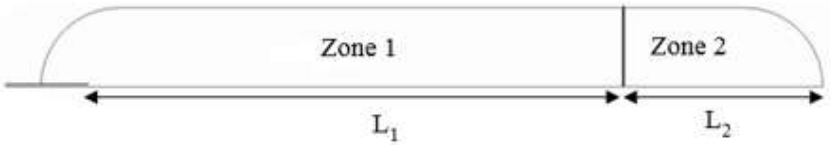

Figure 5.13: Schematic of the 2 fluid regions within the cylinder with a L/D > 3.

Figure 5.14 - 5.16 show that increasing the inlet diameter leads to an increase in the mass-averaged gas temperatures in the cylinders with the isothermal inner wall conditions irrespective of the L/D.

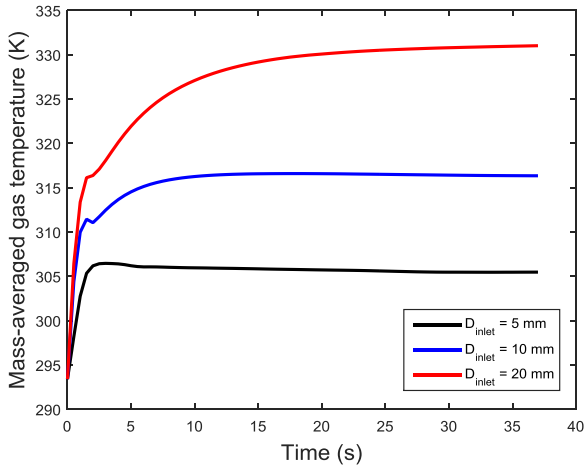

Figure 5.14: Mass-averaged gas temperature in the cylinder with a L/D of 2 with isothermal wall conditions.

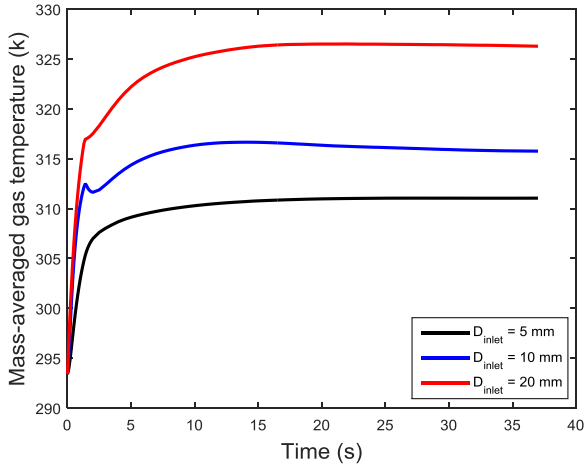

Figure 5.15: Mass-averaged gas temperature in the cylinder with a L/D of 5 with isothermal wall conditions.

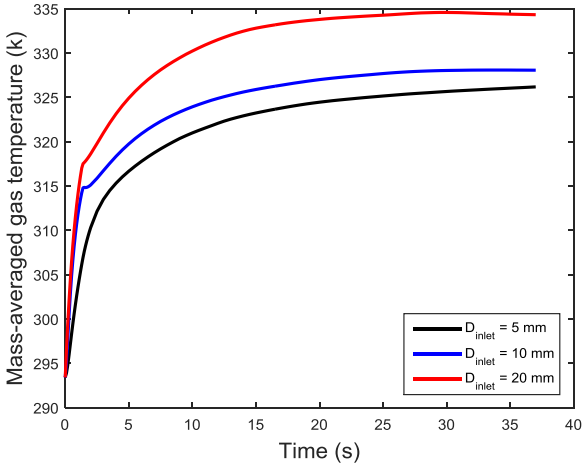

Figure 5.16: Mass-averaged gas temperature in the cylinder with a L/D of 8 with isothermal wall conditions.

Initially, a single-zone model approach was used to determine whether a relationship can be obtained between the Reynolds number at the inlet and the Nusselt number based on the CFD models for all cylinders irrespective of the L/D. The Nusselt number is non-dimensional and is used to model the heat transfer coefficient. The Reynolds number at the inlet and the Nusselt number due to forced convection in the cylinder are defined in Equations 5.5 and 5.6 respectively.

$$Re_{inlet} = \frac{\rho v D_{inlet}}{\mu} \tag{5.5}$$

where ρ is the density, v is the velocity, μ is the dynamic viscosity and D_{inlet} is the diameter of the inlet.

$$Nu_f = \frac{h_f D_{cyl}}{k_{gas}} \tag{5.6}$$

where h_f is the heat transfer coefficient due to forced convection, k_{gas} is the thermal conductivity of the gas and D_{cyl} is the length scale, which is the inner diameter of the cylinder. The heat transfer coefficient due to the forced convection is averaged along the inner wall and the Nusselt numbers of the cylinders having a L/D of 5 and 8 with a constant inlet diameter of 5 mm are respectively plotted against the inlet Reynolds numbers (Figure 5.17) for every 0.5 seconds of the 37 second fill.

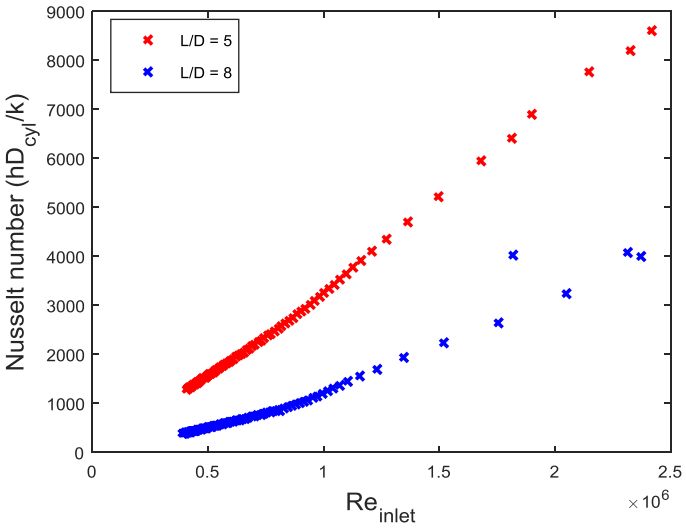

Figure 5.17: Nusselt number v/s Inlet Reynolds number for cylinders with L/D of 5 and 8 for a single-zone model.

As shown in Figure 5.17, a single-zone model cannot be used to establish a single correlation between the Nusselt numbers with respect to the inlet Reynolds numbers for cylinders having different L/D. If a Nusselt number is computed based solely on the heat transfer in zone 1, the data for cylinders with different L/D collapse onto the same line (Figure 5.18).

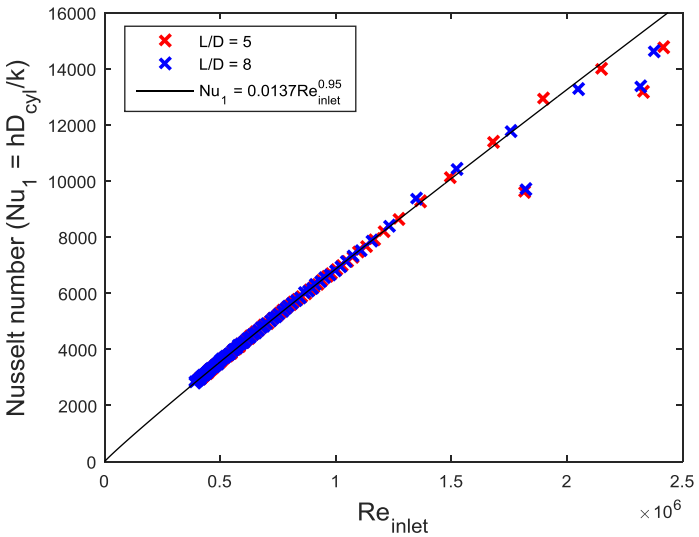

Figure 5.18: Nusselt number v/s Inlet Reynolds number for cylinders with L/D of 5 and 8 in Zone 1.

The data points in Figure 5.18 corresponds to every 0.5 seconds into the fill. For the first two seconds into the fill, a ‘transient’ behaviour is observed. A ‘quasi-steady’ state is reached 2 seconds and onwards into the fill and an empirical correlation for the Nusselt number/Reynolds number is established for zone 1 (Equation 5.7).

$$Nu_1 = 0.0137Re_{inlet}^{0.95} \tag{5.7}$$

In zone 2, the flow is unidirectional and the modelling of the Nusselt number assumes that the heat transfer in zone 2 is mainly due to the convection and diffusion of kinetic energy from zone 1. The Nusselt number in zone 2 is assumed to be a function of the Nusselt number in zone 1. To account for the different parameters such as L/D and inlet diameter, it was found that a linear relationship was obtained when the Nusselt number in zone 2 (Nu_2) is plotted against the Nusselt number in zone 1 that includes the L/D, inlet diameter and cylinder diameter, which is denoted as Nu_λ and is defined in Equation 5.8.

$$Nu_\lambda = \frac{Nu_1 D_{inlet}}{\left({}^{L}/_{D} - 3.3\right)D_{cyl}} \tag{5.8}$$

The numerator $\left({}^{L}/_{D} - 3.3\right)D_{cyl}$ in Equation 5.7 represents the length of zone 2 along the axis of the cylinders.

Figure 5.19 shows a plot of the data of Nu_2 versus Nu_λ for the cylinders with varying L/D and inlet diameters for every 0.5 seconds during the quasi-steady' state, which 2 seconds and onwards into the fill.

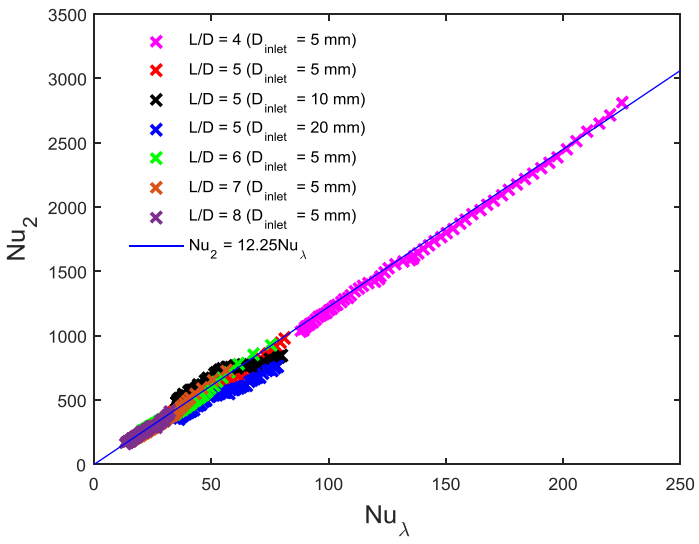

Figure 5.19: Relationship between the Nusselt numbers in zone 1 and zone 2.

The data points for all collapse onto each other and the empirical correlation to determine the Nusselt number in zone 2 (Nu_2) with respect to Nu_λ is as follows:

$$Nu_2 = 12.25Nu_\lambda \tag{5.9}$$

5.6 Implementing the single-zone model

The 2D CFD model for the filling of the cylinders having a L/D of 2 and 3 has shown that the gas temperature profiles are similar (*please refer to Figure 5.10*). A 2D fast-filing simulation was also performed for a cylinder having a L/D of 1.5 and further confirmed that that for cylinders having a L/D ≤ 3.3, the gas temperature is unaffected during the fill (Figure 5.20).

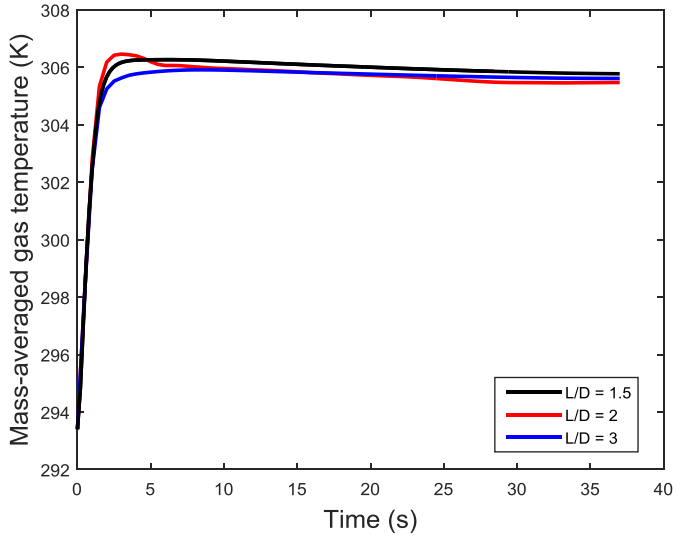

Figure 5.20: Comparison of the mass-averaged gas temperatures obtained from the 2D CFD model during the fill of cylinders having a L/D = 1.5, 2 and 3 with isothermal inner wall conditions.

The single-zone model is applicable if the flow in a particular cylinder only recirculates; i.e. zone 2 is non-existent. The single-zone model is applicable for filling of cylinders that have a L/D ≤ 3.3. The energy equation for the single region is given in Equation 5.10.

$$\frac{d(m_{gas}u_{gas})}{dt} = h_{0_{in}}\dot{m}_{in} + \dot{Q}_{wall} \tag{5.10}$$

where m_{gas} is the mass of gas in the cylinder, u_{gas} is the specific internal energy of the gas in the cylinder. $h_{0_{in}}$ is the stagnation enthalpy at the inlet, $\dot{m}_{in}$ is the mass flow rate at the inlet, $\dot{Q}_{wall}$ is the heat transfer rate at the wall in Zone 1. The heat transfer rate ($\dot{Q}_{wall}$) from the gas to the wall of the cylinders is given in Equation 5.11.

$$\dot{Q}_{wall} = Ah(T_{gas} - T_{wall}) \tag{5.11}$$

where h is the heat transfer coefficient, A is the inner surface area of the cylinder, T_{gas} is the gas temperature and T_{wall} is the wall temperature. For cylinders having

a L/D ≤ 3.3, the heat transfer rates ($\dot{Q}_{wall}$) are similar since the mass-averaged gas temperatures throughout the fill according are similar according to the CFD simulations (Figure 5.20).

The following procedure is used to obtain the heat transfer coefficients for cylinders that have a L/D of less than 3.3:

1. Obtain the heat transfer coefficient for the filling of a cylinder with a L/D of 3.3 by using Nusselt number and inlet Reynolds number relationship from Equation 5.6.
2. Since the product of the heat transfer coefficient and the inner surface area must be similar for cylinders with the L/D ≤ 3.3, use Equation 5.12 to obtain the heat transfer coefficient.

$$h_{(L/D\,<\,3.3)} = \frac{A_{(L/D\,=\,3.3)}}{A_{(L/D\,<\,3)}} h_{(L/D=\,3.3)} \tag{5.12}$$

The single-zone model accurately predicts the profile of the gas temperatures to within 0.1 K during the fast-fill of cylinders that have a L/D of 2 and 3 (Figures 5.21 & 5.22). The accuracy of the single-zone model is also relatively unaffected when the inlet diameter is varied, as shown in Figure 5.23. The single-zone model accurately predicts the rise in gas temperature during the filling of the cylinder that has a L/D of 2 with inlet diameters of 5 mm, 7.07 mm and 20 mm.

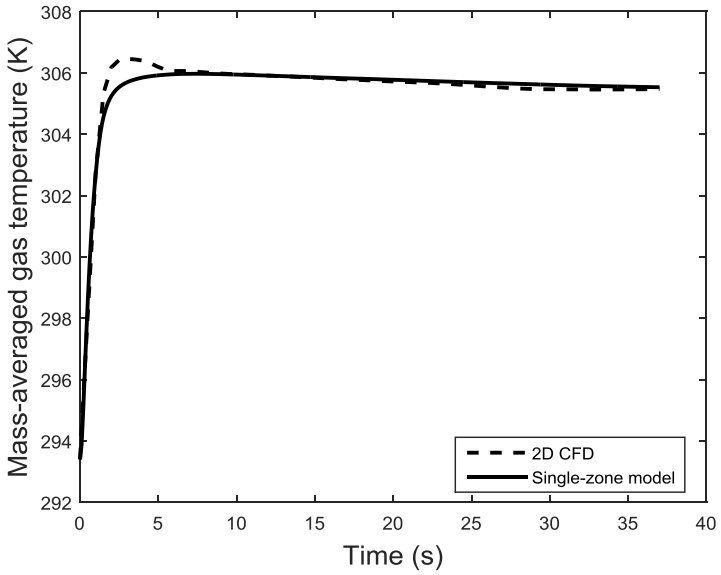

Figure 5.21: Comparison of the mass-averaged gas temperatures between the 2D CFD and the single-zone model for the cylinder with a L/D of 2 with isothermal inner wall conditions.

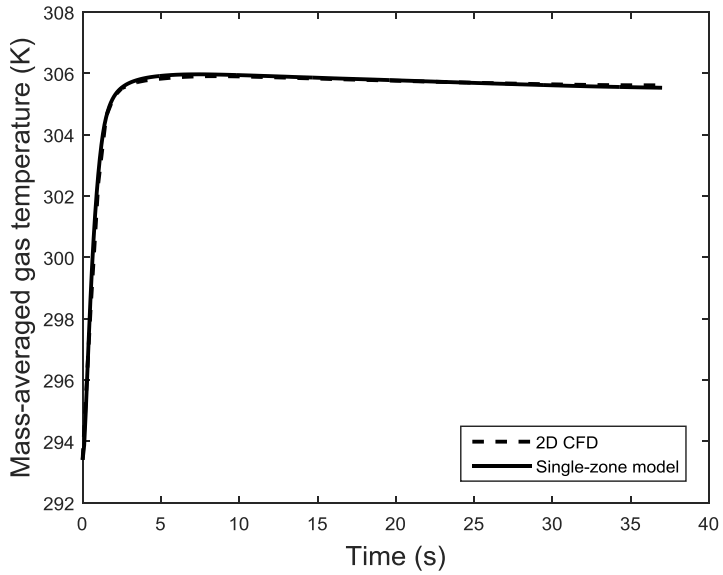

Figure 5.22: Comparison of the mass-averaged gas temperatures between the 2D CFD and the single-zone model for the cylinder with a L/D of 3 with isothermal inner wall conditions.

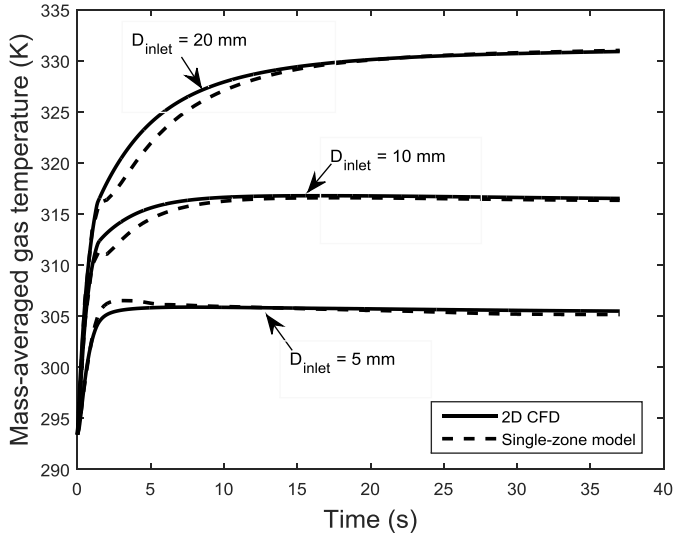

Figure 5.23: Comparison of the mass-averaged gas temperatures between the 2D CFD and the single-zone model for the different cylinders with a L/D = 2 having different inlet diameters with isothermal inner wall conditions.

5.7 Implementing the two-zone model

The two zone model is applicable for cylinders that have a L/D greater than 3.3. The energy equations for zones 1 and 2 are described in Equations 5.13 and 5.14 respectively.

$$\frac{d(m_1 u_1)}{dt} = h_{0_{in}} \dot{m}_{in} + \dot{Q}_1 - h_1 \dot{m}_2 \tag{5.13}$$

where m_1 is the mass of gas in zone 1, u_1 is the specific internal energy of the gas in Zone 1 and h_1 is the specific stagnation enthalpy of the gas in zone 1. $h_{0_{in}}$ is the stagnation enthalpy at the inlet, $\dot{m}_{in}$ is the mass flow rate at the inlet, $\dot{Q}_1$ is the heat transfer rate at the wall in zone 1 and $\dot{m}_2$ is the mass flow rate from zone 1 to zone 2.

$$\frac{d(m_2 u_2)}{dt} = h_1 \dot{m}_2 + \dot{Q}_2 \tag{5.14}$$

where m_2 is the mass of gas in zone 2, u_2 is the specific internal energy of the gas in zone 2 and $\dot{Q}_2$ is the heat transfer rate at the wall in zone 2.

The modelling of the two-zone model assumes that the gas exiting the delivery pipe initially moves into zone 1. The resulting pressure difference between the two distinct regions leads to some mass of gas (m_{1-2}) to transfer from zone 1 into zone 2 until pressure equilibrium is achieved. The value of m_{1-2} at each time step is determined using an iteration method until pressure equilibrium is achieved between zones 1 and 2. Thus $\dot{m}_2$ which is the mass flow rate from zone 1 to zone 2 at each time step Δt is obtained as follows:

$$\dot{m}_2 = \frac{m_{1-2}}{\Delta t} \tag{5.15}$$

Figure 5.24 compares the mass-averaged gas temperatures that were obtained from the two-zone model with the results from the CFD simulations with an isothermal inner wall condition.

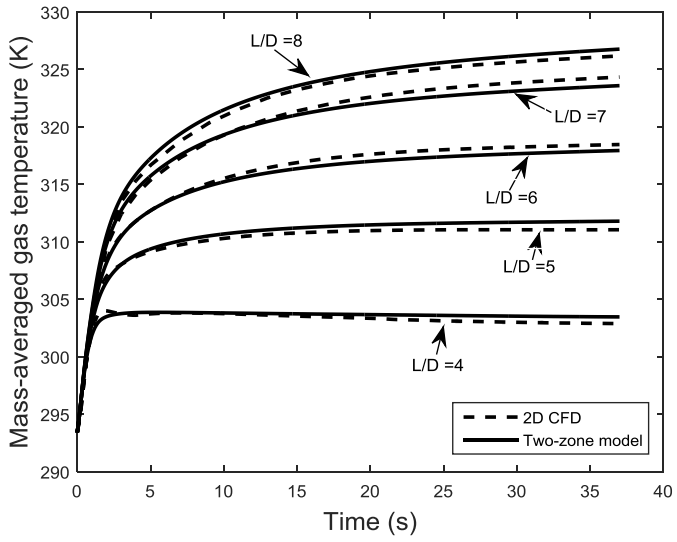

Figure 5.24: Comparison of the mass-averaged gas temperatures between the 2D CFD and the two-zone model for the different cylinders with isothermal inner wall conditions.

As shown in Figure 5.24-5.26 the two-zone model accurately predicts the profiles of the mass-averaged gas temperatures in cylinders with wide range of L/D and inlet diameters; differences between the model and the CFD are within 2 K. In addition, neglecting the transient behaviour that occurs at the start of the fill does not affect the overall profiles of the gas temperatures during the fill.

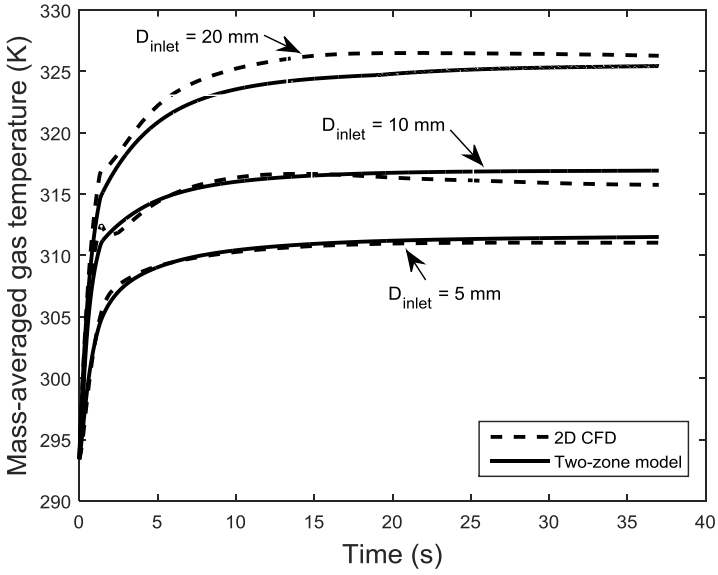

Figure 5.25: Comparison of the mass-averaged gas temperatures between the 2D CFD and the two-zone model for the different cylinders with a L/D = 5 having different inlet diameters with isothermal inner wall conditions.

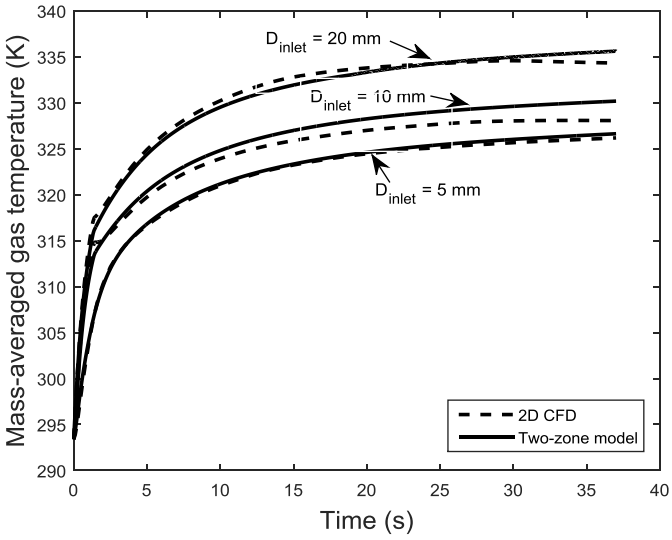

Figure 5.26: Comparison of the mass-averaged gas temperatures between the 2D CFD and the two-zone model for the different cylinders with a L/D = 8 having different inlet diameters with isothermal inner wall conditions.

One of the main advantages of both the single and two-zone models are the negligible computational time as opposed to the 2D CFD simulations (see Table 5.4).

L/D	CPU time (hours)	
	2D CFD (FLUENT)	Two-zone model (MATLAB)
4	~ 866	~ 0.04
5	~ 981	~ 0.04
6	~ 1088	~ 0.04
7	~ 1186	~ 0.04
8	~ 1278	~ 0.04

Table 5.4: Comparison of the computational times (Two-zone model v/s 2D CFD).

5.8 Inclusion of conjugate heat transfer

The inclusion of conjugate heat transfer to both the single-zone and two-zone models was performed by including heat transfer from the gas across the liner and laminate of the cylinders (*please refer to chapter 3*). In addition, the modelling of the discharge coefficient was included using Equation 5.4.

Figure 5.27 shows a comparison of results from the single-zone model and the experimental data of Dicken and Merida [7] who tested the fast-filling of a Type III hydrogen cylinder that has a L/D of 2.4. The model accurately predicts the mass-averaged gas temperature throughout the refuelling particularly for fill times greater than 10s.

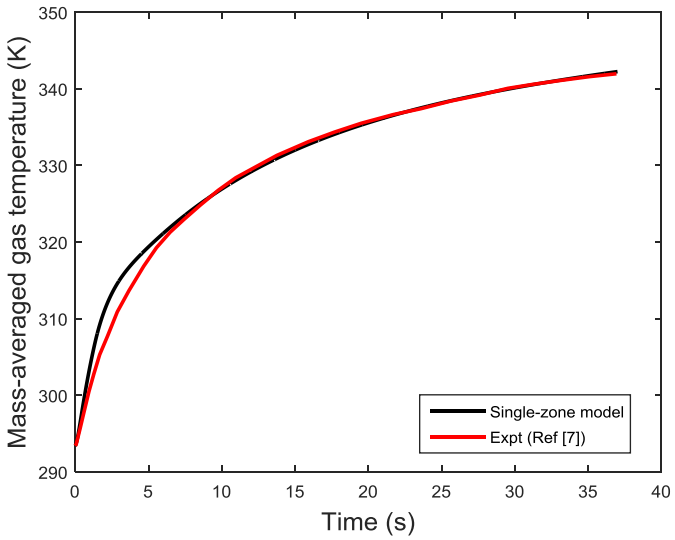

Figure 5.27: Comparison of the mass-averaged gas temperature obtained throughout the fill from the single-zone model and the experiment [7]

A comparison of the two-zone model with conjugate heat transfer and CFD results are shown in Figure 5.28. The model accurately captures the gas temperature within 1 K of the CFD.

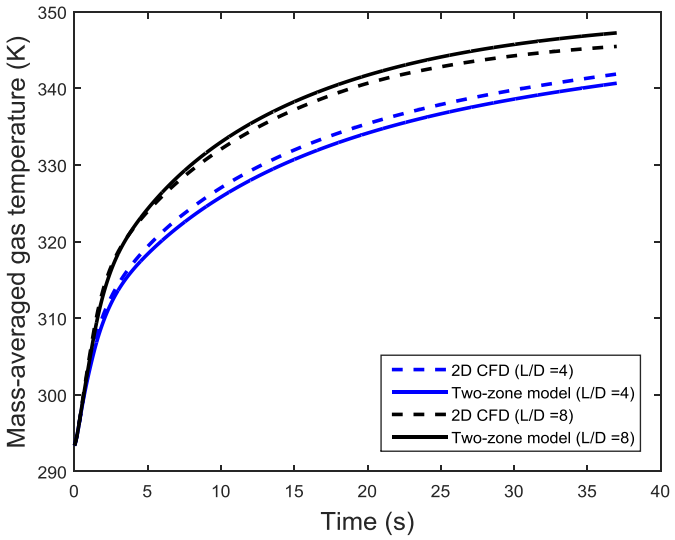

Figure 5.28: Comparison of the mass-averaged gas temperatures between the 2D CFD and the two-zone model including conjugate heat transfer for cylinders with L/D =4 and 8.

5.9 Effect of the viscous discharge coefficient (C_{d1})

In order to determine the sensitivity of C_{d1} on the final gas temperature and the final mass of gas, further simulations of the experiments of Dicken and Merida [7] were carried out using the single-zone model whereby C_{d1} was changed and kept at a constant of 1, 0.8, 0.6, 0.4 and 0.2 throughout the fill (Table 5.7). It should be noted that C_{d1} having a value of one, represents an isentropic flow through the delivery pipe.

Figure 5.29 shows the profile of the gas temperature during the fill with different values of C_{d1}. The results of the final mass and gas temperature at the end of the fill are shown in Table 5.5. Interestingly, the final gas temperature and the final mass of gas is mostly insensitive to the viscous discharge coefficient. While the final gas temperature is relatively unchanged with changing the values of C_{d1}, Figure 5.29 shows that decreasing the value of C_{d1}, lowers the initial rise in gas temperature at the start of the fill.

C_{d1}	Final temperature (K)	Final mass (kg)
Modelled	342.2	1.54
1	342.2	1.54
0.8	342.3	1.54
0.6	342.3	1.54
0.4	342.4	1.54
0.2	342.6	1.53

Table 5.5: Comparison of the final gas temperature and final mass of gas for different values of C_{d1}

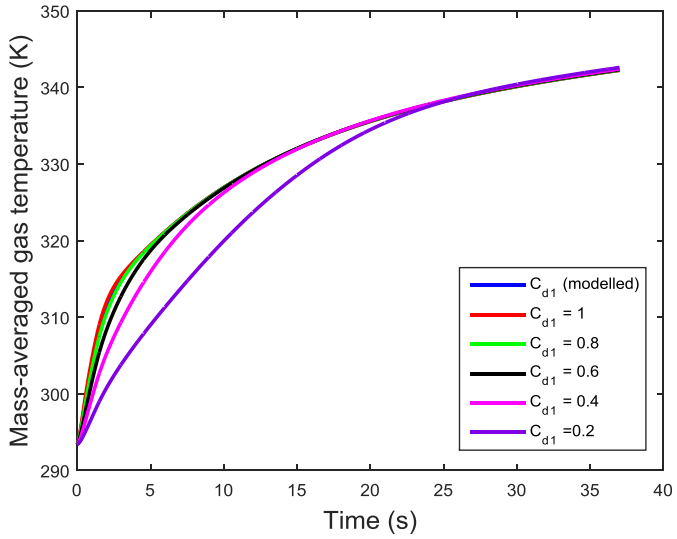

Figure 5.29: Comparison of the gas temperature profiles for different values of C_{d1}.

Figure 5.30 shows the profiles of the mass flow rate for the different values of C_{d1}.

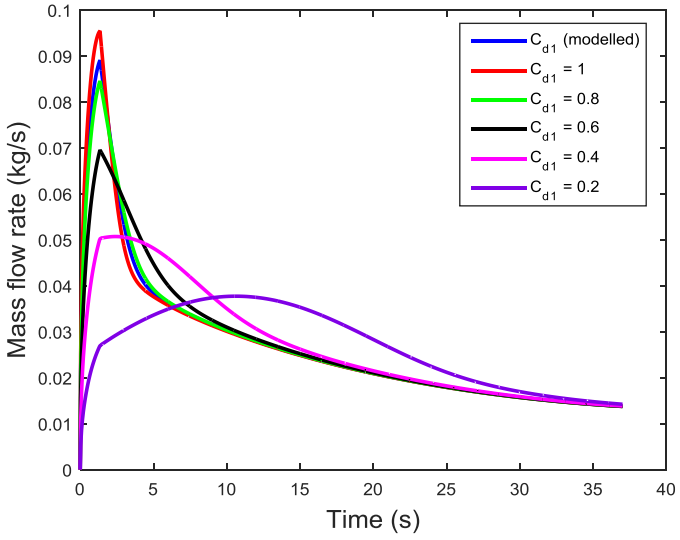

Figure 5.30: Comparison of the mass flow rate profiles for different values of C_{d1}

As shown in Figure 5.30, assuming isentropic flow thought the delivery pipe ($C_{d1} = 1$), results in a slight overestimation of the maximum value of the mass flow rate. On the other hand, a lower discharge coefficient decreases the peak value of the mass flow rate. However, the larger initial peaks in the mass flow rate that is inherent for cases with larger values of C_{d1} lead to larger initial gas pressures within the cylinder (Figure 5.31). Accordingly, this leads to a sharp decrease in the mass flow rate, which is due to a smaller difference between the upstream inlet pressure and the gas pressure.

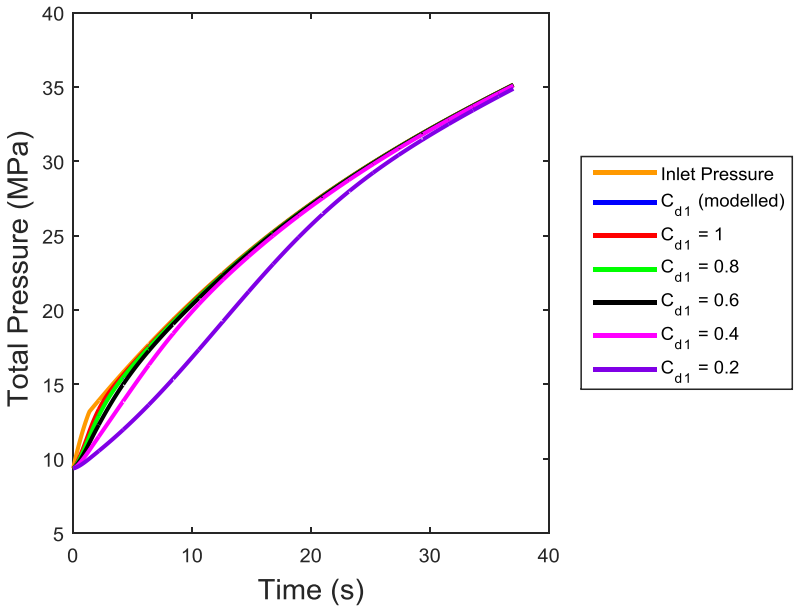

Figure 5.31: Comparison of the inlet pressure and gas pressures within the cylinder for different values of C_{d1}

5.10 Validation of the model

A review of the literature has shown that fast-filling experiments have only been performed on hydrogen cylinders whose L/D is less than 3. However, the 2D CFD model has shown its accuracy in predicting the rise in gas temperature during the filling of a hydrogen cylinder (*see Figure 4.11*). Thus, the assumption can be made that the two-zone model, which has been established for the cylinders having a L/D greater than 3.3 can be validated using the 2D CFD models. Hence, Figures 5.24-5.26 can be used as validation for the two-zone model.

Validation of the single-zone model was carried out by comparing the mass-averaged gas temperatures that were obtained from the model to the experiments during the fast-filling of hydrogen cylinders for the following cases:

1. Case A - The 45 second fill of Johnson et al. [30], which involves the fast-filling of a Type IV 39.6 L cylinder that has a L/D of 2.8 (Figure 5.32).
2. Case B – The 180 second fill of Zheng et al. [28], which involves the filling of a Type III 74.3 L cylinder that has a L/D of 2.5 (Figure 5.33). The material properties of the cylinder that were used in the single-zone model are shown in Appendix A11.
3. Case C – The 200 second fill of Baraldi et al. [27], which involves the filling of a Type IV 28.9 L cylinder that has a L/D of 2.9 (Figure 5.34).

The inlet boundary conditions for the 3 cases are shown in Appendix A12 and are implemented in the model for each of the respective cases. It should be noted that in their publications, both Johnson et al. [30] and Baraldi et al. [27] did not provide the material properties of the Type IV cylinder that was used in the respective experiment. Thus, the material properties of the Type IV cylinder of Alam et al. [86] were used in the single-zone model (*please refer to Appendix A11*).

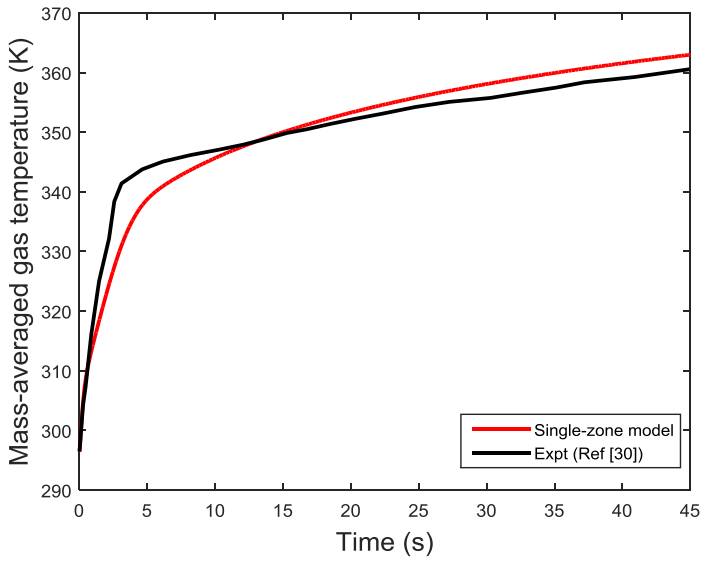

Figure 5.32: Comparison of the mass-averaged gas temperatures between the single-zone model and the experiment of Johnson et al. [30].

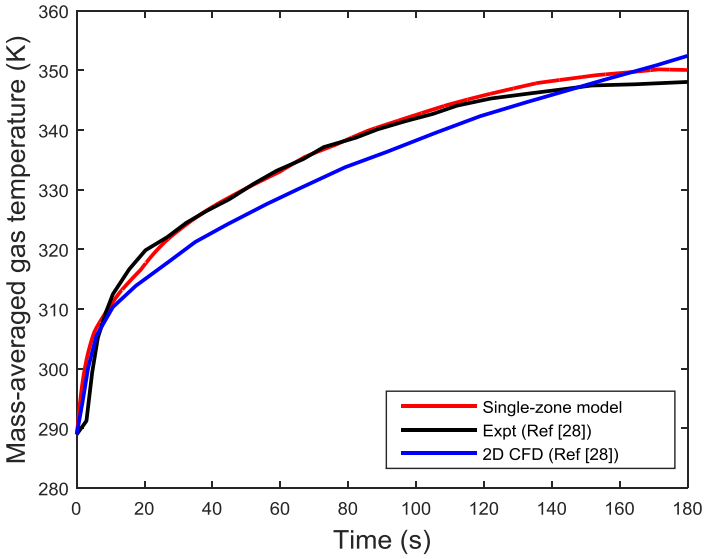

Figure 5.33: Comparison of the mass-averaged gas temperatures between the single-zone model and the experiment and 2D CFD model of Zheng et al. [28].

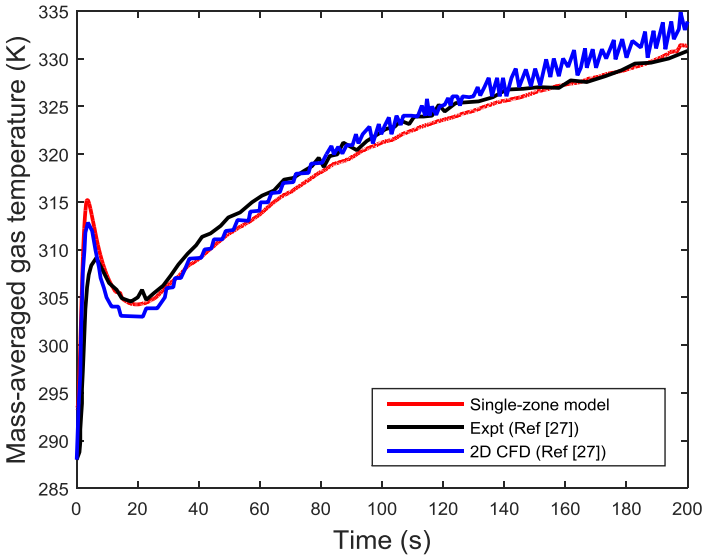

Figure 5.34: Comparison of the mass-averaged gas temperatures between the single-zone model and the experiment and 2D CFD model of Baraldi et al. [27].

As shown in Figures 5.32 – 5.34, the single-zone model accurately predicts the rise/profile of the gas temperatures in the cylinders with different volumes and material properties throughout the respective fills.

5.11 Effect of Natural convection

The single-zone and two-zone models only account for heat transfer due to forced convection. Natural convection, which is due to the possible density variation of the gas within the cylinder may be expected to play a role in heat transfer from the gas

to the structure of the cylinder especially for longer fill times. In order to determine the effect of heat transfer due to buoyancy for a longer fill time, the hydrogen filling case of Zheng et al. [28] was simulated to include the effect of natural convection in heat transfer. The empirical formula of Ranong et al. [65], which has also been validated by Johnson et al.[29], was used to determine the total heat transfer coefficient that is due to both the forced convection and the natural convection (Equation 3.24) for the 180 second fill. Figure 5.35 shows the heat transfer coefficient that is due to both forced and natural convection as well as the total heat transfer coefficient throughout the fill in accordance to the model of Ranong et al. [65].

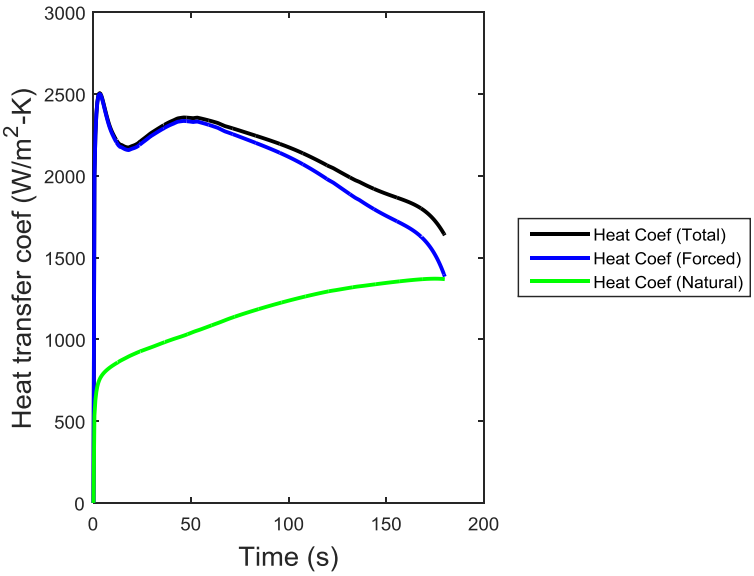

Figure 5.35: Profiles of the heat coefficients during the fill

As shown in Figure 5.35, the heat transfer coefficient due to forced convection is mostly dominant throughout the fill and is at its maximum at the beginning of the fill. The heat transfer due to natural convection increases throughout the fill as a result of the density gradients within the cylinder, but does not play a significant role in heat transfer. The gas temperature profiles obtained by the single-zone model that is based on the hydrogen filling experiment of Zheng et al. [28] with and without heat transfer due to natural convection overlap each other (Figure 5.36). This further confirms that heat transfer due to buoyancy effects is negligible even for longer fill times of 180 seconds.

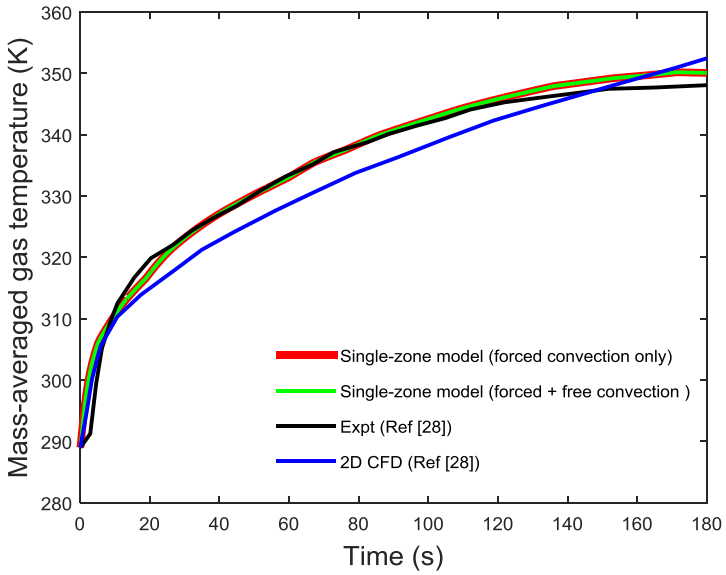

Figure 5.36: Comparison of the mass-averaged gas temperatures with and without natural convection.

5.12 Inclusion of a phase change material (PCM)

The single-zone model is used to determine the effect of PCMs as part of the structure of the cylinder of the fast-fill case of Dicken and Merida [7]. Two different types of PCMs are used in the simulations in order to determine the effect of the thermal conductivity of the phase change material on the gas in the cylinder during the fill:

1. Paraffin wax (PCM-1) that has a low thermal conductivity [76].
2. Paraffin wax embedded with graphite matrices (PCM-2), which has a much higher conductivity [77].

The material properties of PCM-1 and PCM-2 are displayed in 5.6.

Material property	**PCM-1**	**PCM-2**
Melting range (K)	316-329	308-328
Heat of fusion (KJ/kg)	266	185
Liquid specific heat (KJ/kg)	2.51	1.98
Solid specific heat (KJ/kg)	2.95	1.98
Liquid thermal conductivity (W/m K)	0.24	16.6
Solid thermal conductivity (W/m K)	0.24	16.6
Liquid density (kg/m^3)	760	731
Solid density (kg/m^3)	818	789

Table 5.6: Material properties of PCM-1 and PCM-2 [76, 77].

The comparison of the final gas temperature for the 37 second fill with different thickness of PCM-1 and PCM-2 placed in between the liner and laminate is shown in Figure 5.37. The presence of PCM-1 due to its low thermal conductivity, which inhibits heat transfer from the gas to the walls of the cylinder and increases the final gas temperature by 1.7 K. On the other hand, PCM-2 with its higher thermal conductivity, leads to an in heat transfer from the gas to the structure of the cylinder and lowers the final gas temperature as its thickness increases. Since the final gas pressure is similar in all cases, the drop in the final gas temperature due to the presence of PCM-2 leads to an increase in the final mass of gas (Figure 5.38).

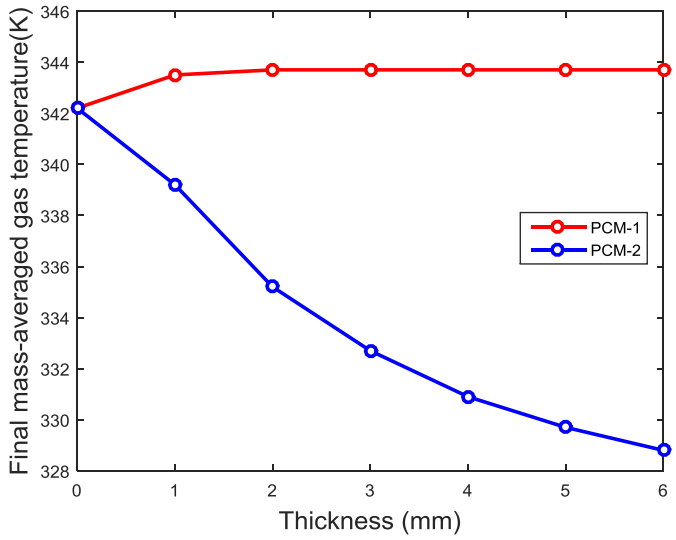

Figure 5.37: Comparison of the final gas temperature with PCM thickness for PCM-1 and PCM-2.

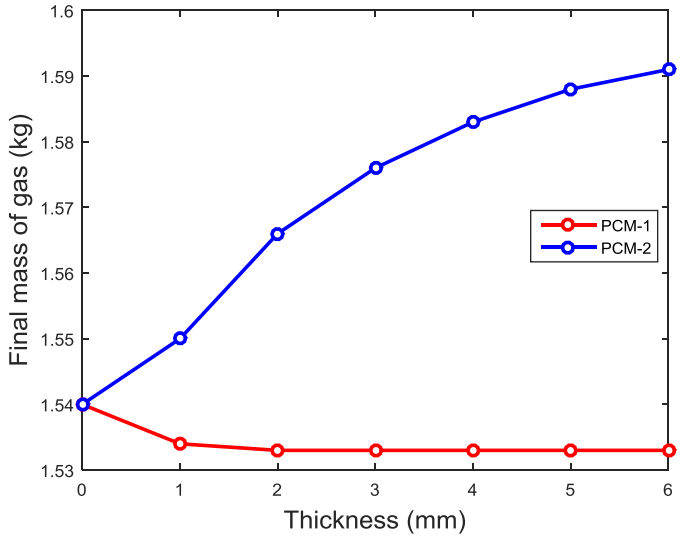

Figure 5.38: Comparison of the final mass of gas with PCM thickness for PCM-1 and PCM-2.

However, the presence of a PCM as part of the structure of the cylinder leads to an increase in its structural mass. The ratio of the final mass of gas to the structural mass of the cylinder decreases with the thickness of the PCM in both cases (Figure 5.39). Even though the presence of PCM-2 has shown an increase in the final mass of gas, the additional mass of gas does not compensate for the additional structural mass of the cylinder.

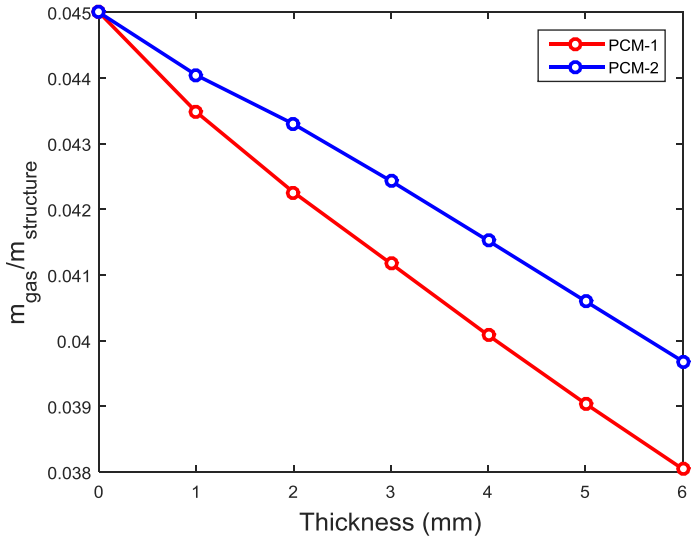

Figure 5.39: Ratio of the final mass of gas to the structural mass with PCM thickness for PCM-1 and PCM-2.

The largest drop in the final gas temperature is observed when the thickness of PCM-2 changes from 1 mm to 2 mm (Table 5.7). Thus, as a trade-off between the drop in the final gas temperature and an increase in the structural mass of the cylinder, PCM-2 having thickness of 2 mm between the liner and the laminate is chosen for further investigations for temperature control for the fast-filling of hydrogen cylinders.

Thickness increase	Drop in gas temperature
0 mm - 1 mm	3 K
1 mm - 2 mm	4 K
2 mm - 3 mm	2.5 K
3 mm - 4 mm	1.8 K
4 mm - 5 mm	1.2 K
5 mm - 6 mm	0.9 K

Table 5.7: Drop in gas temperature with increase in PCM-2 thickness

5.13 Summary

The results showed that viscous discharge coefficient C_{d1} is mostly independent of isentropic Mach number and increases with the isentropic Reynolds number. Two different relationships were obtained for C_{d1} with respect to the isentropic Reynolds numbers for the choked and unchoked conditions of a pipe with the length-to-diameter ratio of 28.6. Simulations that were performed at high pressures, have also shown that real gas effects have no impact on C_{d1}.

The model for the fast-filling of hydrogen cylinders can be split into 2 categories:

1. A single-zone model for cylinders whose L/D is less than 3.3.
2. A two-zone model for cylinders whose L/D is greater than 3.3.

The model has been developed for the fast-filling of cylinders for the following cases:

- $1.5 \leq \left({}^{L}/_{D}\right)_{cyl} \leq 8$
- $11.5 \leq \frac{D_{cyl}}{D_{inlet}} \leq 86.4$

The models have shown that the viscous discharge coefficient does not affect final gas temperature and final mass of gas. The single-zone model has further been validated as it is capable of accurately predicting the rise in the gas temperature for both Types III and IV cylinders that have different geometries ($2.4 \leq L/D \leq 2.9$) and different volumes (24.8 L, 39.6 L and 74 L).

The model has also demonstrated that heat transfer due to forced convection is dominant during the fast-filling of a cylinder. Thus, the effect of heat transfer through natural convection is minimal during the fast-fill and can be neglected in future simulations.

Simulations of the fast-fill that included phase change materials as part of the structure of the cylinder have unveiled the following:

- The inclusion of a phase change material with high conductivity is advantageous in lowering the final gas temperature which subsequently increases the final mass of gas.

- However, the inclusion of a PCM increases the structural mass of the cylinder. A PCM thickness of 2 mm lodged in between the liner and laminate represents a trade-off between enhancing heat transfer, which lowers the gas temperature and the rising structural mass of the cylinder.

6 Modelling of the fast-filling station

6.1 Introduction

This chapter includes the modelling of the fast-filling stations for both hydrogen and CNG light duty vehicles. In the United States, the Environmental Protection Agency (EPA) currently limits the fuel dispenser rates in petrol filling stations to 10 US gallons per minute [87]. As result, the refuelling time for a conventional light duty petrol vehicle such as the 2015 Audi Quattro, which has a tank size of 14.5 US gallons is approximately two and a half minutes. Currently, the fill time of gas powered vehicles (hydrogen and CNG) is between three and five minutes using fast-fill technologies [10]. One of the factors that would deter consumers from switching from conventional gasoline powered cars to CNG/H_2 vehicles would be a slower refuelling process. The feasibility of a fast-fill of approximately one minute as opposed to the conventional 3 to 5 minutes is addressed along with pre-cooling strategies and the use of a phase change material (PCM-2) as part of the structure of the cylinder.

6.2 Hydrogen fast-filling station

This section of the current chapter involves the fast-filling of the 2016 Toyota Mirai, which is a recently developed hydrogen subcompact vehicle. The product information of the vehicle is shown in Table 6.1 [20].

Number of cylinders	2
Cylinder type	IV
Maximum Filling pressure	87.5 MPa
Normal operating pressure	70 MPa
Internal volume (Front)	60 L
Internal volume (Rear)	62.4 L
Total storage mass	~ 5 kg
Refuelling time	3 – 5 mins
Range of vehicle	~ 330 miles

Table 6.1: Product info of the 2016 Toyota Mirai [20].

The material properties as well as the thicknesses of the liner and laminate of the cylinders were not listed in the vehicle manual. In addition, the L/D of the cylinders

were not provided. In the single-zone model, the material properties of the 70 MPa Type IV cylinder of Alam et al. [86] were used (*please refer to Appendix A11*) and the liner and laminate thicknesses were similarly set to 4 mm and 36 mm respectively [86]. The inlet diameter and the L/D of both cylinders were respectively set to 5 mm and 2.4, similar to the fast-filling experiment of Dicken and Merida [7].

Figure 6.1 shows the schematic diagram of a hydrogen fast-fill station during the refuelling of the 2016 Toyota Mirai.

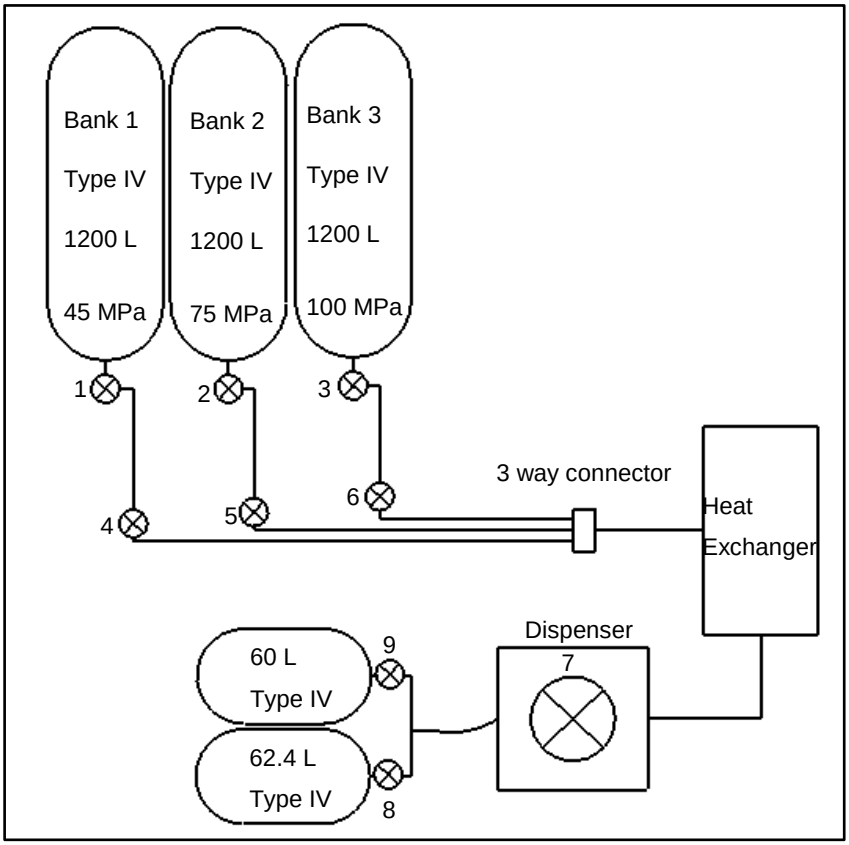

Figure 6.1: Schematic diagram of a hydrogen filling station.

The station consists of three pressure banks: a low pressure bank at a pressure of 45 MPa, a moderately high pressure bank at a pressure of 75 MPa and a high pressure bank at a pressure of 100 MPa. The chosen pressure of 100 MPa for the high pressure bank was based on Ball and Witsel [92], who suggested that for the filling of vehicles that are fitted with 70 MPa cylinders, stationary storage of hydrogen of at least 100 MPa is required. The fast-filling of the 60.0 L and 62.4 L cylinders involves a cascade process. The gas flows from the low pressure bank (Bank 1) and once gas pressure at the entrance of the dispenser is equal to pressure profile set by the pressure control valve of the dispenser, the system immediately switches to the moderately high pressure bank (Bank 2), i.e. valve 4

closes and valve 5 opens. Similarly, once the pressure of the gas (from Bank 2) at the entrance of the dispenser is equal to the pressure profile of the dispenser, filling switches to Bank 3 to cap off the fill. In the current model, the volume of all three banks were set to 1200 L, which corresponds to the largest volume of banks that were used in the experiments of Woodfield et al. [30].

The station also consists of a heat exchanger whose purpose is to cool the incoming gas from the banks to a pre-set temperature. The gas is then fed to the dispenser that consists of a pressure control valve that creates a pressure profile and the gas is delivered into the 60.0 L and 62.4 L cylinders of the Toyota Mirai. The piping system that delivers the gas from the banks to the cylinder also consists of the following:

1. The quarter turn valves (valves 1, 2, 3).
2. The ball valves (valve 4, 5 and 6).
3. The pressure control valve of the dispenser that sets a particular pressure profile (valve 7).
4. A series of 90° bends (4 in total) and a three way connector (pressure losses at the 3 way connector is modelled as a 45° bend).

The model is set up to determine the pressure drop that occurs across of all of the components listed above. However, it should be noted that in the current model, the pressure drop across the heat exchanger and heat transfer in the piping system are both neglected. Valves 8 and 9 are located at the inlet of both cylinders and are not modelled since it has already been pre-determined that the discharge coefficient does not affect the final gas temperature and the final mass of gas (*please refer to Table 5.5*). The discharge coefficient (Equation 5.4) for a straight delivery pipe with length-to-diameter ratio of 28.6 was implemented in the current model. However, as shown in Chapter 5, the discharge coefficient does not affect the final mass and gas temperature.

According to the National Fire Protection Association [61], the internal diameters of pipes for hydrogen and CNG delivery in filling stations can vary between 8 mm and 50 mm. Thus, the internal diameter of the interconnecting pipes in the model was set to 10 mm. Since no current data is currently available regarding the geometry of a hydrogen filling station, the length of the pipe between the banks to

the dispenser was arbitrarily set to 20 m. The delivery of the gas from the banks to the main pipe occurs through a pipe having a diameter of 5 mm that protrudes into the banks and is connected to the main pipe by an angle valve. The length of the pipe that protrudes into the bank was set to 8.2 mm, similar to cylinder filling case of Dicken and Merida [7].

The model is set up in such a way that the filling is stopped if one of the following occurs:

1. The state of charge (SOC) in either one of the cylinders reaches 100 %.
2. The gas pressure within either one of the cylinders is 1.5 times the normal operating pressure of 70 MPa.
3. The gas temperature in either cylinder reaches the 358 K limit.

Initial pressure condition

The simulations that were performed involve the filling of both the 60 L and 62.4 L cylinders in parallel starting from initial pressures of 2.0 MPa, which according to the hydrogen filling protocol SAE J2601 [17] is a condition that corresponds to an almost empty tank.

Outer wall boundary conditions

In the current model, adiabatic conditions are applied to the outer wall for the two cylinders in the vehicle as well as the three high pressure banks. It is assumed that the cylinders in the vehicles and the banks in the filling station are in an enclosed environment and heat exchange with the environment is negligible during the period of filling.

6.2.1 Refuelling at a pressure ramp rate of 28.5 MPa/min

The model was initially tested for the filling of both cylinders with the gas being delivered by the dispenser at a pressure ramp rate of 28.5 MPa/min (Figure 6.2), which corresponds to an approximate fill time of 180 seconds. The fill time of 180 seconds was chosen since it corresponds to the fastest of the typical fill times, which usually vary between three and five minutes The initial/ambient temperature was set to 293 K and the filling was performed with pre-cooling temperatures of 233 K, 243 K and 253 K, which are similar to the pre-cooling temperatures that are

mentioned in SAE J2601 [17]. Additionally, the filling was also performed without any pre-cooling to determine the benefits of lowering the gas temperature prior to being delivered to cylinders.

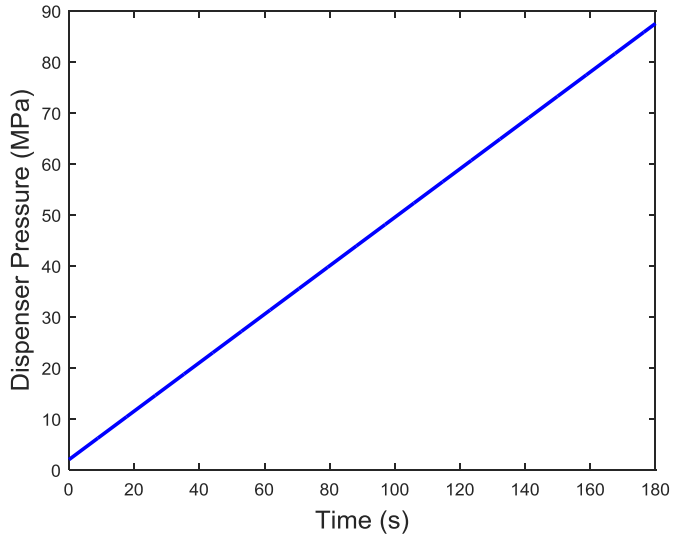

Figure 6.2: Pressure profile at the dispenser (Ramp rate of 28.5 MPa/min).

Figure 6.3 shows the gas temperature that was obtained for all four cases.

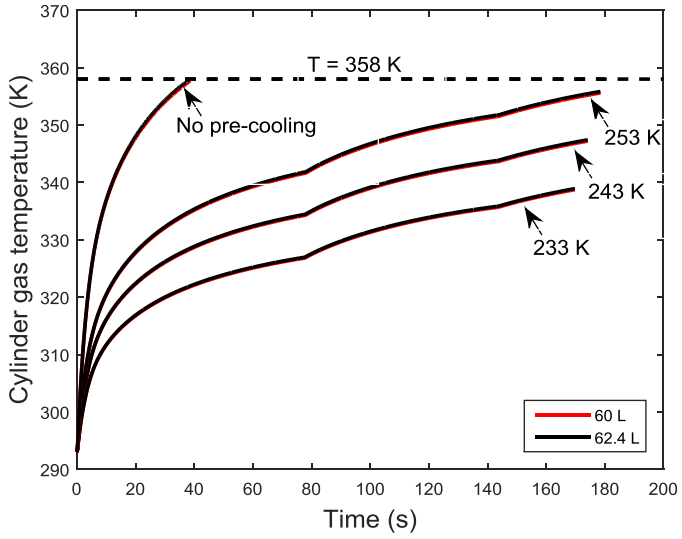

Figure 6.3: Gas temperature profiles in the cylinders with a ramp rate of 28.5 MPa/min with pre-cooling and no pre-cooling (ambient temperature = 293 K).

The lack of pre-cooling results in the gas temperatures in the cylinders reaching the maximum allowable limit of 358 K within 50 seconds into the fill. This leads to the cylinders being only 30 % full, and the final mass of gas is 1.52 kg when the filling is stopped. The fill times as well as the pressures, the SOC and the mass of gas at the end of the fills of both cylinders for the 4 cases are shown in Table 6.2.

Pre-cooling temperature	Cylinder volume	Final Pressure	Final mass		Fill time	SOC
233 K	60.0 L	82.6 MPa	2.41 kg	4.92 kg	170 s	100 %
	62.4 L	82.6 MPa	2.51 kg			100 %
243 K	60.0 L	84.7 MPa	2.41 kg	4.92 kg	174 s	100 %
	62.4 L	84.7 MPa	2.51 kg			100 %
253 K	60.0 L	86.8 MPa	2.41 kg	4.92 kg	179 s	100 %
	62.4 L	86.8 MPa	2.51 kg			100 %
None	60.0 L	20.4 MPa	0.78 kg	1.53 kg	-	30.7 %
	62.4 L	20.4 MPa	0.75 kg			30.7 %

Table 6.2: Fill times and the final state of the gas at the end of the fill for the four different cases (ramp rate = 28.5 MPa/min & ambient temperature = 293 K).

As shown in Table 6.2, a state of charge (SOC) of 100 % is reached for both cylinders in the pre-cooling cases and is the parameter that stops the filling. In addition, the final gas pressures in both cylinders are all below the maximum allowable limit of 87.5 MPa for all three pre-cooling cases. The total final mass of gas in all three pre-cooling cases are similar and have a value of 4.92 kg and is comparable to the final mass of gas of approximately 5 kg that is stated in the car manual [20] of the 2016 Toyota Mirai. A slight 'bump' in gas temperature occurs in the two cylinders whenever the gas being discharged from the banks is switched from the lower pressure banks to the higher pressure banks during the cascade process. This is due to the increase in the gas temperature at the exit of the dispenser (Figure 6.4). In the four cases, the gas temperature in the 60.0 L and the 62.4 L cylinders is mostly similar during the respective fills. Thus, for convenience, only the results for the filling of the 60 L cylinder is further addressed in this report.

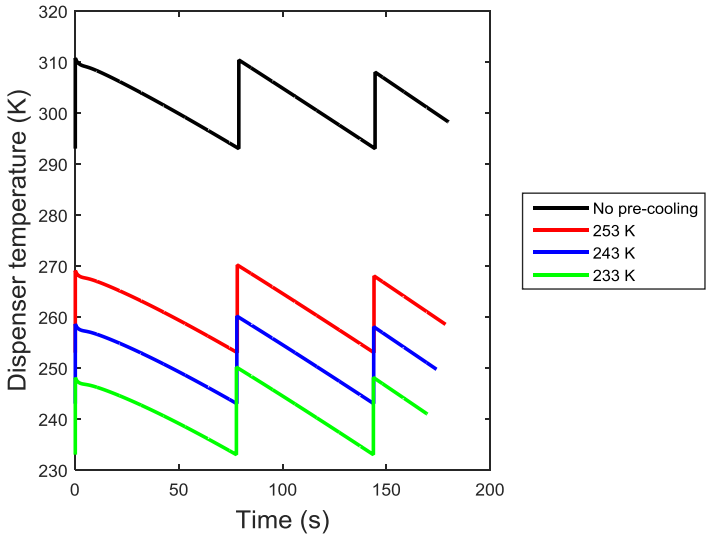

Figure 6.4: Gas temperature at the exit of the dispenser with pre-cooling and no pre-cooling (ramp rate = 28.5 MPa/min & ambient temperature = 293 K).

As shown in Figure 6.4, the gas temperature at the exit of the dispenser increases step-wise in all four cases following the switching of the banks and is followed by a constant decrease at three different times. The pressure drop that occurs at the dispenser explains this phenomenon. Since flow across the pressure control valve is isenthalpic, the drop in pressure results in a rise in temperature due to the negative Joule-Thompson coefficient of hydrogen at the given temperatures and pressures. The pressure drop across the pressure control valve of the dispenser is larger at the beginning of the discharge of the gas from the respective banks and explains the rise in the gas temperature at the exit of the dispenser upon switching of the banks. Figure 6.5 shows the pressure drop (pre-cooling case of 233 K) that occurs across the pressure control valve of the dispenser as well as within the piping network before the dispenser.

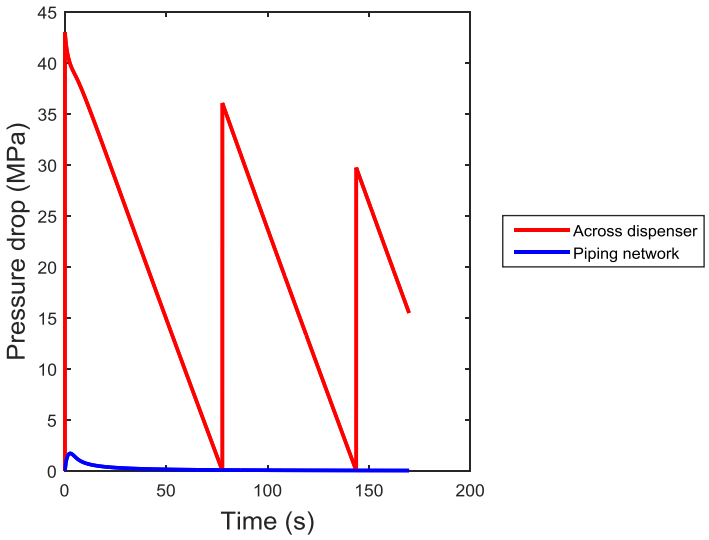

Figure 6.5: Pressure drop across the dispenser and piping network with pre-cooling temperature of 233 K (ramp rate = 28.5 MPa/min & ambient temperature = 293 K).

As shown in Figure 6.5, the pressure drop across the dispenser is significantly larger throughout the fill than the pressure drop across the piping network. The pressure drop across the dispenser reaches a value of zero when the pressure at entrance of the dispenser is equal to the pressure profile imposed by the dispenser upon which, filling is proceeded by switching to the higher pressure bank. The switching from the low pressure bank to the higher pressure bank explains the instantaneous rise in the pressure drop once its value reaches zero, since the gas pressure at the entrance of the dispenser is now significantly larger than the pressure profile being imposed by the dispenser.

In the piping network most of the pressure drop occurs due to friction in main pipe that delivers the gas from the banks to the dispenser (Figure 6.6). In addition to the other components of the piping system (valves, bends and connector), the pressure drop due the expansion of the pipe diameter from 5 mm to 10 mm as the gas flows from the delivery pipe that protrudes into the banks and into the main pipe were found to be insignificant. Similarly, the pressure drop due to the presence of the 5 mm delivery pipe in the banks is negligible.

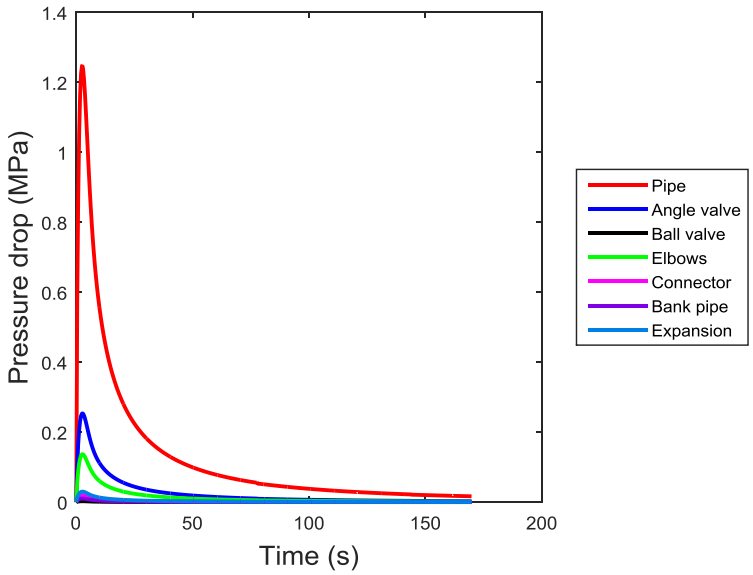

Figure 6.6: Pressure drop due to the components in the piping system with pre-cooling temperature of 233 K (ramp rate = 28.5 MPa/min & ambient temperature = 293 K).

The discharge of the gas from the banks and into the cylinders, leads to a drop in the gas pressure within the banks (Figure 6.7). The drop in pressure leads to the isentropic cooling of the gas and subsequently a drop in the gas temperature (Figure 6.8). When filling is switched from the low pressure banks to high pressure banks, a small rise in the gas temperature is observed in the banks at lower pressures, which is due to the heat transfer as a result of natural convection from the walls of the cylinder to the gas.

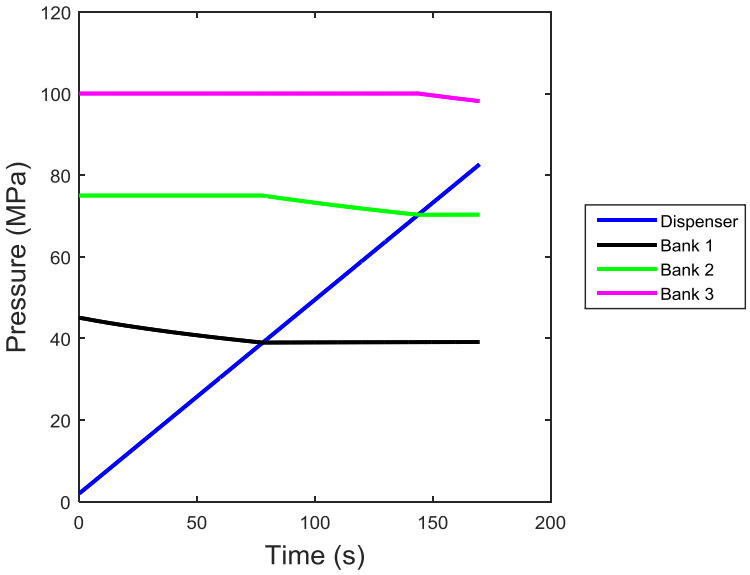

Figure 6.7: Bank Pressures and dispenser pressure during the fill with pre-cooling temperature of 233 K (ramp rate = 28.5 MPa/min & ambient temperature = 293 K).

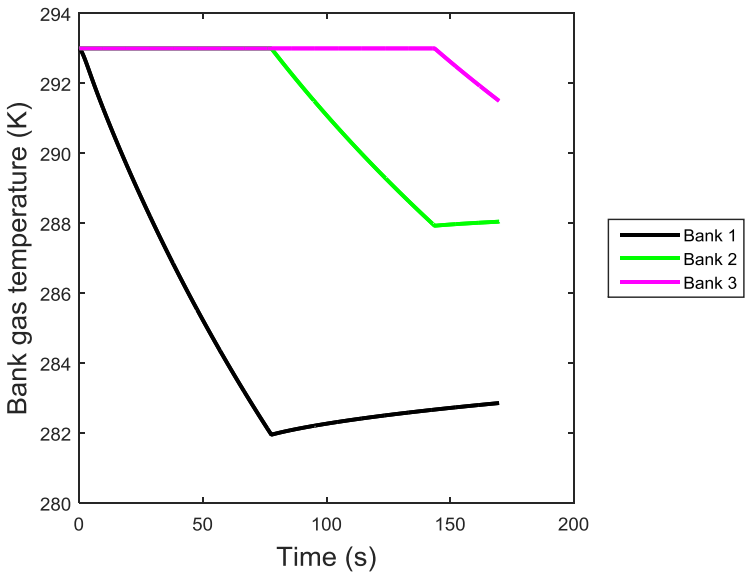

Figure 6.8: Bank temperatures during the fill with the pre-cooling temperature of 233 K (ramp rate = 28.5 MPa/min & ambient temperature = 293 K).

6.2.2 Increasing the pressure ramp rate

Further studies were performed in which the pressure ramp rate at the exit of the dispenser was increased in order to determine if the fill can be achieved faster without exceeding the maximum allowable limit of 358 K. In order to determine if a full fill can be achieved without exceeding the 358 K limit, the code was slightly modified such that the filling does not stop if the 358 K threshold was reached. The filling is stopped if one of the following occurs:

1. The state of charge (SOC) in either one of the cylinders reaches 100 %.
2. The gas pressure within either one of the cylinders is 1.5 times the normal operating pressure of 70 MPa.

A full fill is achieved only if the SOC in the cylinders is 100 %. Thus, if the fill exceeds the 358 K limit, this implies that a full fill has not been achieved below that particular temperature threshold.

The ramp rates that were considered and the expected approximate fill times are displayed in Table 6.3.

Ramp Rate	Expected fill time
28.50 MPa/min	~ 180 s
34.20 MPa/min	~ 150 s
47.75 MPa/min	~ 120 s
57.00 MPa/min	~ 90 s
85.50 MPa/min	~ 60 s

Table 6.3: Pressure ramp rate and expected fill times.

The simulations were performed whereby the ambient temperature was set to 293 K, with pre-cooling temperatures of 233 K, 243 K and 253 K, which are similar to the standards of pre-cooling temperatures for hydrogen refuelling in accordance to the SAE TIR J2601 [17]..

Figures 6.9, 6.10 and 6.11 respectively show the gas temperature profiles during the filling of the 60 L cylinder at the different ramp rates with pre-cooling temperatures of 233 K, 243 K and 253 K.

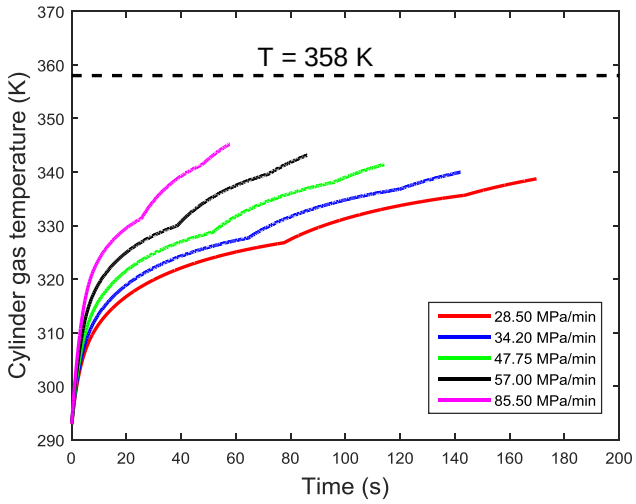

Figure 6.9: Gas temperature profiles in the 60 L cylinder at different ramp rates with pre-cooling temperature of 233 K (ambient temperature = 293 K).

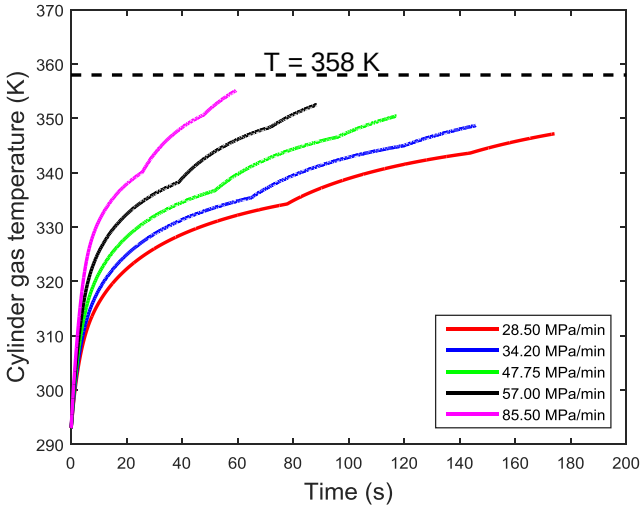

Figure 6.10: Gas temperature profiles in the 60 L cylinder at different ramp rates with pre-cooling temperature of 243 K (ambient temperature = 293 K).

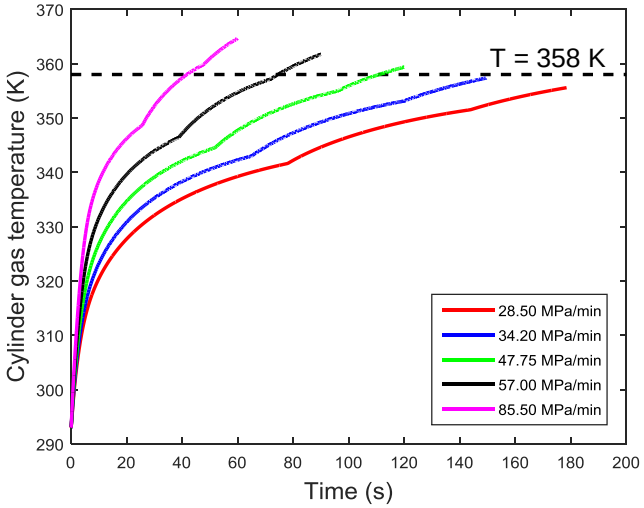

Figure 6.11: Gas temperature profiles in the 60 L cylinder at different ramp rates with pre-cooling temperature of 253 K (ambient temperature = 293 K).

Increasing the pressure ramp rate leads to a rise the final gas temperature for all three pre-cooling cases. With pre-cooling temperatures of 233 K and 243 K, the final gas temperatures in the 60 L cylinder are below the limit of 358 K for all five of the pressure ramp rates and a full fill is achieved. However, for the pre-cooling case of 253 K, a full fill is only accomplished below the 358 K limit when the ramp rates are 34.20 MPa/min and lower. Increasing the pressure ramp rate also increases the pressure drop within the series of interconnected pipes, valves and other components (Figure 6.12).

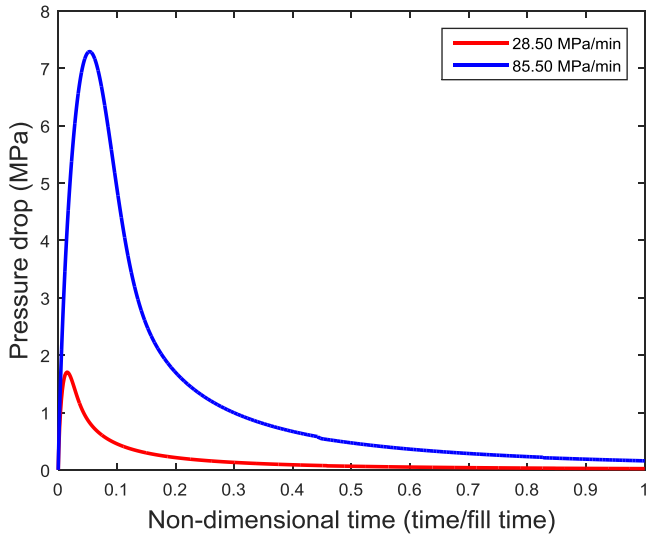

Figure 6.12: Pressure drop across the piping system for pressure ramp rates of 28.5 MPa/min & 85.5 MPa/min (pre-cooling temperature = 233 K, ambient temperature = 293 K).

This increase in the pressure drop indicates that with a higher pressure ramp rate, more gas is required from the highest pressure bank (Bank 3) to complete the fill. The final pressures of bank 3 for both pressure ramp rates are shown in Table 6.4.

Ramp rate	Bank 3 final pressure
28.5 MPa/min	98.1 MPa
85.5 MPa/min	97.9 MPa

Table 6.4: Final pressure in bank 3 for pressure ramp rates of 28.5 MPa/min and 85.5 MPa/min.

The gas pressure at the entrance of the dispenser must be greater than at its exit all times during the fill to maintain the delivery pressure. The gas pressure at the entrance of the dispenser is the gas pressure of the banks subtracted by the pressure drop in the piping system. As expected, the difference in pressure between the banks and at the entrance of the dispenser is at its maximum at the

beginning of the fill due to the larger pressure drop that occurs at the start of the fill (Figure 6.13).

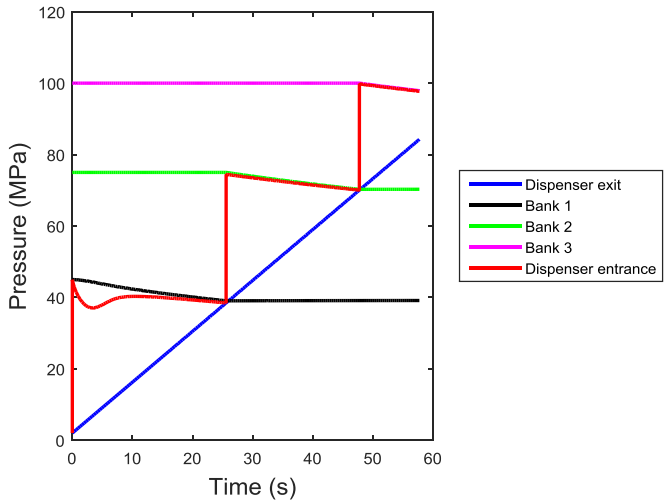

Figure 6.13: Pressure profiles of the banks and at the entrance and exit of dispenser for pressure ramp rate of 85.5 MPa/min (pre-cooling temperature = 233 K, ambient temperature = 293 K).

Further simulations of the fast-filling of the Toyota Mirai were performed for the different gas delivery profiles from Table 6.3 to determine the least amount of pre-cooling that is required to accomplish a safe and full fill of the cylinders over a range of ambient temperatures (273 K, 293 K and 313 K). Figure 6.14 shows the least amount of pre-cooling required to achieve a safe fill for the different pressure profiles at different ambient temperatures. The y-axis of Figure 6.14 is a measure of the amount of pre-cooling required, which is the difference between the ambient temperature and pre-cooling temperature.

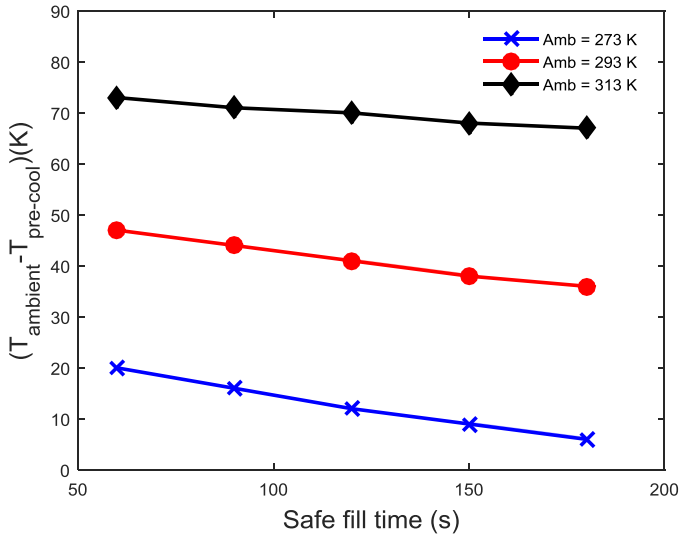

Figure 6.14: Amount of pre-cooling required to achieve a safe fill for the different ambient temperatures.

As shown in Figure 6.14, the least amount of pre-cooling is required when the ambient temperature is the lowest and the fill time is the longest. Table 6.5 shows the maximum pre-cooling temperature and the corresponding fill time for the different dispenser pressure profiles at an ambient temperature of 293 K.

Ramp Rate	Fill time	Ambient temperature	Maximum pre-cooling temperature
28.50 MPa/min	180 s	293 K	257 K
34.20 MPa/min	150 s	293 K	255 K
47.75 MPa/min	120 s	293 K	252 K
57.00 MPa/min	90 s	293 K	249 K
85.50 MPa/min	60 s	293 K	246 K

Table 6.5: Maximum pre-cooling temperature to achieve a full and safe fill for the different delivery pressure ramp rates (Ambient temperature = 293 K).

Figure 6.15 shows the gas temperature profile in the 60 L cylinder during the fill at an ambient temperature of 293 K, different ramp rates and the corresponding maximum pre-cooling temperatures in parentheses.

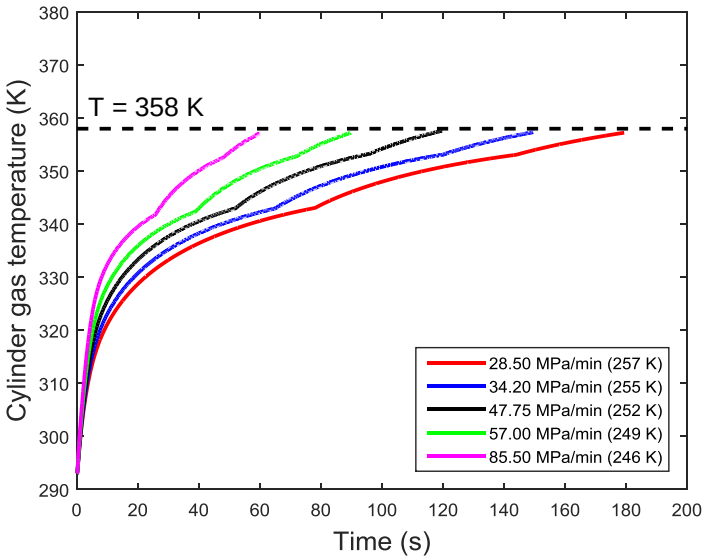

Figure 6.15: Gas temperature profiles in the 60 L cylinder at different ramp rates with maximum pre-cooling temperature (ambient temperature = 293 K).

As shown in Figure 6.15, the final gas temperatures in the cylinder for all five delivery pressure profiles are slightly below the maximum allowable temperature limit of 358 K. This confirms that a full fill in the cylinder is achieved (100% SOC) for the various pressure profiles at the corresponding maximum pre-cooling temperatures.

6.2.3 Type III v/s Type IV cylinder

The material properties of the liner in the 60.0 L cylinder were switched from plastic to an aluminium alloy similar to the Type III cylinder of Dicken and Merida [7]. A fast-fill using the similar pressure profiles was performed in the Type III cylinders with the same ambient temperature of 293 K and the corresponding maximum pre-cooling temperatures from Table 6.5 to determine the effect of material properties on the fill time and final mass of gas. Figure 6.16 shows that at the given established maximum pre-cooling temperatures for Type IV cylinders, a full fill is also achieved in the Type III cylinder and the final gas temperature for all 5 cases are approximately 8 K below the 358 K limit.

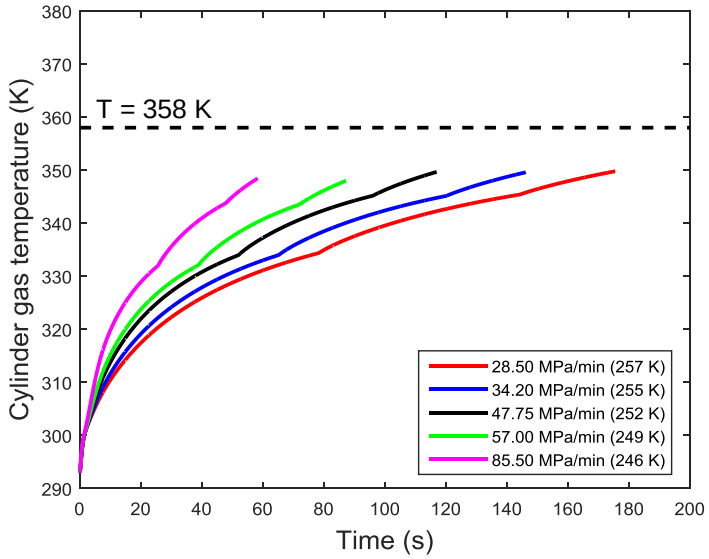

Figure 6.16: Gas temperature profiles in the 60 L Type III cylinder at different ramp rates at an ambient temperature = 293 K (pre-cooling temperatures in parentheses).

Thus, higher pre-cooling temperatures can be used for the complete fill of the Type III cylinder while still keeping the gas temperature below the 358 K. Figure 6.17 compares the maximum required pre-cooling temperatures that leads to a full fill in the Type III and IV cylinders at an ambient temperature of 293 K for the different delivery pressure ramp rates. The higher thermal conductivity and capacity of the aluminium liner of the Type III cylinder as opposed to the plastic liner of the Type IV cylinder increases heat transfer from the gas to the structure of the cylinder and lessens the need for lower pre-cooling temperatures. For a complete fill in Type IV cylinders, lower pre-cooling temperatures are required (Figure 6.17).

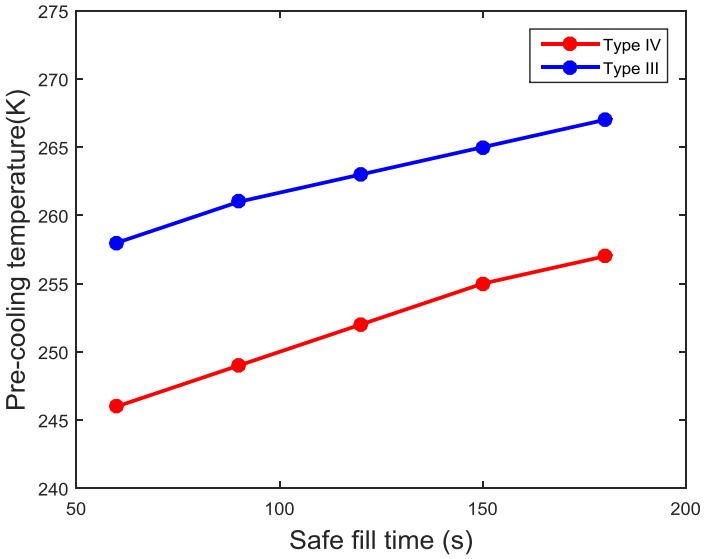

Figure 6.17: Comparison of the maximum pre-cooling temperatures for the Type III and IV cylinders at an ambient temperature of 293 K for the different fill times.

Figure 6.18 compares the gas temperature profiles versus the mass of gas in the 60 L Type III and IV cylinder as well as for an adiabatic case in which no heat is being transferred from the gas to the structure of the cylinder. The simulations were performed with the pressure ramp rate at the inlet set to 85.50 MPa/min, at an ambient temperature of 293 K and the pre-cooling temperature set to 258 K, which are the conditions for a complete 60 second fill in the Type III cylinder.

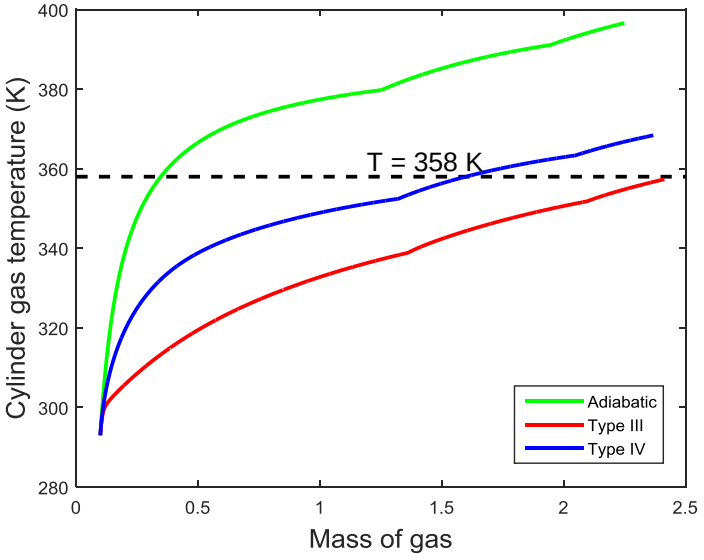

Figure 6.18: Gas temperature profiles v/s mass of gas in Types III & IV 60 L cylinder as well as the adiabatic case (pre-cooling temperature = 258 K, ramp rate = 85 MPa/min & ambient temperature = 293 K).

As shown in Figure 6.18, heat transfer from the gas to the structure of the cylinder is essential for the full fill while maintaining the gas temperature below the 358 K limit.

6.2.4 Inclusion of the phase change material

It has been established from Figure 6.15 that the full fill of the Toyota Mirai with Type IV at an ambient temperature of 293 K can be accomplished in sixty seconds by pre-cooling the gas to 246 K. Switching the cylinders from Type IV to Type III leads to an increase in the pre-cooling temperature to 258 K for a full fill at sixty seconds (Figure 6.17). However, pre-cooling of the gas requires an additional amount of energy. Thus, the higher the pre-cooling temperature, less energy is required and the fast-filling of the hydrogen vehicle will be cheaper.

The introduction of a phase change material to the structure of a cylinder has already been discussed in chapter 4, in which it was determined that a solid-liquid phase change material of high conductivity (PCM-2) that has a thickness of 2 mm and placed in between the liner and the laminate is the most effective in lowering the gas temperature during the a fast-fill. Fast-fill simulations were performed in which PCM-2 at a thickness of 2 mm was included in between the liner and the laminate of both the 60 L and 62.4 L cylinders of the Toyota Mirai. Two different types of liners were considered: plastic (Type IV cylinder) and aluminium alloy (Type III cylinder). The simulations were carried out at an ambient temperature of 293 K and the pressure ramp rate the exit of the dispenser was set to 85.50 MPa/min, with the pre-cooling temperature set to 258 K. It should be noted that the pre-cooling temperature of 258 K was chosen since it represented the maximum pre-cooling temperature for the full fill of the Type III cylinder when the delivery pressure ramp rate is set to 85.50 MPa/min.

Figure 6.19 compares the gas temperature profiles versus the mass of gas in the 60 L Type III and IV cylinder with and without the presence of PCM-2 that has a thickness of 2 mm between the liner and the laminate during their respective fills. A full fill in the Type IV cylinder is not achieved below the 358 K limit. The presence of PCM-2 between the plastic liner and laminate barely lowers the gas temperature during the fill with a difference of 2 K observed in the final gas temperatures. This is due to the low thermal conductivity of the plastic liner, which acts as an obstacle

for heat transfer from the gas to the phase change material during the fill (Figure 6.20). The presence of PCM-2 to the structure of the Type III cylinder lowers the final gas temperature by approximately 5 K. The aluminium liner with its high thermal conductivity does not act as a barrier for heat transfer from the gas to the PCM (Figure 6.21). This indicates that the pre-cooling temperature of 258 K can be further increased for the complete fill of the Type III cylinder while keeping the gas temperature below the 358 K limit.

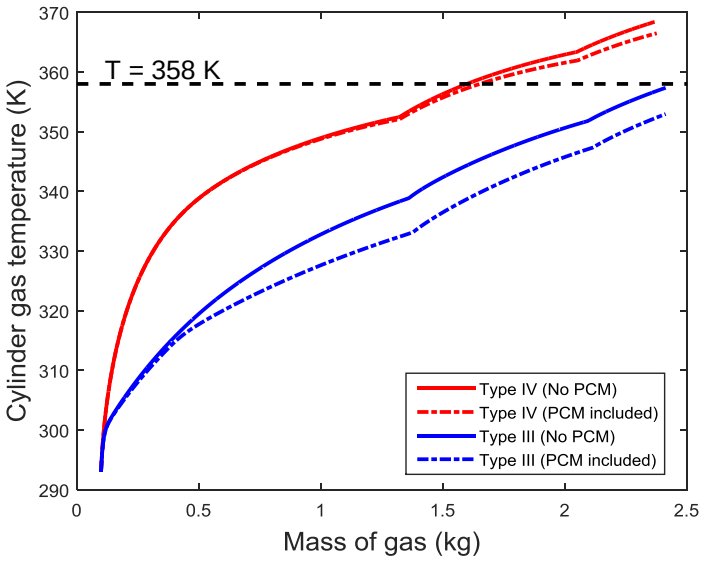

Figure 6.19: Gas temperature profiles v/s mass of gas in Types III & IV 60 L cylinder with and without PCM-2 (pre-cooling temperature = 258 K, ramp rate = 85.50 MPa/min & ambient temperature = 293 K).

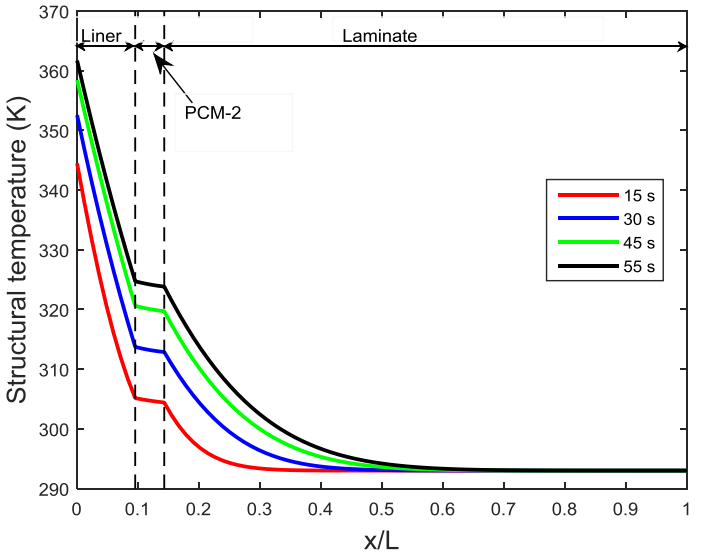

Figure 6.20: Structural temperature in the Type IV cylinder with PCM-2 at different times during the fill (pre-cooling temperature = 258 K, ramp rate = 85 MPa/min & ambient temperature = 293 K).

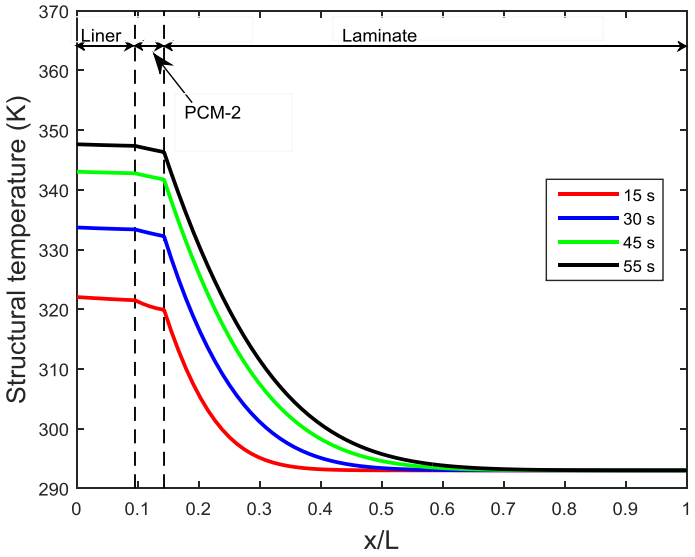

Figure 6.21: Structural temperature in the Type III cylinder with PCM-2 at different times during the fill (pre-cooling temperature = 258 K, ramp rate = 85 MPa/min & ambient temperature = 293 K).

The presence of the PCM is thus more effective for the fast-filling of hydrogen gas in the Type III as opposed to the Type IV cylinder. It was shown in Figure 6.14 that the fast-filling of original hydrogen Type IV cylinders of the Toyota Mirai can be performed faster than the conventional 3-5 minutes by increasing the delivery pressure ramp rate of the gas, while also lowering the pre-cooling temperature. Further simulations of the fast-fill were performed at the different delivery pressure ramp rates (*please refer to Table 6.3*) with ambient temperatures of 273 K, 293 K and 313 K for the original Type IV cylinders of the Toyota Mirai and the newly designed Type III cylinder that includes PCM-2 in between the liner and laminate. The presence of PCM-2 in between the liner and laminate of a Type III cylinder lessens the need for pre-cooling and at an ambient temperature of 273 K, no pre-cooling of the gas is required (Figure 6.22). The y-axis of Figure 6.22 is the difference between the ambient temperature and the pre-cooling temperature and is representative of the amount of pre-cooling required at a given ambient temperature and inlet pressure ramp rate such that a full fill of the hydrogen cylinders in the Toyota Mirai can be performed in accordance to safety regulations of the SAE J2601 [17]. The lowest pre-cooling temperature for the fast-filling of the newly designed cylinders with PCM is 252 K and occurs when the ambient temperature is 313 K and the delivery ramp rate is 85 MPa/min, which corresponds to a fill time of 60 s. The 252 K pre-cooling temperature is 19 K higher than the

minimum pre-cooling temperature of 233 K, which is suggested by the hydrogen refuelling protocol SAE J2601[17].

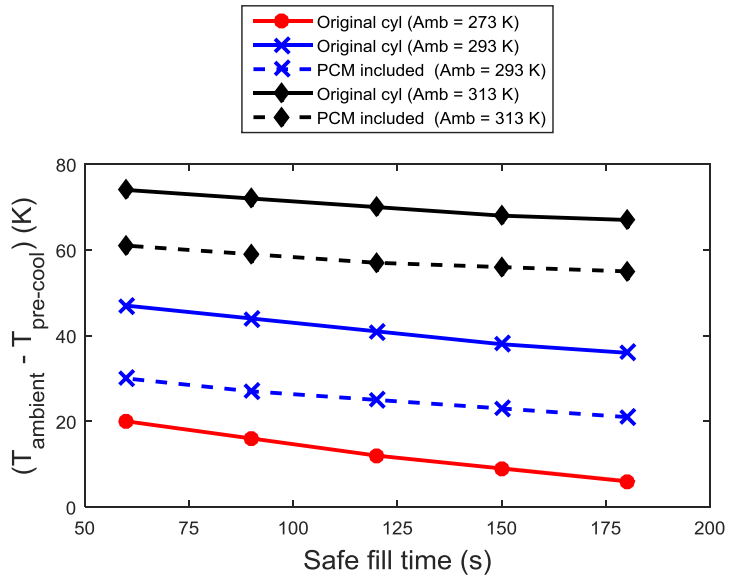

Figure 6.22: Measure of the amount of pre-cooling required at the different ambient temperatures for a complete safe fill of the original Type IV cylinders and the newly designed Type III cylinders with PCM-2.

The higher the pre-cooling temperature, less energy is required and the fast-filling of the hydrogen vehicles will be cheaper. The graph of the specific exergy versus the safe fill time (Figure 6.23) shows that the maximum useful work done per unit mass of gas by the heat exchanger in pre-cooling the gas temperature decreases when PCM-2 is inserted in between the liner and laminate of Type III cylinders, since lower pre-cooling temperatures are no longer required.

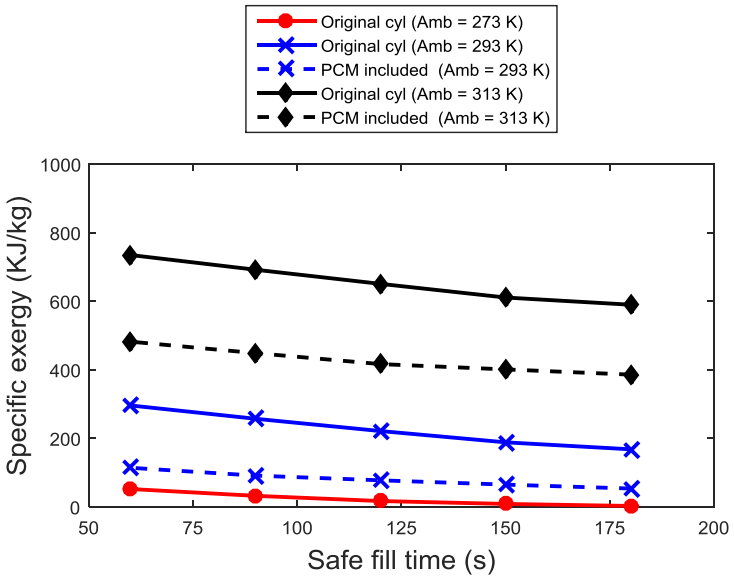

Figure 6.23: Comparison of the specific exergy for pre-cooling at the different ambient temperatures for a complete safe fill of the original Type IV cylinders and the newly designed Type III cylinders with PCM-2.

6.2.5 Step pressure profile at exit of the dispenser

The study has so far only considered ramp pressure profiles being prescribed by the pressure control valve of the dispenser. The filling of the cylinders was also performed using a step pressure profile at the exit of the dispenser (Figure 6.24). The model was set up such that filling was stopped if one of the following occurs:

1. The state of charge (SOC) in either one of the cylinders reached 100 %.
2. The gas pressure within either one of the cylinders was 1.5 times the normal operating pressure of 70 MPa; i.e. 87.5 MPa.

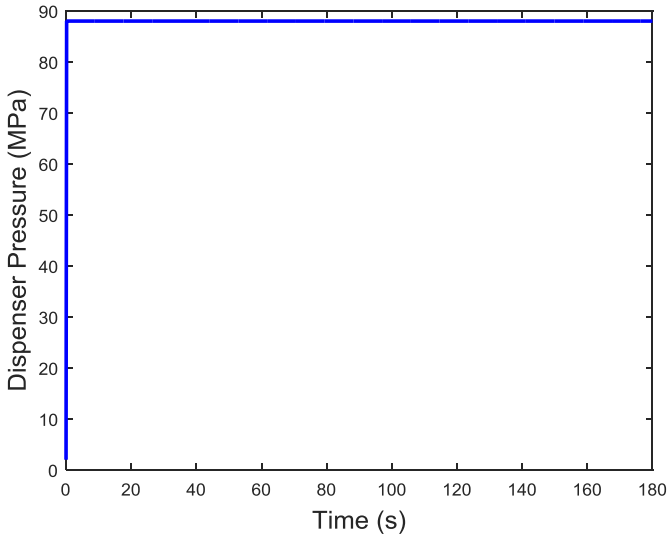

Figure 6.24: Step pressure profile of 88 MPa prescribed at the exit of the dispenser

The simulations were carried out using the newly designed cylinders with the aluminium liner and PCM-2 embedded between the liner and the laminate. According to the Met Office [31], the highest temperature recorded in the UK in 2017 was 307.5 K, thus in the model, an 'extreme' ambient temperature of 313 K was chosen for the filling. The minimum temperature pre-cooling temperature according to the hydrogen refuelling protocol SAE J2601 [17] was used in the simulation. With a step pressure being applied at the exit of the dispenser, the maximum Reynolds numbers in the piping system that connects the banks to the dispenser increases by a factor of 10 (*please refer to Appendix A13*). This leads to a significantly larger pressure drop within the piping system (*please refer to Appendix A13*). Thus, the gas pressure in the banks must be high enough to account for the high pressure drop, while maintaining the step pressure profile at the exit of the dispenser. The volumes of the banks were kept constant at 1200 L

for the simulations and it was determined that the only one bank at a pressure of at least 300 MPa is required to maintain a constant pressure of 88 MPa at the exit of the dispenser (*please refer to Appendix A14*).

The filling stopped once the pressure in one of the cylinders reached 87.5 MPa, which occurred approximately 3 seconds into the fill (Figure 6.25). The large difference between the delivery pressure and the gas pressures in the cylinders at the beginning of the fill, led to a quick rise in the gas temperature in the cylinders due to the Joule-Thompson effect. Thus, the quick rise in the gas pressure in the cylinders is mainly due to fast increase in the gas temperature, which exceeded the maximum allowable limit of 358 K (Figure 6.26).

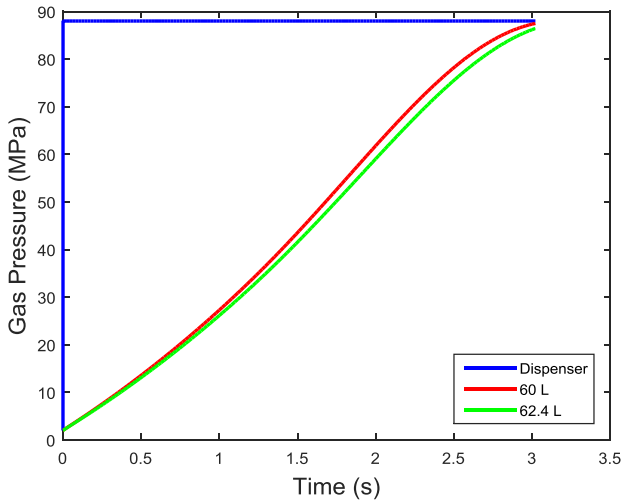

Figure 6.25: Pressure profiles at the exit of the dispenser for the filling of the of the newly designed cylinders (step profile, ambient temp = 313 K, pre-cooling temp = 233 K)

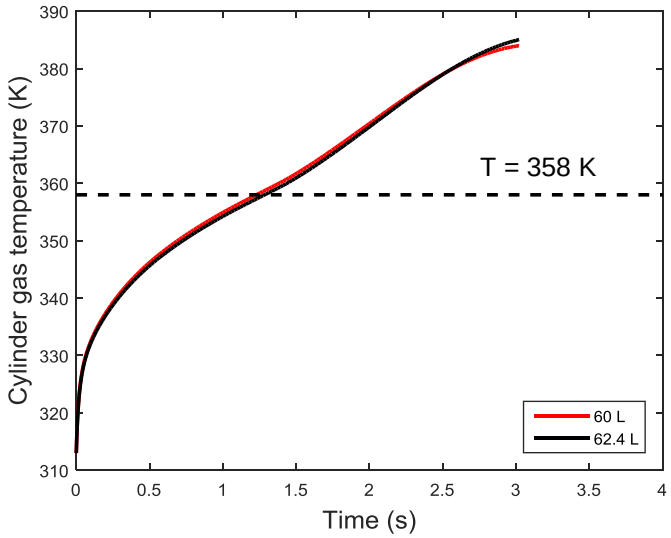

Figure 6.26: Gas temperature profiles in both the 60 L and 62.4 L of the newly designed cylinders (step profile, ambient temp = 313 K, pre-cooling temp = 233 K)

The filling with the step profile was also performed with a lower pre-cooling temperature of 203 K with the ambient staying at a constant of 313 K. In that particular case, a full fill occurred and the gas temperature in the cylinders did not exceed the limit of 358 K (Figure 6.27).

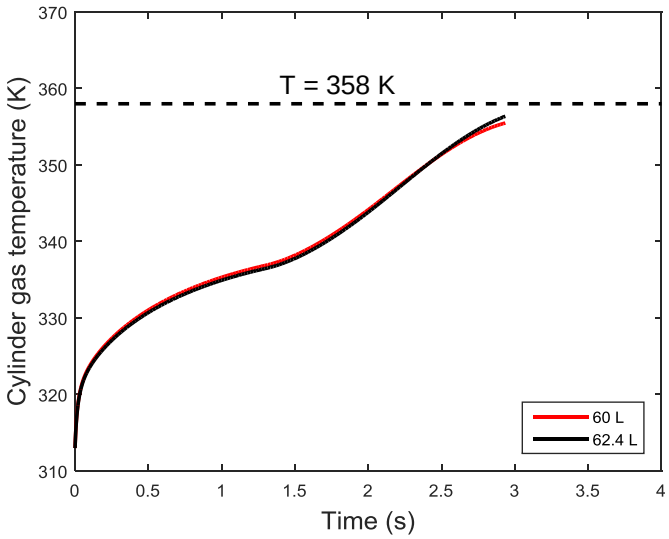

Figure 6.27: Gas temperature profiles in both the 60 L and 62.4 L of the newly designed cylinders (step profile, ambient temp = 313 K, pre-cooling temp = 203 K)

Table 6.6 compares the fill time as well as the pre-cooling temperatures and bank pressure requirements for the filling of the newly designed cylinder at an ambient temperature of 313 K for the ramp pressure profile of 85.5 MPa/min and the step profile.

Pressure profile	Bank volume	Required Bank pressure	Number of banks	Required Pre-cooling temperature	Fill time (s)
Step	1200 L	300 MPa	1	203 K	2.9 s
Ramp (85.5 MPa/min)	1200 L	100 MPa 75 MPa 45 MPa	3	253 K	58.4 s

Table 6.6: Comparison of the requirements and fill times for a ramp pressure profile of 85.5 MPa/min and a step profile for the newly designed cylinders

It should be noted that because of a large difference between the step delivery pressure and the gas pressure in the cylinders at the beginning of the fill, choking initially occurs at the exit of the dispenser as opposed to the case of the ramp delivery pressure of 85.5 MPa/min, whereby the maximum Mach number is approximately 0.7 (*please refer to Appendix A15*). As shown in Table 6.6, for the

given bank volume of 1200 L, the bank pressure must be at least 300 MPa but however, banks capable of withstanding such a high pressure could not be found in the literature. In addition, while a much lower fill time is achieved (2.9 s v/s 58.4 s) with a step pressure profile, a much lower pre-cooling temperature is required (203 K v/s 252 K).

6.3 CNG fast-filling station

This section of the current chapter involves the fast-filling of the 2015 Honda Civic GX, which is a CNG subcompact vehicle. The product information of the vehicle is shown in Table 6.7 [25].

Number of cylinders	1
Cylinder type	III
Maximum Filling pressure	24.8 MPa
Normal operating pressure	20.7 MPa
Internal volume	100 L
Refuelling time	3 – 5 mins
Total storage mass (20.7 MPa)	15.0 kg
Total storage mass (24.8 MPa)	16.7 kg

Table 6.7: Product info of the 2015 Honda Civic GX [25]

The material properties as well as the thicknesses of the liner and laminate of the cylinders were not listed in vehicle manual. In the single-zone model, the material properties of the Type III cylinder of Dicken and Merida [7] were used (*please refer to Appendix A4*) and the liner and laminate thicknesses were set to 4 mm and 15 mm respectively [7]. The inlet diameter and the L/D of the cylinder were respectively set to 5 mm and 2.4, similar to the fast-filling experiment of Dicken and Merida [7].

The filling procedure for the CNG vehicle is similar to the cascade filling process of the hydrogen vehicle, with the exception that no pre-cooling is required. According to the CNG fast-filling protocol SAE TIR J1616 [17], bank pressures are usually in the range of 24.82 MPa and 34.48 MPa. In the initial model, three banks are considered with volumes of 1200 L, similar to the hydrogen filling station. The pressures in the banks are as follows:

- Low pressure bank – 24.82 MPa
- Moderately high pressure bank – 29.65 MPa
- High pressure bank – 34.48 MPa

The pressure in the moderately high pressure bank was chosen as 29.65 MPa, since it represents the average pressure of the low and high pressure banks. The piping system of the CNG filling station is similar to that of the previously discussed hydrogen filling station and its schematic representation for the filling of the 2015 Honda Civic GX is shown in Figure 6.28.

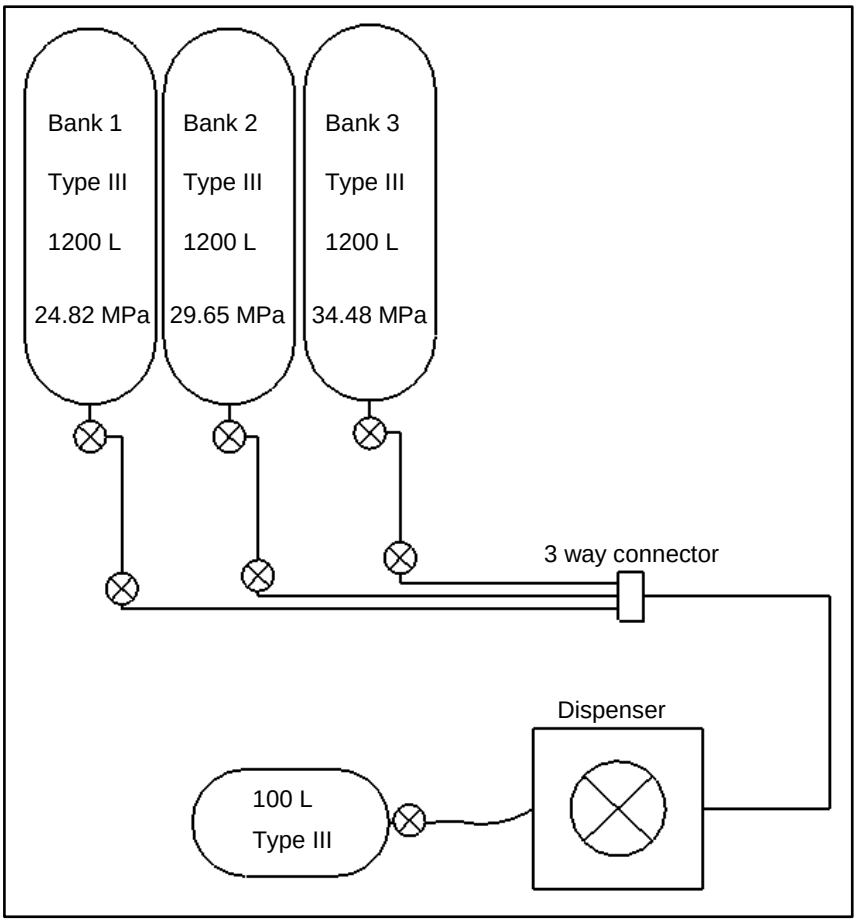

Figure 6.28: Schematic diagram of a CNG filling station during the filling of 2015 Honda Civic GX.

The CNG fast-filling protocol SAE TIR J1616 [17] makes no mention of the state of charge (SOC) as being a limiting factor in the fast-filling of natural gas vehicles (NGVs). Thus, the model is set up in such a way that the filling is stopped only when the gas pressure in cylinder is 28.4 MPa, which 1.5 times the normal operating pressure of 20.7 MPa.

Initial pressure conditions & outer wall boundary conditions

Similar to the hydrogen refuelling case, all of the simulations were performed whereby:

- The initial pressure within the 100 L cylinder is 2.0 MPa.
- Adiabatic wall conditions were applied to the outer walls of both the banks and the 100 L cylinder.

6.3.1 Refuelling at a pressure ramp rate of 7.7 MPa/min

The model was initially tested for the filling of both cylinders with the gas being delivered by the dispenser at an initial pressure ramp rate of 7.7 MPa/min), which is followed constant pressure of 25 MPa (Figure 6.29).[1] This corresponds to an approximate filling time of 180 seconds. The fill time of 180 seconds was chosen since it corresponds to the fastest of the typical fill times, which usually vary between three and five minutes. The initial gas temperature in the cylinder and ambient temperature were set to 293 K.

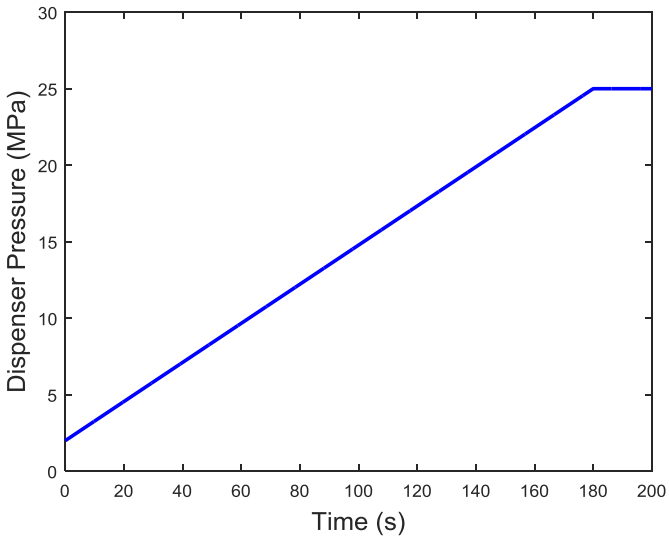

Figure 6.29: Pressure at the exit of the dispenser (initial ramp rate = 7.7 MPa/min).

CNG is made up of a mixture of different gases and its main component is methane [88]. According the NIST database of REFPROP 9.0, the mole fraction of methane in typical natural gas is 0.95. The fast-fill simulations were initially tested using natural gas followed by methane. It was determined that the use of natural gas in

[1] No literature on the dispenser profile for the filling of natural gas vehicles could be found. Gas companies have been contacted and have mentioned that the delivery system/profile is of commercial propriety. Thus in this study, the same delivery pressure profile (ramp profile) that was used in hydrogen filling is applied for CNG/methane.

the simulation requires a large computational time for the calculation of the gas properties due to its complexity.

Table 6.8 shows the computational time for fifteen seconds into fill for natural gas and methane.

Gas type	Time into the 180s fill	Computational time
Natural gas	20 s	~ 15 hours
Methane	20 s	~ 4 minutes

Table 6.8: Comparison of the computational time using methane and natural gas.

Figure 6.30 compares the profiles of the gas temperatures for the first 20 seconds during fill in the Type III cylinder of the Honda 2015 Honda Civic GX for methane and natural gas.

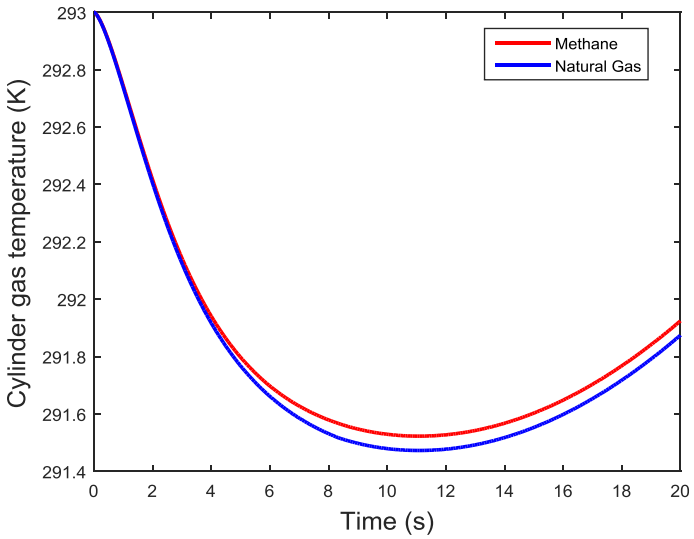

Figure 6.30: Comparison of the gas temperatures in the Type II cylinder for the first 15 seconds of the fill for methane and natural gas.

As shown in Figure 6.30, the profiles of the gas temperature in the cylinder during the first 20 seconds of the fill for methane and CNG are quasi-similar. Thus, for computational time savings, methane was chosen for the fast-filling simulations of the Honda Civic GX in this study.

Figure 6.31 shows the gas temperature that was obtained for the filling of 100 L Type III cylinder with the pressure ramp rate of 7.7 MPa/min.

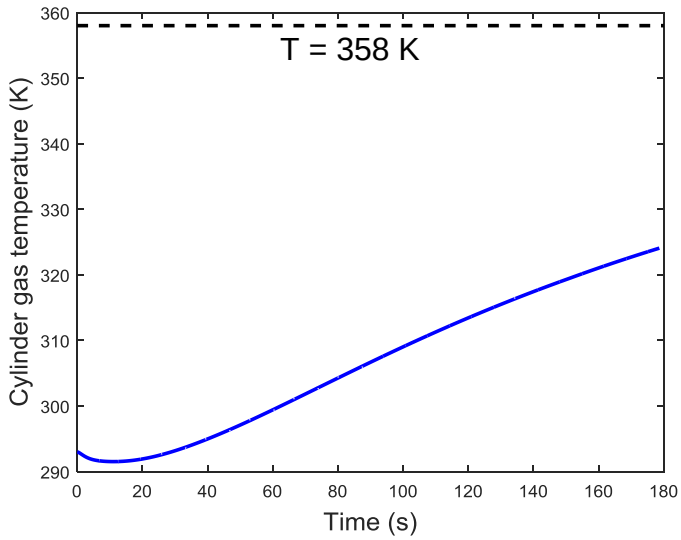

Figure 6.31: Gas temperature during the fill of the 100 L cylinder (ramp rate = 7.7 MPa/min & ambient temperature = 293 K).

As shown in Figure 6.31, the final gas temperature is significantly below the maximum allowable limit of 358 K. The fill time as well as the pressure and the mass of gas in the cylinder at the end of the fill are shown in Table 6.9.

Ramp rate	Final pressure	Final mass	Fill time
7.7 MPa/min	24.8 MPa	16.3 kg	178.7 s

Table 6.9: Fill time and the final state of the gas at the end of the fill (ambient temperature = 293 K).

The final mass of gas that was obtained from the simulation is 16.3 kg and is comparable to the final mass of gas of 16.7 kg that is stated in the car manual [25] of the 2015 Honda Civic GX (difference of 2.4%). At the start of the fill, the gas temperature in the cylinder initially decreases and then as the filling continues, a rise in the gas temperature is observed. This phenomenon can be explained by the Joule-Thompson effect as the pressure of the gas from the bank that reaches the entrance of the dispenser is highest at the start of the fill and is lowered to a significantly lower pressure (Figure 6.32), leading to a decrease in the inlet temperature (Figure 6.33). Eventually, the compression of the gas in the cylinder coupled with the rise in the gas temperature at the dispenser from its initial drop leads to an increase in the gas temperature in the cylinder as the filling proceeds.

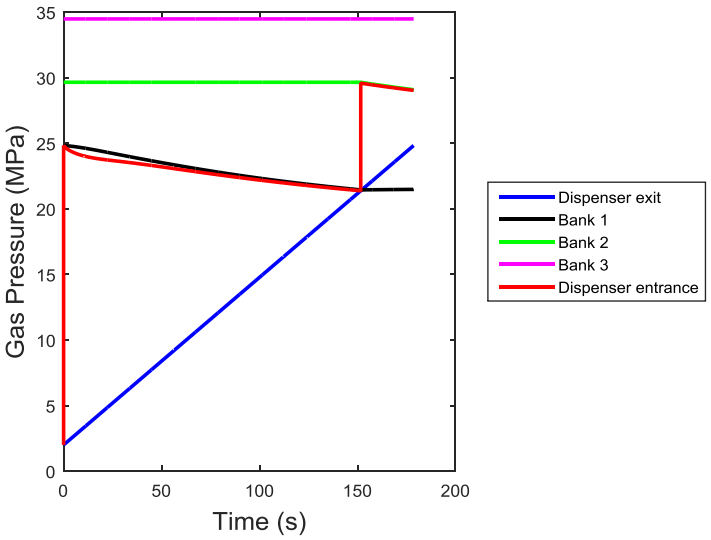

Figure 6.32: Pressure profiles of the banks and at the entrance and exit of dispenser for a pressure ramp rate of 7.7 MPa/min (ambient temperature = 293 K).

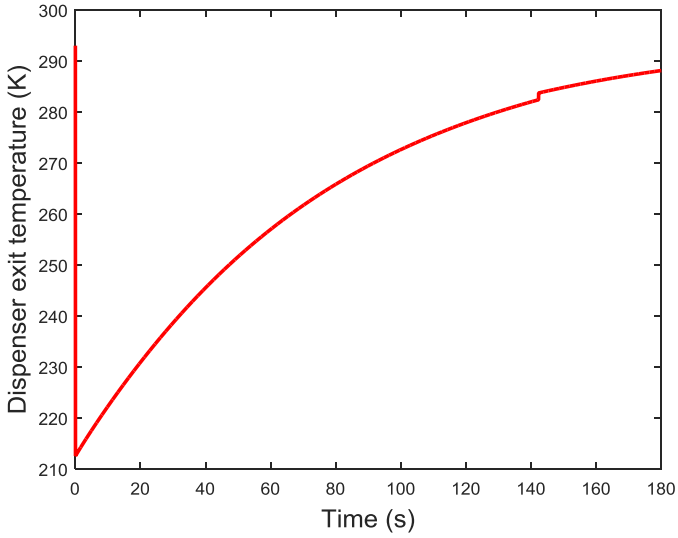

Figure 6.33: Gas temperature at the exit of the dispenser (ramp rate = 7.7 MPa/min & ambient temperature = 293 K).

6.3.2 Varying the volume of the banks

As shown in Figure 6.32, only 2 banks are required for the fast-filling of the vehicle. The pressure drop in the low pressure bank is not as significant, due to its large volume. Further simulations were performed for the fast-filling under the same conditions but the bank volumes were reduced from 1200 L in increments of 200 L. Figure 6.34 shows that even with reducing the bank volumes to 400 L, only 2 banks are required for the filling of the 100 L cylinder.

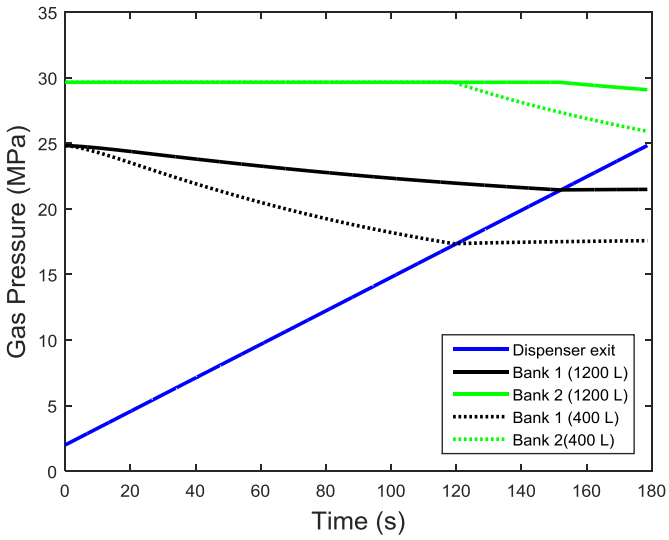

Figure 6.34: Pressure profiles of the banks with volumes of 400 L and 1200 L (ramp rate 7.7 MPa/min & ambient temperature = 293 K).

Further reducing the bank volumes to 200 L, requires all 3 banks for the filling of the 100 L cylinder, but the pressure in Bank 3 is barely above the required pressure profile of the dispenser (Figure 6.35). Thus, for the rest of this study, banks with volumes of 400 L were chosen for the fast-filling of the 100 L cylinder.

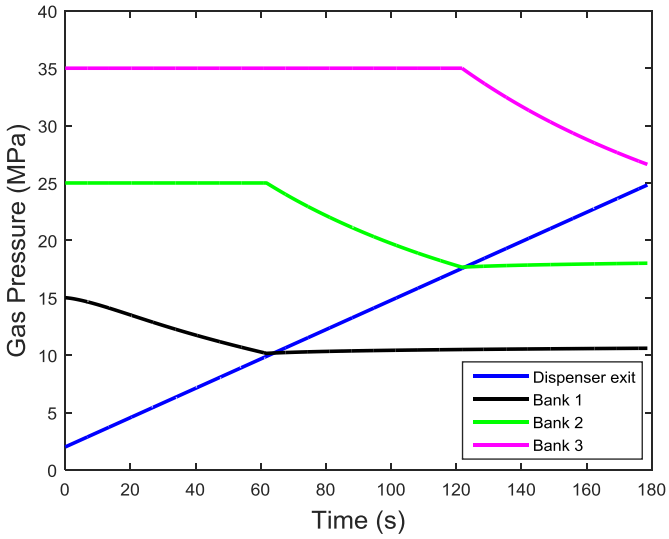

Figure 6.35: Pressure profiles of the banks with volumes of 200 L (ramp rate 7.7 MPa/min & ambient temperature = 293 K).

The fill time as well as the temperature, pressure and the mass of gas in the cylinder at the end of the fill for the different bank volumes are shown in Table 6.10.

Volume of banks	Final pressure	Fill time	Final temperature	Final mass
1200 L	24.8 MPa	178.7 s	324.1 K	16.32 kg
1000 L	24.8 MPa	178.7 s	323.8 K	16.34 kg
800 L	24.8 MPa	178.7 s	323.4 K	16.37 kg
600 L	24.8 MPa	178.7 s	322.8 K	16.42 kg
400 L	24.8 MPa	178.7 s	321.9 K	16.50 kg

Table 6.10: Fill time and the final state of the gas at the end of the fill for the different bank volumes (ramp rate = 7.7 MPa/min & ambient temperature = 293 K)

Lowering the volume of the banks lead to a decrease in the final temperature of the gas and subsequently leads to a slight increase in the final mass of gas. With the volume of the banks set to 400 L, the final mass of gas is 16.5 kg and is only 1.2% off the 16.7 kg of gas that is stated in the manual [25] of the Honda Civic GX. The drop in the final gas temperature within the cylinder with decreasing volume of the banks can be explained by the subsequent drop in the gas temperature at the exit of the dispenser (Figure 6.36). A larger drop in the gas pressure occurs in the banks with decreasing volume (please refer to Figure 6.37), which results in increase in the isentropic cooling of the gas within the banks, thus further lowering the gas temperature at the exit of the dispenser (Figure 6.36).

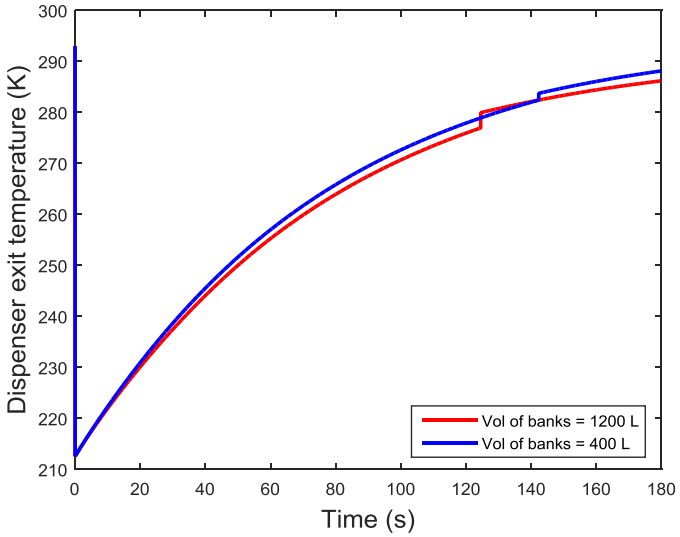

Figure 6.36: Comparison of the gas temperature at the exit of the dispenser with bank volumes of 400 L & 1200 L (ramp rate = 7.7 MPa/min & ambient temperature = 293 K).

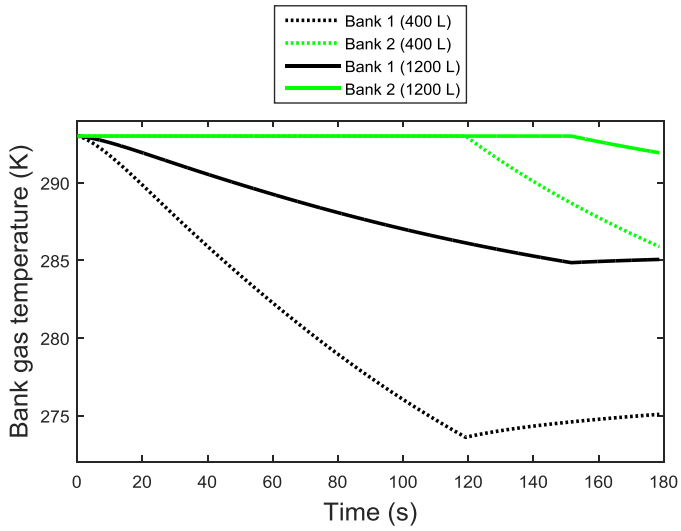

Figure 6.37: Comparison of the gas temperatures in the banks with volumes of 400 L & 1200 L (ramp rate = 7.7 MPa/min & ambient temperature = 293 K).

For both cases, an initial large drop in the gas temperature is observed at the exit of the dispenser at the start of the fill, which is due to the Joule-Thompson effect as the gas at the entrance of the dispenser is lowered to match the pressure profile at the exit. As the filling proceeds, the gas temperature at the exit of the dispenser increases for both cases, since the pressure drop across the dispenser decreases (Figure 6.38). A slight increase in the gas temperature is observed at the exit of the dispenser as the discharge switches from Bank 1 to Bank 2 (Figure 6.36) even though a sharp rise in the pressure drop is observed (Figure 6.38). This is due to the change in the gas temperature being discharged as the gas in Bank 2 is at the ambient temperature of 293 K, which is much higher than the gas temperature at the end of the discharge of Bank 1 (Figure 6.37).

The gas temperature in the smaller banks (400 L) decreases at a much faster rate than the temperature in the larger 1200 L banks (Figure 6.37). This is due to the faster rate in the pressure drop within the 400 L banks. However, the difference in the gas temperature is significantly narrowed at the exit of the dispenser (Figure 6.36) and can be explained by Joule-Thompson effect, since a larger pressure drop occurs at the dispenser for the gas that is discharged from the banks with the larger volume of 1200 L (Figure 6.38).

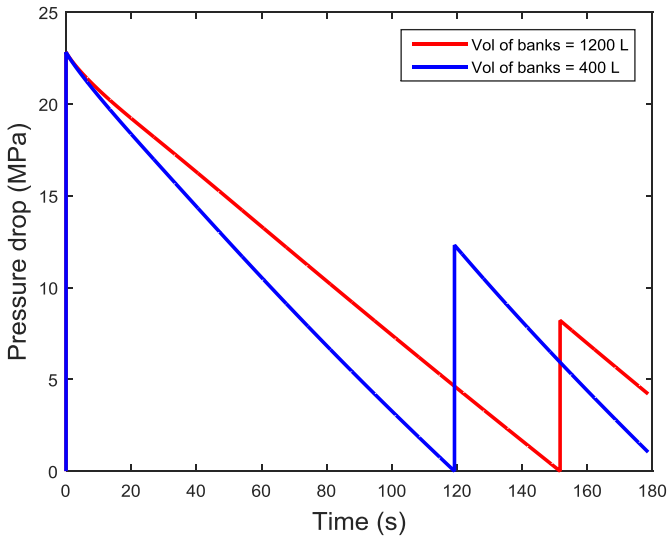

Figure 6.38: Pressure drop across the dispenser with banks volumes of 400 L and 1200 (ramp rate = 7.7 MPa/min & ambient temperature = 293 K).

6.3.3 Type III v/s Type IV cylinder

The material properties of the liner in the 100 L cylinder were switched from plastic to plastic similar to the Type IV cylinder of Alam et al. [86]. A fast-fill with the Type IV cylinder was performed with the ambient temperature set to 293 K and at a ramp rate of 7.7 MPa/min. In addition, another fast-fill was also performed for similar conditions except that adiabatic conditions were imposed at inner walls of the cylinder. Figure 6.39 shows the gas temperatures in the cylinder for all three cases throughout their respective fills.

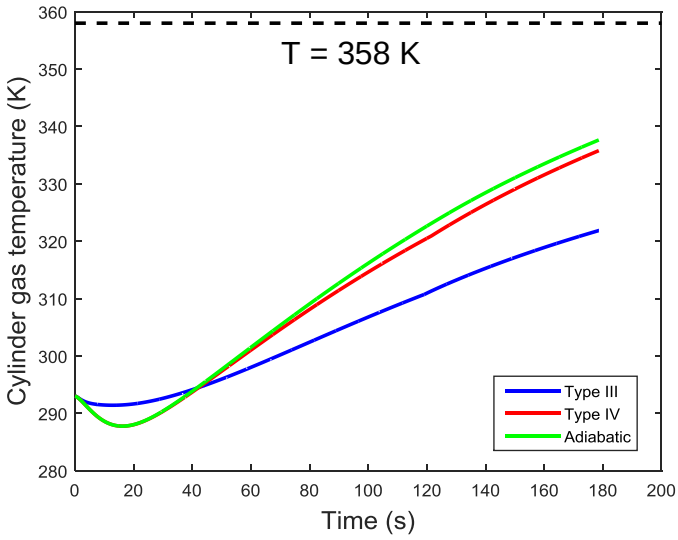

Figure 6.39: Comparison of the gas temperatures for the Type III and IV cylinders as well as for adiabatic conditions (ramp rate = 7.7 MPa/min & ambient temperature = 293 K)

A shown in Figure 6.39, the final gas temperature for all three cases are well below the maximum allowable limit of 358 K. The low thermal conductivity of the plastic liner in the Type III cylinder inhibits heat transfer from the wall to the gas and thus for the first 40 seconds into the fill, a lower gas temperature is observed in the Type III cylinder as opposed to the Type IV cylinder. The gas temperature profiles for the adiabatic case and the Type IV cylinder are similar for the first 30 seconds into the fill. As the filling proceeds, the gas temperature in the Type IV cylinder is slightly lower than the adiabatic case due to the heat transfer from the gas to the plastic liner. On the other hand, due to the larger thermal conductivity of the aluminium liner, heat transfer occurs from the wall of cylinder to the gas at the beginning of the fill, which explains the higher gas temperature at the Type III cylinder as opposed to the Type IV cylinder and the adiabatic case. As the filling proceeds and the compression of the gas in the cylinder leads to a higher gas temperature. Heat transfer is larger in the Type III cylinder due to the high thermal conductivity and capacity of the aluminium liner and results in a lower gas temperature than in the Type IV cylinder. The final mass of gas in Type IV cylinder is 15.5 kg as opposed to 16.5 kg in the Type III cylinder. This represents a decrease of approximately 6.6 % in the final mass of gas when the liner in the cylinder is switched from aluminium to plastic. Thus, Type III cylinders are more suitable for the fast-filling of Natural Gas Vehicles. For the rest of this study, only Type III cylinders will be considered for the fast-filling of the Honda Civic GX.

6.3.4 Increasing the pressure ramp rate

Further studies were performed in which the pressure ramp rate at the exit of the dispenser was increased determine if the fast-filling of the cylinder can be achieved faster without exceeding the maximum allowable limit of 358 K. The ramp rates that were considered and the corresponding expected approximate fill times are displayed in Table 6.11.

Ramp Rate	Expected fill time
7.7 MPa/min	~ 180 s
9.2 MPa/min	~ 150 s
11.5 MPa/min	~ 120 s
15.3 MPa/min	~ 90 s
22.8 MPa/min	~ 60 s

Table 6.11: Pressure ramp rate and expected fill times

The simulations were performed whereby the original material of the liner (Al-alloy) was selected for both the 100 L cylinder and the ambient temperature was set to 293 K. Figure 6.40 shows the profile of the gas temperature throughout the fills with the various ramp rates.

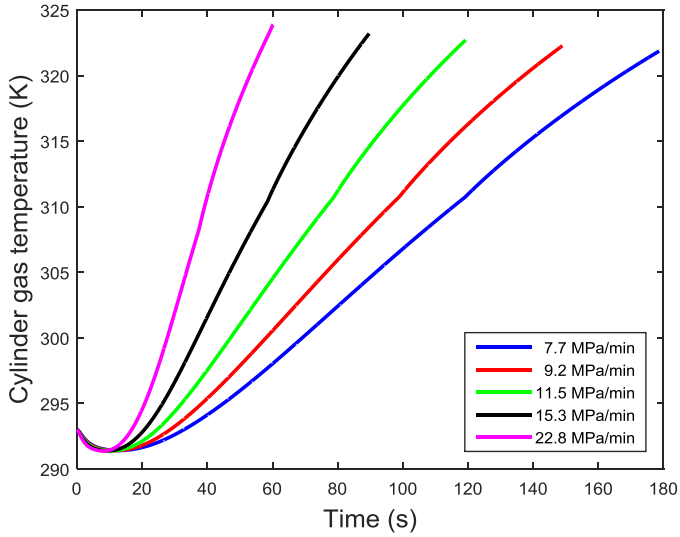

Figure 6.40: Comparison of the gas temperature Comparison for the Type III 100 L cylinder at different ramp rates (ambient temperature = 293 K)

As shown in Figure 6.40, increasing the ramp rate does not significantly increase the final gas temperature. Increasing the ramp rate, leads to a rise in the Reynolds number at exit of the dispenser and subsequently increases the heat transfer coefficient (*please refer to Appendix A16*). Thus, with higher ramp rates, the heat flux at the wall of the cylinder increases (Figure 6.41) and compensates the faster rate of the compression of the gas in the cylinder and thus the change in the final gas temperature is insignificant.

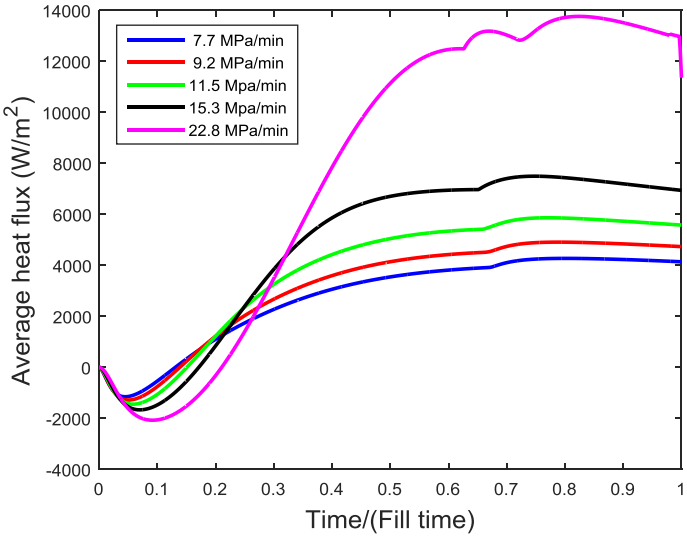

Figure 6.41: Heat flux for the different pressure ramp rates (ambient temperature = 293 K)

Increasing the pressure ramp rate at the dispenser, leads to larger pressure losses in the piping system. With the pressure ramp rate of 22.8 MPa/min, the third high pressure bank is required in the filling of the 100 L cylinder (Figure 6.42).

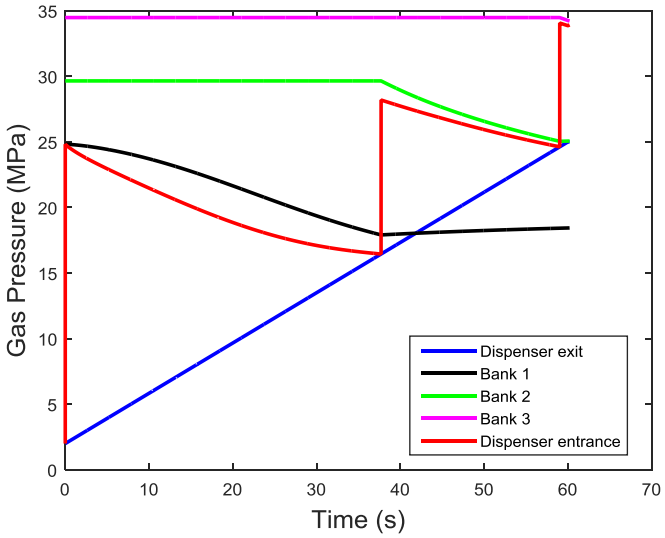

Figure 6.42: Pressure profiles of the banks and at the entrance and exit of dispenser for a pressure ramp rate of 22.8 MPa/min (ambient temperature = 293 K)

The high pressure bank (Bank 3), is barely required in the filling of the 100 L cylinder, and this indicates that two banks slightly larger than the 400 L volume can be used for the filling of the 100 L cylinder at the ramp rate of 22.8 MPa/min. However, it should be noted that the length of the main pipe that connects the banks to the dispenser was set to 20 m in the current model and filling stations that are fitted with a longer pipe will require a third bank due larger pressure losses in the piping system. The fill times as well as the pressures, the mass of gas at the end of the fills of the 100 L cylinder for the different ramp rates and with the ambient temperature of 293 K are shown in Table 6.12.

Ramp rate	Fill time	Final gas temperature	Final pressure	Final mass
7.7 MPa/min	178.7 s	321.9 K	24.8 MPa	16.5 kg
9.2 MPa/min	149.0 s	322.2 K	24.8 MPa	16.5 kg
11.5 MPa/min	119.2 s	322.7 s	24.8 MPa	16.4 kg
15.3 MPa/min	89.7 s	323.2 K	24.8 MPa	16.4 kg
22.8 MPa/min	60.1 s	323.9 K	24.8 MPa	16.3 kg

Table 6.12: Fill times and the final state of the gas at the end of the fill for the different ramp rates (ambient temperature = 293 K)

As shown in Table 6.12, the slight rise of 2 K occurs when the ramp rate is increased from 7.7 MPs/min to 22.8 MPa/min, which leads to a drop of 1% in the final mass of gas. However, the fill time is significantly lowered (a decrease of 66.3 %).

6.3.5 Effect of the ambient temperature

The simulations of the fast-filling of the 100 L Type III vessel in the Honda Civic GX have been performed so far with the ambient temperature set to 293 K. Further fast-filling simulations were carried out at ambient temperatures varying from 273 K to 313 K in increments of 10 K with the pressure ramp rate at the exit of the dispenser set to 22.8 MPa/min. Figure 6.43 shows the profiles of the gas temperature during the filling at the different ambient temperatures with the ramp rate set to 22.8 MPa/min.

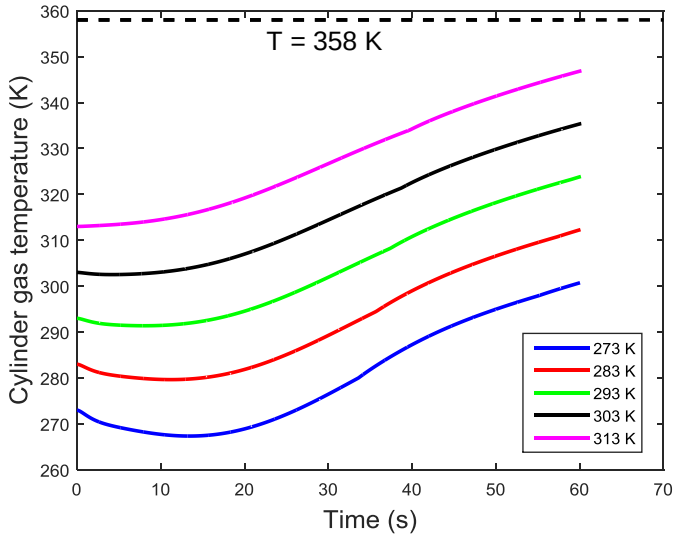

Figure 6.43: Comparison of the gas temperature profiles at the different ambient temperatures (ramp rate = 22.8 MPa/min)

As shown in Figure 6.43, the gas temperature never exceeds the maximum limit of 358 K, even when the filling occurs at an ‘extreme’ ambient temperature of 313 K. The pressure, temperature and mass of gas at the end of the fills of the 100 L cylinder for the different ambient temperatures with the ramp rate at the exit of the dispenser set to 22.8 MPa/min are shown in Table 6.13.

Ambient temperature	Final pressure	Final temperature	Final mass	Fill time
273 K	24.8 MPa	300.7 K	18.4 kg	60 s
283 K	24.8 MPa	312.3 K	17.3 kg	60.1 s
293 K	24.8 MPa	323.9 K	16.3 kg	60.1 s
303 K	24.8 MPa	335.4 K	15.5 kg	60.2 s
313 K	24.8 MPa	346.9 K	14.7 kg	60.2 s

Table 6.13: Fill times and the final state of the gas at the end of the fill for the ambient temperatures (ramp rate = 22.8 MPa/min)

As shown in Table 6.13, the final mass of gas decreases with increasing ambient temperature. Thus at higher ambient temperatures of 303 K and 313 K, the range of the vehicle is lower due to the lower final mass of gas. On the other hand, with ambient temperatures less than 293 K, the range of the vehicle increases since a larger final mass of gas is obtained during the fill.

6.3.6 Step pressure profile at exit of the dispenser

The filling of the cylinder was also performed using a step pressure profile of 25 MPa at the exit of the dispenser (Figure 6.44). The simulations were carried out at the different ambient temperatures that have been previously chosen in this study.

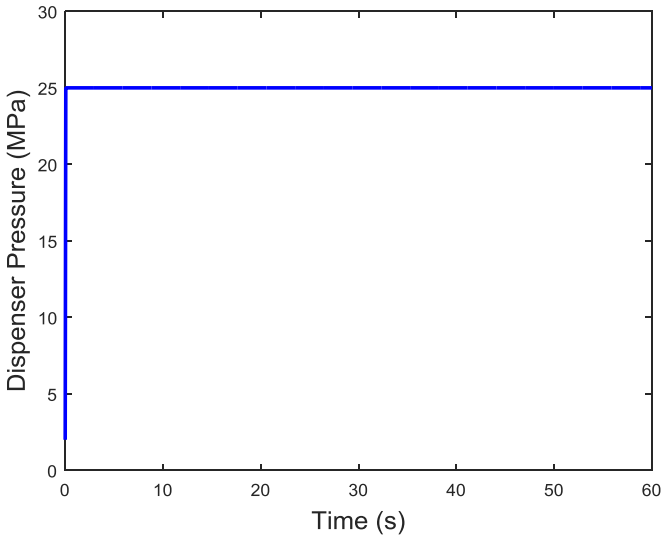

Figure 6.44: Step pressure profile of 25 MPa prescribed at the exit of the dispenser

The filling stops whenever the gas pressure in the cylinder reaches 24.8 MPa as shown in Figure 6.45 that displays the pressure rise in the cylinder at the different ambient temperatures.

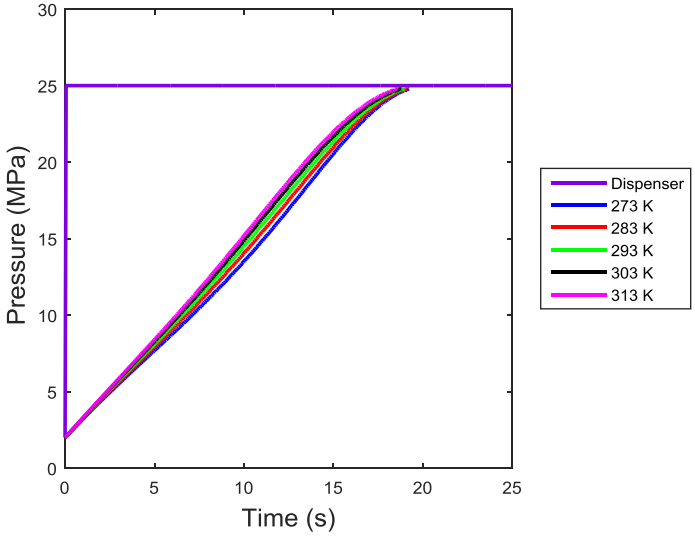

Figure 6.45: Comparison of the pressure profiles in the cylinder at different ambient temperatures with a step pressure profile at the exit of the dispenser

As shown in Figure 6.45, the fill times at the various ambient temperatures are all below 20 seconds. A large difference is observed between the exiting gas pressure at the dispenser and the gas pressure within the cylinder. The resulting Joule-Thompson effect, which is due to the difference in pressures, results in lowering the gas temperature in cylinder (Figure 6.46) and increases the final mass of gas (Figure 6.47).

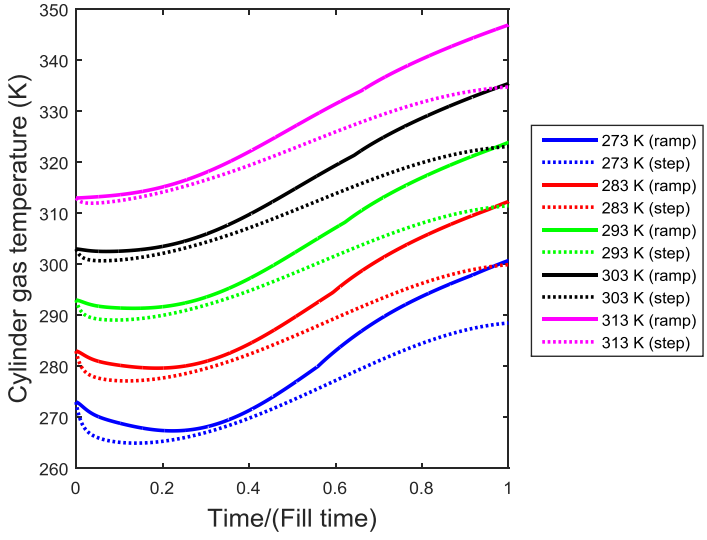

Figure 6.46: Comparison of the gas temperature profiles in the cylinder at the different ambient temperatures with a ramp pressure profile of 22.8 MPa/min v/s a step pressure profile at the exit of the dispenser.

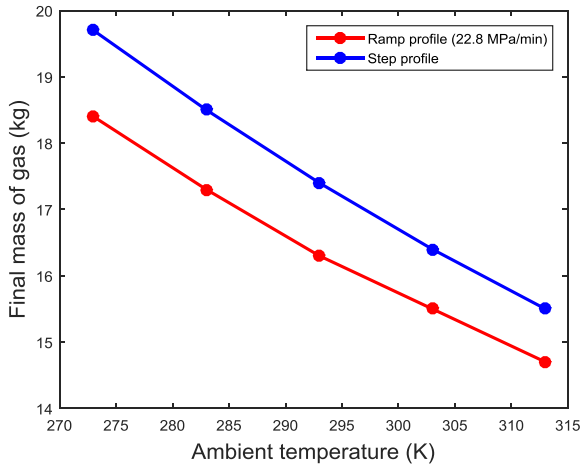

Figure 6.47: Comparison of the final mass of gas in the cylinder at the different ambient temperatures with a ramp pressure profile of 22.8 MPa/min v/s a step pressure profile at the exit of the dispenser.

6.3.7 Bank Pressure requirement

The use of a step pressure profile for the filling of the 100 L cylinder, increases the maximum Reynolds numbers in the piping system that connects the banks to the dispenser increases by a factor of 5 and leads significant pressure drop (*please refer to Appendix A17*). Thus, the gas pressure in the banks must be high enough to account for the larger pressure drop in the piping system, while maintaining the step pressure profile at the exit of the dispenser. The volumes of the banks were kept constant at 400 L and it was determined that over the range of ambient temperatures that were used in this study, only one bank at a pressure of at least 70 MPa is required maintain a constant pressure of 25 MPa at the exit of the dispenser (Figure 6.48).

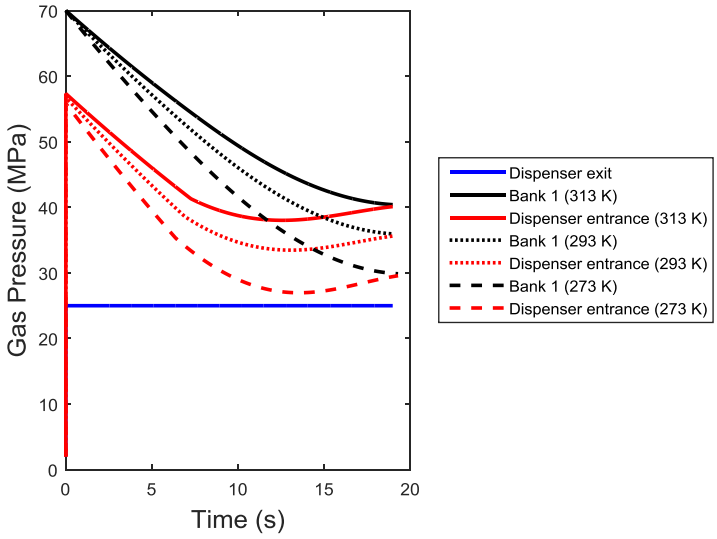

Figure 6.48: Pressure profile at the entrance and exit of the dispenser as well as the bank pressure for the step pressure profile of 25 MPa at ambient temperatures of 273 K, 293 K and 313 K

As shown in Figure 6.48, the gas pressure in the banks and at the entrance of the dispenser decreases with decreasing ambient temperatures. When the ambient temperature is 273 K, the gas pressure at the entrance of the dispenser at approximately 14 seconds into the fill is only slightly above the prescribed pressure at the exit. With decreasing ambient temperatures, the mass flow rate at exit of the dispenser increases (Figure 6.49) and results in a larger mass of gas being discharged by the bank, which leads to a larger drop in pressure in the bank. The resulting increase in the mass flow rate at the lower ambient temperatures leads to an increase in the average Reynolds number in the piping system and subsequently increases the pressure drop within the pipes and components that connect the bank to the dispenser (*please refer to Appendix A17*). Thus, for ambient temperatures lower than 273 K or for filling stations whose piping systems are longer than 20 m, the following should be considered in order to maintain the step pressure profile of 25 MPa at the exit of the dispenser:

- If the same initial bank pressure of 70 MPa is used, a bank with a volume greater than 400 L will be required.
- If the volume is kept at 400 L, the initial bank pressure must be greater than 70 MPa.

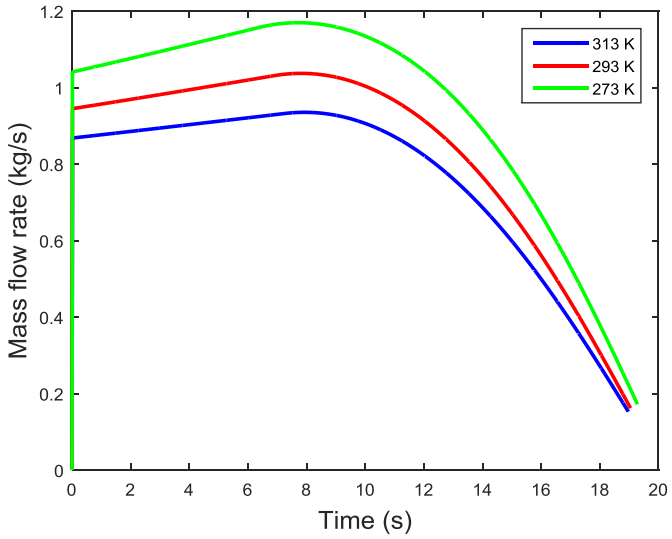

Figure 6.49: Comparison of the mass flow rate with a step pressure profile of 25 MPa being applied at the exit of the dispenser (ambient temperature = 273 K, 293 K, 313 K).

6.3.8 Inclusion of the phase change material

The fast-filling of the cylinder that includes PCM-2 with a thickness of 2 mm between the liner and laminate were also carried out whereby the step pressure profile of 25 MPa was applied at the exit of the dispenser for the various ambient temperatures. The simulations showed that the presence of the phase change material in between the liner and the laminate is mostly effective at the 'extreme' high ambient temperature of 313 K (Table 6.14). An increase of 2% in the final mass of gas is observed when the ambient temperature during the fill is 313 K. The melting range of PCM-2 is between 308 K and 328 K and thus the phase change material is mostly ineffective in lowering the gas temperature when the ambient temperature is below 303 K. (Figure 6.50). In addition to being mostly ineffective in increasing the final mass of gas, the presence of the PCM as part of the structure of the cylinder will increase its structural mass by approximately 3 %.

Ambient temperature	Final mass (No PCM-2)	Final mass (PCM-2 included)	% increase in final mass of gas
273 K	19.7 kg	19.8 kg	0.5 %
283 K	18.5 kg	18.6 kg	0.5 %
293 K	17.4 kg	17.5 kg	0.5 %
303 K	16.4 kg	16.5 kg	0.6 %
313 K	15.5 kg	15.8 kg	2.0 %

Table 6.14: Comparison of the final mass of gas at the different ambient temperatures with a step pressure profile at the exit of the dispenser in the cylinder with and without PCM.

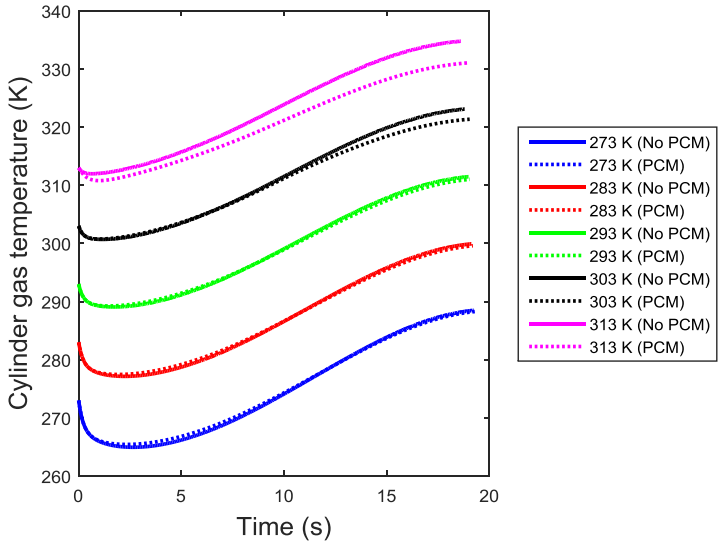

Figure 6.50: Comparison of the gas temperature profiles in the cylinder at the different ambient temperatures with a step pressure profile at the exit of the dispenser for the cylinder with and with PCM.

6.4 Summary

A computational model of a fast-fill station that delivers either hydrogen or CNG has been established. The fill station consists of the high pressure storage banks, the piping system that feeds the gas from the banks to the dispenser, which in turn delivers the gas to the fuel storage system within the vehicle. In the case of the hydrogen filling, the filling station includes a heat exchanger whose purpose is to cool the gas before the refuelling of the hydrogen vehicle.

Hydrogen Filling

The simulations for the fast-filling of the 2016 Toyota Mirai at an ambient temperature of 293 K showed that pre-cooling of the gas is required before being dispensed into the two cylinders of the vehicle to prevent the gas temperature from exceeding the maximum allowable limit of 358 K. The three pre-cooling temperatures initially used in the model were 233 K, 243 K and 253 K as listed in the hydrogen filling protocol SAE J2601 [17]. For all three pre-cooling cases, a 100% state of charge was obtained in both cylinders in addition to the final gas temperatures being lower than the 358 K limit.

The fast-filling of the hydrogen cylinders can be performed faster than the typical 3-5 minutes as suggested by the SAE J2601 [17] by increasing the delivery pressure ramp rate and lowering the pre-cooling temperatures. Pre-cooling temperatures for different fill times ranging from 60 seconds to 180 seconds for Type IV cylinders at ambient temperatures of 273 K, 293 K and 313 K have been established.

The switch of the lining material from plastic to an aluminium alloy similar to that of a Type III cylinder for both cylinders of the Toyota Mirai, showed that for the established pre-cooling temperatures for Type IV cylinders, a full fill is achieved approximately 8 K below the 358 K limit. The aluminium alloy liner acts as a better heat sink than the plastic and thus, Type III cylinders are more suitable as a storage medium in hydrogen vehicles. The inclusion a thin layer of high conductivity PCM (2 mm thickness) between the liner and laminate of the cylinder has shown its effectiveness in increasing the pre-cooling temperatures in Type III cylinders. In Type IV cylinders, the low thermal conductivity of the plastic liner acts as an obstacle for heat transfer from the gas to the phase change material during the fill.

The lowest pre-cooling temperature for the fast-filling of the newly designed Type III cylinders with PCM is 252 K and occurs when the ambient temperature is 313 K for the fill time of 60 s. The 252 K pre-cooling temperature is 19 K higher than the minimum pre-cooling temperature of 233 K, which is suggested by the hydrogen refuelling protocol SAE J2601 [17]. The higher pre-cooling temperatures that are required for the filling of the Type III cylinders with PCM as part of the structure leads energy savings.

Imposing a step pressure profile of 88 MPa at the exit of the dispenser has shown that for the filling of the newly designed cylinder (Type III with PCM), the minimum pre-cooling temperature must be lowered to at least 203 K to prevent the gas temperature from exceeding the 358 K limit. Although the fill time is lowered to 3 seconds, a significant amount of additional energy will be required to pre-cool the gas to 203 K. In addition, with the high pressure loses in the piping system, the initial pressure in the 1200 L bank must be at least 300 MPa and banks/cylinders that are currently on the market are not capable of withstanding such high pressure.

CNG filling

The fast-filling of the 2015 Honda Civic GX was initially performed using both natural gas and methane with the pressure ramp rate at the exit of the dispenser set to 7.7 MPa/min, which represents a fill time of approximately 180 seconds and at ambient temperature of 293 K. The use of natural gas required a computational time of 15 hours for 20 seconds into the 180 seconds fill as opposed to methane whereby only 4 minutes were required. The profiles of the gas temperature in the cylinder during the first 20 seconds of the fill for methane and CNG are quasi-similar. Thus, further simulations of the fast-fill were performed using methane which is the main component (95% mole fraction) of natural gas. With the ramp rate of 7.7 MPa/min and the volume of the banks set to 1200 L, the final mass of gas that was obtained at the end of the fill was 16.3 kg, which represented a difference of 2.4 % from the 16.7 kg that is specified in the car manual of the vehicle [25]. Lowering the volume of the banks to 400 L, led to an increase in the final mass of gas to 16.5 kg, which is due to the larger drop in the gas pressure occurring in the banks with decreasing volume. This results in increase in the isentropic cooling of the gas within the banks, thus further lowering the gas temperature at the exit of

the dispenser. The final gas temperature in the cylinder is 322 K, which is significantly lower than the maximum allowable limit of 358 K.

Similar to hydrogen filling, Type III cylinders were found to be more suitable for the fast-filling of natural gas. The aluminium liner with its high thermal conductivity and capacity results in a larger amount of heat transfer from the gas during the fill than the plastic liner. This results in a lower final gas temperature in the Type III cylinder as opposed to the Type IV cylinder and leads to an increase of 6.6 % in the final mass of gas.

The pressure ramp rate at the exit of the dispenser was also increased incrementally so as to reduce the fill time to approximately 150 s, 120 s, 90 s and 60 s. The simulations showed that increasing the dispensing pressure ramp does not significantly increase the gas temperature, since the heat flux at the wall of the cylinder also increases and compensates the faster rate of the compression of the gas in the cylinder. A fill time of approximately one minute was obtained when the dispensing pressure ramp rate was set to 22.8 MPa/min with the final mass of gas being 16.3 kg.

The fast-filling simulations also showed that the ambient temperature plays a huge role in the final mass of gas. Simulations of the fast-fill with the ambient temperatures varying ranging from 273 K to 313 K showed with increasing ambient temperatures, the final mass of gas reduces and thus lowers the range of the vehicle.

Imposing a step pressure profile of 25 MPa at the exit of the dispenser has shown that a faster fill can be achieved along with an increase in the final mass of gas. The large pressure difference that exists between the dispensing pressure and the gas pressure in the cylinder during the fill, leads to an initial large drop in the gas temperature in the cylinder due to the Joule-Thompson effect. The fill time is reduced by approximately 89% and is around 19 seconds compared of the lowest of the typical fill time of 3 minutes, while the final mass of gas is increased by approximately 6%. However, imposing a step pressure profile also leads to high pressure loses in the piping system, and thus for the range ambient temperatures used in the model (273 K – 313 K), the initial pressure in the 400 L bank must be at least 70 MPa.

The use of PCM-2 as part of the structure of the cylinder is mostly ineffective for the fast-filling of natural gas, since its melting range is between 308 K and 328 K, which is higher than the gas temperature in the cylinder when the ambient temperature is lower than 303 K.

7 Conclusions & Recommendations

Fast filling of high-pressure gas storage cylinders causes heating that can damage the cylinder. This thesis presents the development of computational models that predict the thermal response during the fast filling of high-pressure gas storage cylinders with hydrogen or natural gas. The study leads to conclusions relating, first, to how the thermal response to the filling process can be modelled in an accurate and computationally-efficient way, and second, relating to a range of approaches for achieving rapid filling without overheating the cylinder.

7.1 Computational modelling of cylinder filling

- Fast filling of high-pressure cylinders with a co-axial inlet nozzle can be accurately modelled with Computational Fluid Dynamics using the k-epsilon Reynolds Averaged Navier Stokes approach, provided accurate thermodynamic models are employed.
- Lumped models for the filling process can be applied in order to reduce the computational cost of assessing alternative filling strategies. A single-zone model with conjugate heat transfer through the cylinder wall is adequate for modeling cylinders with length-to-diameter aspect ratios up to four. For greater aspect ratios, multi-zone models should be used to account for uneven temperatures and heat transfer rates. The two main closure models required for the lumped models relate to the Nusselt number describing the convective heat transfer to the cylinder wall, and the discharge coefficient for the inflow through the nozzle.
    - The convective heat transfer to the cylinder wall rapidly develops quasi-steady behaviour in which the Nusselt number is approximately proportional to the jet Reynolds number. Modeling for the Nusselt number in each zone is provided, accounting for the effects of the length-to-diameter ratio and the ratio of cylinder and nozzle diameters.
    - The viscous discharge coefficient (C_{d1}) is found to depend on the isentropic Reynolds number, but it is not affected by real gas phenomena. The dependence on isentropic Mach number can be

accounted for by using different relationships for choked and unchoked conditions.

7.2 Analysis of the fast filling process

- Computational fluid dynamic simulations of fast-filling reveal that the region near to the inflow nozzle exhibits an axi-symmetric recirculating flow pattern that extends to approximately three cylinder diameters downstream from the inlet. Wall heat transfer in the recirculation region of the flow is driven strongly by the jet of turbulent fluid from the nozzle. The wall heat transfer in the recirculation region rapidly develops quasi-steady behaviour in which the Nusselt number is approximately proportional to the jet Reynolds number. The flow approaches this quasi-steady state over a time period that can be related to the convective timescales within the recirculation region.
- In cylinders with length-to-diameter aspect ratio greater than three, there is a region of axial flow downstream of the recirculation zone in which wall heat transfer is driven by convection and diffusion of turbulence from the recirculation zone. Noting that heat transfer is driven by turbulence produced within the recirculation zone, the quasi-steady Nusselt number in the downstream region can be modelled as a function of the cylinder aspect ratio and the Nusselt number in the recirculation zone.

7.2.1 Improved heat transfer in large aspect ratio cylinders

- The simulations show that wall heat transfer can be enhanced and peak wall temperatures reduced by dividing the fluid flow between separate nozzles. Directing the nozzles axially, ideally at intervals of around 4 cylinder diameters, prevents the formation of hot-spots due to regions of stagnant fluid. This can be achieved using co-axial inlet pipes in order to avoid the structural challenges and cost of introducing additional flow passages through the high-pressure cylinder.

7.2.2 Heat absorption with phase change materials

- The inclusion of a phase change material (PCM) with high conductivity to the structure of the cylinder is advantageous in lowering the final gas temperature, which subsequently increases the final mass of gas. However,

the inclusion of a PCM increases the structural mass of the cylinder and a PCM thickness of 2 mm placed in between the liner and laminate is the most effective in enhancing heat transfer while keeping the mass of the structure at its lowest.

7.3 Modelling of the CNG/H_2 filling station

- The model showed that the fast-filling of the Type IV hydrogen cylinders can be performed faster than the typical 3-5 minutes by increasing the delivery pressure ramp rates and lowering the pre-cooling temperatures. Type III cylinders are more suitable as a storage medium in hydrogen vehicles due to the higher thermal conductivity and capacity of the aluminium alloy. The presence of the PCM between the liner and laminate is mostly effective in Type III cylinders. The lowest pre-cooling temperature for the fast-filling of the newly designed Type III cylinders with PCM is 252 K and occurs for a fill time of 60 s when the ambient temperature is 313 K. The 252 K pre-cooling temperature is 19 K higher than the minimum pre-cooling temperature of 233 K, which is suggested by the hydrogen refuelling protocol SAE J2601 [17]. The decrease in the amount of pre-cooling that is required for the safe filling of the newly designed cylinders leads to energy savings.
- The fast-filling simulations of the Honda Civic GX with natural gas showed that the ambient temperature plays a huge role in the final mass of gas. Simulations of the fast-fill with the ambient temperatures varying ranging from 273 K to 313 K showed with increasing ambient temperatures, the final mass of gas is reduced and thus lowers the range of the vehicle. Imposing a step pressure profile of 25 MPa at the exit of the dispenser has shown that a faster fill can be achieved along with an increase in the final mass of gas. The fast-fill simulations of the natural gas vehicle also showed that the addition of a phase material (PCM-2) to the structure of the cylinder is mostly ineffective.

7.4 Recommendations for future work

The research presented in this thesis suggest a number of directions for further investigation:

- The two-zone model currently calculates an average temperature for both zone 1 and zone 2. The CFD models have shown that in cylinders that have a L/D greater than 3, the gas temperature increases axially in Zone 2. Further improvements to the two-zone model can be made whereby zone 2 is split into several zones and treated as a 1D in the axial direction.
- Modelling and determining the size of the compressor that is required for a particular filling station
- The accurate and efficient cylinder filling models developed in this thesis can be used as a basis for techno-economic and environmental optimisation of natural gas and hydrogen filling stations and distribution infrastructures.

Bibliography

[1] Gullberg M, Gahnstrom J, (2011). A Feasibility study for an LNG Filling Station Infrastructure and test of Recommendations. Baseline report, North European LNG Infrastructure Project.

[2] Valenti G, (2015). Hydrogen liquefaction and liquid hydrogen storage. Compendium of Hydrogen Energy, Vol 2, Pages 27-51.

[3] International Standard Organisation, (2009). Gaseous hydrogen and hydrogen blends- land vehicle fuel tanks, ISO/TS 15869.

[4] International Standard Organization, (2005). Gas Cylinders – High Pressure Cylinders for on-Board Storage of Natural Gas as Fuel for Automotive Vehicles, ISO 11439.

[5] Kim S.C, Lee S.H, Yoon K.B, (2010). Thermal characteristics during hydrogen fueling process of type IV cylinder. International Journal of Hydrogen Energy, Vol 35, Pages 6830-6835.

[6] Dicken C.J.B & Merida W, (2007) Measured effects of filling time and initial mass on the temperature distribution within a hydrogen cylinder during refuelling. Journal of Power Sources, Vol 165, Pages 324-336.

[7] Dicken C.J.B & Merida W, (2007) Modelling the Transient Temperature Distribution within a Hydrogen Cylinder during Refueling. Nuerical Heat Transfer, Part A: Applications: An International Journal of Computation and Methodology, Vol 53:7, Pages 685-708.

[8] Suryan A, Kim H.D, Setoguchi T, (2012). Three-dimensional numerical computations on the fast-filling of a hydrogen tank under different conditions. International Journal of Hydrogen Energy, Vol 37, Pages 7600-7611.

[9] Wilcox D.C, (1998). Turbulence modelling for CFD. California: DCW Industries.

[10] Liss W, Czachorski M, Kountz K, (2015). Sizing and Operating Considerations For Natural Gas and Hydrogen Fueling Systems. Gas Technology Institute.

[11] Guo X.Y, (1996). Pre-feasibility of Developing Compressed Natural Gas Automobiles in Beijing. China North Vehicle Research Institute, Beijing.

[12] British Petroleum (BP), (2014). BP Statistical Review of World Energy. http://www.bp.com/en/global/corporate/about-bp/energy-economics/statistical-review-of-world-energy.html. [Last accessed: Oct 20, 2015].

[13] Khan M.I, Yasmin T, Shakoor A, (2015). Technical overview of compressed natural gas (CNG) as transportation fuel. Renewable and Sustainable Energy Reviews, 51, 785-797.

[14] U.S. Department of Energy, (2015). EPAct Transportation Regulatory Activities. http://www1.eere.energy.gov/vehiclesandfuels/epact/fuel_conversion_factors.html. [Last accessed: Oct 20, 2015].

[15] U.S. Department of Energy, (2015). Alternative Fuels Data Center – Fuel Properties Comparison. http://www.afdc.energy.gov/fuels/fuel_comparison_chart.pdf. [Last accessed: Oct 20, 2015].

[16] U.S. Department of Energy, (2015). Fuel Economy of 2015 Subcompact Cars. http://fueleconomy.gov/feg/byclass/Subcompact_Cars2015.shtml. [Last accessed: May 01, 2016].

[17] SAE INTERNATIONAL, (2010). Fueling Protocols for Light Duty Gaseous Hydrogen Surface Vehicles. http://standards.sae.org/j2601_201003/. [Last accessed: Oct 20, 2015].

[18] Ambrose A.F, Al-Amin A.Q, Rasiah R, Saidur R, Amin N, (2016). Prospects for introducing hydrogen fuel cell vehicles in Malaysia. International Journal of Hydrogen Energy.

[19] Lane, B, (2016). Hydrogen fuel cell cars. http://www.nextgreencar.com/fuelcellcars/. [Last accessed: July 16, 2016].

[20] Toyota Motor Corporation, (2016). Powering the future – Hydrogen fuel cell vehicles could change mobility forever. http://www.toyota-global.com/innovation/environmental_technology/fuelcell_vehicle/. [Last accessed: July 16, 2016].

[21] SAE INTERNATIONAL, (1994). Recommended Practice for Compressed Natural Gas Vehicle Fuel. http://standards.sae.org/j1616_199402/. [Last accessed: Oct 20, 2015].

[22] Gas Vehicle Hub, (2014). Gas Vehicle Availability. http://www.gasvehiclehub.com/gas-vehicle-availability. [Last accessed: Oct 24, 2015].

[23] Ramsey M, (2015). Honda to Discontinue CNG and Hybrid Civic Models. http://www.wsj.com/articles/honda-to-discontinue-cng-and-hybrid-civic-models-1434386062. [Last accessed: Nov 10, 2015].

[24] U.S. Department of Energy, (2016). Hybrids, Diesels, and Alternative Fuel cars. http://www.fueleconomy.gov/feg/alternatives.shtml. [Last accessed: April 13, 2016].

[25] Honda, (2016). Owner's Manual and Warranty Booklet. http://www.owners.honda.com/vehicles/information/2015/Civic-Natural-Gas/manuals. [Last accessed: April 15, 2016].

[26] Hirotani R, Tomioka J, Meada Y, Mitsuibishi H, Watanabe S, (2006). Thermal Behavior in Hydrogen Storage Tank for Fuel Cell Vehicle on Fast-filling. In Proceedings of the 16th World Hydrogen Energy Conference, Lyon, France.

[27] Baraldi D, Melideo D, Galassi M.C, Cebolla R.O, Iborra B.A, Moretto P, (2014). CFD model performance benchmark of fast-filling simulations of hydrogen tanks with pre-cooling. International Journal of Hydrogen Energy, Vol 39, Pages 4389-4395.

[28] Zheng J, Guo J, Yang J, Zhao Y, Zhao L, Pan X, Ma J, Zhang L, (2013). Experimental and numerical study on temperature rise within a 70MPa type III cylinder during fast refuelling. International Journal of Hydrogen Energy, Vol 38, Pages 10956-10962.

[29] Woodfield P.L, Monde M, Takano T, (2008). Heat Transfer Characteristics for Practical Hydrogen Pressure Vessels Being Filled at High Pressure. Journal of Thermal Science and Technology. Vol 3, Pages 241-254.

[30] Johnson, T, Bozinoski R, Ye J, Sartor, G, Zheng J, Yang J, (2015). Thermal development and validation for rapid filling of high pressure hydrogen tanks. International Journal of Hydrogen Energy, Vol 40, Pages 9803-9814.

[31] Met Office, (2016). Where's hot when? http://www.metoffice.gov.uk/holiday-weather/where-is-hot. [Last accessed: April 15, 2016].

[32] Cebolla R.O, Acosta B, Miguel N, Moretto P, (2015). Effect of precooled inlet gas temperature and mass flow rate on final state of charge during hydrogen vehicle refuelling. International Journal of Hydrogen Energy, Vol 40, Pages 4698-4706.

[33] Kim H.D, Suryan A, Setoguchi T, (2013). Comparative study of turbulence models performance for refuelling of compressed hydrogen. International Journal of Hydrogen Energy, 38, 9562-9569.

[34] Redlich O, Kwong J.N.S, (1949). On the thermodynamics of solutions, an equation of state, fugacities of gaseous solutions. Chemical Reviews, Vol 44, Page 233.

[35] Keszei, E, (2012). Chemical Thermodynamics: An Introduction. Springer-Verlag, Berlin. Pages 22-23.

[36] Compressed Gas Association, (1990). Handbook of Compressed Gases. Chapman & Hall, New York, Page 22.

[37] Launder B.E, Spalding D.B, (1972). Lectures in Mathematical Models of Turbulence. Academic Press, London.

[38] Shih T.H, Liou W.W, Shabbir A, Yang Z, Zhu J.A, (1995). A new k-ε eddy viscosity model for high Reynolds number turbulent flows – model development and validation. Computational Fluids, Vol 24, Pages 227-238.

[39] Yakhot V, Orszag S.A, (1986). Renormalization group analysis of turbulence: 1. Basic theory. Journal of Scientific Computation, Vol 1, Pages 3-51.

[40] Menter F.R, (1994). Two-equation eddy-viscosity turbulence models for engineering applications. AIAA Journal, Vol 32, Pages 1598-1605.

[41] Kim H.D, Suryan A, Setoguchi T, (2012). Three-dimensional numerical computations on fast-filling of a hydrogen tank under different conditions. International Journal of Hydrogen Energy, Vol 37, 7600-7611.

[42] Soave G, (1972). Equilibrium constants from a modified Redlich-Kwong equation of state. Chemical Engineering Science, Vol 27, Page 1197.

[43] Aungier R.H, (1995). A fast, accurate real gas equation of state for fluid dynamic analysis applications. ASME Journal of Fluids Engineering, Vol 117, Pages 277-281.

[44] Peng D.Y, Robinson D.B, (1976). A new two-constant equation of state. Industrial & Engineering Chemistry Fundamentals, Vol 15, Pages 59-64.

[45] Lienhard J.H IV, Lienhard J.H V, (2008). A heat transfer textbook. Phlogiston Press, Massachusetts, 3rd Edition, Page 10.

[46] Galassi M.C, Papanikolaou E, Heitsch M, Baraldi D, Iborra B.A, Moretto P, (2014). Assessment of CFD models for hydrogen fast-filling simulations. International Journal of Hydrogen Energy. Vol 39, Pages 6252-6260.

[47] Wang L, Zheng C, Wei S, Wang B, Wei Z, (2015). Thermo-mechanical investigation of composite high-pressure hydrogen storage cylinder during fast-filling. International Journal of Hydrogen Energy, Vol 40, Pages 6853-6859.

[48] Melideo D, Baraldi D, (2014). CFD analysis of fast-filling strategies for hydrogen tanks and their effects on key parameters. International Journal of Hydrogen Energy. Vol 40, Pages 735-745.

[49] Kountz K, (1994). Modelling The Fast-fill Process in Natural Gas Storage Cylinders. American Chemical Society Paper at the 207th National ACS Meeting.

[50] Molerus O, Wirth K.E, (1997). Heat Transfer in Fluidized Beds. Chapman & Hall, London, 1st Edition. Pages 126-127.

[51] Farzaneh-Gord M, (2011). REAL AND IDEAL GAS THERMODYNAMIC ANALYSIS OF SINGLE RESERVOIR FILLING PROCESS OF NATURAL

GAS VEHICLE CYLINDERS. Journal of Theoretical and Applied Mechanics, Vol 41, 21-36.

[52] Shah R.K, Sekulic D.P, (2003). Fundamentals of Heat Exchanger Design. John Wiley & Sons, New Jersey. Page 446.

[53] Means J.D, (1973). Transient Convective Heat Transfer in Closed Containers during and After Gas Injection. Brigham Young University, Ph.D Thesis.

[54] Clark G.L, (1983). A zero-Dimensional Model of Compressible Gas Flow in Networks of Pressure Vessels – Program TRIC. Sandia National Laboratories, USA.

[55] Monde M, Mitsutake Y, Woodfield P.L, Maruyama S, (2006). Characteristics of Heat Transfer and Temperature Rise of Hydrogen during Rapid Hydrogen Filling at High Pressure. Japan Society of Mechanical Engineers, Ser B 72, Pages 738-744.

[56] Zheng J, Guo J, Yang J, Zhao Y, Pan X, Zhang L, Zhao, (2014). Investigations on temperature variation within a type III cylinder during the hydrogen cycling test. International Journal of Hydrogen Energy, Vol 39, Pages 13926-13934.

[57] Striednig M, Brandstatter S, Sartory M, Klell M, (2014). Thermodynamic real gas analysis of tank filling process. International Journal of Hydrogen Energy, Vol 39, Pages 8495-8509.

[58] Petukhov B.S, (1970). Heat transfer and friction in turbulent pipe flow with variable physical properties. Advances in Heat Transfer, Vol 6, Pages 504-564.

[59] Ranong C.N, Mauss S, Hapke J, Fieg G, Wenger D, (2011). Approach for the Determination of Heat Transfer Coefficients for Filling Processes of Pressure Vessels With Compressed Gaseous Media. Heat Transfer Engineering, Vol 32:2, Pages 127-132.

[60] Deymi-Dashtebayaz M, Gord M.F, Rahbari H, R, (2012). Studying Transmission of Fuel Storage Bank to NGV Cylinder in CNG Fast-filling

Station. Journal of Brazil Society of Mechanical Science and Engineering. Vol XXXIV, No 4, Pages 429-435.

[61] National Fire Protection Association, (2010). Vehicular Gaseous Fuel Systems Code, 2010 Edition.

[62] Cengel Y.A, Cimbala M.J, (2006). Fluid Mechanics – Fundamentals and Applications. McGraw Hill, New York. Pages 321 – 364.

[63] White F.M, (2011). Fluid Mechanics. McGraw Hill, New York, 7th Edition. Pages 347 – 429, Page 827.

[64] CRANE, (1988). Flow of fluids through valves, fitting and pipe – Technical Paper No 410. CRANE CO. Pages 1-7 – 1-9.

[65] U.S. Energy Information Administration (2007). Natural gas compressor stations on the interstate pipeline network: Development since 1996. EIA, Office of Oil and Gas.

[66] Weymouth T.R, (1912). Transactions of American Society of Mechanical Engineers. Vol 34, Page 197.

[67] Grizzle B.F, (1945). Simplification of Gas Flow Calculations by Means of a New Special Slide Rule. Petroleum Engineer.

[68] Moody L.F, (1944). Friction Factors for Pipe Flow. ASME Trans, Vol 66, Pages 671 – 684.

[69] Balachandran P, (2006). Fundamentals of Compressible Fluid Dynamics. PHI Learning Pvt. Ltd, India. Pages 87-88.

[70] Johnson, A, and Wright J, (2008). Comparison Between Theoretical CFV Flow Models and NIST's Primary Flow Data in the Laminar, Turbulent, and Transition Flow Regimes. Journal of Fluids Engineering, Vol 130, Pages 071202-1 – 071202-12.

[71] Ding, H., and Wang, c., (2014). Flow characteristics of hydrogen gas through critical nozzle, International Journal of Hydrogen Energy, Vol 39, Pages 3947-3955.

[72] ISO 5167, (2003). Measurement of fluid flow by means of pressure differential devices inserted in circular cross-section conduits running full, British Standards, London, United Kingdom.

[73] Mehling H, Cabeza L.F, (2008). Heat and cold storage with PCM.Springer-Verlag, Berlin, Pages 11-51 & Pages 128-130.

[74] Air Liquide, (2014). RESERVOIR COMPOSITE DE GAZ SOUS PRESSION ET PROCEDE DE REMPLISSAGE. Institut National de la Propriete Industrielle. Numero de publication : 3 017 442. Numero d'enregistrement national : 14 51104.

[75] Benson D.K, Webb J.D, McFadden J.D.O, Christensen C, (1985). Materials Research for Passive Solar Systems: Solid-State Phase-Change Materials. Solar Energy Research Institute, Colorado. Page 3.

[76] Mansoori G, Barnes H.L, Webster G.M, (2003). Fuels and Lubricants Handbook. ASTM International, Pennsylvania, Page 535.

[77] Mills A, Farid M, Selman J.R, Al-Hallaj S, (2006). Thermal conductivity enhancement of phase change materials using a graphite matrix. Applied Thermal Engineering, Vol 26, Pages 1652-1661.

[78] Cabeza L, Mehling H, Hiebler S, Ziegler F, (2002). Heat transfer enhancement in water when used as PCM in thermal energy storage. Applied Thermal Engineering. Vol 22, Pages 1141-1151.

[79] Rothuizen E.D, Rokni M, Elmegaard B, (2013). Hydrogen Fuelling Stations: A Thermodynamic Analysis of Fuelling Hydrogen Vehicles for Personal Transportation. Technical University of Denmark. Department of Mechanical Engineering.

[80] Omdahl N.H, (2014). Modeling of a Hydrogen Refueling Station. Norvegian University of Science and Technology, Master Thesis.

[81] ANSYS, Inc. (2012). ANSYS FLUENT Theory Guide.

[82] Younglove B.A, (1982). Thermophysical Properties of Fluis. I. Argon, Ethylene, Parahydrogen, Nitrogen, Nitrogen Trifluoride and Oxygen. Journal Physics & Chemistry, Vol 11, Pages 1-11.

[83] Farokhi S, (2014). Aircraft Propulsion. John Wiley & Sons Ltd, United Kingdom. Pages 21-103.

[84] Deaver F.K and Eckert E.R.G, (1970) An interferometric Investigation of Convective Heat Transfer in a Horizontal Fluid Cylinder with Wall Temperature Increasing at a Uniform Rate. Proceedings of the Fourth International Heat Transfer Conference, Vol 4, Paris, paper NC 1.1.

[85] Ozisik M.N, (1994). Finite Difference Methods in Heat Transfer. CRC Press, Florida, Pages 275-306.

[86] Alam M.M.A, Setoguchi T, Matsuo, (2014). An Attempt of Simulating the Real Time Filling of H2 Cylinder at 70 MPa. OTEC, Vol 19, Pages 27-32.

[87] Environmental Protection Agency, (1996). The EPA 10 Gallon per minute fuel dispensing limit. https://www3.epa.gov/otaq/regs/ld-hwy/evap/spitback.txt. [Last accessed: August 15, 2016].

[88] Rojey A, Jaffret C, (1997). Natural Gas – Production Processing Transport.Editions Technip, Paris, Page 80.

[89] Haaland S.E, (1983). Simple and Explicit Formulas for the Friction Factor in Turbulent Pipe Flow. Journal of Fluids Engineering, Pages 89-90.

[90] Colebrook C.F, (1938-1939). Turbulent Flow in Pipes, with Particular Reference to the Transition between Smooth and Rough Pipe Laws. Journal of the Institute of Civil Engineers, London, Vol 11, Pages 133-156.

[91] Kyle B.J, (2000). Chemical and Process Thermodynamics 3/E 564. Pearson Education, Inc., Upper Saddle River, NJ, USA.

[92] Ball M, Wietschel M, (2009). The Hydrogen Economy – Opportunities and Challenges. Cambridge University Press, UK, Page 34.

[93] Favre A, (1965). Equations des Gaz Turbulents Compressible. Journal de Mecanique, Vol 4, No 3, Pages 361-390.

[94] Nave C.R, (2017). Specific Heats of Gases. http://hyperphysics.phy-astr.gsu.edu/hbase/Kinetic/shegas.html. [Last accessed: March 15, 2018].

[95] Engineering ToolBox, (2004). Universal and Individual Gas Constants. https://www.engineeringtoolbox.com/individual-universal-gas-constant-d_588.html. [Last accessed: March 15, 2018].

Appendix A1 - Thermal properties of hydrogen gas

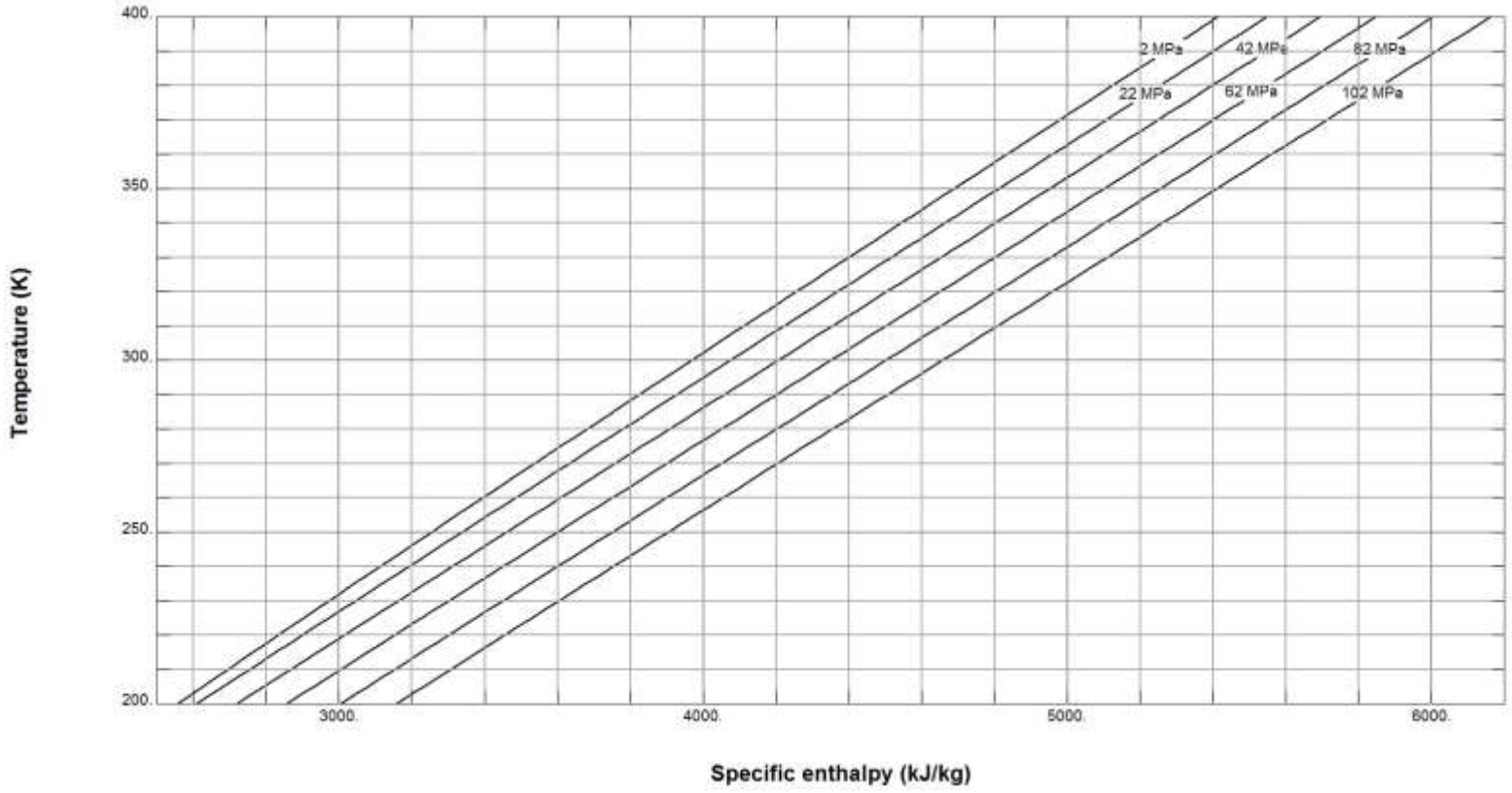

Figure 0.1: Specific enthalpy of hydrogen at different temperatures and pressures.

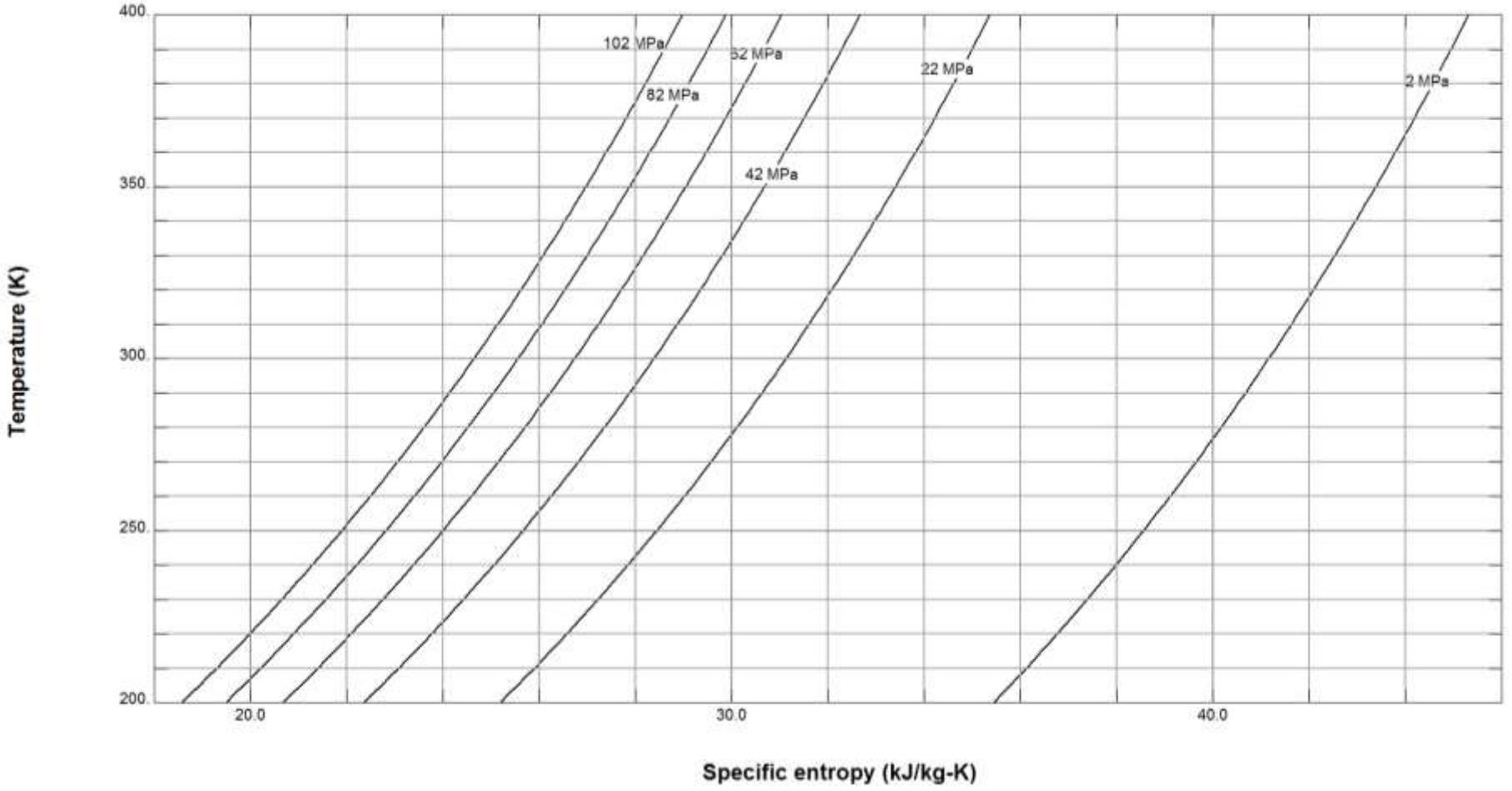

Figure 0.2: Specific entropy of hydrogen at different temperatures and pressures.

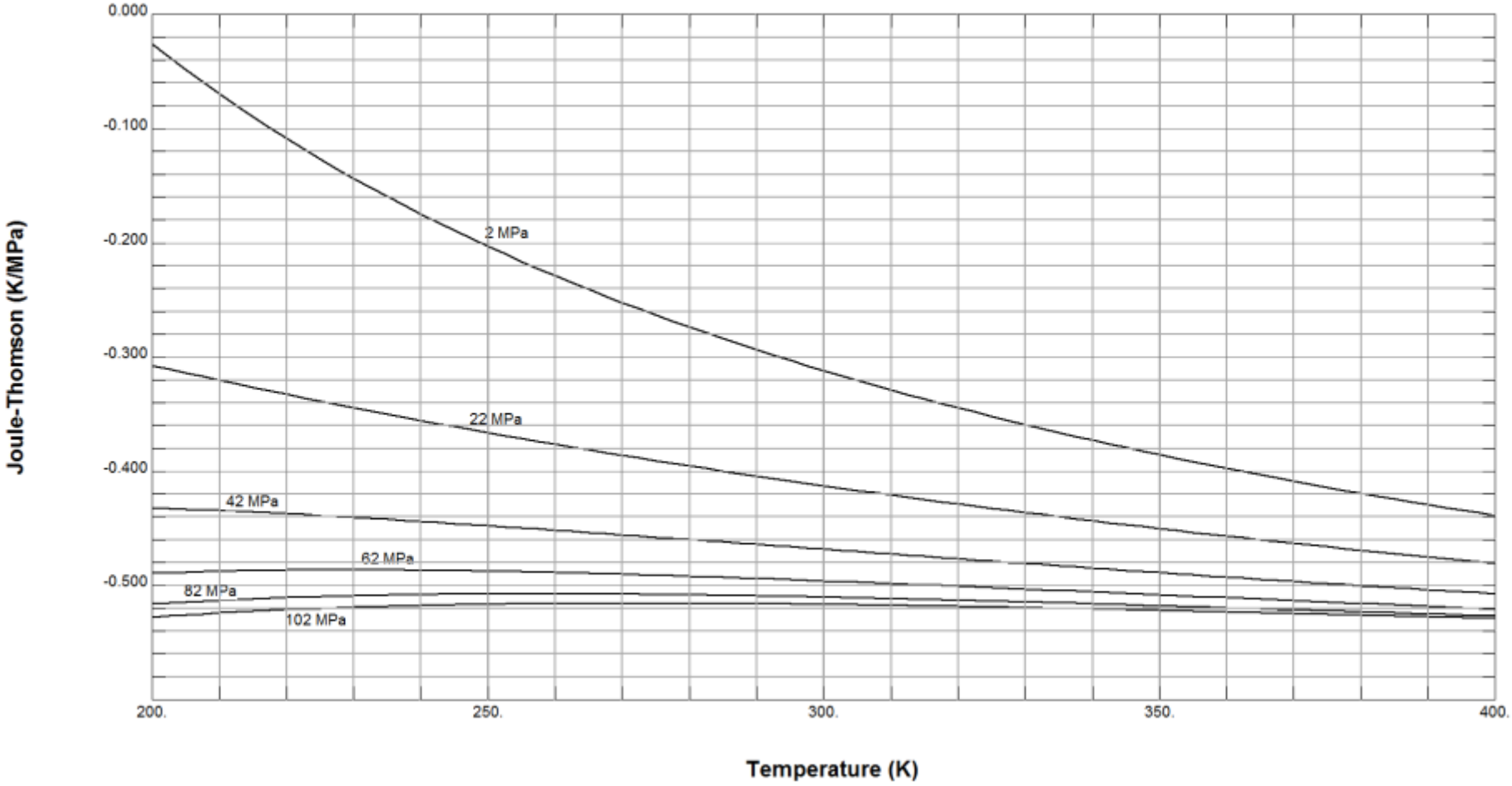

Figure 0.3: Joule-Thomson coefficient of hydrogen at different temperatures and pressures.

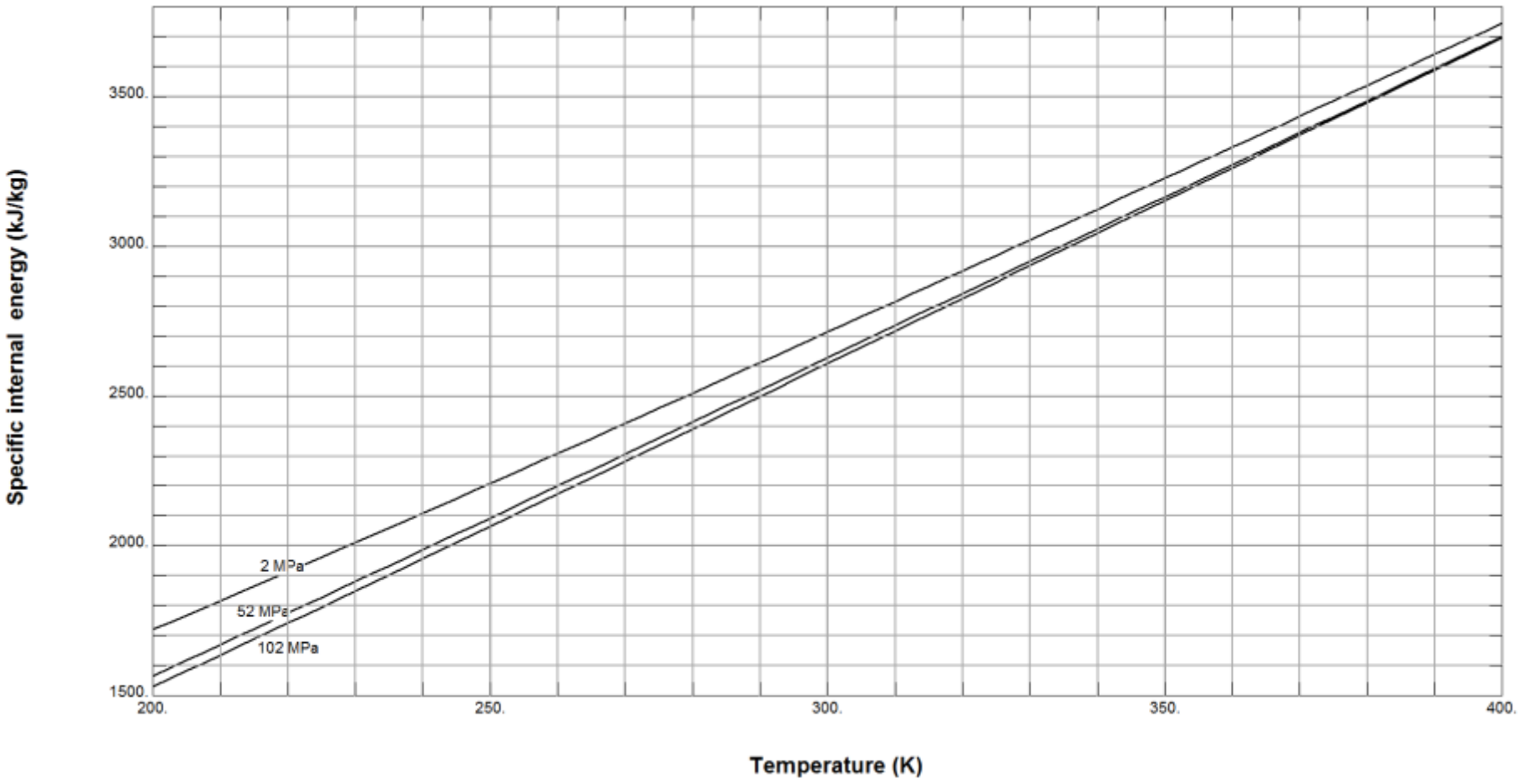

Figure 0.4: Specific internal energy of hydrogen at different pressures and temperatures.

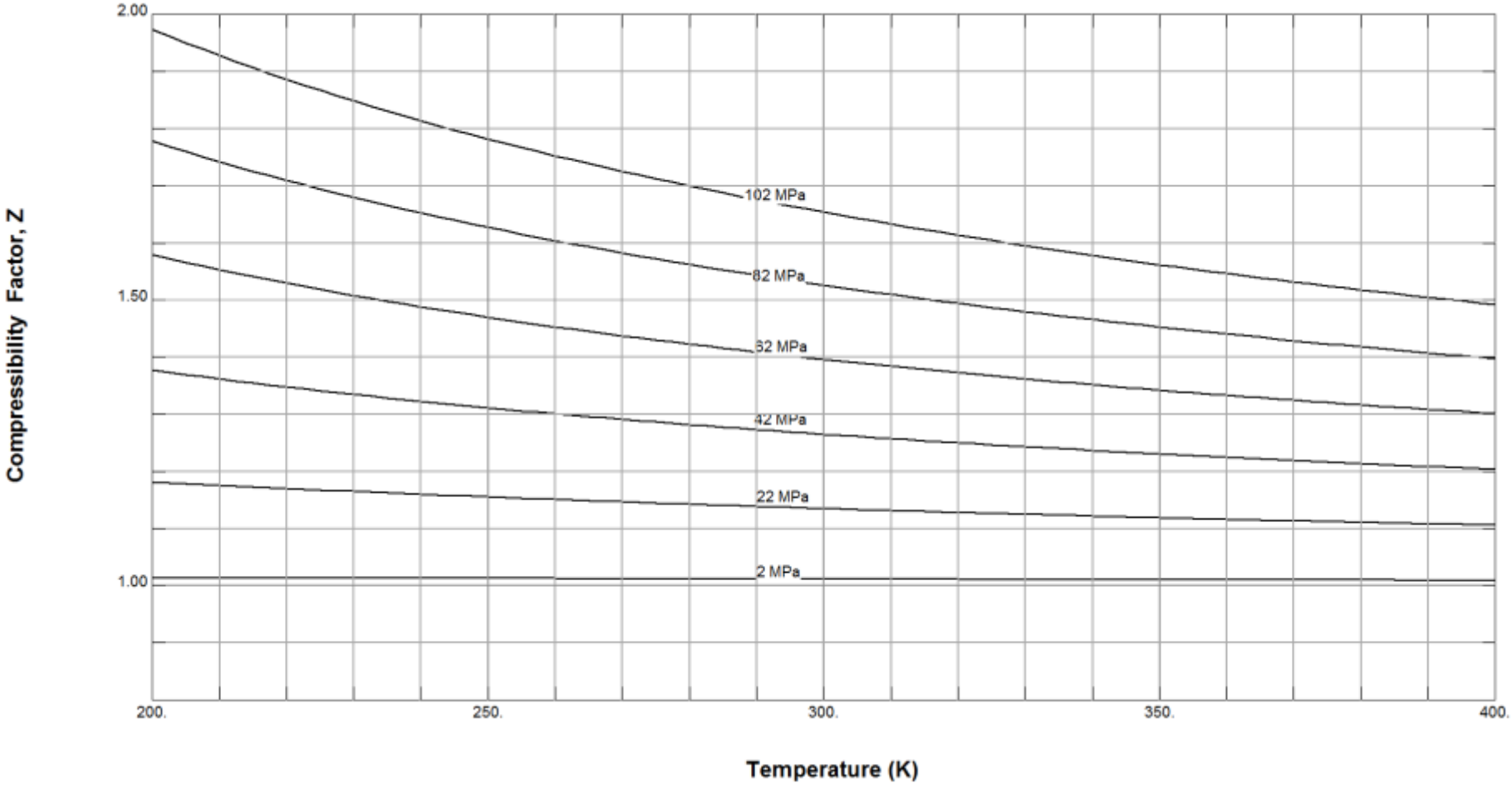

Figure 0.5: Compressibility factor of hydrogen at different pressures and temperatures.

Appendix A2 - Thermal properties of methane

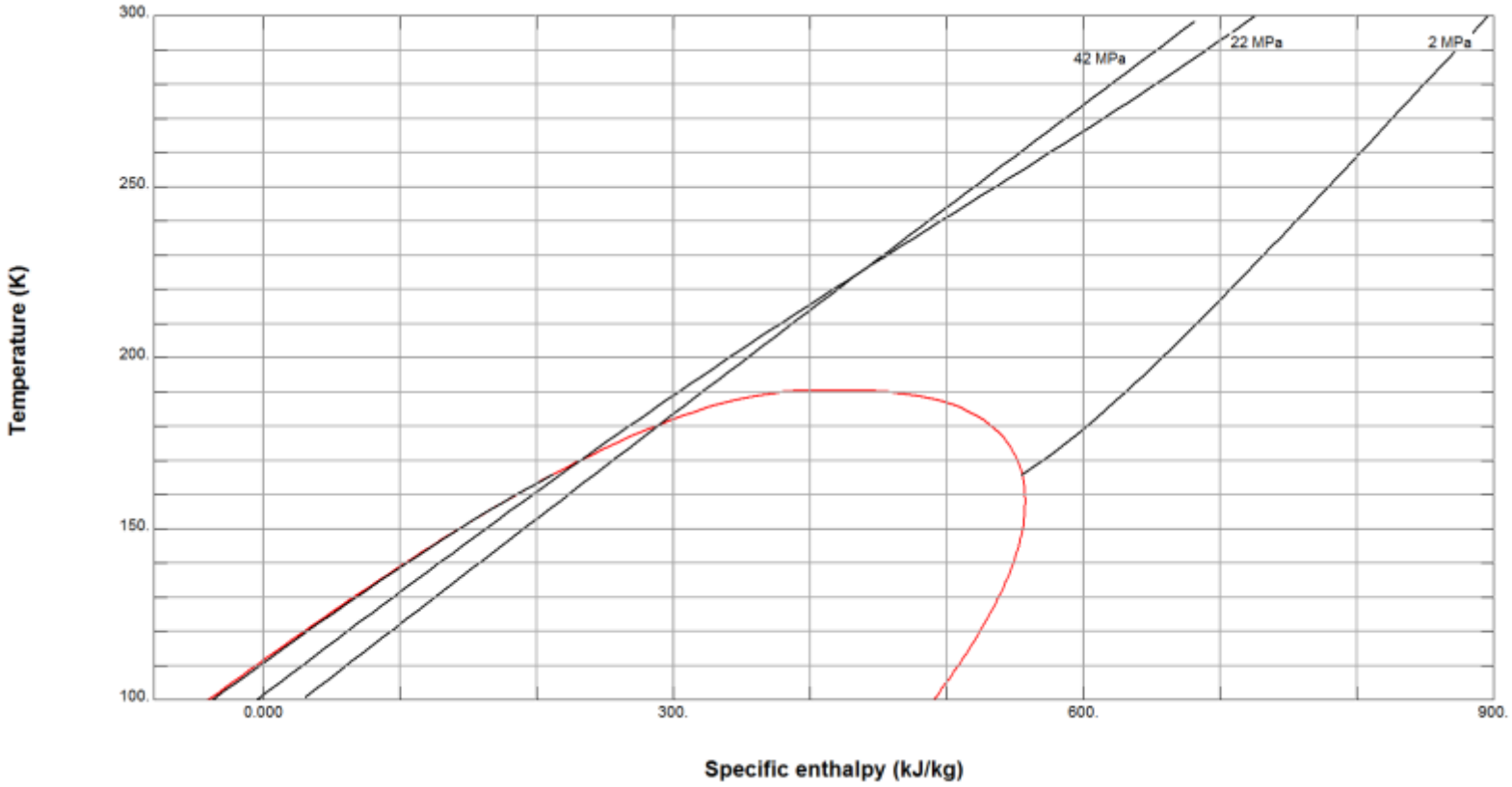

Figure 0.1: Specific enthalpy of methane at different temperatures and pressures.

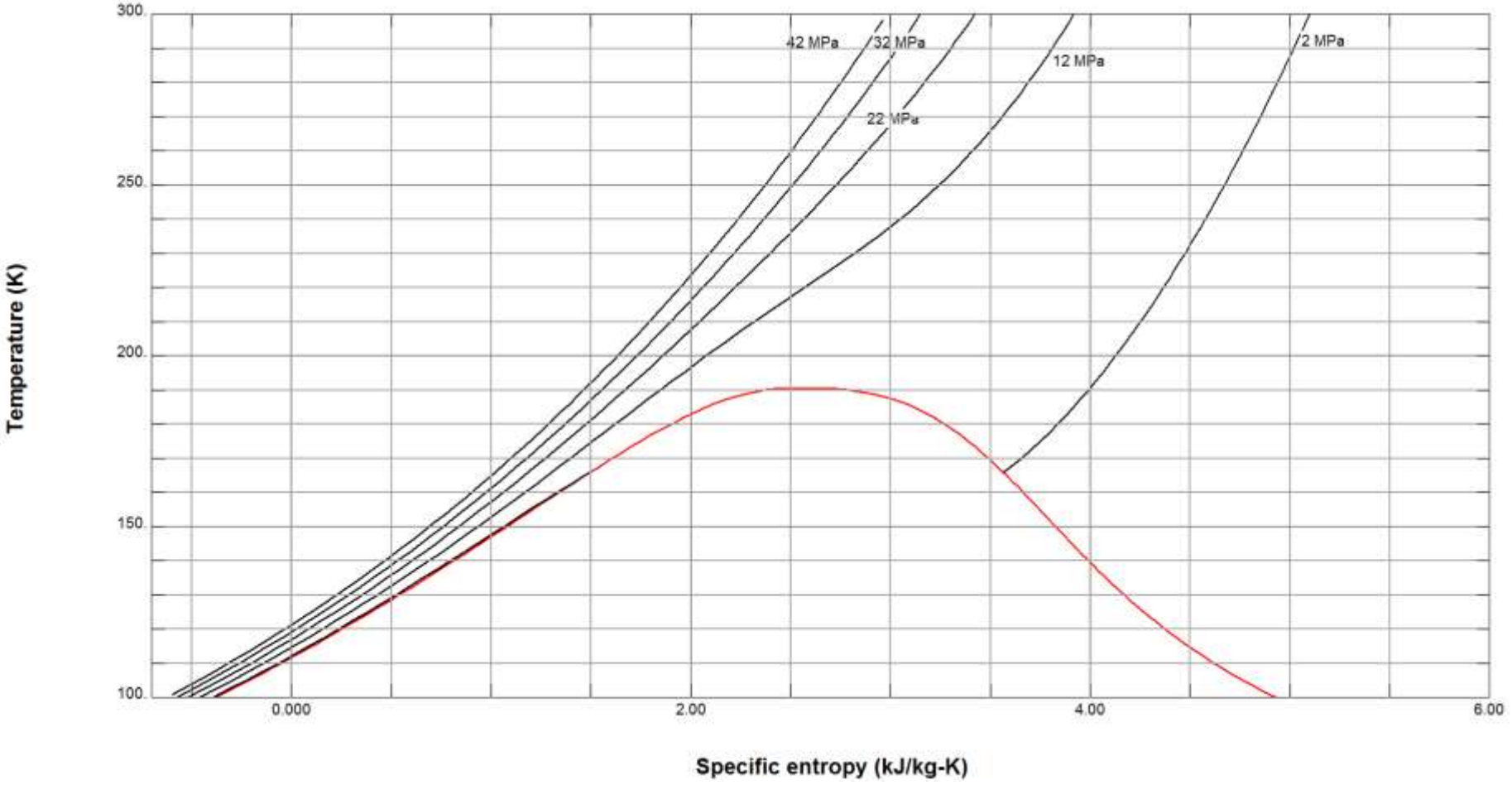

Figure 0.2: Specific entropy of methane at different temperatures and pressures.

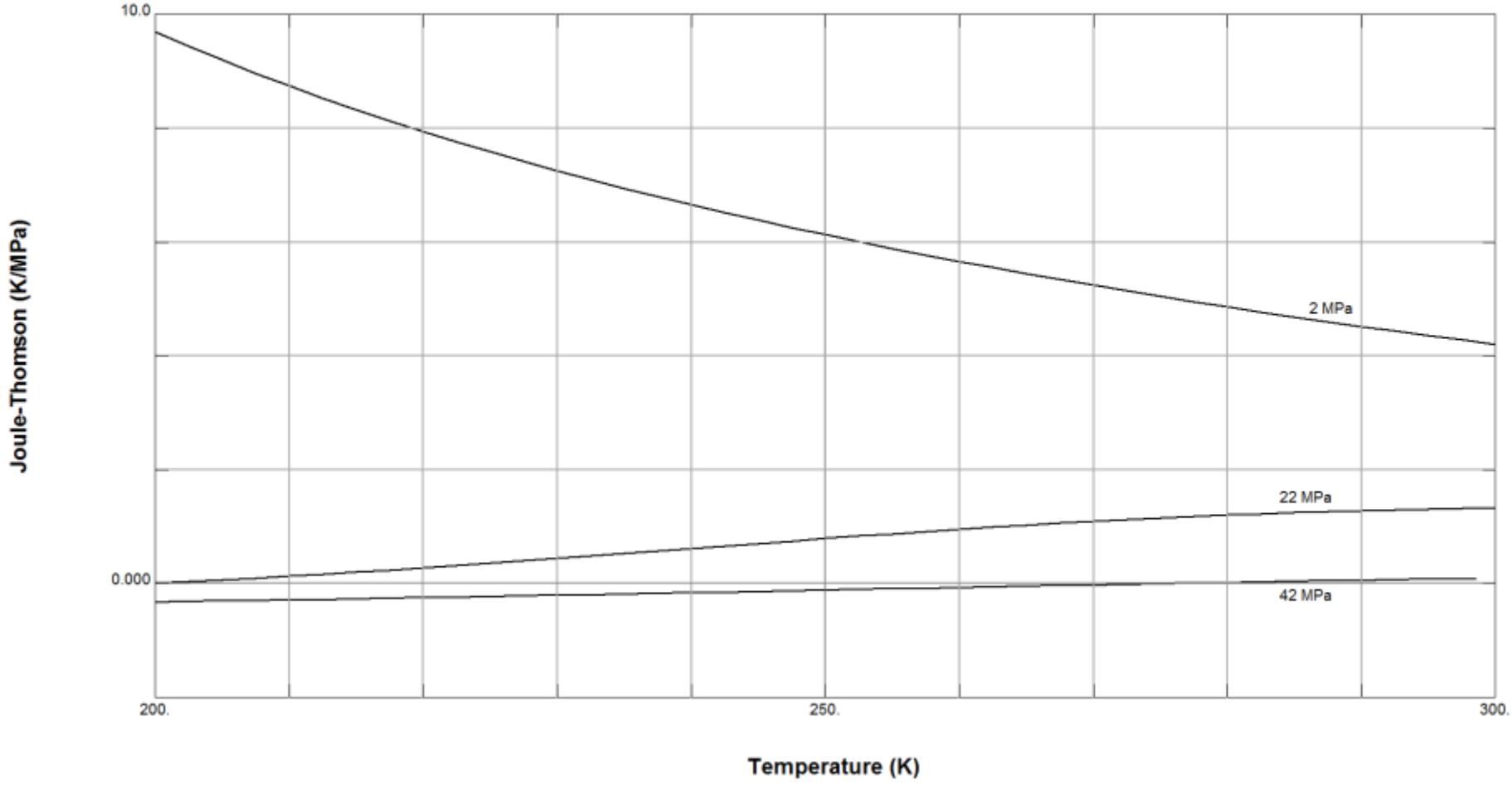

Figure 0.3: Joule-Thomson coefficient of methane at different temperatures and pressures.

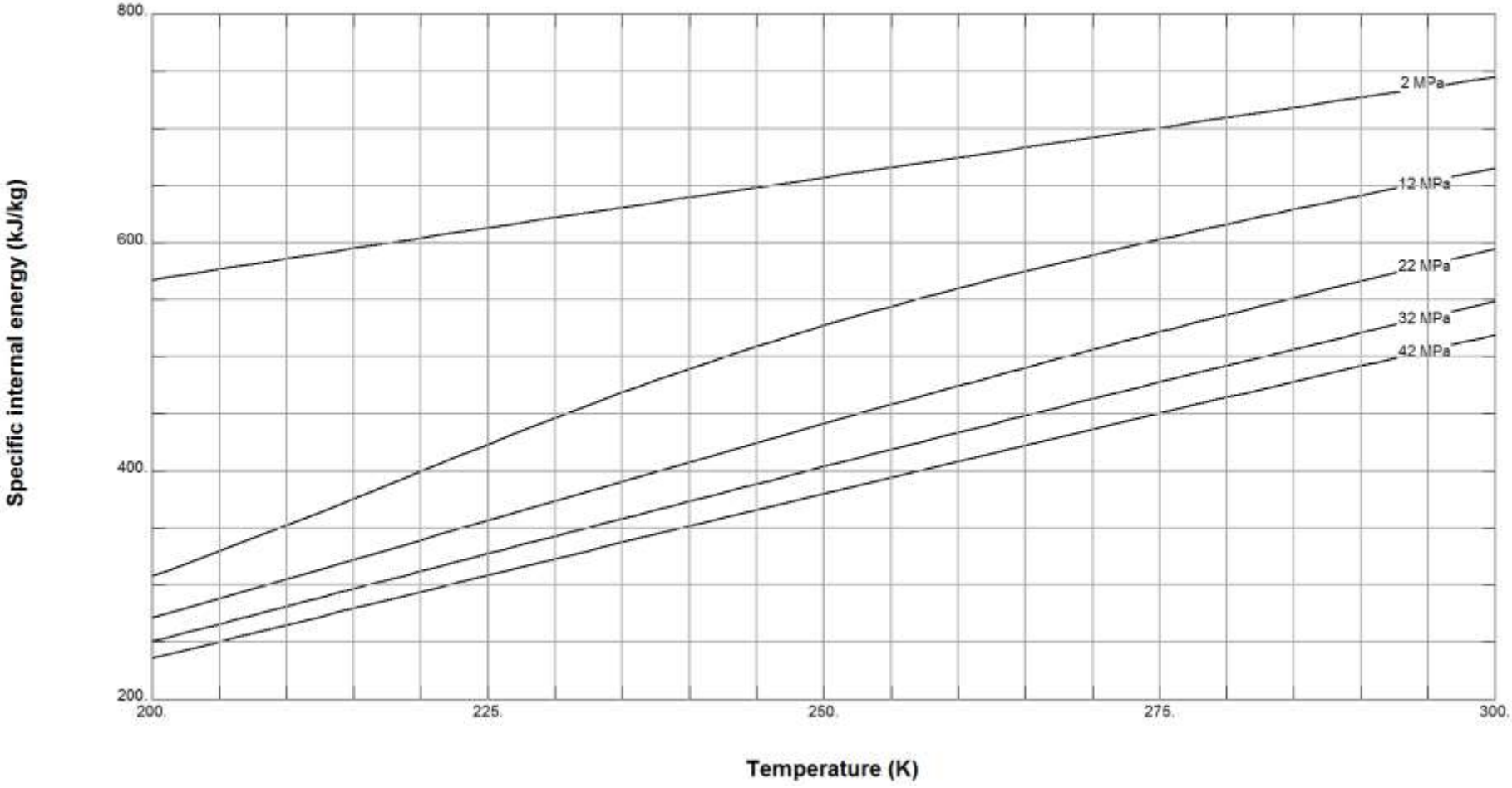

Figure 0.4: Specific internal energy of methane at different pressures and temperatures.

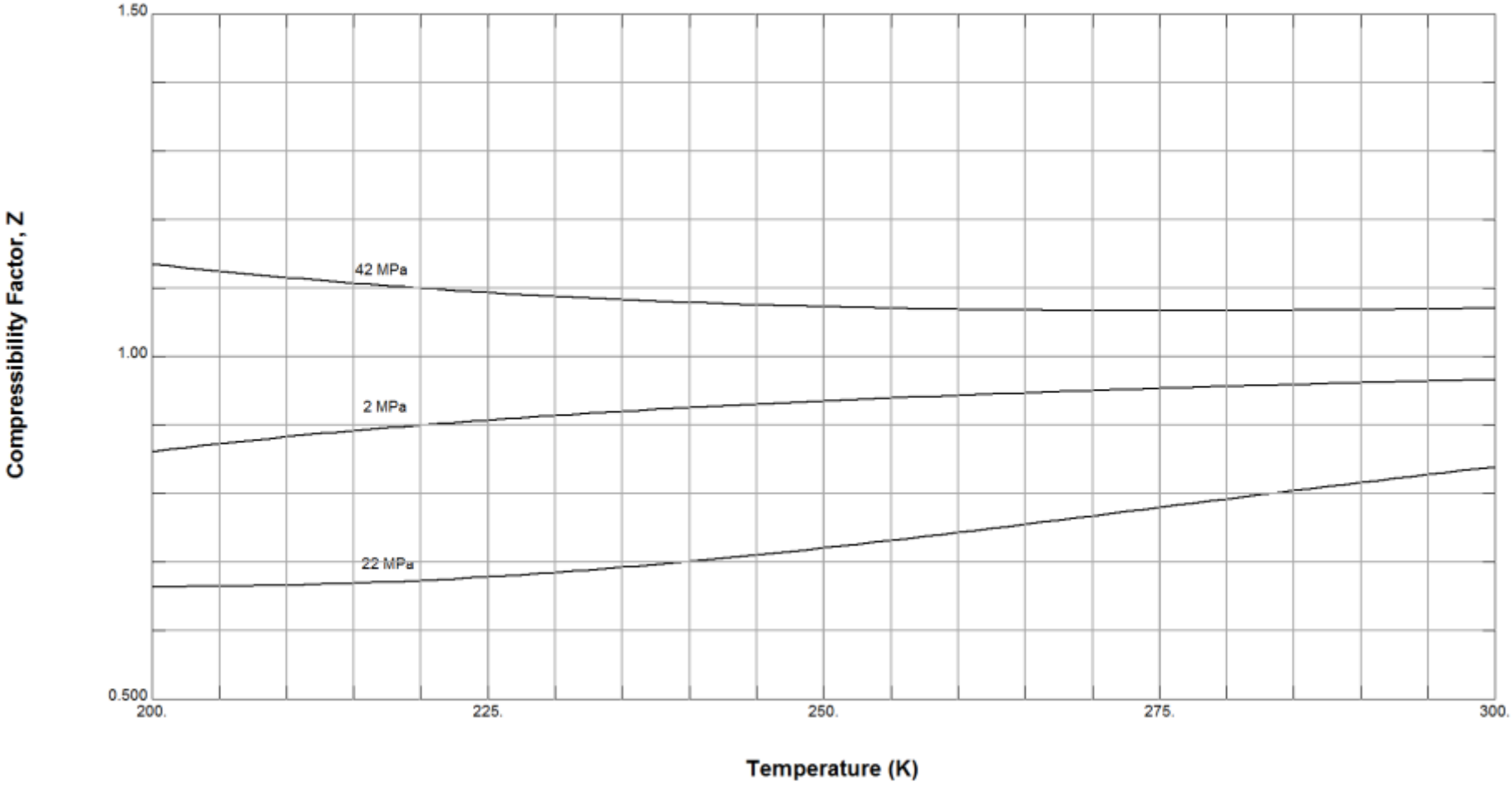

Figure A2.5: Compressibility factor of methane at different pressures and temperatures.

Appendix A3 - Closure Strategies

A3.1 The Reynolds stress

The standard *k-ε* model uses the Boussinesq approximation to close the Reynolds stress tensor $\left(-\overline{\rho u_j'' u_i''}\right)$.

$$-\overline{\rho u_j'' u_i''} = \nu_T \left(\frac{\partial \tilde{u}_i}{\partial x_j} + \frac{\partial \tilde{u}_j}{\partial x_i} - \frac{2}{3} \frac{\partial \tilde{u}_k}{\partial x_k} \delta_{ij} \right) - \frac{1}{3} \overline{\rho u_l'' u_l''} \delta_{ij}$$

The *k-ε* model involves PDE of the transport equations of the turbulent kinetic energy per unit mass *k* and the dissipation rate per unit mass *ε*. The two-transport PDE that are implemented in FLUENT [85] are as follows:

$$\frac{\partial}{\partial t}(\bar{\rho} k) + \frac{\partial}{\partial x_i}(\bar{\rho} k \tilde{u}_i) = \frac{\partial}{\partial x_j}\left[\left(\bar{\mu} + \frac{\nu_T}{\sigma_k} \right) \frac{\partial k}{\partial x_j} \right] + G_k + G_b - \rho \varepsilon - Y_M + S_k$$

$$\frac{\partial}{\partial t}(\bar{\rho} \varepsilon) + \frac{\partial}{\partial x_i}(\bar{\rho} \varepsilon \tilde{u}_i) = \frac{\partial}{\partial x_j}\left[\left(\bar{\mu} + \frac{\nu_T}{\sigma_\varepsilon} \right) \frac{\partial \varepsilon}{\partial x_j} \right] + C_{1\varepsilon} \frac{\varepsilon}{k} (G_k + C_{3\varepsilon} G_b) - C_{2\varepsilon} \bar{\rho} \frac{\varepsilon^2}{k} + S_\varepsilon$$

$C_{1\varepsilon}$, $C_{2\varepsilon}$, $C_{3\varepsilon}$ are constants and have values of 1.44, 1.92 and 1.

The eddy viscosity is determined as follows:

$$\nu_T = \bar{\rho} C_\mu \frac{k^2}{\varepsilon}$$

C_μ is a constant of the model and has a value of 0.09.

A3.2 The turbulent kinetic energy

In the case of the standard two-equation *k-ε* model, closure of the turbulent kinetic energy occurs naturally since it is expressed in terms of the turbulent kinetic energy, k and the dissipation rate per unit mass, *ε*.

A3.3 The Reynolds heat flux

The Reynolds heat flux vector $-\overline{\rho u_j'' h''}$ which is due to the correlation of the turbulent fluctuations of velocity and enthalpy is closed by a model heat flux. The unclosed term$-\overline{\rho u_j'' h''}$ is replaced by a model flux Q_j which can be written as:

$$Q_j \equiv -k_t \frac{\partial \tilde{T}}{\partial x_j}$$

The term k_t is known as the eddy thermal conductivity and is a function of both the lent Prandtl number and the eddy viscosity obtained by the turbulence model such that:

$$k_t \equiv \frac{C_p \nu_T}{Pr_t}$$

Where the Prandtl number is assumed to be constant.

Thus the Reynolds heat flux $-\overline{\rho u_j'' h''}$ can thus be written in terms of the Favre-averaged enthalpy as:

$$-\overline{\rho u_j'' h''} = Q_j \equiv \frac{\nu_T}{Pr_t} \frac{\partial \tilde{h}}{\partial x_j}$$

A3.4 The turbulent transport and molecular diffusion terms

The turbulent transport and molecular diffusion terms $-\overline{\rho u_j'' \frac{1}{2} u_\iota'' u_\iota''} + \overline{t_{j\iota} u_\iota''}$ are a function of the turbulent kinetic energy. Those terms $(-\overline{\rho u_j'' \frac{1}{2} u_\iota'' u_\iota''} + \overline{t_{j\iota} u_\iota''})$ are substituted by a flux model F_j as follows:

$$F_j \equiv (\bar{\mu} + \sigma_k \mu_t) \frac{\partial k}{\partial x_j}$$

where the term $\bar{\mu}$ is the averaged kinematic viscosity and σ_k is a calibration parameter depending on the turbulence model.

Appendix A4 - Tank Dimensions & Material Properties [7]

Description	Dimension (m)
Length of tank	0.893
Inner radius of tank	0.179
Outer radius of tank	0.198
Liner thickness	0.004
Laminate thickness	0.015
Inner diameter of inlet tube	0.005
Thickness of tube wall	0.002
Length of tube protruding into tank	0.082

Table A4.1: Tank dimensions [7].

	Material	Density (kg/m^3)	Specific heat (J/kg K)	Thermal conductivity (W/m K)
Liner	Aluminium alloy	2730	900	167
Laminate	Carbon-fiber/epoxy	1494	938	1.0

Table A4.2: Tank material properties [7].

Appendix A5 - Inlet boundary conditions [7]

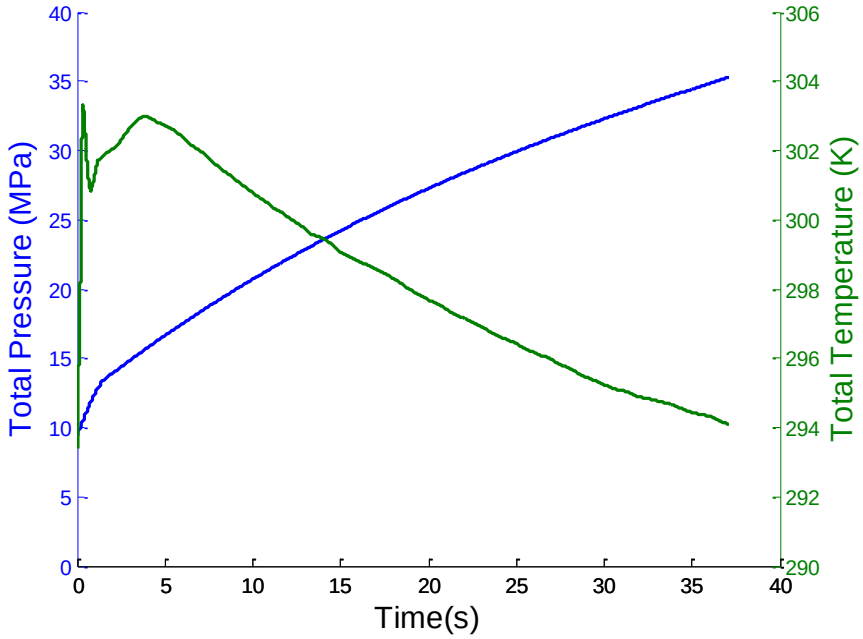

Figure A5.1: Inlet boundary conditions [7].

Appendix A6- Isentropic relations for pipe flow

The isentropic Reynolds number at the exit of the pipe is as follows:

$$Re_{isen} = \frac{\rho_{exit} v_{exit} d}{\mu} \tag{A6.1}$$

The entropy s can be determined from the upstream stagnation pressure P_0 and temperature T_0 (Equation A4.2) from the REFPROP 9.0 software. Since the flow is assumed to be isentropic, the density (ρ_{exit}), the speed of sound (a) and the dynamic viscosity (μ) are just functions of the entropy s and the back pressure p (Equations A4.3 – A4.5).

$$s = s(P_0, T_0) \tag{A6.2}$$

$$\rho_{exit} = \rho(s, p) \tag{A6.3}$$

$$a = a(s, p) \tag{A6.4}$$

$$\mu = \mu(s, p) \tag{A6.5}$$

The Mach number at the exit is determined from Equation A4.6 using the isentropic relations of Equation 3.11.

$$M_{isen} = \sqrt{\frac{2\left(\left(\frac{P_0}{p}\right)^{\frac{\gamma-1}{\gamma}} - 1\right)}{\gamma - 1}} \tag{A6.6}$$

Thus v_{exit} can be determined using the Mach number from Equation A4.6 and the speed of sound from Equation A4.4 as follows:

$$v_{exit} = M_{isen} a \tag{A6.7}$$

As shown in Equations A4.2 – A4.7, the density, velocity and dynamic viscosity at the exit are all independent of the diameter d. Thus, the isentropic Reynolds number can be varied by simply changing the diameter d of the pipe.

Appendix A7 - Diameter & Isentropic Reynolds number values for different pressure ratios and Mach number (H_2)

$P_0\ (MPa)$	$p\ (MPa)$	$^{p}/_{P_0}$	$\dot{m}_{isen}\ \left(^{kg}/_{s}\right)$	Re_{isen}	M_{isen}	$diameter\ (m)$
1	0.99	0.99	4.73E-05	1.00E+04	0.120	6.86E-04
1	0.99	0.99	2.36E-02	2.23E+05	0.120	1.53E-02
1	0.99	0.99	9.43E-02	4.46E+05	0.120	3.06E-02
1	0.99	0.99	3.77E-01	8.92E+05	0.120	6.12E-02
1	0.99	0.99	1.51E+00	1.78E+06	0.120	1.22E-01
1	0.99	0.99	6.03E+00	3.57E+06	0.120	2.45E-01
1	0.99	0.99	4.73E+01	1.00E+07	0.120	6.86E-01
1	0.99	0.99	1.18E+03	5.00E+07	0.120	3.43E+00

Table A7.1: Diameter & isentropic Reynolds number values for pressure ratio of 0.9 (Mach number = 0.120).

$P_0\ (MPa)$	$p\ (MPa)$	$^{p}/_{P_0}$	$\dot{m}_{isen}\ \left(^{kg}/_{s}\right)$	Re_{isen}	M_{isen}	$diameter\ (m)$
1	0.9	0.9	1.52E-05	1.00E+04	0.390	2.24E-04
1	0.9	0.9	7.55E-03	2.23E+05	0.390	5.00E-03
1	0.9	0.9	3.02E-02	4.46E+05	0.390	1.00E-02
1	0.9	0.9	1.21E-01	8.92E+05	0.390	2.00E-02
1	0.9	0.9	4.83E-01	1.78E+06	0.390	4.00E-02
1	0.9	0.9	1.93E+00	3.57E+06	0.390	8.00E-02
1	0.9	0.9	1.52E+01	1.00E+07	0.390	2.24E-01
1	0.9	0.9	3.79E+02	5.00E+07	0.390	1.12E+00

Table A7.2: Diameter & isentropic Reynolds number values for pressure ratio of 0.9 (Mach number = 0.390).

$P_0\ (MPa)$	$p\ (MPa)$	p/P_0	$\dot{m}_{isen}\ \left(kg/s\right)$	Re_{isen}	M_{isen}	$diameter\ (m)$
1	0.8	0.8	1.09E-05	1.00E+04	0.573	1.65E-04
1	0.8	0.8	5.43E-03	2.23E+05	0.573	3.68E-03
1	0.8	0.8	2.17E-02	4.46E+05	0.573	7.36E-03
1	0.8	0.8	8.68E-02	8.92E+05	0.573	1.47E-02
1	0.8	0.8	3.47E-01	1.78E+06	0.573	2.94E-02
1	0.8	0.8	1.39E+00	3.57E+06	0.573	5.89E-02
1	0.8	0.8	1.09E+01	1.00E+07	0.573	1.65E-01
1	0.8	0.8	2.73E+02	5.00E+07	0.573	8.25E-01

Table A7.3: Diameter & isentropic Reynolds number values for pressure ratio of 0.8 (Mach number = 0.573).

$P_0\ (MPa)$	$p\ (MPa)$	p/P_0	$\dot{m}_{isen}\ \left(kg/s\right)$	Re_{isen}	M_{isen}	$diameter\ (m)$
1	0.7	0.7	9.08E-06	1.00E+04	0.731	1.41E-04
1	0.7	0.7	4.52E-03	2.23E+05	0.731	3.15E-03
1	0.7	0.7	1.81E-02	4.46E+05	0.731	6.29E-03
1	0.7	0.7	7.23E-02	8.92E+05	0.731	1.26E-02
1	0.7	0.7	2.89E-01	1.78E+06	0.731	2.52E-02
1	0.7	0.7	1.16E+00	3.57E+06	0.731	5.03E-02
1	0.7	0.7	9.08E+00	1.00E+07	0.731	1.41E-01
1	0.7	0.7	2.27E+02	5.00E+07	0.731	7.05E-01

Table A7.4: Diameter & isentropic Reynolds number values for pressure ratio of 0.7 (Mach number = 0.731).

$P_0\ (MPa)$	$p\ (MPa)$	$^{p}/_{P_0}$	$\dot{m}_{isen}\ \left(^{kg}/_{s}\right)$	Re_{isen}	M_{isen}	$diameter\ (m)$
1	0.6	0.6	8.05E-06	1.00E+04	0.885	1.29E-04
1	0.6	0.6	4.01E-03	2.23E+05	0.885	2.88E-03
1	0.6	0.6	1.60E-02	4.46E+05	0.885	5.75E-03
1	0.6	0.6	6.41E-02	8.92E+05	0.885	1.15E-02
1	0.6	0.6	2.56E-01	1.78E+06	0.885	2.30E-02
1	0.6	0.6	1.03E+00	3.57E+06	0.885	4.60E-02
1	0.6	0.6	8.05E+00	1.00E+07	0.885	1.29E-01
1	0.6	0.6	2.01E+02	5.00E+07	0.885	6.45E-01

Table A7.5: Diameter & isentropic Reynolds number values for pressure ratio of 0.6 (Mach number = 0.885).

$P_0\ (MPa)$	$p\ (MPa)$	$^{p}/_{P_0}$	$\dot{m}_{isen}\ \left(^{kg}/_{s}\right)$	Re_{isen}	M_{isen}	$diameter\ (m)$
1	0.5274	0.5274	7.55E-06	1.00E+04	1	1.24E-04
1	0.5274	0.5274	3.76E-03	2.23E+05	1	2.77E-03
1	0.5274	0.5274	1.50E-02	4.46E+05	1	5.54E-03
1	0.5274	0.5274	6.02E-02	8.92E+05	1	1.11E-02
1	0.5274	0.5274	2.41E-01	1.78E+06	1	2.22E-02
1	0.5274	0.5274	9.62E-01	3.57E+06	1	4.43E-02
1	0.5274	0.5274	7.55E+00	1.00E+07	1	1.24E-01
1	0.5274	0.5274	1.89E+02	5.00E+07	1	6.21E-01

Table A7.6: Diameter & isentropic Reynolds number values for pressure ratio of 0.5274 (Mach number = 1).

Appendix A8 - Pipe length with the l/d of 28.6 (H_2)

Re_{isen}	M_{isen}	$diameter\ (m)$	$^{l}/_{d}$	$l\ (m)$
1.00E+04	0.120	6.86E-04	28.6	1.96E-02
2.23E+05	0.120	1.53E-02	28.6	4.38E-01
4.46E+05	0.120	3.06E-02	28.6	8.76E-01
8.92E+05	0.120	6.12E-02	28.6	1.75E+00
1.78E+06	0.120	1.22E-01	28.6	3.50E+00
3.57E+06	0.120	2.45E-01	28.6	7.01E+00
1.00E+07	0.120	6.86E-01	28.6	1.96E+01
5.00E+07	0.120	3.43E+00	28.6	9.81E+01

Table A8.1: Length of pipe for the different isentropic Reynolds number with Mach number of 0.120.

Re_{isen}	M_{isen}	$diameter\ (m)$	$^{l}/_{d}$	$l\ (m)$
1.00E+04	0.390	2.24E-04	28.6	6.41E-03
2.23E+05	0.390	5.00E-03	28.6	1.43E-01
4.46E+05	0.390	1.00E-02	28.6	2.86E-01
8.92E+05	0.390	2.00E-02	28.6	5.72E-01
1.78E+06	0.390	4.00E-02	28.6	1.14E+00
3.57E+06	0.390	8.00E-02	28.6	2.29E+00
1.00E+07	0.390	2.24E-01	28.6	6.41E+00
5.00E+07	0.390	1.12E+00	28.6	3.20E+01

Table A8.2: Length of pipe for the different isentropic Reynolds number with Mach number of 0.390.

Re_{isen}	M_{isen}	$diameter\ (m)$	$^{l}/_{d}$	$l\ (m)$
1.00E+04	0.573	1.65E-04	28.6	4.72E-03
2.23E+05	0.573	3.68E-03	28.6	1.05E-01
4.46E+05	0.573	7.36E-03	28.6	2.11E-01
8.92E+05	0.573	1.47E-02	28.6	4.21E-01
1.78E+06	0.573	2.94E-02	28.6	8.42E-01
3.57E+06	0.573	5.89E-02	28.6	1.68E+00
1.00E+07	0.573	1.65E-01	28.6	4.72E+00
5.00E+07	0.573	8.25E-01	28.6	2.36E+01

Table A8.3: Length of pipe for the different isentropic Reynolds number with Mach number of 0.573.

Re_{isen}	M_{isen}	$diameter\ (m)$	$l/_d$	$l\ (m)$
1.00E+04	0.731	1.41E-04	28.6	4.03E-03
2.23E+05	0.731	3.15E-03	28.6	9.00E-02
4.46E+05	0.731	6.29E-03	28.6	1.80E-01
8.92E+05	0.731	1.26E-02	28.6	3.60E-01
1.78E+06	0.731	2.52E-02	28.6	7.20E-01
3.57E+06	0.731	5.03E-02	28.6	1.44E+00
1.00E+07	0.731	1.41E-01	28.6	4.03E+00
5.00E+07	0.731	7.05E-01	28.6	2.02E+01

Table A8.4: Length of pipe for the different isentropic Reynolds number with Mach number of 0.731.

Re_{isen}	M_{isen}	$diameter\ (m)$	$l/_d$	$l\ (m)$
1.00E+04	0.885	1.29E-04	28.6	3.69E-03
2.23E+05	0.885	2.88E-03	28.6	8.23E-02
4.46E+05	0.885	5.75E-03	28.6	1.65E-01
8.92E+05	0.885	1.15E-02	28.6	3.29E-01
1.78E+06	0.885	2.30E-02	28.6	6.58E-01
3.57E+06	0.885	4.60E-02	28.6	1.32E+00
1.00E+07	0.885	1.29E-01	28.6	2.63E+00
5.00E+07	0.885	6.45E-01	28.6	1.84E+01

Table A8.5: Length of pipe for the different isentropic Reynolds number with Mach number of 0.885.

Re_{isen}	M_{isen}	$diameter\ (m)$	$l/_d$	$l\ (m)$
1.00E+04	1.000	1.24E-04	28.6	3.55E-03
2.23E+05	1.000	2.77E-03	28.6	7.92E-02
4.46E+05	1.000	5.54E-03	28.6	1.58E-01
8.92E+05	1.000	1.11E-02	28.6	3.17E-01
1.78E+06	1.000	2.22E-02	28.6	6.34E-01
3.57E+06	1.000	4.43E-02	28.6	1.27E+00
1.00E+07	1.000	1.24E-01	28.6	3.55E+00
5.00E+07	1.000	6.21E-01	28.6	1.78E+01

Table A8.6: Length of pipe for the different isentropic Reynolds number with Mach number of 1

Appendix A9 - Diameter & length of pipe for different pressure ratios and isentropic Reynolds number (CH_4)

Re_{isen}	$p/_{P_0}$	M_{isen}	$diameter\ (m)$	$l\ (m)$
1.00E+04	0.991	0.120	3.14E-04	8.98E-03
1.00E+04	0.906	0.390	1.02E-04	2.93E-03
1.00E+04	0.810	0.573	7.50E-05	2.15E-03
1.00E+04	0.713	0.731	6.39E-05	1.83E-03
1.00E+04	0.614	0.885	5.82E-05	1.66E-03
1.00E+04	0.542	1.000	5.59E-05	1.60E-03

Table A9.1: Diameter of pipe for different pressure ratios when $\mathrm{Re}_{\mathrm{isen}} = 10^4$

Re_{isen}	$p/_{P_0}$	M_{isen}	$diameter\ (m)$	$l\ (m)$
2.23E+05	0.991	0.120	7.00E-03	2.00E-01
2.23E+05	0.906	0.390	2.29E-03	6.54E-02
2.23E+05	0.810	0.573	1.67E-03	4.79E-02
2.23E+05	0.713	0.731	1.43E-03	4.08E-02
2.23E+05	0.614	0.885	1.30E-03	3.71E-02
2.23E+05	0.542	1.000	1.25E-03	3.57E-02

Table A9.2: Diameter of pipe for different pressure ratios when $\mathrm{Re}_{\mathrm{isen}} = 2.23 \times 10^5$

Re_{isen}	$p/_{P_0}$	M_{isen}	$diameter\ (m)$	$l\ (m)$
1.78E+06	0.991	0.120	5.60E-02	1.60E+00
1.78E+06	0.906	0.390	1.83E-02	5.23E-01
1.78E+06	0.810	0.573	1.34E-02	3.82E-01
1.78E+06	0.713	0.731	1.14E-02	3.25E-01
1.78E+06	0.614	0.885	1.04E-02	2.97E-01
1.78E+06	0.542	1.000	9.98E-03	2.85E-01

Table A9.3: Diameter of pipe for different pressure ratios when $\mathrm{Re}_{\mathrm{isen}} = 1.78 \times 10^6$

Re_{isen}	$p/_{P_0}$	M_{isen}	$diameter\ (m)$	$l\ (m)$
1.00E+07	0.991	0.120	3.14E-01	8.98E+00
1.00E+07	0.906	0.390	1.02E-01	2.93E+00
1.00E+07	0.810	0.573	7.50E-02	2.15E+00
1.00E+07	0.713	0.731	6.39E-02	1.83E+00
1.00E+07	0.614	0.885	5.82E-02	1.66E+00
1.00E+07	0.542	1.000	5.59E-02	1.60E+00

Table A9.4: Diameter of pipe for different pressure ratios when $\mathrm{Re}_{\mathrm{isen}} = 1 \times 10^7$

Appendix A10 - Diameters, pipe lengths and isentropic Mach numbers using the real gas EOS

EOS	Re_{isen}	P_0 (MPa)	p (MPa)	p/P_0	diameter (m)	l/d	l (m)
real	5.00E+07	30	15.82	0.527	2.24E-02	28.6	6.41E-01
real	5.00E+07	40	21.10	0.527	1.74E-02	28.6	4.99E-01
real	5.00E+07	50	26.37	0.527	1.45E-02	28.6	4.15E-01
real	5.00E+07	60	31.65	0.527	1.26E-02	28.6	3.60E-01
real	5.00E+07	70	36.92	0.527	1.12E-02	28.6	3.22E-01

Table A10.1: lengths and pipe diameters for $Re_{isen} = 5 \times 10^7$ and pressure ratio of 0.527 using real gas EOS

EOS	Re_{isen}	P_0 (MPa)	p (MPa)	p/P_0	diameter (m)	l/d	l (m)
real	3.57E+06	30	24	0.8	2.23E-03	28.6	6.38E-02
real	3.57E+06	40	32	0.8	1.77E-03	28.6	5.05E-02
real	3.57E+06	50	40	0.8	1.49E-03	28.6	4.27E-02
real	3.57E+06	60	48	0.8	1.31E-03	28.6	3.76E-02
real	3.57E+06	70	56	0.8	1.19E-03	28.6	3.40E-02

Table A10.2: lengths and pipe diameters for $Re_{isen} = 3.57 \times 10^6$ and pressure ratio of 0.8 using real gas EOS

Appendix A11 - Tank Material Properties [28, 86]

	Material	Density (kg/m^3)	Specific heat (J/kg K)	Thermal conductivity (W/m K)
Liner	Aluminium alloy	2700	840	238
Laminate	Carbon-fiber/epoxy	1570	902	0.612

Table A11.1: Material properties of liner and laminate of Type III cylinder [28].

	Material	Density (kg/m^3)	Specific heat (J/kg K)	Thermal conductivity (W/m K)
Liner	Plastic	1286	1578	1.17
Laminate	Carbon-fiber/epoxy	1375	1075	1.14

Table A11.2: Material properties of liner and laminate of Type IV cylinder [86].

Appendix A12 – Inlet Boundary Conditions [27, 28, 30]

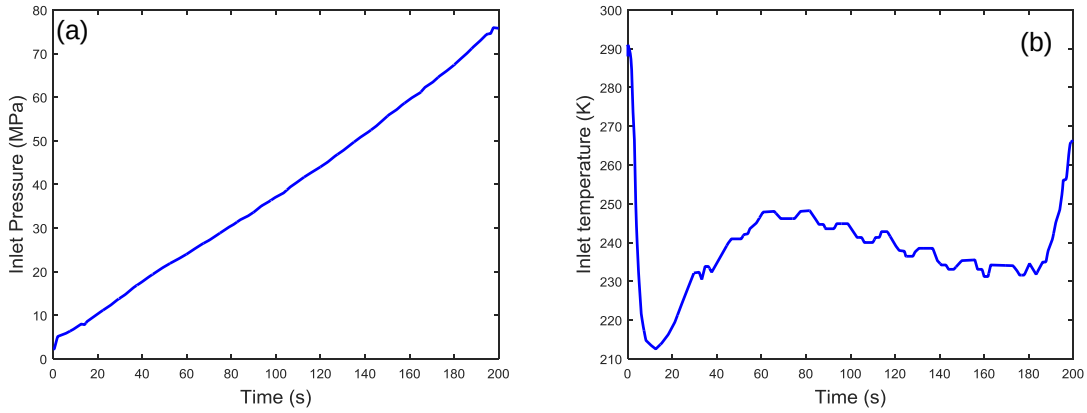

Figure A12.1: (a) Inlet pressure [27], (b) Inlet temperature [27].

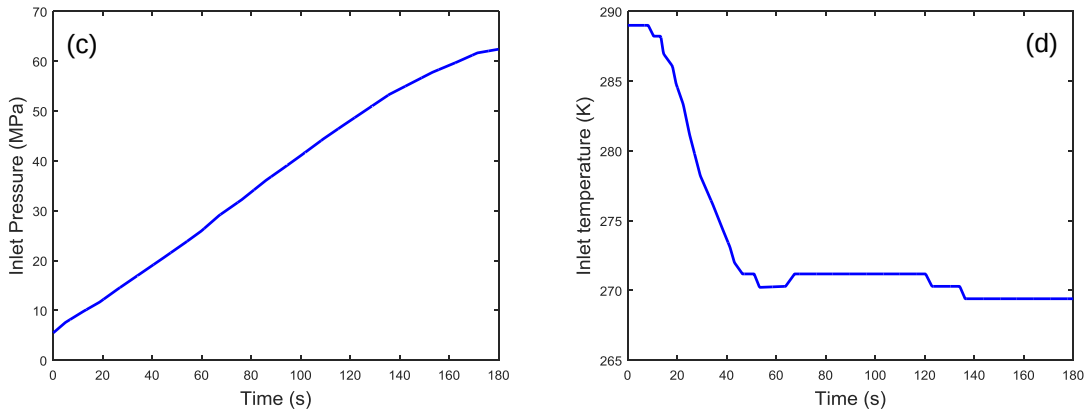

Figure A12.2: (c) Inlet pressure [28], (d) Inlet temperature [28].

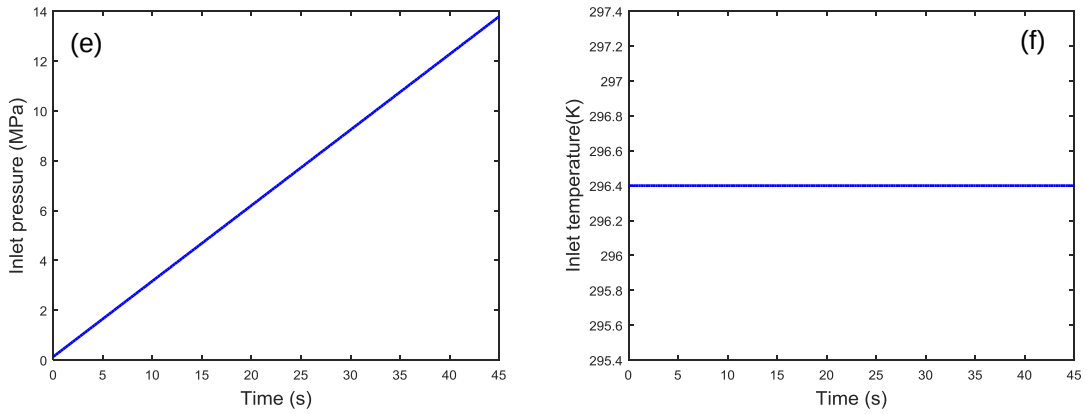

Figure A12.3: (e) Inlet pressure [30], (f) Inlet temperature [30].

Appendix A13 – Reynolds number & Pressure drop within the piping system

Ambient temperature of 313 K and pre-cooling of 233 K

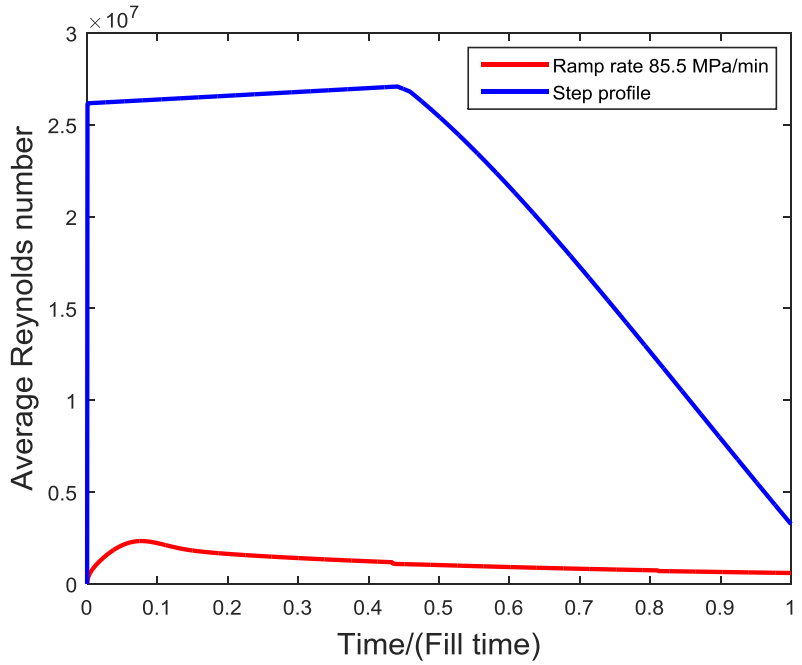

Figure A13.1: Comparison of the Reynolds number in piping system (ramp of 85.5 MPa/min v/s step profile)

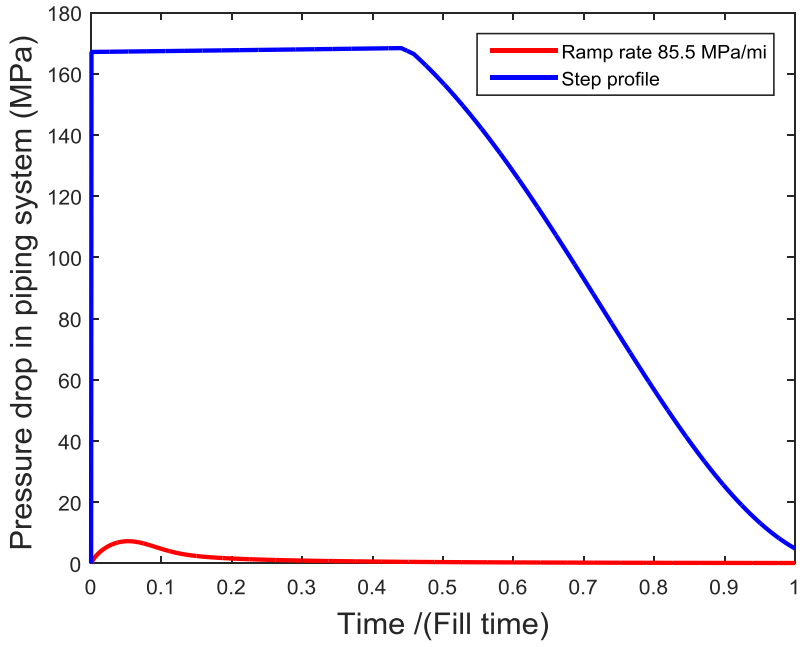

Figure A13.2: Comparison of the pressure drop in piping system (ramp of 85.5 MPa/min v/s step profile)

Appendix A14 - Pressure of bank and dispenser (step profile) for H_2 filling

Ambient temperature of 313 K and pre-cooling of 233 K

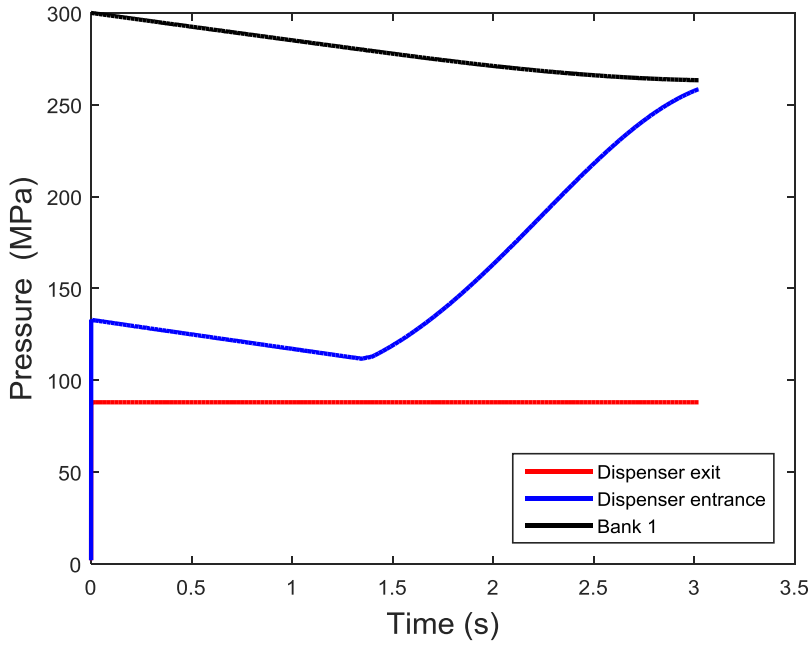

Figure A14.1: Pressure profile at the entrance and exit of the dispenser as well as the bank

Appendix A15 - Comparison of Mach numbers at the exit of dispenser

Ambient temperature - 313 K

- Pre-cooling temperature for step profile - 203 K
- Pre-cooling temperature for ramp profile (85.5 MPa/min) - 253 K

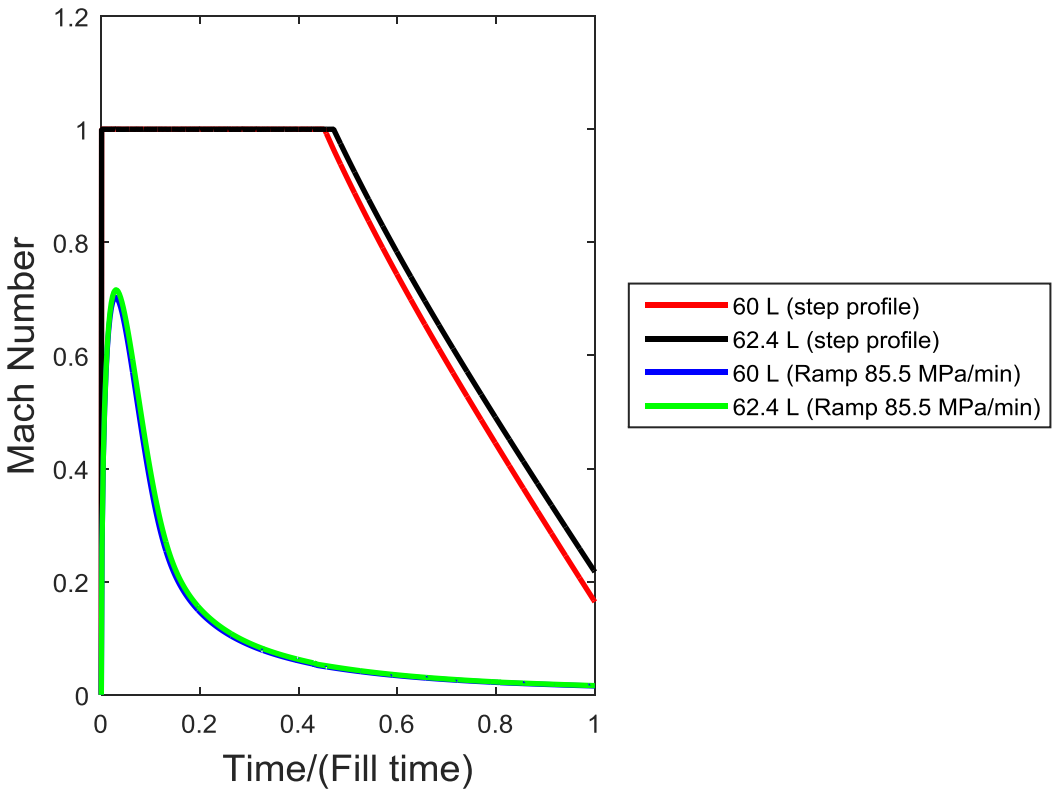

Figure A15.1: Comparison of Mach numbers at the exit of the dispenser at the ambient temperature of 313 K (Step profile v/s ramp rate = 85.5 MPa/min)

Appendix A16 - Reynolds number & heat transfer coefficient (methane)

Ambient temperature - 293 K

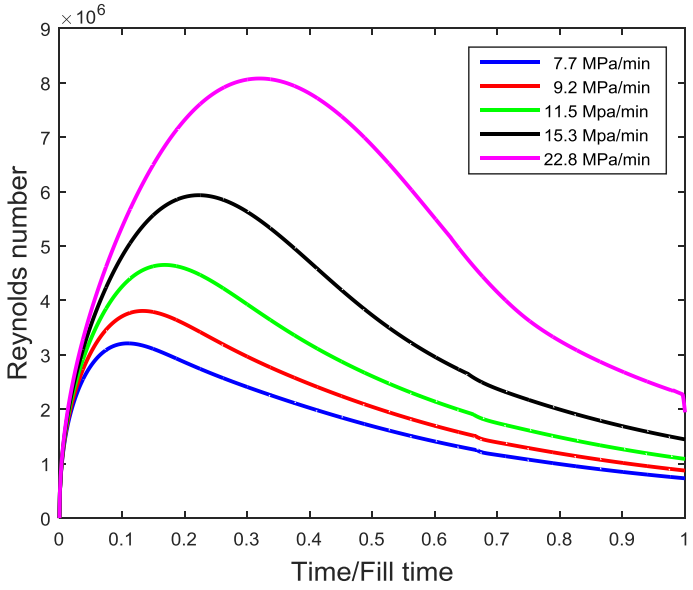

Figure A16.1: Comparison of the Reynolds number at the exit of the dispenser for the different pressure ramp rates.

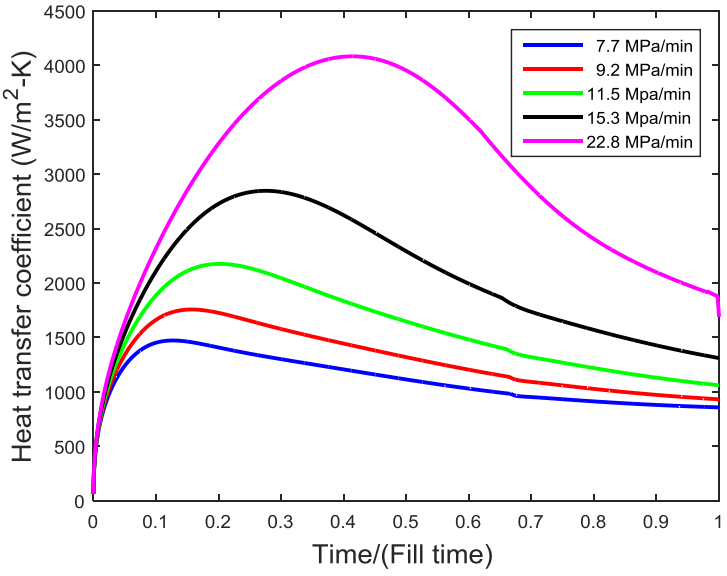

Figure A16.2: Comparison of the heat transfer coefficient in the cylinder for the different pressure ramp rates.

Appendix A17 - Reynolds number and Pressure drop in the piping system (methane)

Step Pressure = 25 MPa v/s Pressure Ramp rate = 7.7 MPa/min

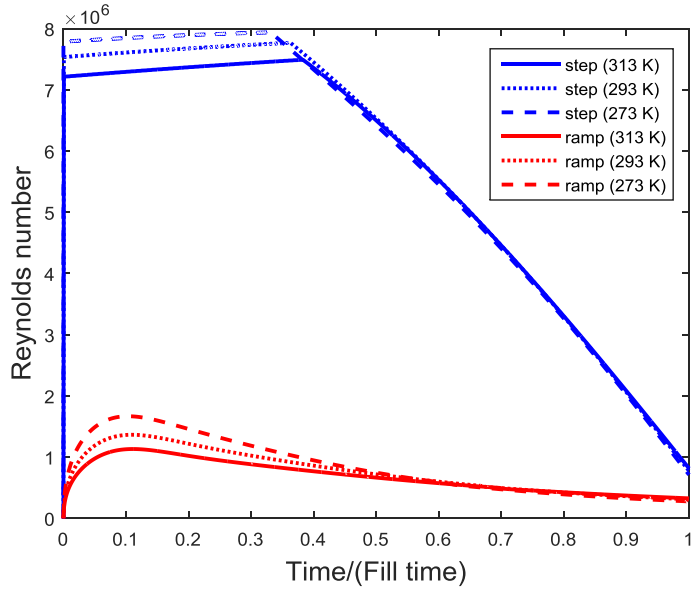

Figure A17.1: Comparison of the Reynolds number in the piping system with the pressure at the exit of the dispenser having step profile of 25 MPa and ramp rate of 7.7 MPa/min for the different ambient temperatures

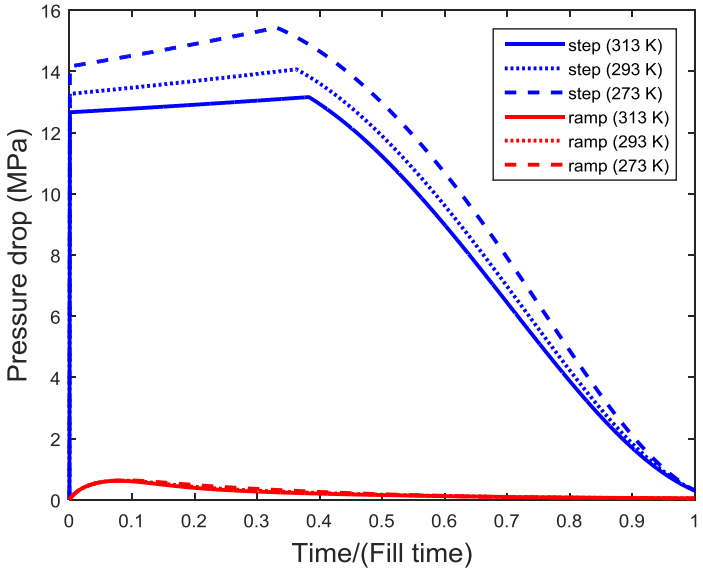

Figure A17.2: Comparison of the pressure drop in the piping system with the pressure at the exit of the dispenser having step profile of 25 MPa and ramp rate of 7.7 MPa/min for the different ambient temperatures